Cyprus
University of
Technology

Faculty of Geotechnical
Sciences and Environmental
Management

Doctoral Dissertation

STUDY AND EVALUATION OF INNOVATIVE METHODS FOR PRINTING SOLID CATALYSTS INTENDED FOR NO$_x$ POLLUTION CONTROL

Vasiliki K. Chatziiona

Limassol, December 2019

CYPRUS UNIVERSITY OF TECHNOLOGY

FACULTY OF GEOTECHNICAL SCIENCES AND
ENVIRONMENTAL MANAGEMENT

DEPARTMENT OF CHEMICAL ENGINEERING

Doctoral Dissertation

STUDY AND EVALUATION OF INNOVATIVE METHODS FOR PRINTING SOLID CATALYSTS INTENDED FOR NO$_x$ POLLUTION CONTROL

Vasiliki K. Chatziiona

Limassol, December 2019

Approval Form

Doctoral Dissertation

STUDY AND EVALUATION OF INNOVATIVE METHODS FOR PRINTING SOLID CATALYSTS INTENDED FOR NO$_x$ POLLUTION CONTROL

Presented by

Vasiliki K. Chatziiona

Supervisor: Costas Costa, Professor

Signature _____

Member of the committee: Ioannis Yentekakis, Professor

Signature _____

Member of the committee: Charis Theocharis, Professor

Signature _____

Cyprus University of Technology

Limassol, December 2019

Copyrights

To my loving grandparents

ACKNOWLEDGEMENTS

Vasiliki K. Chatziiona

ABSTRACT

The present Doctoral Dissertation concerns the evaluation and development of an innovative method for preparing solid supported-Pt catalysts intended for NO_x pollution control. In particular, the alternative and cutting-edge approach of developing catalysts via multilayer inkjet printing was examined, so as to control the structure of solid catalysts at a nanoscale level, using two different printers, i.e., a modified Epson L800 printer and a commercial material printer (DMP-2850). For the first time ever, one 0.1 wt% $Pt/MgO/CeO_2$ and two 0.1 wt% Pt/Al_2O_3 catalysts were prepared by novel inkjet printing and compared, in terms of their catalytic behaviour towards the $NO/H_2/O_2$ reaction, against four catalysts prepared by a standard and a modified wet impregnation method.

It is worth mentioning that the inkjet-printed Pt/Al_2O_3 catalysts presented excellent activity and wide operating temperature window (T_R=100-250°C) towards the selective catalytic reduction of NO by H_2 under strongly oxidizing conditions (H_2-SCR) in the very low-temperature range of 100-200°C. Specifically, the Epson printed Pt/Al_2O_3 catalyst, presented X_{NO}= 91% at 150°C, while the DMP printed Pt/Al_2O_3 catalyst presented an average X_{NO}= 97% for the low-temperature range of 140-200°C and X_{NO}= 99.5% at 175°C. As for the DMP inkjet-printed $Pt/MgO/CeO_2$ catalyst, it showed remarkable catalytic performance (X_{NO}= 100%, S_{N2}= 100%, $T_R \geq$ 200°C) in the absence of oxygen (NO/H_2 reaction), a result which has never been reported before, according to the author's knowledge, in particular without the formation of NH_3 as a by-product.

Surface reactivity studies by transient methods performed within the present work indicated that the inkjet printing process leads to a unique surface structure of the printed catalysts that probably favours the formation of different intermediate NO_x species, which are active at very low reaction temperatures. Moreover, it was proven through combined SSITKA-DRIFTS studies, that the different catalyst preparation methods utilized for the development of $Pt/MgO-CeO_2$ catalysts, affects the formation and concentration of different active adsorbed intermediate NO_x species on Pt surface, as well as on the support and the metal-support interphase. Furthermore, the transient experiments revealed important information towards the understanding of basic mechanistic issues of the present catalytic system (e.g., surface coverage of NO_x intermediate species and N-containing species, H_2 spillover).

Keywords: novel catalyst inkjet printing, supported Pt catalysts, H_2-SCR, NO reduction.

TABLE OF CONTENTS

LIST OF TABLES

LIST OF FIGURES

LIST OF ABBREVIATIONS

ΔT	Operating Temperature Window
θ	Surface Coverage
BET	Brunauer-Emmet-Teller (method)
BSE	Backscattered Electrons
CUT	Cyprus University of Technology
D	Dispersion (%)
DMP	Dimatix Material Printer
DoD	Drop-on-Demand
DRIFTS	Diffuse Reflectance Infrared Fourier Transform Spectroscopy
EDS	Energy Dispersive X-ray Spectroscopy
FTIR	Fourier Transform Infrared Spectroscopy
GCMS	Gas Chromatography-Mass Spectrometry
GHSV	Gas Hourly Space Velocity
ICPMS	Inductively Coupled Plasma Mass Spectrometry
IF	Ink Formula
IJP	Inkjet Printing
IR	Infrared
JM	Jetting Module
LNT	Lean NO_x Traps
MS	Mass Spectroscopy
NO_x	Nitrogen oxides
N_2	Nitrogen
O_2	Oxygen
OSC	Oxygen Storage Capacity
Pt	Platinum
SCR	Selective Catalytic Reduction
SE	Secondary Electrons
SEM	Scanning Electron Microscopy
SMSI	Strong Metal-Support Interactions
S_{N2}	Nitrogen Selectivity
SSITKA	Steady State Isotopic Transient Kinetic Analysis

t	Time
T_M	Maximum Temperature
T_R	Reaction Temperature
TPD	Temperature Programmed Desorption
TPSR	Temperature Programmed Surface Reaction
TWC	Three-Way Catalytic Converter
WI	Wet Impregnation
wt	Weight Percentage
XRD	X-Ray Diffraction
X_{NO}	Nitric Oxide Conversion

SCOPE AND INNOVATION

The scope of the present doctoral dissertation is to develop and evaluate Pt-supported catalysts, via innovative catalyst synthesis methods. In particular, this work introduces a state-of-the-art methodology for the design and development of novel solid catalysts through multilayer inkjet printing. The specific catalysts are intended for environmental applications, such as the selective catalytic reduction of nitric oxide by hydrogen in the presence of excess oxygen (H_2-SCR of NO), a reaction which has been utilized for the evaluation of the catalytic performance of the prepared catalysts.

The main purpose of this dissertation is to improve existing catalysts such as Pt/Al_2O_3 and Pt/MgO-CeO_2, with the latter being granted an International Patent [1] and found to show remarkable catalytic performance with extremely high N_2 selectivity. Subsequently, in the present work, much effort has been devoted in synthesizing 0.1 wt% Pt/Al_2O_3 and 0.1 wt% Pt/MgO-CeO_2 catalysts with innovative preparation methods. Initially, the Pt-supported catalysts were prepared by the standard wet impregnation method, which have been used as benchmarked catalysts. Afterwards, the same catalysts were prepared, by modifying the existing preparation method of wet impregnation with the use of an ink formula as the solvent.

Furthermore, as a proof of concept, an Epson L800 printer was modified to allow the development of the first-ever inkjet printed Pt/Al_2O_3 catalyst, using the same ink formula. The scope of this work also included the preparation of the Pt/Al_2O_3 and Pt/MgO-CeO_2 catalysts using a commercial material printer so as to have more control over the printing process. Thus a new Dimatix Materials Printer (DMP-2850) was employed to continue and advance the initial work. In particular, the material printer provided two high-speed cameras that guaranteed that the printing technique was executed correctly, by allowing the direct viewing of the jetting nozzles and ensuring exceptional drop placement accuracy.

In addition, the present dissertation aimed to examine the efficiency of all the catalysts towards the low-temperature H_2-SCR of NO, under strong oxidizing conditions. Further studies were also performed on the examined catalysts in order to determine their physical characteristics (e.g., surface area, surface morphology, particle sizes). Extensive mechanistic and transient studies were performed on all the catalysts so as to study the interaction between the reaction gases with the solid surfaces, the surface and interface

structure (crystalline phases), the surface coverage of N-containing intermediate species and the chemical structure of adsorbed NO_x intermediates (active or inactive/spectator) formed during the H_2-SCR of NO.

The innovative methods that were used during this doctoral dissertation provide a starting point for the development of novel catalysts that can be utilized to address air pollution control (e.g., De-NO_x). The Pt/Al_2O_3 and Pt/MgO-CeO_2 catalysts that were prepared for the first time ever using a modified wet impregnation method (ink formula), as well as the novel inkjet printing technique, were synthesized solely for the purposes of this dissertation and up to now, they have never been used for nitric oxide reduction.

It is worth mentioning that the present work provides an example of how the combination of applied and basic research can lead to improved catalysts' development, especially through the novel technique of "Catalysts Printing". The successful implementation of the innovative inkjet-printing technique allowed the ''building/development'' of the catalysts, drop by drop, and took full advantage of the picolitre precision and control of deposition of each layer that was provided via the printing devices.

This dissertation attempts to achieve catalyst design through printing, which is essentially the connection of the catalyst preparation techniques with the final characteristics of a catalyst. Therefore, the novel inkjet printing technique strives to attain almost perfect dispersion of the metallic phase, near-perfect contact between various crystalline phases, ideal morphology and excellent catalytic performance in the very low-temperature range of 100-200ºC. Successful development and application of this technique are expected to revolutionize the way of catalyst synthesis used in the industry.

CHAPTER 1: INTRODUCTION

1.1. NO_x Emissions

Catalysis is a key technology to provide realistic solutions to many environmental issues. Environmental catalysis has continuously grown in importance over the last four decades not only in terms of the worldwide scientific and market interest but also as a driver of advances in the whole area of catalysis [2]. Environmental catalysis can be defined as technologies using catalysts to reduce the emission of environmentally unacceptable compounds. The exhausts from automobiles and stationary sources, such as power plants, contain CO, NO_x and hydrocarbons and converting these pollutants to desirable products with the use of catalysts is a challenging process [2], [3]. The current PhD work focuses on the catalytic elimination of nitrogen oxides (NO_x) and specifically the reduction of nitric oxide (NO) to nitrogen (N_2) with the use of hydrogen (H_2), under strongly oxidizing conditions.

The main source of NO_x emissions is the combustion of fuels (coal, gas, petroleum, hydrogen, biogas, etc) at high temperatures in electrical power plants (stationary sources), vehicles and ships (mobile sources). The gases resulting from the combustion of fossil fuels contain NO_x pollutants consisting mainly of NO and NO_2, with NO representing 90 to 95% of the total NO_x emissions [4], [5]. Bosch and Janssen [6] categorize three types of NO_x formed during the combustion process. The first type (thermal NO_x) is formed by the oxidation of N_2 at high temperatures (Eq. 1.1) and is the main source of NO in gaseous combustion systems.

$$N_2 + O_2 \leftrightarrow 2NO, \Delta H^o_{298}= 180.6 \text{ kJ/mol} \tag{1.1}$$

This reaction takes place above 1000°C and follows the Zeldovich mechanism of chain reactions (Equations 1.2 and 1.3) involving N^* and O^* activated atoms. The rate of NO formation is essentially controlled by reaction 1.2, due to its high activation energy, and increases exponentially with temperature. The Zeldovich mechanism is the most well-known chemical pathway for NO formation under most engine conditions [3], [7], [8]. The thermal NO reactions take place in a few tens of microseconds and are highly dependent on temperature, residence time, and atomic oxygen concentration [9].

$$N_2 + O^* \rightarrow NO + N^* \tag{1.2}$$

$$N^* + O_2 \rightarrow NO + O^* \hspace{6cm} (1.3)$$

The second type is fuel NO_x which is formed by the oxidation of the nitrogen-containing compounds in the fuel. Fuel NO is the main source of NO in coal-fired systems, where coal contains approximately 1% N_2 by weight, depending on the coal type. Contrary to thermal NO_x, fuel NO_x formation is relatively independent of temperature at normal combustion temperatures [3], [9]. The third type, prompt NO_x, is produced by the formation first of intermediate HCN via the reaction of nitrogen radicals and hydrocarbons followed by the oxidation of the HCN to NO. The formation of prompt NO_x is only significant in fuel-rich conditions and at low temperatures [6].

NO_x can also be produced by natural sources, such as lightning, oxidation of atmospheric NH_3 and volcano activities. However, natural sources are not as crucial as the anthropogenic ones and their prevalence is limited [10]. NO_x sources can be classified by the emitting entity as well, and not only by the formation mechanism. According to Vestreng et al. [11], anthropogenic NO_x emissions in 2005 were caused by 54% due to mobile sources (road transport, off-road transport) and by 46% due to stationary sources (power plants, industry, residential sector) [11], [12]. Figure 1.1 compares the emissions of NO_x by EU members from 1990 until 2016 [13]. During 2016, a similar trend can be observed, since around 54% is caused by mobile sources (agriculture, road and non-road transport) and almost 46% due to stationary sources. A diminishing trend can also be observed in the last 25 years in the EU countries.
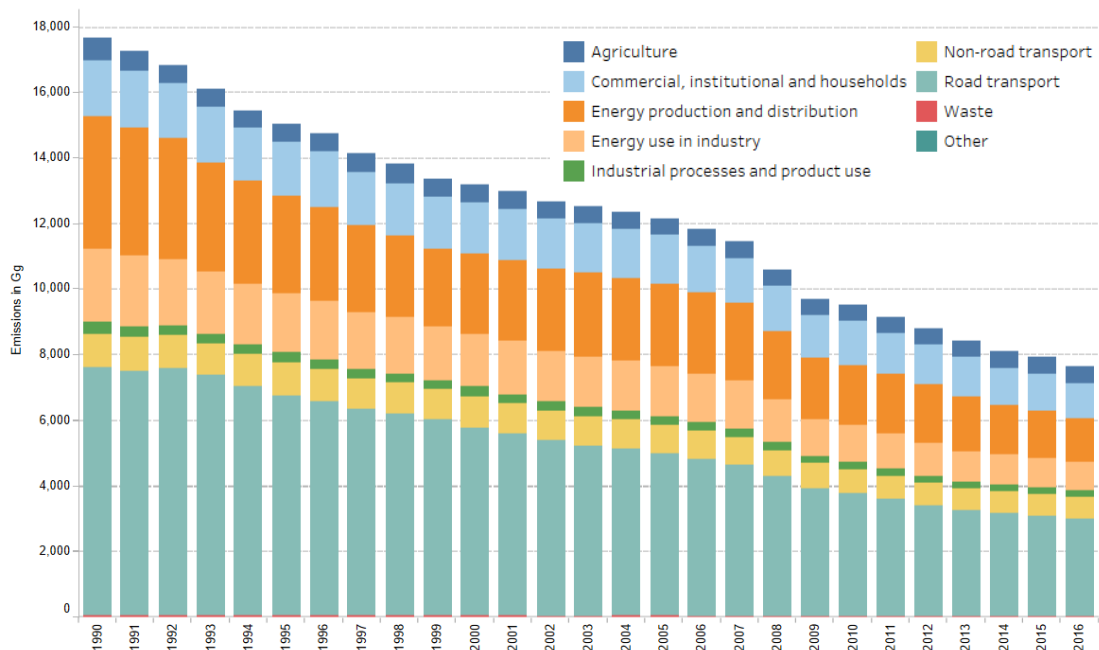
Figure 1.1: NO_x emissions by EU members over time [13].

1.2. NOx Pollution

Nitrogen oxides can react with atmospheric components leading to unfavourable changes in their state of equilibrium as can be seen in Figure 1.2 [4]. The reaction of NO_x with VOCs (volatile organic compounds) in sunlight (i.e. photochemical reactions) leads to the formation of tropospheric ozone (O_3). This ground-level ozone presents health problems and causes damage to vegetation and wildlife [14]. NO_x, O_3 and hydrocarbons are the key substances for the appearance of photochemical smog [7].
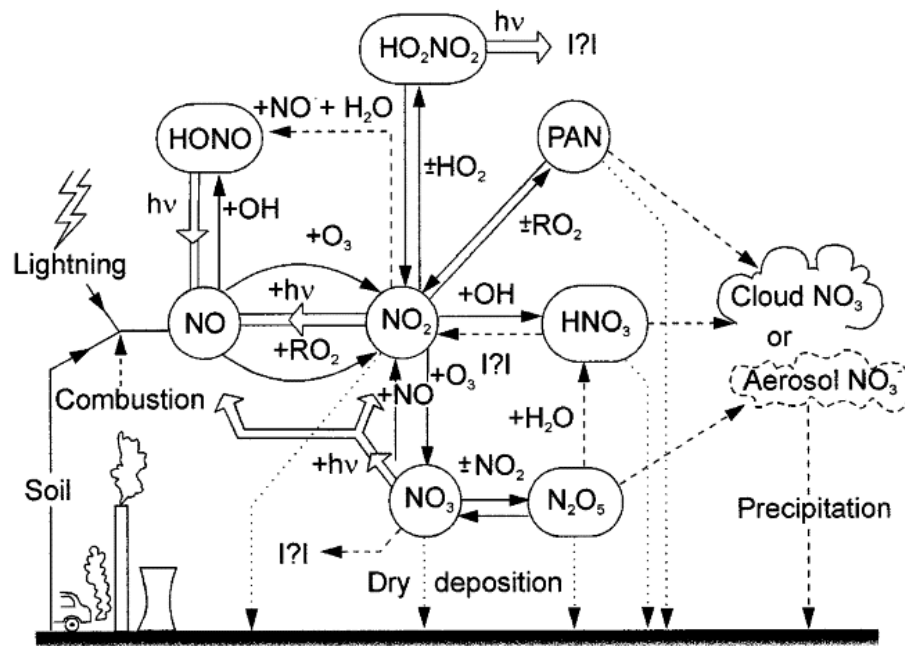
Figure 1.2: Chemical transformations of atmospheric NO_x: ($\Rightarrow$) photochemical processes, ($\rightarrow$) thermal gas-phase processes, (--$\blacktriangleright$) heterogeneous reaction, ($\cdots\blacktriangleright$) dry deposition [4].

Additionally, NO is oxidized very quickly to NO_2 in the presence of oxygen, which is a toxic substance that affects the respiratory system of humans and animals. In the presence of water, NO_2 converts to nitrous (HNO_2) and nitric acid (HNO_3), which are components of acid rain [4], [15], [16]. Acid rain causes acidification of many aquatic ecosystems and can cause their biological death. It has been demonstrated to impact cultural resources by accelerating the weathering of buildings and outdoor sculptures [17], [18]. Also, the reaction between NO_2 and hydrocarbons leads to peroxyacetyl-nitrate (PAN) which is more stable and harmful than ozone and inhibits photosynthesis [4], [15], [16]. NO produced by aircraft traffic, or by decomposition of N_2O plays a role in the destruction of the vital stratospheric ozone layer, which protects the earth from the harmful UV radiation

($\lambda < 242$ nm) [4], [7], [10]. The reaction mechanism can be summed up in the following scheme (Figure 1.3).
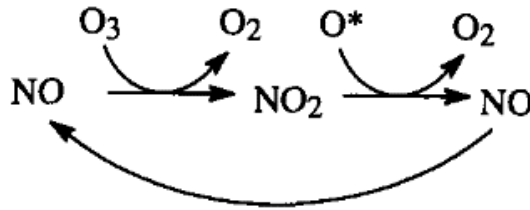
Figure 1.3: Participation of NO in the photochemical decomposition cycle of O_3 [7].

NO is a major atmospheric pollutant and is immediately dangerous to life and health at levels of 100ppm according to the National Institute for Occupational Safety and Health [19]. Nitric oxide is able to reach all parts of the respiratory system because of its low solubility in water. According to epidemiological studies, it was shown that biologically active NO is a poisonous product of the in vivo enzyme-catalyzed transformation of the amino acid, arginine. It diffuses through the epithelium (alveolar-cells) and the adjacent capillary vessels of the lungs and damages the epithelium structures and their function throughout the lungs, provoking both lung infections and respiratory allergies like bronchitis, pneumonia, etc. [3], [6], [15]. On the other hand, some biological studies, have shown that NO acts as an essential messenger, which transmits the necessary information to the white blood cells within the bloodstream to destroy tumour cells and to the neurotransmitters to dilate the blood vessels [3], [15].

As the presence of NO_x in the atmosphere results in many ecological and health hazards, the control of its emission is of utmost importance. The global concern for air quality, in general, has introduced tougher pollutants emission standards for both stationary and mobile sources. The NO concentration in exhaust gas typically averages between 600 and 1200ppm, depending on the engine combustion conditions, diesel or gasoline, and on the driving conditions [8]. Increasingly stringent emission legislations, such as EPA US 2010 (Environmental Protection Agency) and Euro VI, for NO_x in mobile applications, require the use of intensification of NO_x reduction after-treatment technologies, such as the selective catalytic reduction (SCR) [20]. US EPA and the Department of Transportation's National Highway Traffic Safety Administration past new regulations on fuel economy and emission standards, such as 20mg/mile for NO_x emission. Also, European Union (EU) regulation No 715/2007 aims to decrease NO_x emissions down to 0.08 g/km for diesel and 0.06 g/km for gasoline engines for passenger cars [21], [22].

A number of policies have been implemented that directly or indirectly reduce the emissions of nitrogen oxides. Figure 1.4 demonstrates the commitment for NO_x reduction for 2020 and 2030 by EU28 and the Member States under the National Emission Ceilings (NEC) Directive 2016/2284 of the European Parliament and the council of the EU. It should be noted that emissions for 2020 and 2030 are projected data, as submitted by the Member States under the new NEC Directive [23], [24].
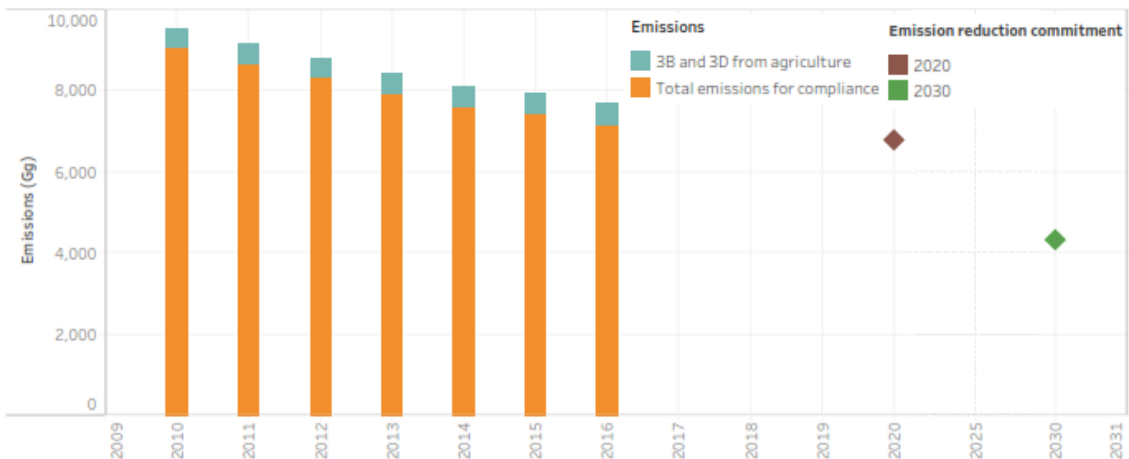
*Note: NO_x emissions from the two main agricultural activities, manure management (3B) and agricultural soils (3D), are subtracted, as required by the new NEC Directive

Figure 1.4: Emission reduction commitment for NO_x pollutant by EU28 and the Member States under the NEC Directive for 2020 and 2030 [23].

1.3. Basic Principles of Catalytic Effect

1.3.1. Catalyst

The definition of a catalyst has been discussed many times and it can be generally described as a 'material that converts reactants into products, through a series of elementary steps, in which the catalyst participates while being regenerated to its original form at the end of each cycle during its lifetime' [25]. It is noted that while a catalyst changes the kinetics of a chemical reaction, it does not influence the thermodynamic equilibrium of the process, i.e. a catalyst cannot induce a reaction that is not allowable under the laws of thermodynamics [25]–[27]. Also, catalysts are not consumed during a reaction, but in reality they are submitted to a slow transformation with use, causing a general decrease in their activity and/or selectivity [26].

A catalyst affects the kinetics of a chemical reaction and it can only increase the rate at which the reaction approaches equilibrium [28]. Consequently, a catalyst can provide an alternative reaction path that lowers the activation energies of the different reaction steps,

reaching, therefore, the equilibrium in an easier and faster way. Figure 1.5 compares the energy profile for two different reaction paths, with and without the use of a catalyst. As seen in Figure 1.5, the energy that is related to the activation of the chemical reaction between reactants on the catalyst surface is less than the energy needed for the uncatalyzed reaction. The enthalpy change (ΔH) for the overall reaction, normally referred to as the heat of reaction, is the same for both reactions [27], [29].
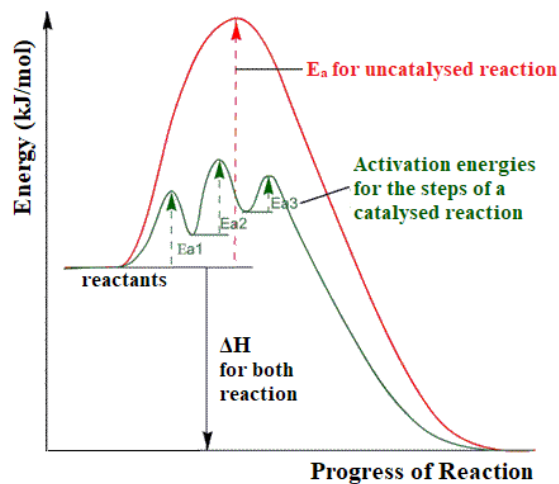
Figure 1.5: Reaction energy profile for a chemical reaction with and without a catalyst.

Figure 1.5 also illustrates an activation barrier that always exists and must be overcome so as to complete the chemical reaction. The activation energy (E_a) of a reaction can be calculated by the Arrhenius equation:

$$k = Ae^{\frac{-E_a}{RT}}$$
(1.4)

where; k is the rate constant, A is the pre-exponential factor which is constant for each chemical reaction system, E_a is the activation energy for the reaction, R is the universal gas constant and T is the absolute temperature (K) [5]. The real activation energy of a reaction is determined by the rate-limiting or rate-determining step of the reaction. As it was pointed out by Balakos et al. [30], the rate-limiting step is a delicate balance of intermediate concentrations, surface intrinsic properties and experimental reaction conditions.

A catalytic reaction includes several steps: (i) diffusion of the reactants through a boundary layer surrounding the catalyst particle, (ii) intraparticle diffusion of the reactants into the catalyst pores to the active sites, (iii) adsorption of the reactants onto active sites, (iv) surface reactions involving formation or conversion of various adsorbed intermediates, possibly including surface diffusion steps, (v) desorption of products from

catalyst sites, (vi) intraparticle diffusion of the products through the catalyst pores and finally (vi) diffusion of the products across the boundary layer surrounding the catalyst particle. One or more of the above steps could be the rate-determining step, regulating the total speed of the reaction [25], [26].

Catalytic reactions can be categorized as homogeneous or heterogeneous based on the catalyst nature in relation to the reactants. In homogeneous reactions, the catalyst is in the same physical phase as the reactants and products (liquid, solid, gaseous), whereas in heterogeneous reactions the catalyst is in a different phase. Usually, in the latter case, the catalyst is solid and the reactants are either gases or liquids [26], [27]. The current dissertation examines a heterogeneous reaction.

According to Dumesic et al. [25], a catalyst can be considered as a ''good'', when it exhibits the following properties.

- Good selectivity (see subchapter 1.3.2) for production of the desired products and hence minimal production of undesirable by-products.
- Achieve adequate rates of reaction at the desired reaction conditions of the process (remembering that achieving good selectivity is usually more important than achieving high catalytic activity).
- Stable performance at reaction conditions for long periods of time, or it should be possible to regenerate good catalyst performance by an appropriate and simple treatment of the deactivated catalyst after short periods.
- Good accessibility of reactants and products to the active sites such that high rates can be achieved per reactor volume.

1.3.2. Activity and Selectivity

The most important properties of a catalyst are its activity and selectivity under operating conditions. Activity is defined as the speed at which a chemical reaction reaches the equilibrium. Catalytic activity is expressed in terms of reaction rates, preferably normalized to the surface area of the active phase (e.g., metal surface area for supported metal catalysts) or to catalyst weight. From the industrial point of view, activity is also defined as the amount of reactant transformed into product per unit of time and unit of reactor volume. The best measure for the comparison of catalytic activity between different catalysts is the turnover rate or turnover frequency (TOF) since it is normalized to the number of active sites and represents the rate at which the catalytic cycle is

performed. In cases where the rate is not uniform within the catalytic reactor, it is useful to report the rate as a space-time yield (STY), expressed in units of amount of product made in the reactor per unit time and unit reactor volume [25], [29].

The simplest measure of catalytic activity that is used very often is the conversion (X_i, %) of a reactive substance, generally defined through the following equation.

$$X_i(\%) = \frac{n_{io} - n_i}{n_{io}} \cdot 100 \qquad (1.5)$$

where, n_{io} are the moles of the reactant (i) at the beginning of the reaction (at t=0) and n_i at different reaction times (t=t). Considering that the reaction is under constant volume, where no reactant fluid is added or removed during the duration of the reaction, then the moles from the previous equation can be divided with the constant volume, resulting in the concentration of the reactant, i.e.:

$$X_i(\%) = \frac{C_{io} - C_i}{C_{io}} \cdot 100 \qquad (1.6)$$

Moreover, when evaluating the catalytic performance emphasis is given on the selectivity of the desired product and not only on activity. In catalytic reactions, there is often more than one product formed by the reactants, where usually one of these products is most desirable. The selectivity of a catalyst is a measure of the extent at which a catalyst accelerates the reaction leading to the formation of one or more desired products. It is defined as the ratio of the rate of formation of the desired product to the rate of consumption of the reactant. Considering a simple reaction where: A$\rightarrow$ B + C, then the selectivity of the first product (S_B) can be calculated based on equation 1.7 [31].

$$S_B(\%) = \frac{C_B}{C_{AO} - C_A} \cdot 100 \qquad (1.7)$$

where, C_A and C_B are the concentrations of the reactant and the product, respectively, at t=t, and C_{AO} is the initial concentration of the reactant. By combining equations 1.6 and 1.7, then, selectivity can be calculated by equation 1.8. As can be seen, selectivity depends on the conversion of the reactants. A desired catalyst has good selectivity, even at high conversions. Therefore, the multiplication of $S_B \cdot X_A$ that results in C_B/C_{AO} should be as high as possible. This parameter ($S_B \cdot X_A$) is called the yield of a catalyst towards product B (Y_B).

$$S_B(\%) = \frac{C_B}{C_{Ao} \cdot X_A} \cdot 100 \qquad (1.8)$$

Selectivity usually depends on the temperature, pressure, composition of the reactants, degree of conversion of the reaction and, of course, the chemical composition of the catalyst. For this reason, the selectivity of a product is necessary to be referred to specific experimental conditions [29], [32]–[34]. It should be noted that in the development process, emphasis is usually put on three aspects of catalyst performance in the order: selectivity > deactivation > activity [32].

1.3.3. Operating Temperature Window (ΔT)

An operating temperature window is defined as the temperature range (ΔT) in which the catalyst exhibits conversion (X_i) greater than or equal to a certain percentage of its maximum conversion (X_{NO}^{max}). Figure 1.6 indicates the operating temperature window of NO during the selective catalytic reaction of $NO/H_2/O_2$. In the latter figure, ΔT is defined as the temperature range in which the catalyst retains at least half of its maximum conversion. The temperature window is a very important parameter when evaluating a catalyst since in most industrial catalytic processes the temperature of the catalytic bed is not constant and changes within a temperature range. For this reason, the larger the value of ΔT is, the better the desired operation of the catalyst is under practical conditions [33].
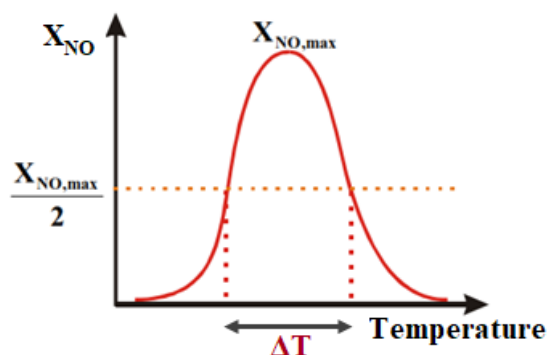
Figure 1.6: Operating Temperature Window for the selective catalytic reaction of $NO/H_2/O_2$ [33].

1.3.4. Active Sites

The principle of Sabatier states that a good heterogeneous catalyst is a material that exhibits a moderate strength of interaction with the reactants, products, and intermediates of the catalytic process. He formulated a chemical theory of catalysis involving the formation of unstable chemical compounds as intermediate stages, which determine the direction and rate of the reaction. Those unstable surface intermediates require chemical bonding of reactants to the catalyst surface, most likely between atoms or functional groups of reactant and surface atoms of the catalyst. This leads to the principle of active

sites [25], [29], [35]. The Sabatier principle is related to linear free energy relationships such as a Brønsted relation, where, ΔE is the decrease in activation energy corresponding to an increase Δq in the heat of reaction (enthalpy) [29].

$$\Delta E = \alpha \cdot \Delta q \tag{1.9}$$

The principle can be shown graphically through ''volcano plots''. These volcano curves (Figure 1.7), first reported by Balandin [36], result when a quantity correlated with the rate of a reaction under consideration is plotted against a measure of the stability (heat of adsorption, bond strength) of the intermediate compound. The volcano curve indicates that the strength of chemisorption has to be adequate to modify the electronic structure of the substrate but not too strong to be close to the compound formed by the catalytic centre [37]. Particularly, if the interactions of the catalyst surface (active sites) with the various adsorbed species of the reaction mechanism are too weak, then this leads to high activation energies for surface reactions and thus low catalytic activity. On the other hand, if the interactions are strong, then excessive blocking of surface sites will happen by these adsorbed species, resulting again in low catalytic activity [25]. If a catalyst turns out to lie in the narrow region of dissociative chemisorption energies for a given process, the volcano relation will lead to a reasonably good catalyst [38], [39].
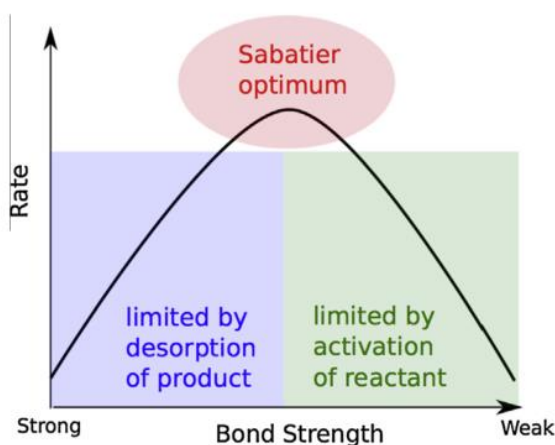
Figure 1.7: Schematic representation of the qualitative Sabatier principle [38].

The principle of active sites is not limited to metals as they include metal cations, anions, Lewis and Brønsted acids, organometallic compounds, etc. Moreover, active sites may include more than one species (or atom) to form multiplets or ensembles. The active sites must provide coordination sites so as to be accessible for chemisorption from the fluid phase [29], [36]. Burwell et al. [40] suggested that many types of active sites would involve coordinatively unsaturated surface ions and that chemisorption might occur at such sites.

Thus, active sites are to be considered as atoms or groups of atoms which are embedded in the surface of a matrix in which the neighbouring atoms (or groups) act as ligands [29], [36].

The heterogeneity of active sites on solid catalyst surfaces and its consequences were emphasized in 1925 by Taylor [41]. Taylor suggested that the concentration of sites where rate-determining catalytic reaction steps occur is much smaller than the total concentration of available surface sites [41], [42]. Heterogeneous catalysts typically contain different types of surface sites, because crystalline solids exhibit crystalline anisotropy. Equilibrated single crystals expose different faces with different atomic structures to minimize total surface energy. It should be noted that most catalytic solids are polycrystalline [25].

Also, in order to achieve high surface areas, most catalysts contain particles with sizes in the nanometer length scale. The surfaces of these nanoscopic particles contain sites associated with terraces, ledges, kinks, and vacancies (Figure 1.8) with sites having different coordination numbers. The variation of coordination numbers of surface atoms will lead to different reactivity and activity of the corresponding sites. Moreover, the surface atomic structure and composition may change as the catalytic reaction proceeds [25], [29]. The surface atomic structure plays a very important role during a surface reaction. For instance, flat Pt surfaces do not dissociate CO, whereas stepped surfaces do. Similarly, H_2 dissociation is activated on Pt (111) surface, though on stepped surfaces dissociation takes place practically without an activation barrier [43].
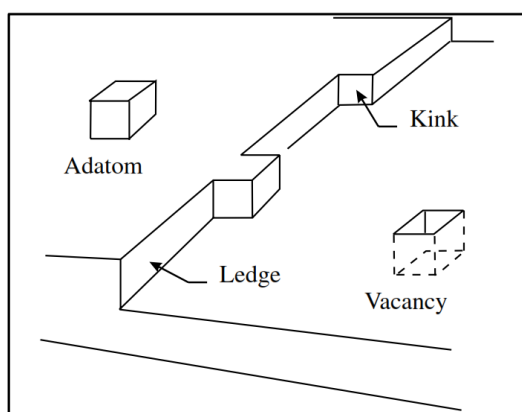
Figure 1.8: Typical surface sites and defects of a catalytic surface, showing terraces, ledges (steps), kinks, adatoms and vacancies [44].

A heterogeneous catalytic reaction proceeds on the surface of the catalytically active material following various steps such as diffusion, adsorption, and desorption. Therefore,

the performance of a catalyst depends on many variables. For instance, the adsorption sites must be simultaneously numerous and readily available to the reactant molecules. The heart of a heterogeneous catalyst involves the active sites which appear on the surface of the solid. However, in some cases, they can be located below the surface and thus are not accessible by the reactants. Moreover, if they are located deep within a micropore that is too narrow for the reactant molecule to enter or for the reaction product to exit, then the sites cannot be an active participant in the reaction. Also, if a site is located along a tortuous path that interferes the efficient flow of reactants towards the active site and products away from the site, it cannot be described as active. Therefore, the catalyst must have easily accessible outer and inner surfaces [27], [28].

Consequently, it is normal to expect that a catalytic surface exposes a variety of surface sites, in contrast to displaying a single type of active site. A meaningful characterization of active sites requires experiments under in situ conditions of the catalytic system, something that is rather difficult [25], [29].

1.3.5. Chemical Adsorption

Adsorption is a process that occurs when a gas or liquid solute (adsorbate) accumulates on the surface of a solid or a liquid (adsorbent), forming a molecular, ionic, or atomic film [37], [45]. When examining adsorption, it is useful to distinguish between physical and chemical one. Physical adsorption or physisorption, involves only relatively weak intermolecular forces, Van der Waals forces, between molecules and/or atoms of the adsorbent surface and adsorbate. Moreover, physically adsorbed molecules may diffuse along the surface of the adsorbent and are not typically bound to a specific location on the surface. Physical adsorption is easily reversed, due to the weak bonds involved [28], [45], [46].

On the other hand, chemical adsorption or chemisorption involves, essentially, the formation of a chemical bond between the adsorbate (molecule and/or atoms) and the surface of the adsorbent. Chemisorption is literally defined as adsorption which involves chemical bonding [45], [46]. A chemical bond involves sharing of electrons between atoms of the adsorbate and the adsorbent. These chemisorption interactions are essentially those responsible for the formation of chemical compounds. Also, chemisorbed molecules are linked to reactive parts of the surface and the adsorption is necessarily confined to a monolayer, whereas physisorption generally occurs as a multilayer at relatively high

pressures. During chemisorption, if a chemisorbed molecule undergoes reaction, it loses its identity and cannot be recovered by desorption to its original form, unlike physisorption. Also, chemical adsorption is difficult to reverse due to the bond strength. When all the active sites on the solid surface are occupied by chemisorbed molecules, then chemisorption has reached its endpoint [28], [45]–[47].

Other important distinguishing features of chemisorption and physisorption are the fact that physical adsorption takes place on all surfaces provided that temperature and pressure conditions are favourable. Chemisorption, however, is highly selective and occurs only between certain adsorptive and adsorbent species and only if the chemically active surface is cleaned of previously adsorbed molecules. Furthermore, the energy of chemisorption is in the same order of magnitude as the energy change in a comparable chemical reaction (20-400kJ/mol). The energy involved in physisorption, is generally not much larger than the energy of condensation of the adsorbate (10-40kJ/mol), but physisorption is always exothermic. Moreover, chemisorption often involves an activation energy, and hence at low temperatures, the system may not have sufficient thermal energy to attain thermodynamic equilibrium. Physisorption systems generally attain equilibrium fairly rapidly, but equilibration may be slow if the transport process is rate-determining [28], [37], [46], [48].

Chemical adsorption process can be characterized as dissociative (or second-order adsorption) when the adsorbate is separated into two or more molecular or atomic entities (ions or radicals), each entity forming a bond with individual active surface sites. On the contrary, during first-order or non-dissociative adsorption, the adsorptive molecule remains intact during adsorption. The result of dissociative adsorption is that the number of adsorptive molecules determined to have been taken up per gram of sample does not equal the number of active surface atoms that participated in chemisorption [28].

The essential factor determining whether or not chemisorption occurs is the Gibbs free-energy of the process. A negative value of ΔG is a prerequisite, based on the following equation [5], [49].

$$\Delta G° = \Delta H° - T \cdot \Delta S° \tag{1.10}$$

where $\Delta G°$ is the Gibbs free-energy change (kJ/mole), $\Delta H°$ is the enthalpy change (kJ/mole), T is the temperature (Kelvin) and $\Delta S°$ is the entropy change (J/K·mole).

Based on equation 1.10, the values of $\Delta H°$ and $\Delta S°$ determine whether chemisorption is possible. The change of entropy is always negative since in the transition of a substance from the gas phase to the adsorbed phase its degrees of freedom are reduced. Thus, the term $-T \cdot \Delta S°$ becomes positive, resulting in $\Delta H°$ needing to become negative in order to have a spontaneous process with a negative $\Delta G°$. In a few cases, endothermic adsorption has been observed and this is interpreted by the existence of an intermediate reaction [5], [27], [33].

It should also be noted that there are two fundamental kinds of mechanistic situations that can arise in bimolecular reactions, i.e. between two molecules over the surface of a heterogeneous catalyst. According to the first mechanism of Langmuir-Hinshelwood, both species are attached to the surface, and an atomic reorganisation takes place on the surface converting the gaseous reactants into the products. On the contrary, the second mechanism of Eley-Rideal states that only one of the reactants adsorbs to the surface and the other molecule reacts with it directly from the gas phase without adsorbing [26], [27].

1.3.6. H$_2$ Dissociative Chemisorption

Dissociative adsorption takes place following physical adsorption of the H_2 molecule. A hydrogen molecule (H_2) may dissociate into two hydrogen atoms and adsorb on two active surface atoms of the catalytic surface. For this process to occur, a certain "activation" energy is necessary. For hydrogen molecule the dissociation energy is $\Delta_{H-H}=$ 434kJ [27], [28], [50]. It is generally believed that two adjacent vacant sites are necessary and sufficient for dissociative adsorption. However, it was recently demonstrated via scanning tunnelling microscopy studies that a larger arrangement of three or more vacancies is necessary [51]. Figure 1.9 presents the periodic table of elements, along with their capability for hydrogen dissociation, as well as the types of hydrides formed [52].

Figure 1.9: Periodic table of elements with (+) high and (-) zero probability of H_2 dissociation.

When a hydrogen molecule dissociates on adsorption, the simple Langmuir Isotherm can no longer be used to describe the adsorption behaviour. The process of adsorption can be described using the Lennard-Jones potential energy diagram [27], [50]. Figure 1.10a depicts the Lennard-Jones potential energy diagram for the adsorption of H_2 on a metal surface. This diagram shows the potential energy of hydrogen molecules and hydrogen atoms as a function of the distance of each species from the metal surface. As seen in Fig.1.10a, when the H_2 molecule approaches the surface from the right-hand side, it becomes physically adsorbed and then, following dissociation due to the interaction with the metal surface, hydrogen atoms are chemisorbed on the surface [27].
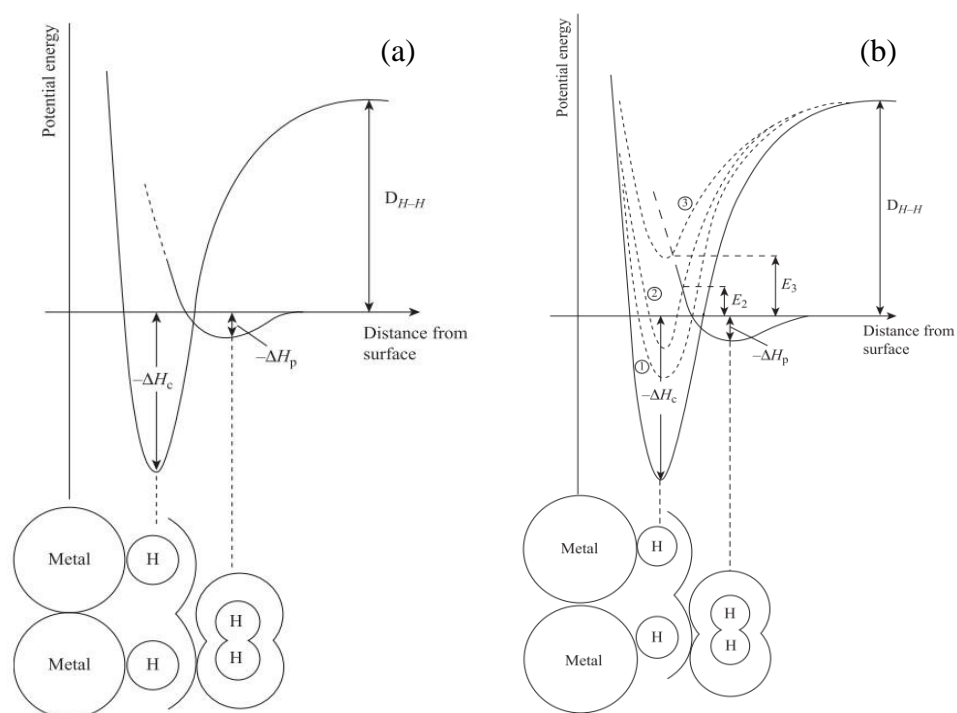
Figure 1.10: (a) Lennard-Jones potential energy diagram for the adsorption of hydrogen on a metal surface, (b) Extension of the Lennard-Jones potential energy diagram, showing the effect of increasing the coverage of hydrogen on the surface (curves 1, 2, 3) [27].

Specifically, when the molecule is far from the surface (at an infinite distance), there is no attraction between them, i.e. the molecule is at zero potential energy. As the molecule comes closer to the surface, physisorption occurs by the attractive forces of Van der Waals, where the molecule is held by physical forces of attraction, $-\Delta H_p$. If the molecule gets closer to the surface, then a strong repulsion will take place between the electron clouds of the molecule and the surface. However, if a hydrogen atom approaches the surface, it will feel a much greater force of attraction than the hydrogen molecule and will be able to form a metal-hydrogen bond, hence becoming adsorbed with a heat of

adsorption $-\Delta H_c$ (chemisorption curve). As shown in Figure 1.10, the chemisorption curve ($-\Delta H_c$) intersects the physical adsorption curve ($-\Delta H_p$) at a value below or very close to the zero of the energy axis. Regarding transition metals, such as Pt, the hydrogen molecule approaches the surface and it transfers smoothly from the physically adsorbed state to the chemisorbed state, hence there is no activation energy barrier to overcome [27].

However, the situation may change as the surface is covered by hydrogen. Fig. 1.10b indicates that the minimum of the chemisorption curve decreases in absorbate value (dotted curves 1, 2, 3) and as a result might reach positive energy values. The decrease of the heat of adsorption (ΔH_c) with coverage can result in the occurrence of an activation energy for adsorption (see E_2 and E_3 in Fig 1.10b). In the case that the adsorbed hydrogen is to desorb to the gas phase, then the reversed path has to be followed in order to become re-associated with another hydrogen atom to form a hydrogen molecule. If desorption from the adsorbed state can occur, the activation energy for desorption becomes ($\Delta H_c + E$), the value of this decreases with increasing coverage [27].

When studying the electron interactions developed during the dissociation of H_2 on a metal surface, the s and d orbitals of the surface metal play an important role. As hydrogen molecule approaches the surface, an overlap happens between the molecular orbitals (1σ and $1\sigma^*$) of the molecule and the s and d electrons of the surface metal. Thus, in the case the surface's valence electrons are fully occupied, the 1σ electron of H_2 is repulsed, resulting in an energy barrier [52]. As H_2 approaches more the surface, there is a shift of charge from the 1σ bonding orbital of H_2 into the d orbital of the metal. Simultaneously, there is a movement of the charge from the d orbital of the metal to the $1\sigma^*$ antibonding orbital of H_2 (back-donation), where the latter is at a higher energy level than 1σ. In this way, the dissociation adsorption of H_2 on the surface of the metal is enhanced [52]–[54].

1.3.7. Chemical Adsorption of NO

Although NO decomposition is thermodynamically favourable ($\Delta G = -86$ kJ/mol), it is hindered by a high activation energy of 364 kJ/mol [3]. However, the kinetics of the decomposition of NO can be favoured if NO is chemisorbed on a solid surface. The chemisorption of NO on a metal surface, such as Pt, and on metal oxides are discussed below.

1.3.7.1. Chemical Adsorption of NO on Metal Surface

Nitric oxide adsorption can lead to dissociation (dissociation energy of 630kJ/mol) which produces N_a and O_a on the surface, or to adsorption of the chemisorbed monomer (molecular adsorption), or to a combination of both. NO normally dissociates on base metals and is molecularly adsorbed at room temperature on noble metals. Moreover, other species such as $(NO)_2$, NO dimers, N_2O, and NO_2 can also be formed on metal surfaces. NO dimer formation on transition metal surfaces is important because of the potential for such interactions to lead to N-N bond formation in the catalytic reduction of the NO molecule [3], [8], [55].

The orbitals that play the most important role in the interaction of a molecule with another molecule or a surface are the frontier orbitals. NO has an unpaired electron in its $2\pi^*$ antibonding orbital. It can therefore either donate its $2\pi^*$ electron to the surface, leading to the formation of a molecularly adsorbed NO or it can accept electron density from the surface into the half-filled $2\pi^*$ orbital. Moreover, it shows a very wide variety of chemistry on surfaces, adsorbing in many different binding geometries [52], [55]. In addition, electrons from the 5σ NO orbital can move to the orbitals of the metal, leading to the destabilization of the NO molecule and dissociative adsorption [33], [52]. Figure 1.11 shows schematically the orbital mixing model for NO chemisorption on a metal surface, derived from calculations for NO adsorption on a Pt{111} surface [56]. It should be noted that Pt adsorbs NO without dissociation on the {111} face, but dissociatively on more rough crystal faces [57].
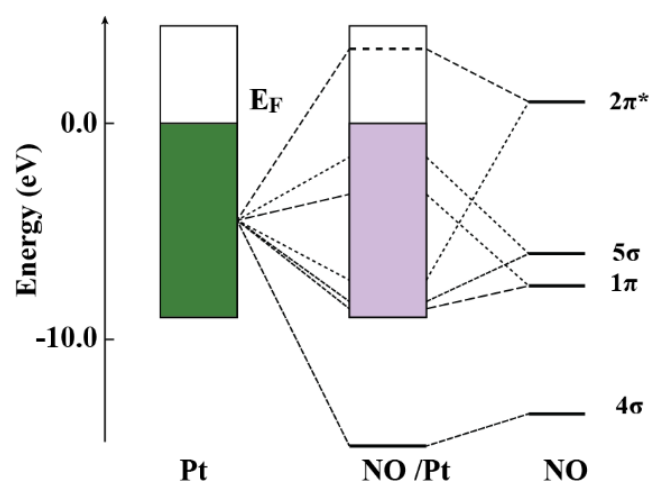
Figure 1.11: Schematic illustration of orbital mixing during NO chemisorption on Pt{111} [52], [55].

Dissociation of NO on most surfaces, dependents directly on surface coverage, surface temperature, surface structure and the concentration of surface defects. According to the research reported by Brown and King [55], the dissociation of NO is usually inhibited at high coverages, either due to a lack of vacant sites or to a thermodynamic switch to molecular NO. The influence of temperature on NO dissociation strongly dependents on the initial coverage of NO. At low temperatures, molecular adsorption takes place until saturation coverage, where some desorption is usually required, by heating the surface, before dissociation can take place [55], [58], [59]. Therefore, a vacant site is required for NO dissociation. Figure 1.12 shows a possible two-step mechanism for NO dissociation, where NO adsorbs firstly on the surface, and then reorients to allow the O atom to come into contact with the surface (possibly via a lying down NO precursor state) before dissociation takes place [55].
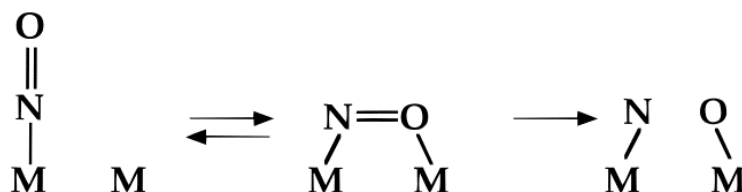
Figure 1.12: Schematic diagram of the two-step NO dissociation process [55].

A lot of research has been dedicated in order to classify the bonding involved in NO complexes [8], [60]–[64]. The development of computational methods for the study of structural characteristics of adsorbed NO_x species in combination with spectroscopic techniques such as Diffuse Reflectance Infra-Red Fourier Transform Spectroscopy, DRIFTS, have led to significant understanding of NO adsorption on solid surfaces. NO readily reacts with many transition metal compounds to give nitrosyl complexes and these are also frequently formed in reactions involving other oxo-nitrogen species [65].

Figure 1.13 illustrates the wide variety of coordination geometries of NO. As seen in Fig. 1.13, NO can be adsorbed on metal surfaces in different geometries like linear (atop), bent, bridge, etc. A general observation from the N-O vibrational frequencies, which are presented in the following table, is that the N-O stretching frequency in the ''atop'' (linear) NO is more than that of the ''bent'' NO, hence, the NO dissociation will be facile if the NO is adsorbed on the surface in bent geometry than atop geometry [3]. It should also be noted that bending withdraws an electron-pair from the metal centre to the N atom thus creating a vacant coordination site. Therefore, bent NO can be considered as a 1e⁻ donor. This may be a significant factor in the catalytic activity of such complexes. Linear NO

transfers 1 electron from NO to the metal and the coordination of NO^+ transfers 1 electron (e^-) to the reduced metal centre as a $2e^-$ σ donor. Overall NO acts as a $3e^-$ donor [8], [65].

Linear (~sp)   Bent (~sp^2)   Bridging (~sp^2)
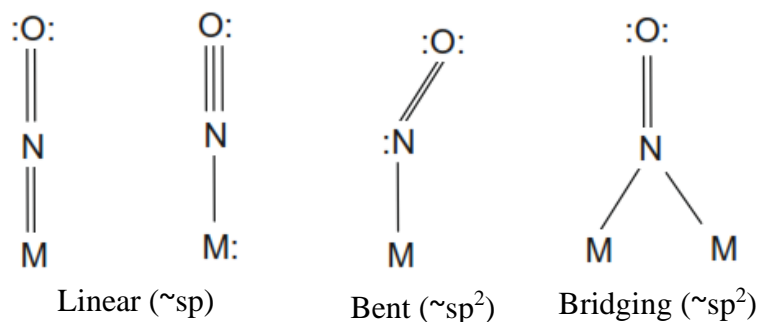
Figure 1.13: Schematic representation of the bonding in NO complexes [8].

Moreover, Table 1.1 indicates the observed vibrational frequencies for adsorbed NO species on various metal surfaces, after high-resolution electron energy-loss spectroscopy (HREEL) studies [8].

Table 1.1: Assignments of peaks in HREEL spectra for NO on surfaces of various metals (M).

Substrate	Adsorption site	ν(N–O) (cm^{-1})	ν(M–NO) (cm^{-1})	δ(M–NO) (cm^{-1})
Ni(1 1 1)	Bent	1490	400	740
	Bridge	1600	375	
Pd(1 1 1)	Bridge	1510–1660	460–490	
	Top	1720–1850	510–550	
Pd(1 0 0)	Bridge	1505–1510		
	Top	1660–1720		
Pt(1 1 1)	Bridge	1476–1516	306	
	Top	1700–1725	450	
Pt(1 0 0)-(1 × 1)	Bent	1645	230	380
Pt(1 0 0)-(5 × 20)	Bent	1690–1790	310	465
Rh(1 1 1)	Bridge	1480–1635	405	
	Top	1815–1840	485	
Rh(1 1 1) + CCH$_3$	fcc hollow	1405–1435		
Rh(1 0 0)	Bent	910		
	Bridge	1600		
Rh(3 3 1)	Bent	1704		403
	Top	1815		
Ru(0 0 1)	Hollow	1400	680	
	Bent	1500	410	
	Top	1783–1823	510–570	

Figure 1.14 shows that the majority of the transition metals of group VIII, adsorb NO dissociatively. Non dissociatively adsorbed NO is formed at low temperatures; and upon heating, dissociation is initiated at temperatures between 150 and 300 K, with Pt surfaces most resistant to dissociation. On group IB metals, monomeric NO adsorption is weak

and non-dissociative. At low temperatures however dimers can be formed, which are reactive, producing, for example, N_2O and $O_{adatoms}$ at temperatures above ~ 60 K [55], [66].

Figure 1.14: Diagram showing the tendency of different metal surfaces to dissociate NO, depending on their position on the periodic table [55], [66].

1.3.7.2. Chemical Adsorption of NO on Metal Oxides

There is a large number of publications concerning studies performed on chemical adsorption of NO on metal oxide surfaces such as ZrO_2, La_2O_3, V_2O_5, Al_2O_3, MgO and CeO_2 [60], [63], [67]–[72]. The principles of chemical adsorption on a metal oxide surface do not differ much from adsorption on any solid surface. However, in the case of metal oxides, chemical adsorption is more complex than in the case of a metal surface, since, besides the orbitals of the metal cations, there are also those of the surface oxygen. In addition, defects in the solid surface structure are more frequent in the case of metal oxides than in metals, which significantly affects chemical adsorption. In particular, it has been found that the NO molecule has the potential to adsorb to oxygen vacant sites in certain metal oxides such as CeO_2 and ZrO_2 [68], [69]. Specifically, the reduction of CeO_2 by O_2 transfer also frees sites for NO adsorption, and thus NO decomposes readily on reduced ceria. This may provide an additional reaction pathway for NO decomposition [68].

Moreover, Burch et al. [70] found that not only the metal-support interface participates, but also plays a key role in the mechanism of the NO reduction. This metal-support interface provides suitable catalytic centres where the active intermediate species of the reaction can be formed. Costa et al. [73] reported that the two active NO_x species are formed within the metal-support interphase region, whereas inactive NO_x species are populated on both the metal and support surfaces during H_2-SCR of NO. Figure 1.15a illustrates the active adsorbed NO_x intermediate species that are formed near the interface between Pt nanoparticles and the support surface of MgO-CeO_2 [73]. Figure 1.15b shows

the active NO_x species ($M-NO_2^+$ and $M-O-(NO)-O-M$) which are populated on the metal-support inter-phase region of the $Pt/La_{0.5}Ce_{0.5}MnO_3$ catalyst [74].
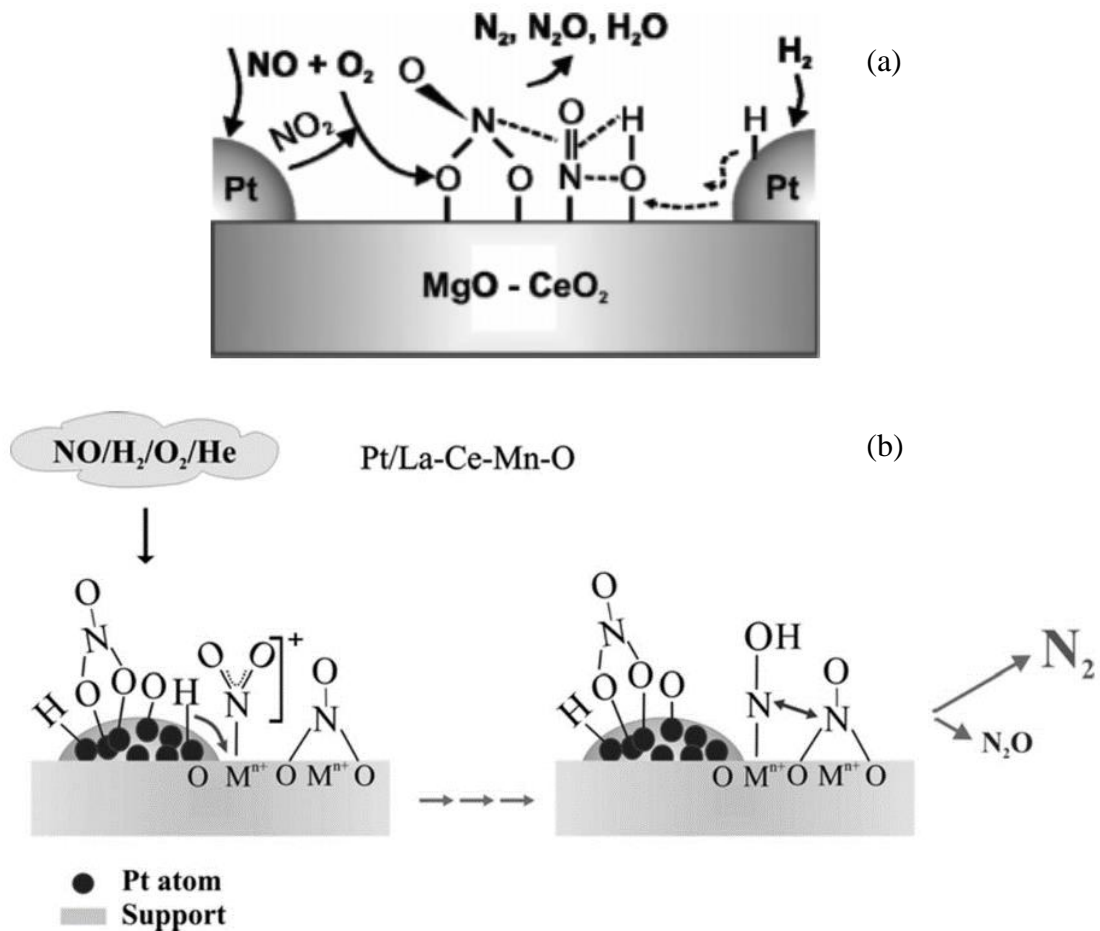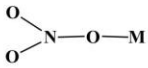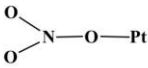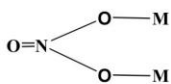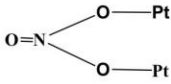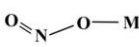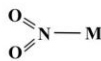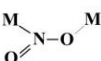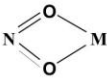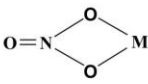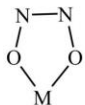
Figure 1.15: (a) Adsorbed NO_x intermediate species on the $Pt/MgO-CeO_2$ catalyst [73] and (b) Illustration of the site population and interaction of the two active adsorbed precursor intermediate NO_x species formed on $Pt/La_{0.5}Ce_{0.5}MnO_3$ that lead to N_2 and N_2O formation [74].

Table 1.2 reports the chemical structure and absorption bands (stretching mode) of all the important adsorbed NO_x species observed during well-documented experimental and theoretical studies reported in the literature [60], [73]–[79].

Table 1.2: Chemical structures and absorption IR bands (stretching modes) of various adsorbed NO_x species on metal oxide-supported Pt catalysts, where M= metal cation of metal oxide [60], [73]–[79].

Species	Structure	Vibration	Wavenumber (cm^{-1})
Nitric Oxide	NO (g)	ν(NO)	1883
Nitrogen hypoxide	$M-N_2O$	ν(NO)	2224
		ν(NN)	1286
Nitrosyls on support	$M-NO^+$	ν(NO)	2220
	$M-NO_2^+$	ν(NO_2,a)	2360-2375
		ν(NO_2,s)	1400
Nitrogen Dioxide	$M-NO_2^{\delta+}$, $M-NO^{\delta+}$		2100-2200
Nitrosyls on Pt	$NO-Pt_{ox}$	ν(NO)	~1840
	$NO-Pt_{red}$	ν(NO)	~1800
	$NO^{\delta+}-Pt$	ν(NO)	1900-2000
Bridged or bent NO on Pt	Pt_n-NO	ν(NO)	1500-1700 (depending on n)
Unidentate Nitrates		ν(NO_2,a)	1450-1570
		ν(NO_2,s)	1250-1330
		ν(NO)	970-1035
			1620-1660
Bidentate (Bridged) Nitrates		ν(NO_2,a)	1170-1300
		ν(NO_2,s)	1000-1030
		ν(NO)	1590-1660
			1520-1610
Nitritos		ν(N=O)	1400-1485
		ν(NO)	1050-1110
		ν(ONO)	820-850
Nitrito complex		ν(NO_2,a)	1335-1470
		ν(NO_2,s)	1315-1350
		ν(ONO)	820-850
Bridging nitro complex		ν(NO_2,a)	1390-1520
		ν(NO_2,s)	1180-1260
Chelating nitrite (NO_2^-)		ν(NO_2,a)	1260-1390
		ν(NO_2,s)	1170-1210
		ν(ONO)	840-860
Bidentate (Chelated) Nitrates		ν(NO_2,a)	1200-1310
		ν(NO_2,s)	1003-1040
		ν(N=O)	1500-1620
Dimeric NO, $N_2O_2^{2-}$		ν(NO)	1383
		ν(NN)	1115

1.3.8. Supported Catalysts

There are many different types of heterogeneous catalysts in use in various processes. Most of the catalysts are metals, oxides and sulphides. Even though each may exist as single-component material, the active material is often accompanied by other components, e.g., as "support" or "promoter" [29], [80].

In some cases, the support is more or less inert (e.g., a-alumina, porous glass) supplying high surface area for dispersion of the active component. Whereas in other cases the support contributes to the activity, selectivity and stability of the catalyst under operation conditions (e.g., alumina, alumina-silicate, zeolites, etc). Those materials make up to 80% of all industrial supports. Support materials can also be classified into supports that influence the active component by strong interactions (e.g., partially reducible oxides, TiO_2, Nb_2O_5, V_2O_5, etc.) and structural supports which are of increased importance for exhaust gas purification (monoliths). Therefore, a support can be produced with the desired thermostable porosity, high surface area and mechanical strength. Most commercial heterogeneous catalysts are supported catalysts [29], [80], [81].

A catalyst can have different active components, such as one or more metals and one or more oxides. The active form of a catalyst can be highly dependent on the reaction mixture to which it is exposed, i.e., reducing or oxidizing conditions or even sulfiding. It must be noted that the active material consists only a minor part of the supported catalysts and is deposited on the surface of the support [27], [29], [82]. Furthermore, if the active phase is a noble metal and since they are expensive, it is important to utilize the precious metal most effectively. This can be achieved by dispersing very small metal particles on the surface of the support in order to maximize the number of active sites per unit of metal [27], [29], [52].

Additionally, some supports can alter the catalytic properties of the active phase. This strong metal-support interactions, known as SMSI, can decrease, for example, the chemisorption capacity of supported metals ($Pt–TiO_2$) or can hinder the reduction of supported metal oxides (Ni-silicate) [29]. SMSI is discussed further in subchapter 1.3.10.

1.3.8.1. Supported Metal Catalysts

When examining reactions where the rate of surface reaction determines the rate of the reaction, then the metallic surface area of the catalyst becomes the most important factor. That is the reason why it is important to make and stabilize the highest possible and easily

accessible metal surface area through the supported metal catalysts. The supported catalysts, as mentioned before, have typically a high-surface area material (e.g., 10–1000 m^2/g). In order to obtain such high surface areas and therefore increase the rate of the reaction, it is desirable to achieve a highly dispersed material (e.g., metal, oxide or sulfide). Even though finely divided metallic powders can be made with high surface areas, these are very unstable under reaction conditions, since they may undergo sintering and deactivate the catalyst (see subchapter 1.3.9: Deactivation of Catalysts) [27].

Another reason that metal dispersion on high surface supports is needed, is the fact that metals typically have high surface free energies and thus have a pronounced tendency to reduce their surface areas by particle growth [83]. Therefore, for catalysts, the metals are dispersed on high surface area supports, preferentially oxides (e.g., transitional aluminas) with the aim of stabilizing small, nanosized particles under reaction conditions [81], [84]. Also, the low availability of noble metals led to the study and development of supported low-loading catalysts of about 1 wt%, which leads to particles between 10 and 1000nm [28], [29], [80]. Even in the case that less expensive active metals or oxides are used, then it is important to maximize the activity per unit volume. A large active surface area per unit volume allows a considerable conversion with moderately sized reactors at relatively low temperatures [80].

Supported metal catalysts are used in various processes in the industry. For instance, supported metal catalysts, including noble (Pt, Pd, Rh) or non-noble (Ru, Ni, Fe, Co) metals that are supported on Al_2O_3, SiO_2, or active carbon can be used for hydrogenation and dehydrogenation reactions in refinery processes. Also, Ag/Al_2O_3 catalysts are used for ethene epoxidation, while supported Au catalysts are active for low-temperature CO oxidation. Moreover, Pt supported on chlorinated Al_2O_3 is the bifunctional catalyst used for catalytic reforming and isomerization of petroleum fractions. Another well-known example of the use of supported Pt catalysts is in automobile exhaust catalysts, where Pt along with Rh and Pd are supported by a cordierite honeycomb monolith coated with high surface area γ-Al_2O_3, thermal stabilizers like La_2O_3, as well as the oxygen-storage component CeO_2. These multimetal catalysts are used on a large scale in the three-way catalytic converter (TWC), where they simultaneously convert NO_x, CO, and HC to N_2, CO_2, and H_2O [27], [29], [71].

1.3.8.2. Physicochemical Characteristics of Support Materials

The most commonly used supports are single oxides such as alumina or silica, complex oxides such as silica-alumina or zeolites and active carbons. These materials are refractory oxides, having therefore high melting points which makes them very stable under most operating conditions. It is noted that the constituent ions of an oxide become mobile at temperatures around the Tamman temperature (Table 1.3), that is approximately half the temperature of the melting point (in Kelvin) [27], [85].

Table 1.3: Melting points and Tamman temperatures for different oxides [31].

Oxide	Melting Point (K)	Tamman Temperature (K)	Oxide Type/Comments
γ-Al_2O_3	(2318)	(1159)	Acidic. Transforms into α-Al_2O_3 upon heating
α-Al_2O_3	2318	1159	Amphoteric
SiO_2	1973	987	Acidic
SiO_2-Al_2O_3	1818	909	Very Acidic
MgO	3073	1537	Basic
CaO	2853	1427	Basic
$CASiO_4$	2407	1204	Basic
ZrO_2	2988	1494	Amphoteric
Cr_2O_3	2708	1354	Amphoteric
CeO_2	2873	1437	Amphoteric
La_2O_3	2588	1294	Amphoteric
$MgAl_2O_4$	2408	1204	Neutral
$ZnAl_2O_4$	2100	1050	Neutral

Alumina is one of the supports which is most commonly used in the preparation of heterogeneous catalysts. Alumina is relatively inexpensive and can be prepared easily in forms that have high surface areas and readily accessible pore structures. It is also relatively inert and does not easily form compounds with the supported components. In practice, aluminas are available in a wide range of surface areas (100-$600m^2$/g) and pore sizes and are characterized by excellent thermal stability, although, heating above 600^oC results in the closure of micropores and reduction of the surface area [27], [81], [86].

The raw materials that can be used for alumina preparation are bayerite, nordstrandite, boehmite, and gibbsite. During the preparation of alumina, the conditions used for drying and calcination can be crucial in determining the structure of the resultant solid. Aluminas are amphoteric oxides since acidic and basic sites and acid-base pair sites have been identified on their surfaces. The acidic surfaces can be explained by the significant concentrations of hydroxyl groups (OH^-) formed either during the decomposition of the

precursor or by interaction subsequently with water from the atmosphere. The hydroxyl groups may contribute to the catalytic behaviour of the final catalyst [27], [29], [81]. The most commonly used phase is the γ-Al_2O_3, which is often described as defect spinel structure that incorporates Al^{3+} cations in both tetrahedral and octahedral sites as depicted in Figure 1.16 [5], [29].
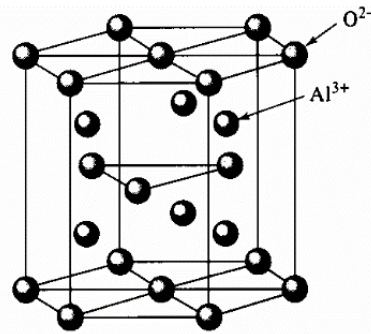
Figure 1.16: 3D structure of γ-Al_2O_3 [5].

MgO, SiO_2, and ZrO_2 are also examples of non-reducible oxides that generally function as inert supports that help to stabilize the metal particles. These non-reducible oxides can also function as solid acids or bases. When calcined at low temperatures, MgO has basic properties [27]. MgO has the simple rock salt structure (cubic lattice of NaCl), with octahedral coordination of magnesium and oxygen. The electronic structure is highly ionic, with the $Mg^{2+}O^{2-}$ formalism being an accurate representation of both bulk and surface structures. It has been assumed that {100} faces are predominantly exposed incorporating five-coordinate (5c) Mg^{2+} and O^{2-} ions (Figure 1.17) [29], [81], [87].
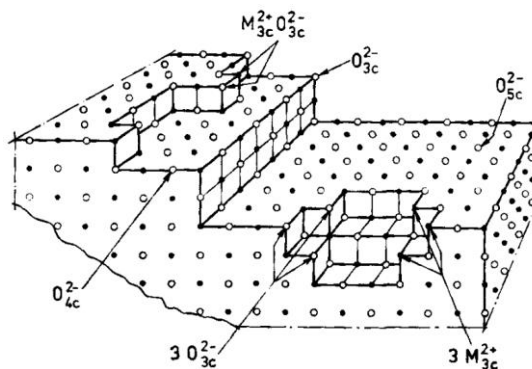
Figure 1.17: Representation of a surface plane {100} of MgO showing surface imperfections such as steps, kinks, and corners which provide sites for ions of low coordination [87].

Although the {100} plane, which is indicated in Figure 1.17, is electrically neutral, hydroxyl groups are present on the surfaces of polycrystalline MgO. The hydroxyl groups as well as the O^{2-} anions are responsible for the basic properties, while the unsaturated

Mg^{2+} ions are weak Lewis acid sites. It should also be noted that the hydroxyl groups are highly nucleophilic [29], [81].

Cerium (IV) oxide (CeO_2 or ceria), is a cubic material with a relatively simple structure, as can be seen in Figure 1.18. Each of its stable, low-index crystallographic faces exposes Ce cations and O anions with different numbers of coordination vacancies [71]. The surface area of CeO_2 generally drops to a few m^2/g at around 725-825°C, depending on preparation procedure and type of treatment, although a high degree of textural stability can be obtained by doping and modifying the preparation procedure [88]. Unmodified surfaces of CeO_2 nanomaterials, with wetting angles up to 116°, are dominated by the lower energy {111} planes, which tend to exhibit lower surface energy. Moreover, the surface functionality of CeO_2 originates largely from its intrinsic hydrophobicity [89], [90].
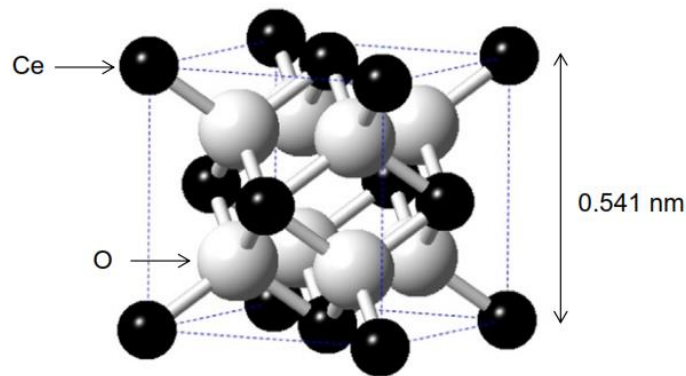
Figure 1.18: The unit cell of CeO_2 [71].

Ceria is an active component of the Three-Way Catalytic Converter (TWC), as mentioned before. Some of the advantages of using ceria are that it can improve the dispersion of noble metals and the thermal stability of γ-Al_2O_3 towards thermal sintering. It also enhances the oxygen storage capacity (OSC) of the catalyst, i.e., it can store and/or release reversibly a large amount of oxygen, responding to the gas-phase oxygen concentration. Due to this unique property, ceria is a base component of automobile TWC, so as to control the actual surface oxygen concentration under working conditions. Moreover, the property of storing and releasing oxygen permits desirable reactions of oxidation and reduction [91]–[93].

The property of OSC of ceria is enhanced by the presence of precious metals such as Pt, Pd and Rh [94]. According to Mullins [71], CeO_2 is known for its intrinsic property of having surface and bulk oxygen vacant sites, where NO chemisorption on surface oxygen vacant sites occurs. When O vacancies are created, two of the Ce cations adjacent to the

vacancy change from Ce^{4+} to Ce^{3+}. It should be noted that according to the state of ceria (reduced or fully oxidized), the chemistry of the same adsorbate differs dramatically during adsorption and reaction [71].

1.3.9. Deactivation of Catalysts

Catalyst deactivation is essentially the loss of catalytic activity and/or selectivity over time. It is a problem of great and continuing concern in the practice of industrial catalytic processes since there are many paths for a heterogeneous catalyst to decay. It is also inevitable that all catalysts will decay at some time. In general, the activity loss can be compensated within certain limits by increasing the reaction temperature. Still, if such compensation is not efficient enough, the catalyst must be regenerated or replaced [95], [96].

The mechanisms of solid catalyst deactivation are many; nevertheless, they can be grouped into six intrinsic mechanisms of catalyst decay: (1) poisoning, (2) fouling, (3) thermal degradation (sintering), (4) vapor compound formation and/or leaching accompanied by transport from the catalyst surface or particle, (5) vapor-solid and/or solid-solid reactions, and (6) attrition/crushing [25], [29], [85], [96]. If the deactivation is classified by type then there are three, i.e. chemical, mechanical and thermal; examples of them are discussed further below. It should be noted that some of the aforementioned mechanisms for catalyst deactivation are reversible, such as catalyst fouling and some special types of poisoning. Other types of deactivation are mostly irreversible [97]–[99]. A brief description of all deactivation mechanisms can be found in Table 1.4 [95].

Table 1.4: Mechanisms of catalyst deactivation.

Mechanism	Type	Brief definition/description
Poisoning	Chemical	Strong chemisorption of species on catalytic sites, thereby blocking sites for catalytic reaction
Fouling	Mechanical	Physical deposition of species from fluid phase onto the catalytic surface and in catalyst pores
Thermal Degradation	Thermal	Thermally-induced loss of catalytic surface area, support area, and active phase–support reactions
Vapour formation	Chemical	Reaction of gas with the catalyst phase to produce a volatile compound
Vapour-solid and solid-solid reactions	Chemical	Reaction of fluid, support, or promoter with catalytic phase to produce inactive phase
Attrition/crushing	Mechanical	Loss of catalytic material due to abrasion
		Loss of internal surface area due to the mechanical-induced crushing of the catalyst particle

- **Catalyst Poisoning**

Catalyst poisoning is the strong chemisorption of reactants, products or impurities on active sites that were otherwise available for the catalytic reaction. Although most catalytic surfaces are heterogeneous with respect to their number and type of active sites, only a few active sites are involved in catalysis. As a result, it is not surprising that catalysts can be poisoned by only small amounts of strongly adsorbed molecules [96], [99]. In industrial applications, heterogeneous catalysts are deactivated during time on stream, which varies from a few seconds or minutes (e.g. fluid-bed catalytic cracking, propene ammoxidation), to several years (NH_3 and CO oxidation) [97]–[99].

Poisoning has a relative meaning; that is, whether a species acts as a poison depends upon its adsorption strength relative to the other species competing for catalytic sites. For instance, O_2 can be a reactant in partial oxidation of ethylene to ethylene oxide on a silver catalyst whereas it is a poison in the hydrogenation of ethylene on nickel [81]. It should also be noted that sometimes the poisoning effect could be useful to stop the formation of undesired side-products [26]. If the chemisorption of the poison is weak, reactivation may occur as the poisoning is reversible (e.g. removal of nitrogen poisoning compounds like ammonia and cyanide, from the syngas of cobalt Fischer-Tropsch catalysts). However, if the chemisorption is strong, deactivation is irreversible (e.g. sulfur on most metals). Regardless of whether the poisoning is reversible or irreversible, the deactivation effects while the poison is adsorbed on the surface of the catalyst are the same [81].

Chemical species which are often concerned as poisons are the elements from group 15 and 16 (e.g. As, P, S, Se, Te), metals and ions (e.g., Pb, Hg, Sb, Cd) and molecules with free electron pairs that are strongly chemisorbed (e.g., CO, HCN, NO). Moreover, NH_3, H_2O and organic bases (e.g., aliphatic or aromatic amines) and various compounds which can react with different active sites (e.g., NO, SO_2, SO_3, CO_2) can also become poisons under certain conditions [29], [85], [96]–[98]. Figure 1.19 shows the two-dimensional model of sulphur poisoning during ethylene hydrogenation. The mechanisms by which a poison may affect catalytic activity are multifold, i.e. physical block of adsorption/reaction sites, electronical modification of the nearest neighbour metal atoms and possibly its next nearest neighbour atoms, resulting in a modification of their ability to adsorb and/or dissociate reactant molecules. Another effect of poisoning is the possible restructuring of the surface by the strongly adsorbed poison, causing changes in the catalytic properties, as well as preventing/slowing the surface diffusion of adsorbed reactants [95].
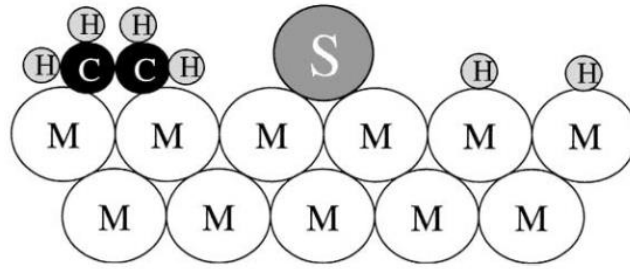
Figure 1.19: Conceptual model of poisoning by sulphur atoms of a metal surface during ethylene hydrogenation [95].

Catalyst regeneration is feasible in some circumstances and can partially recover activity loss. The regeneration of a poisoned catalyst can be achieved with the removal of the poison from the feed as efficiently as possible and with the installation of a guard-bed containing effective poison adsorbents in front of the reactor for further prevention. Moreover, Ni catalysts poisoned with CO or HCN can be regenerated by H_2 treatment at temperatures that allow the formation of methane and NH_3, respectively. Acidic catalysts poisoned by H_2O, alcohols, NH_3 and amines can restore their original activity by thermal treatment at sufficiently high temperatures [29], [99].

- **Fouling**

Another common mechanism of deactivation is fouling, which is the deposition of species from the fluid phase onto the catalyst surface, which results in activity loss due to physical blockage of sites and/or pores. Important examples of fouling are the deposition of carbon and coke in porous catalysts. Carbon is typically a product of CO disproportionation while coke is produced by decomposition or condensation of hydrocarbons on catalyst's surfaces. There are different types of coke, such as C_a which is atomic carbon (formed as a result of hydrocarbon cracking on nickel surfaces above 600^oC), C_b which has strongly deactivating effect, carbidic or graphitic coke, and whisker carbon [96], [99].

Especially sensitive to coking are the catalysts possessing acidic or hydrogenating–dehydrogenating functions. Coke formation can be minimized, for example, in methane steam reforming by sufficiently high steam/methane ratio or/and by the alkalization of the carrier [29]. Figure 1.20 indicates the possible effects of fouling by carbon (or coke) on the functioning of a supported metal catalyst. Carbon may chemisorb strongly as a monolayer or even adsorb physically in multilayers and can block access of reactants to metal surface sites and plug micro- and mesopores and therefore block access of reactants to many crystallites inside these pores [95].
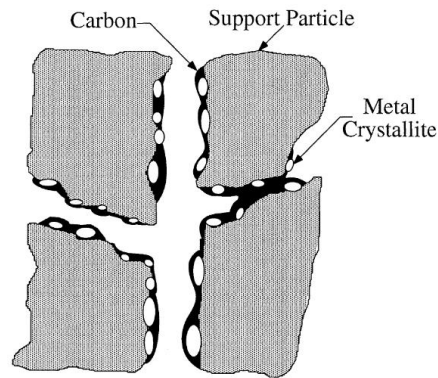
Figure 1.20: Conceptual model of fouling, crystallite encapsulation and pore plugging of a supported metal catalyst due to carbon deposition [95].

From the industrial point of view, the regeneration of coked catalysts is very important, in order to obtain desired run lengths. Coke formation can be minimized, for example, in methane steam reforming by sufficiently high steam/methane ratio or/and by the alkalization of the carrier. Alkali metals, especially potassium, accelerate coke gasification. Moreover, fouling with coke and carbon is generally rapid and reversible by regeneration with O_2. Oxidation is the fastest gasification reaction, but it is highly exothermic. In order to maintain the temperature within allowed limits, mixtures of O_2, steam, and N_2 are usually used to remove the coke [29], [96].

- **Thermal Degradation**

Thermal degradation, which is a physical process, is another cause for catalyst deactivation, where the loss of catalyst active surface is exhibited due to three main reasons. The first reason concerns the crystallite growth of the catalytic phase (agglomeration). The second reason derives from the loss of support area due to support collapse and of catalytic surface area due to pore collapse and blockage of the crystallites of the active phase. These processes are typically known as sintering (Figure 1.21), which is a direct consequence of temperature, time and catalyst ageing [95].

Sintering processes are generally accelerated at increasing temperatures (T>500°C), such as during catalytic oxidation of catalyst regeneration, and by the presence of water vapour which can accelerate solid-solid interactions. The third process involves the chemical transformations of catalytic phases to noncatalytic phases (solid-solid reactions), occurring especially at even higher temperatures (T>700°C) [85], [96], [99]. For instance, reactions between Cu, Ni, Co metals, and alumina carriers result in the formation of inactive metal aluminates [100].
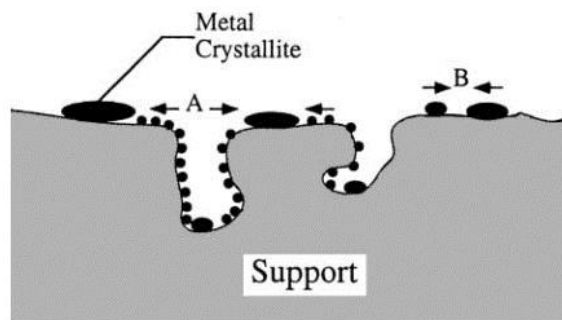
Figure 1.21: Conceptual models for crystallite growth due to sintering by (A) atomic migration or (B) crystallite migration [95].

Thermal degradation can occur in all stages of the life cycle of a catalyst. It might occur due to local heating during preparation (calcination), activation (pretreatment), reduction (fresh or used catalyst), removal of hydrogen after reduction, reaction, or regeneration (coke burn-off). During these processes, if the temperature overtakes certain limits, depending on the catalyst nature, the metal particles migrate to form larger aggregates due to the increase of their mobility. This effect reduces directly the metal dispersion and the number of active sites exposed to the fluid reactants. Consequently, all these processes are often accompanied by activity loss and can cause mechanical strain in catalysts. Therefore, the mechanical strength of catalyst particles is of major industrial importance [29], [85].

The regeneration of a catalyst that has endured thermal degradation is very difficult. Sintering is usually a non-reversible phenomenon and the original metal surface area and dispersion cannot be restored. However, certain Pt–Al$_2$O$_3$ catalysts, which are deactivated due to sintering of Pt, can be partly regenerated by chlorine treatment at elevated temperatures, which makes Pt redistribution possible (Figure 1.22) [29], [96].

It should be noted that prevention of deactivation requires an optimal choice of catalyst design and process conditions. However, if deactivation occurs then typically, regeneration or rejuvenation strategies are dictated by process or economic necessity to obtain desired process run lengths. When evaluating those strategies, life cycle operating strategies are considered as opposed to replacement decisions. Rejuvenation treatments can extend the useful life of catalysts [96].
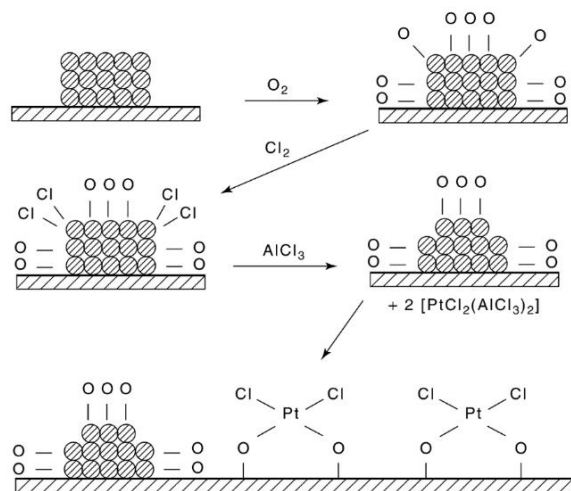
Figure 1.22: Proposed mechanism for redispersion by oxychlorination of alumina-supported platinum [29].

1.3.10. Strong Metal-Support Interactions (SMSI)

Strong Metal-Support Interactions, known as SMSI, are used to explain the modification of the chemisorption and reaction properties of supported noble metals (Group VIII) under reducing conditions and at elevated temperatures (T>400°C). Tauster et al. [101], introduced the term of SMSI in order to interpret the diminished H_2 and CO chemisorption values on titania-supported platinum groups metals reduced above 400°C. They concluded that a plausible SMSI effect is associated with the formation of bonds between the noble metal and titanium cations or titanium atoms, with the latter involving the formation of intermetallic compounds [101].

When the platinum metals are supported on TiO_2 and reduced in hydrogen at 500°C, they lose most of their ability to chemisorb H_2 and CO, and for certain reactions, they also lose much of their catalytic activity. Specifically, SMSI effect over Pt/TiO_2 catalysts originates initially from the formation of a Pt-Ti alloy and the insertion of the Pt atoms into oxygen vacancies on the substrate surface. Moreover, it is due to the formation of Pt atoms-Ti^{3+} cation bonds and electron transfer from Ti^{3+} to Pt atoms by the spontaneous alignment of their Fermi levels. This phenomenon can be partially or fully reversed by oxidation treatment [33], [81], [102].

According to literature, metals, including noble metals, form interfacial bonds with the surfaces of reduced transition metal oxides [81], [101]–[104]. Direct evidence for this, is the spontaneous increase in the metal-oxide interfacial area that is observed in many systems, often at the expense of rupturing strong bonds in order to bring these phases together. The

most probable explanation is the encapsulation of the metal particle by the support oxide material [29], [81].

SMSI effects include intermetallic compound formation and electronic changes due to electron interchange processes between metal particles and the support possibly accompanied by structural changes [81], [104], [105]. Although the electronic properties of the metal particle may be affected by the support oxide in the SMSI state, the decrease of the adsorption capacity appears to be largely due to a geometric effect, namely, the resulting inaccessibility of the metal surface [29].

Supports which are claimed to form strong interactions with metals include reducible oxides such as TiO_2, Nb_2O_5, Ta_2O_5, V_2O_3, and non-reducible oxides such as Al_2O_3, SiO_2 and MgO. In the case of TiO_2, which has received the most attention, direct interactions between metal atoms and reduced titanium ions have been observed with a variety of spectroscopic techniques [81].

Some of the general features of metals in the SMSI state are the diminished H_2 and CO adsorption as mentioned before, unchanged O_2 chemisorption and enhanced N_2 chemisorption as observed for Ni/TiO_2 and Rh/TiO_2 catalysts. Also, decreased activities for hydrocarbon hydrogenolysis, isomerization and hydrogenation reactions have been observed, as well as enhanced activities for reactions involving CO (e.g. Fischer-Tropsch synthesis,) [81]. It should be mentioned that the extent to which chemisorption and reaction properties are modified depends critically on the severity of the reduction treatment, the type of support and the nature of metal. In general, the temperatures necessary to induce SMSI increases in the following order: $TiO \sim Ti_2O_3 < TiO_2 < Al_2O_3 < SiO_2$ [81].

1.3.11. Spillover

Spillover, a phenomenon highly associated with SMSI, which involves the migration of an active chemisorbed species, formed on a first active phase (metal) onto a second phase that usually could not react if present alone under the same conditions. The spillover species can create new types of active centres on the second phase, as well as modify or regenerate the catalytic centres of the second phase. Therefore, the catalytic activity and selectivity may be affected, i.e., promoted or modified by the spillover of adsorbed species [26], [106].

A well-known example of spillover phenomena is hydrogen spillover. When the H_2 molecule approaches the metal surface, it dissociates and then adsorbs on the metal particles of the surface, where hydrogen atoms may easily migrate to another phase of the catalyst which has hydrogen acceptor sites. Figure 1.23 indicates three cases in which hydrogen spillover effects can take place, where (a) the first active phase is directly supported on the second phase (the acceptor), (b) the first active phase is supported on an activated support, mixed with a non-activated support and (c) the first active phase is fixed on a support that is activated by another active phase [26], [106].
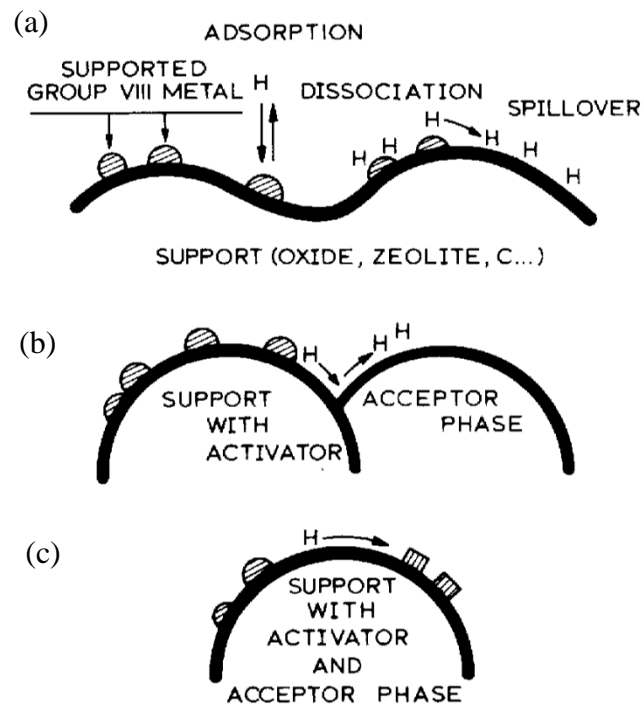
Figure 1.23: Schematic diagrams of types of hydrogen spillover: (a) metal (activator) on a support, (b) metal (activator) on a support with an admixed support (acceptor) and (c) metal (activator) on a support with a reactant (acceptor) [106].

The process, which was first reported by Khoobiar [107], has primarily been observed using Pd or Pt noble metals. The spilled over hydrogen may reside on the surface of the support or it can diffuse into it, and fully or partially reduce the support, generating new catalytic centres that are otherwise not present without the spillover hydrogen [53], [108], [109]. Additionally, spilled over hydrogen can lower the reduction temperature in numerous metal oxides, including easily reducible supports like TiO_2. The reactivity of the supported metal is strongly influenced by interactions with the support oxide. Consequently, any partial reduction of the support may result in a large change in the

metal–support interaction leading to a modification of the catalytic properties of the supported metal [108]–[110].

Several research studies are presented in the literature and report increased chemical adsorption of H_2 on supported Pt catalysts [110]–[113]. Bianchi et al. [114], showed that hydrogen atoms which migrated by the spillover mechanism from Pt/Al_2O_3, to Al_2O_3 were active in ethylene hydrogenation. Furthermore, Maret et al. [115], stated that the hydrogen spillover activation of amorphous or crystallized delta alumina triggers hydrogenating activity in these solids at fairly low temperatures, which was never observed after any conventional activation procedure. During the research of Conner et al. [110], it was pointed out that the method of catalyst preparation can influence the rate of spillover and the subsequent exchanges, where not all types of Pt/SiO_2 behave the same. Moreover, spillover associated with Pt/SiO_2 catalyst may differ from Pt/Al_2O_3, Pd/SiO_2, etc, since the interface between the phases influence the kinetics and the nature of the effects of spillover.

Factors influencing the spillover of hydrogen were summarized by Conner et al. [110]. These factors are: the range of the temperatures of hydrogen adsorption (below room temperature or significantly above); the possible necessity of a co-catalyst such as water or other proton acceptors; the amount and dispersion of the source of hydrogen spillover and the nature of the contact between the source and the acceptor (see Figure 1.23). Moreover, the specific areas of the coupled source-acceptor; the possibility of migration through the gas phase and not exclusively on the surface; the role of the partial pressure of H_2; the strength of the bond between spilt-over hydrogen and acceptor sites and the chemical nature of the acceptor and source.

While in a catalytic reaction, the spillover phenomenon may act positively by increasing the number of active sites, it is not desired when determining the adsorption stoichiometry, since it always involves an increase of the amount of adsorbed gas. More specifically, when spillover occurs, then there is always an overestimation of the free metal surface and the dispersion of the active phase (i.e., during selective H_2 chemisorption experiments) [26], [108].

CHAPTER 2: LITERATURE REVIEW

2.1. Catalytic Decomposition of NO

Nitric oxide (NO) is a colourless, monomeric and paramagnetic gas. It is the simplest thermally stable odd-electron molecule known and has the electron configuration of $(\sigma^2{}_g)$ $(\sigma^2{}_u)$ (σ_g, π_u) $(\pi^1{}_g)$. NO has an unpaired electron in its $2\pi^*$ antibonding orbital and this supports the notion of an amphoteric bonding of NO on a surface. NO, as mentioned before, can donate its electron to the surface (like CO molecule) or it can accept electron density from the surface into the half-filled $2\pi^*$ orbital. By donating the electron, the energy of the molecule lowers, which results in higher stability. On the contrary, the introduction of another electron on the antibonding orbital π^* will make the molecule unstable and enable its dissociation. Consequently, the dissociation of NO can take place at sites capable of donating an electron, which comes to an agreement with the finding that the reaction rate is faster on reduced catalysts [3], [4], [8], [65]. Figure 2.1 indicates the molecular orbital diagram of nitric oxide [116].
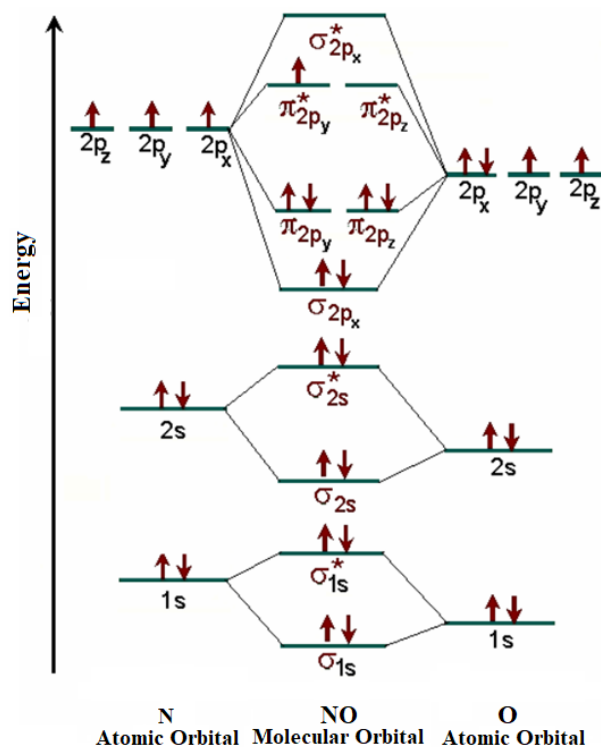
Figure 2.1: Molecular orbital diagram of nitric oxide.

Even though nitric oxide is an endothermic, relatively unstable compound, no decomposition is observed at 825K. The thermodynamic parameters of entropy, enthalpy,

Gibbs free energy of NO, as well as the Gibbs free energy of the NO decomposition, for a relatively broad range of temperatures are presented in Table 2.1 [16].

Table 2.1: Thermodynamic parameters of NO decomposition: entropy (S^0), enthalpy (ΔH_f^0), Gibbs free energy of NO (ΔG_f^0), and Gibbs free energy [16].

T (K)	NO		NO reaction	
	S^0 (cal mol K)	ΔH_f^0 (kcal mol^{-1})	ΔG_f^0 (kcal mol^{-1})	$(\Delta G_f^0)_r$ (kcal mol^{-1})
298	50.35	21.60	20.72	-2×20.72
300	50.40	21.60	20.71	-2×20.71
400	52.45	21.61	20.41	-2×20.41
500	54.06	21.62	20.11	-2×20.11
600	55.41	21.62	19.81	-2×19.81
700	56.57	21.62	19.51	-2×19.51
800	57.61	21.63	19.21	-2×19.21
900	58.54	21.63	18.91	-2×18.91
1000	59.39	21.64	18.60	-2×18.60

Nitric oxide is thermodynamically unstable even at 298K (25°C) and 1 atm, due to the electronic structure of its bond. However, the decomposition reaction is spin forbidden, and thus NO is kinetically stable. Therefore, the high thermal stability of NO is due to its high energy of dissociation (153.3 kcal/mol) and to corresponding extremely low decomposition rates. In practice, it decomposes into its elements at elevated temperatures (1100-1200°C) even though at low temperatures, NO decomposition reaction is thermodynamically favourable (ΔG= -86 kJ/mol). The direct decomposition of NO to N_2 and O_2 (eq. 2.1) is one of the most attractive methods (in a commercial point of view) since it eliminates the need for reductants, which subsequently eliminates the additional pollution associated with other methods [8], [16], [65].

$$2NO \rightarrow N_2 + O_2, \Delta H^o_{298}= -86.6 \text{ kJ/mol} \tag{2.1}$$

Having that in mind, its catalytic decomposition seems to be the simplest and cheapest method to remove NO_x from exhaust gases by decomposing into N_2 and O_2. However, the high activation energy of NO decomposition (364 kJ/mol) hinders the reaction. Therefore, a catalyst is necessary to lower the activation energy in order to facilitate the reaction. Additionally, in the presence of a reductant, reactions lead to a strong decrease in the Gibbs free energy values, and this is why such reactions are preferred for practical applications [4], [15], [16], [117].

Nitric oxides electronic structure and reaction chemistry have been very extensively studied. Direct NO decomposition with catalysts has been initially studied by Jellinek in 1906 [118], while afterwards many researchers focused on this area [3], [4], [8], [119], [120]. It is noted that many papers have been devoted to the catalytic decomposition of NO over noble metals, transition metal oxides, and zeolites. In fact, among the supported noble metals, Pt catalysts were found to be the most active [4].

The catalytic decomposition of NO_x can be classified by two major paths, one in which the catalytic decomposition of NO_x occurs in absence of a reducing agent (eq. 2.1) and the second in which the catalytic reduction of NO_x occurs in the presence of a reducing agent. The latter path contains four sections, where NO can be reduced by (i) CO, (ii) H_2, (iii) NH_3, and with (iv) hydrocarbons (HCs) in the presence or absence of oxygen. The four sections are expressed by the following equations 2.2 - 2.6 [3], [4].

(i) $\quad NO + CO \rightarrow \frac{1}{2} N_2 + CO_2, \Delta H^o_{298} = -328$ kJ/mol $\qquad\qquad$ (2.2)

(ii) $\quad NO + H_2 \rightarrow \frac{1}{2} N_2 + H_2O, \Delta H^o_{298} = -287$ kJ/mol $\qquad\qquad$ (2.3)

(iii) $\quad 6NO + 4NH_3 \rightarrow 5N_2 + 6H_2O$ $\qquad\qquad\qquad\qquad\qquad$ (2.4)

$\quad\quad 4NO + 4NH_3 + O_2 \rightarrow 4N_2 + 6H_2O, \Delta H^o_{298} = -1627$ kJ/mol $\qquad$ (2.5)

(iv) $\quad NO + CH_4 + \frac{3}{2} O_2 \rightarrow \frac{1}{2} N_2 + CO_2 + 2H_2O, \Delta H^o_{298} = -847$ kJ/mol $\qquad$ (2.6)
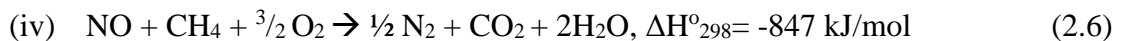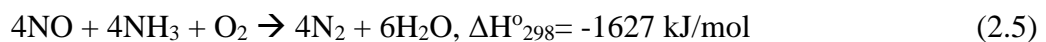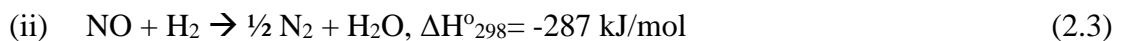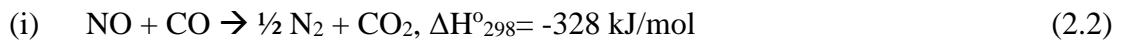
While NO can be reduced with any of the above reducing agents, based on equations 2.2-2.4, SCR processes are usually carried out in the presence of oxygen (eq. 2.5 and 2.6) in order to increase reaction's selectivity towards N_2.

2.2. NO_x Control Technologies

Reduction of NO emissions has become one of the greatest challenges in environmental protection. The development of innovative "environmental" catalysts is also the crucial factor towards the objective of developing a new sustainable industrial chemistry. This is why it is being intensely studied by numerous groups from academic as well as industrial research laboratories for the last five decades [4], [15], [16], [121]–[123]. NO_x emissions can be reduced by a variety of methods during pre-combustion, combustion and post-combustion methods.

2.2.1. Pre-combustion and Combustion Methods

Pre-combustion and combustion methods are not relatively very expensive, and they generally reduce NO_x by less than 50% [4]. The aim of pre-combustion methods is to decrease the emission of NO_x, as well as reduce the need for other combustion and post-combustion methods [124]. Pre-combustion methods focus on purifying the fuel, by lowering the content of nitrogen compounds in the fuel, or by choosing the fuel with low nitrogen content, such as natural gas instead of diesel oil [10], since the fuel type affects the formation of NO_x through the amount of fuel bound nitrogen [125].

The combustion control technologies that are mainly used are summarized in the next table. They include alteration of operational conditions, such as control of temperature, optimal air/fuel ratio and residence time in the combustion zone by designing furnaces and burners. Generally, combustion controls are the least expensive approach for obtaining an initial reduction in the uncontrolled NO_x emissions on any stationary furnace. Particularly, by lowering the temperature of the flame, the thermal NO formation can be limited. Also, the injection of steam water into the combustion chamber or partial flue-gas recirculation achieves the reduction of NO_x emissions, specifically the thermal NO [4], [10], [126]. By replacing the air in the combustion process with pure oxygen it can significantly diminish the formation of thermal and prompt NO_x according to Sterner and Tunheim [127]. However, the main drawback of this solution is its high cost. It should be noted that the efficiency of the combustion process is often affected by the implementation of combustion control [126].

Table 2.2: Summary of Combustion Control Technologies [126].

	NO_x Emissions Control Technology	Application	NO_x Reduction (%)
1	Low NO_x Burners-Oil & Gas	Boilers/Process Heaters	40-60
2	Low NO_x Burners-Coal	Boilers	40-60
3	Over Fire Air (close coupled)	Boilers	30-50
4	Over Fire Air (separated)	Boilers	40-60
5	Reburn	Coal-Fired Boilers	40-50
6	Induced Flue Gas Recirculation (existing fan)	Boilers/Process Heaters (Internal)	30-40
7	Forced Flue Gas Recirculation (additional fan)	Boilers	40-50
8	Water/Steam Injection	Boilers/Process Heaters	20-25

2.2.2. Post-combustion Methods

Post-combustion methods, which are summarized in Figure 2.2, deal with NO_x in exhaust gases from incineration processes and are much more effective than pre-combustion and combustion methods. They can reduce NO_x up to 100% but are usually very expensive. Some of the post-combustion methods include selective catalytic reduction (SCR), selective non-catalytic reduction (SNCR) and lean-burn NO_x adsorbers (NO_x traps) [3], [4], [21].

The post-combustion technologies can be used as alternative or supplementary to combustion modifications. For instance, the combination of SNCR with combustion technologies can achieve up to 90% reduction levels, which are achievable with the SCR process alone. Moreover, combining control technologies has several advantages over the installation of only SCR, such as the significant reduction in the size and operating costs for the SCR, when implementing combustion control techniques with the SCR [126].
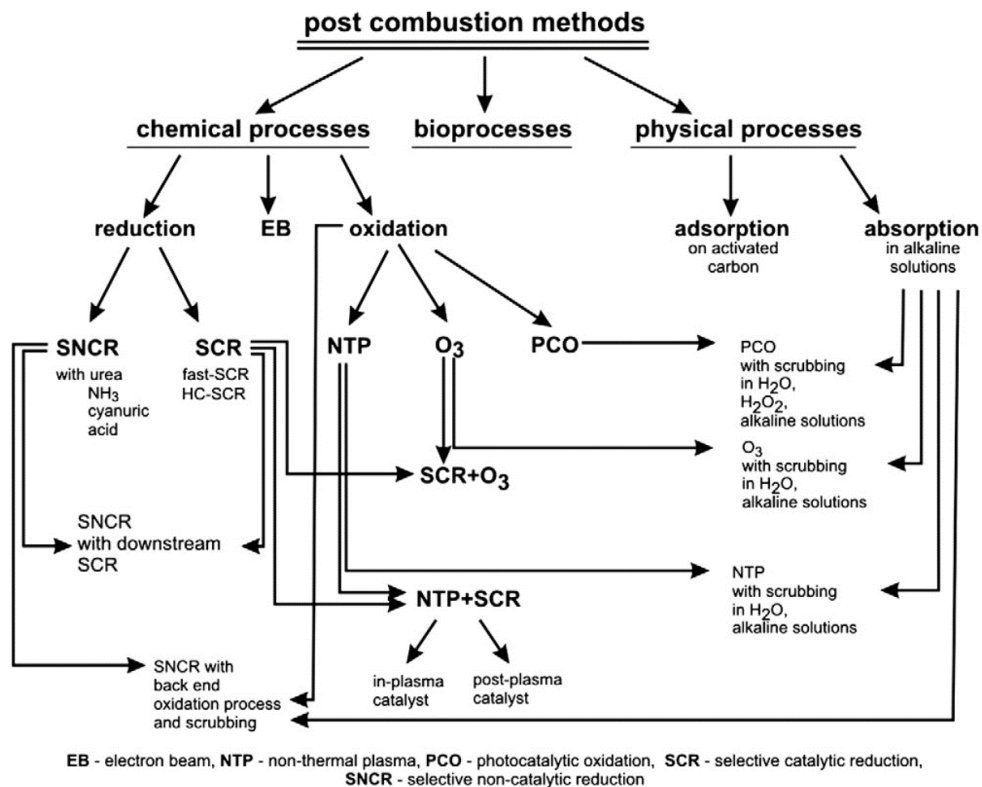
Figure 2.2: Schematic presentation of NO_x abatement post-combustion methods [10].

2.2.2.1. NO_x Storage/Reduction (NSR) Catalysts

NO_x storage/reduction (NSR) catalysts, which are also referred to as NO_x adsorption catalysts (NAC) and lean NOx traps (LNT), have been developed as an alternative after-

treatment device which can be applied in lean-burn gasoline and diesel engines so as to reduce NO_x emissions. It should be noted that the LNT design was devised to counter problems experienced in other after-treatment devices. For instance, the need for a continued reductant supply to maintain a given $C_1:NO_x$ ratio in SCR [128]–[130]. It is also noted that LNT and SCR are the most predominant technologies for the control of NO_x emissions from diesel passenger cars in the European market. According to Yang et al. [131], LNTs are used predominately for smaller applications (95% of Diesel euro 6 vehicles with engine displacements below 1.5 liters sold in the EU in 2014), although some manufacturers (e.g., Peugeot-Citroën, Mercedes) have chosen to apply SCR in the US market [131].

The NO_x storage/reduction (NSR) catalysts operate in a cyclic manner. During the lean period of operation, the catalyst stores or "traps" NO_x as nitrate species. In order to release the trapped NO_x and reduce it to N_2, a periodic and short rich pulse is introduced for a few seconds and thereby the catalyst is not saturated but is regenerated. Specifically, a NO_x adsorber catalyst consists of three main components, i.e. an oxidizing catalyst (e.g. Pt), storage medium with high surface area (e.g. such as alumina, alkaline earth metals or alkaline earth metal oxides like barium and barium oxide) and a reducing catalyst (e.g. Rh). The Ba component can adsorb NO_x at T>250ºC, while at lower temperatures substantial storage is also provided by Al_2O_3 and CeO_2 [129]–[133].

Figure 2.3 illustrates the general working principle of a $Pt/BaCO_3/Al_2O_3$ LNT with a Rh-based reducing catalyst. NO_x is initially removed from the lean exhaust gas through adsorption onto Pt sites. It then oxidizes to NO_2 and converts to a solid nitrate phase (Figure 2.3a). When the exhaust gas is enriched, the LNT NO_x capacity is recovered by releasing NO_x that is reduced to N_2 over Rh catalyst sites (Figure 2.3b). In order to reduce NO_x and form N_2, the presence of CO and/or HC and/or H_2 is required [132].
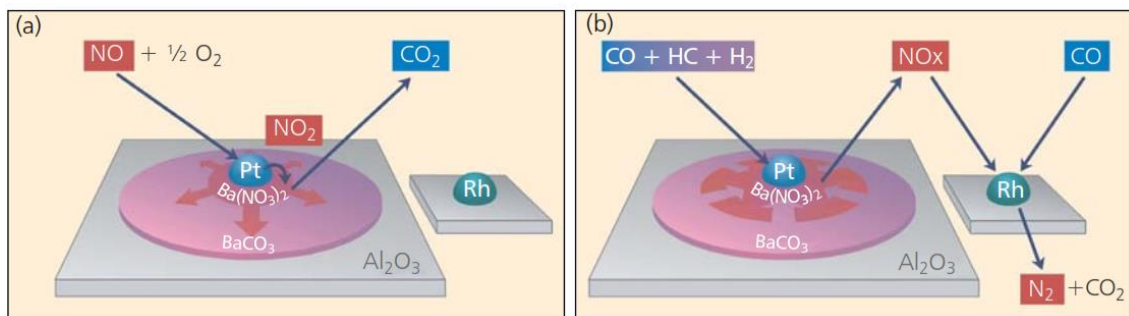
Figure 2.3: Schematic showing the LNT process under, (a) lean exhaust gas operation (trapping) and (b) rich exhaust gas operation (regeneration) [132].

The key reaction steps according to Gill et al. [128], are summarized through equations 2.7 - 2.11. The reaction sequence includes five general reaction steps, with, (i) NO oxidation to NO_2, (ii) NO_x storage on the catalyst surface, (iii) reductant evolution, (iv) NO_x release from the trapping site and (v) NO_x reduction to N_2 over noble metals [130].

$$2NO + O_2 \rightarrow 2NO_2 \tag{2.7}$$

$$MCO_3 + 2NO_2 + \tfrac{1}{2}O_2 \rightarrow M(NO_3)_2 + CO_2 \tag{2.8}$$

where, M is the storage medium

$$M(NO_3)_2 + 2CO \rightarrow MCO_3 + NO + NO_2 + CO_2 \tag{2.9}$$

After a period of time, the adsorber catalyst becomes saturated and unable to adsorb further NO_x. Therefore, the adsorption sites need to be regenerated by inducing rich conditions in the exhaust gas, which increases the temperature causing the stored nitrate species to become thermodynamically unstable and desorb from the adsorber forming NO and NO_2.

$$NO_2 + CO \rightarrow NO + CO_2 \tag{2.10}$$

$$NO + CO/HC \rightarrow \tfrac{1}{2}N_2 + CO_2/H_2O \tag{2.11}$$

One of the major disadvantages of the lean NOx trap system is its poor low-temperature performance, i.e. problematic reaction's selectivity. Particularly, an incomplete reduction leads to the formation of N_2O (toxic and powerful greenhouse gas), especially at low temperatures (200-300°C), while at higher temperatures (400°C) it diminishes. Another disadvantage is the susceptibility to poisoning by species such as sulfur oxides, to form barium sulfate which is more stable than nitrate. Therefore, these sites are no longer available to react with NO_x. Unfortunately, the procedure to regenerate the catalyst requires considerably high-temperatures. Additionally, the competitive adsorption of CO_2 (contained in the exhaust gas) and NO can have an adverse effect on NO storage [117], [134], [135].

Moreover, it should be mentioned that an LNT generates N_2 during the fuel-rich phase, whereas NO_x is stored during the lean phase. In order to address this limitation and reduce NO_x to N_2 in both lean and rich conditions, a transient catalytic NO_x reduction catalyst was developed by the Nakatsuji's group [134]. The catalyst contains a Pt-based oxygen storage component (OSC) and a solid acid. Additionally, the NSR technology proposed by Toyota researchers in the middle of 1990s has been recognized as one of the most promising solutions for lean NO_x abatement [136], [137]. Pt-K/Al_2O_3 sorbents-catalysts

were used for NO_x removal under lean conditions and later, the Toyota researchers found that by adding 33 mol% TiO_2 and 67 mol% lithium-doped γ-alumina support, it can maintain the amount of NO_x storage and improve the sulfur tolerance [102], [137].

2.2.2.2. Selective Catalytic Reduction (SCR) of NO

Selective Catalytic Reduction treatment is the preferred technology used worldwide for the control of NO_x emissions in fuel combustion from stationary sources due to its high efficiency, selectivity and economics. The SCR process is the only technology that selectively converts NO or NO_2 to N_2 and water. This can be achieved even under strongly oxidizing conditions. This subchapter focuses on the selective catalytic reduction of NO in the presence of different reducing agents. NH_3-SCR or Urea-SCR uses ammonia and is typically used in chemical industrial plants and stationary power stations. The selective catalytic reduction of NO in the presence of hydrocarbons, particularly methane, (HC-SCR) is used for automotive pollution control and various industrial plants. The catalytic reduction of NO in the presence of CO and/or H_2 is also used for automotive pollution control [16], [121], [138].

- **Selective Catalytic Reduction of NO_x by NH_3 (NH_3-SCR)**

The catalytic control of NO_x emissions from nitric acid plants, power stations, industrial boilers, gas turbines, etc., is based on the selective catalytic reduction of NO_x with ammonia, i.e. NH_3-SCR. The SCR with ammonia as a reducing agent has been a subject of interest for many decades and it is still being researched [16], [29], [139], [140]. The SCR by ammonia has found many applications in Japan, Germany and the USA since the early 1970s when it was applied for the first time. The main reactions that occur during SCR with ammonia as a reducing agent can be described by equations 2.12 - 2.15 [4], [16].

$$4NO + 4NH_3 + O_2 \rightarrow 4N_2 + 6H_2O \qquad\qquad (2.12)$$

$$6NO + 4NH_3 \rightarrow 5N_2 + 6H_2O \qquad\qquad (2.13)$$

$$6NO_2 + 8NH_3 \rightarrow 7N_2 + 12H_2O \qquad\qquad (2.14)$$

$$2NO_2 + 4NH_3 + O_2 \rightarrow 3N_2 + 6H_2O \qquad\qquad (2.15)$$

For the NH_3-SCR the traditional active metal oxides that have been examined are V_2O_5, TiO_2, WO_3 and MoO_3. For instance, the V_2O_5/TiO_2 catalysts can achieve NO_x conversions greater than 80% at 350°C and they were proven very stable in the presence of water vapour or SO_2. Even though NH_4NO_3 or $(NH_4)_2SO_4$ compounds can be formed

on the catalyst surface, they can readily decompose below 300°C. By incorporating WO_2 into the V_2O_5/TiO_2 formulation, 80% NO_x conversion is attained at the lower temperature of 225°C. Additionally, MoO_3/TiO_2 catalyst showed relatively high activity which increased with increasing the MoO_3 loading, whereas the N_2 selectivity (S_{N2}) decreased due to the formation of N_2O, which is undesired [121], [138], [139], [141].

Generally, the commercial SCR catalysts are composed of V_2O_5 (vanadium pentoxide, vanadia) and WO_3 (tungsten trioxide) as the active components which are supported on a high surface area TiO_2 carrier. V_2O_5 is responsible for the activity of the catalyst during the reduction of NO_x as well as the undesired oxidation of SO_2 to SO_3. WO_3 is a promoter that widens the temperature window of the SCR reaction and imparts superior thermal stability and better mechanical properties to the catalysts. Another commercial catalyst is V_2O_5-MoO_3/TiO_2 (using MoO_3 instead of WO_3), which is more tolerant to As but is less active than V_2O_5-WO_3/TiO_2 [27], [141].

The commercial SCR catalysts are in the form of honeycomb monoliths or plates. They are assembled into standard steel cased modules, which are then placed into the reactor to form catalyst layers (typically three layers), as shown in Figure 2.4. The injection of ammonia in the flue gas stream is achieved through a distribution grid, where ammonia, either anhydrous liquified or in aqueous solution, is vaporized and diluted with air. NH_3 is dosed to the system in stoichiometric quantities (NH_3/NO mole ratio), depending on the NO_x content of the gas being treated [27], [138].
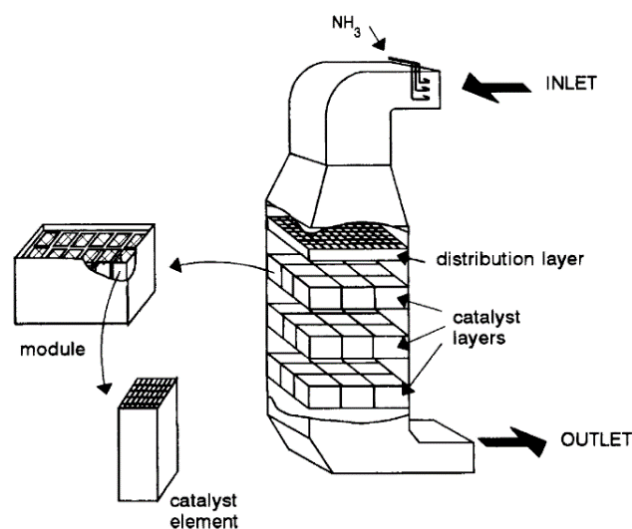
Figure 2.4: A schematic representation of an NH_3-SCR plant [138].

An integral mechanism for the reduction of NO with NH_3 over V_2O_5 on TiO_2 catalysts is indicated in Figure 2.5. Vanadia-titania catalysts exhibit two separate catalytic functions,

one on which an oxidation-reduction process occurs (V^{5+} to V^{3+} and back) and another involving the acidic function of V^{5+} sites [16], [27].
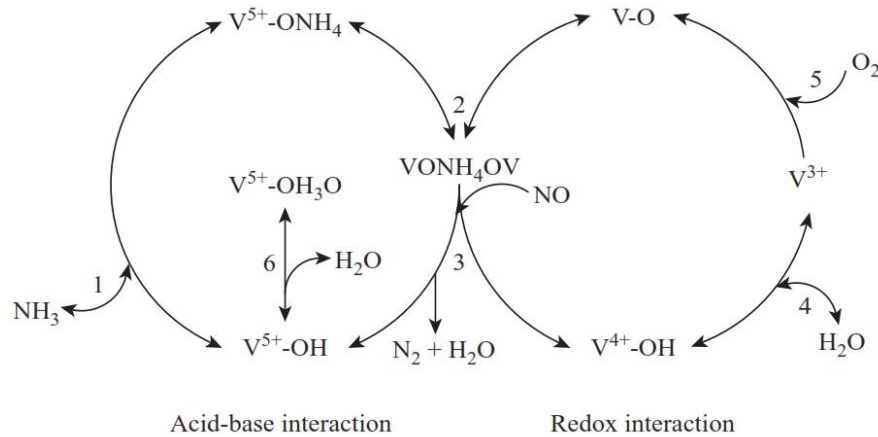
Figure 2.5: Mechanistic scheme of the NH$_3$-SCR reaction [16].

The NH$_3$-SCR process has many drawbacks that triggered the examination of other, alternative reducing agents, such as hydrocarbons or hydrogen. Moreover, the high costs of the SCR installations, as well as the size of the installation, limits its application to stationary sources of NO$_x$ emission. In addition, they can produce secondary environmental pollution as a result of ammonia leaks, known as ammonia slip, which is the emission of unreacted ammonia. Also, the transportation and storage of ammonia is a burden, as well as the corrosive properties of some of its undesired by-products. This is the main reason why gaseous NH$_3$ has been replaced by urea during the last couple of decades, in most applications Urea, ($CO(NH_2)_2$), is used as reductant instead of ammonia as it is safer and less toxic, which makes storage and handling much easier. Urea, which is solid, can be hydrolyzed to generate ammonia on demand according to the following reaction (eq. 2.16). In particular, urea decomposes at 440K to form NH$_3$ and CO$_2$ [4], [16], [20], [139].

$$CO(NH_2)_2 + H_2O \rightarrow CO_2 + 2NH_3 \qquad\qquad (2.16)$$
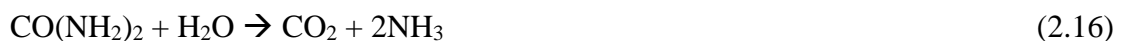
Although NH$_3$ (or urea) is very efficient as a reducing agent, there are some factors that prevent the widespread use of this technology for mobile applications. Firstly, there is not a nationwide infrastructure for urea distribution. In addition, since urea is not required to operate the engine, an additional/separate injection system is needed. However, proper injection equipment for such an application is complex in order to ensure proper atomization and to prevent urea crystallization. Creating a uniform concentration of NH$_3$ in the reactor can also be problematic. Therefore, the requirement for such a complex

injection system affects the economics and practicability of this technology for mobile vehicles [121], [139]. Moreover, using urea as the dosed reducing agent, causes a constraint in the lower temperature range of the temperature window, because the conversion of urea to NH_3 is not complete below 200°C. It is noted that during urban driving, the temperature of the exhaust gasses at the urea injection point, can often fall below 200°C [20].

- **Selective Catalytic Reduction of NO$_x$ by Hydrocarbons (HC-SCR)**

The SCR of NO by hydrocarbons (HC-SCR) is believed to be the most promising way to eliminate NO. The main advantage of the corresponding reaction is the use of a gas mixture very similar to that found in exhaust gas streams. A lot of researchers have studied the HC-SCR, because of the practicability and cost-effectivity of using a hydrocarbon as a reducing agent [15], [16], [142]–[144]. Regarding the reaction mechanism of HC-SCR, three kinds of reaction schemes have been proposed and are summarized below (eq. 2.17 - 2.19) [144].

$$2NO \rightarrow N_2 + 2O_{ads} \qquad (2.17)$$

$$HC + O_{ads} \rightarrow CO_2 + H_2O$$
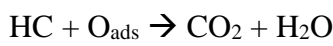
where, decomposition of NO proceeds to yield N_2 and then the hydrocarbons clean up the surface oxygen, or in other words, the oxidation reaction of hydrocarbon by oxygen is used to adjust the oxidation state of an active metal ion.

$$HC + O_2 \text{ (or } NO_x) \rightarrow HC^* + CO_2 + H_2O \qquad (2.18)$$

$$HC^* + NO_x \rightarrow N_2 + CO_2 + H_2O$$

where, some reaction intermediates (HC*) formed by the oxidation of the hydrocarbon have the ability to reduce NO selectively.

$$NO + \frac{1}{2}O_2 \rightarrow NO_2 \qquad (2.19)$$

$$HC + NO_2 \rightarrow N_2 + CO_2 + H_2O$$
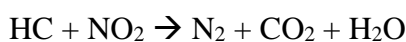
where, nitrogen oxides, generated from the oxidation of NO (for example NO_2), can preferentially react with the hydrocarbon.

The reduction of NO by HC has been investigated over zeolite-based catalysts, over metallic catalysts and over metal oxide catalysts [4], [139]. The early research of Iwamoto et al. [145] over zeolite-based catalysts, reported the desirable properties of Cu-ZSM-5 catalysts for the HC-SCR of NO. Cu-ZSM-5 was found to be active even in the presence

of oxygen. Moreover, Cu-ZSM-5, was found to be active using several HCs, as reducing agents, which have been classified into two groups, selective reductants (e.g. C_2H_4, C_3H_8, C_4H_8) and non-selective reductants (H_2, CO, CH_4). According to the literature [15], [146], alkanes or alkenes (selective reductants) are able to reduce NO on Cu-ZSMS, not only in the presence of oxygen but also under extremely oxidative conditions.

Apart from zeolite-based catalysts, much attention has been paid on noble metal-supported catalysts. An investigation of the platinum-group metals (e.g. Pt, Ir, Pd, Rh, Ru) supported on γ-Al_2O_3 was conducted by Obuchi et al. [147]. They concluded that Pt and Rh supported catalysts had high NO conversion activities under model (propene) and real diesel exhaust mixtures, especially at the low-temperature range of 200-350°C. It was also confirmed that the Pt/Rh and Pt supported catalysts had higher activity and durability than the Cu/ZSM-5 catalyst under real diesel exhaust conditions. It should be mentioned that Pt catalysts have the advantage of resisting to water deactivation. However, during the HC-SCR of NO, on noble metal-supported catalysts, N_2O is also formed at considerable concentrations, reaching selectivity values of up to 65%. Burch and Ottery [148], have found that the formation of N_2O can be lowered to 50% when using toluene as the reducing agent.

Moreover, Burch et al. [149], investigated the mechanism of HC-SCR on Pt-catalysts, as well as metal ion-exchanged zeolites and concluded that the key reaction is the decomposition of NO, while hydrocarbons are used to remove surface oxygen species. Since the NO dissociation over a single crystal metal surface oxidizes the metal surface, which in turn prevents further NO dissociation, therefore a reducing agent is required to scavenge the formed surface oxygen species.

Additionally, HC-SCR of NO was also examined over metal oxide catalysts. Zegaoui et al. [150] researched the V_2O_5/TiO_2 catalyst at different metal loadings for the SCR of NO by propane. The best activity (X_{NO}= ~90%) was observed for the samples containing 4.4wt% of vanadia, as the number of active coordinated surface species increased until the appearance of crystalline V_2O_5 beyond that loading. At higher loadings, a decrease in the conversion was observed. Shimizu et al. [151], studied a Ga_2O_3/Al_2O_3 catalyst for the SCR of NO by CH_4. Ga_2O_3/Al_2O_3 presented high activity and selectivity, which was attributed to highly dispersed gallium oxide species on Al_2O_3. The activity of various base oxides and supported metal catalysts for HC-SCR is reported in Table 2.3 [143]. As it can be seen Ag/Al_2O_3 is the most promising catalyst for HC-SCR, a fact which was also

confirmed by the research of Shimizu et al. [152], who reported its high catalytic performance and its tolerance to SO_x and water vapour.

Table 2.3: Activity of various base oxides and supported metal catalysts for HC-SCR.

Catalyst	Reaction Conditions				T_{max} (^{o}C)	NO Reduction Efficiency	
	NO (ppm)	O_2 (%)	Reducing agent	H_2O (%)		X_{NO} (%)	S_{N2} (%)
Ga_2O_3-ZrO_2	400	9	240ppm $C_{10}H_{22}$	1.5	300	71	89
Al_2O_3-ZrO_2	400	9	240ppm $C_{10}H_{22}$	1.5	300	60	91
1wt% Sn/Al_2O_3	1000	10	1000ppm CH_4O	8	350	50	92
Pt/Al_2O_3	1000	10	1000ppm C_3H_8		350	37	50
1%Pt/γ-Al_2O_3	995	5	870ppm C_3H_6		250	50	N/A
1%Rh/γ-Al_2O_3	995	5	870ppm C_3H_6		300	45	N/A
Pt/γ-Al_2O_3	400	3	400ppm CH_4		300	40	N/A
0.17%Au/Al_2O_3 DP	1000	10	1000ppm C_3H_6	10	400	80.7	N/A
2.5%Ag/Al_2O_3	50	10	2500ppm C_2H_6O		300	98	60

Since the first study on the HC-SCR technology, various types of catalysts have been examined. Even though ion-exchanged zeolites show very high activity on HC-SCR, they are unstable in hydrothermal conditions, under which they become deactivated. Also, supported precious metal catalysts, especially supported Pt catalysts, show high stability, high tolerance to SO_x and water vapour, and very high activity at lower temperatures. However, the low selectivity towards N_2 and their narrow temperature range of operation, inhibit a possible practical application [3].

- **Selective Catalytic Reduction of NO_x by H_2 (H_2-SCR)**

In order to reduce the environmental footprint of marine and land diesel engines, new technological solutions are needed to overcome the intrinsic drawbacks of existing emission control technologies (NH_3-SCR, HC-SCR). Specifically, the increasing CO_2 emissions as well as the many problems of using NH_3 as a reducing agent (low activity at low temperatures, ammonia slip, high running cost, NH_3 storage, ash odour, deterioration of catalysts and complex of systems), lead to a demand for finding appropriate non-carbon-containing reducing molecules for the catalytic removal of NO from combustion exhaust streams [15], [16], [121], [122], [153].

Recently, selective catalytic reduction of NO_x by H_2 (H_2-SCR) has attracted more and more attention for NO_x removal. It must be noted that, when H_2 is used as a reducing agent, NO_x can be effectively reduced even at low reaction temperatures (T < 200°C).

Since the combustion of H_2 produces exclusively H_2O, without undesired by-products (e.g. CO_2), H_2 can be characterized as a "clean carrier", and the H_2-SCR method as being environmentally benign [72], [121]. On the other hand, if H_2 is produced from fossil fuels, this makes H_2 an indirect source of CO_2. Consequently, the real opportunity for the future, regarding the environment, is to produce hydrogen from non-fossil fuels. As stated by many researchers, hydrogen is an exceptional alternative option to the matter of the reducing agent in the case of SCR of NO and has also been described as the fuel of the future [72], [121], [154].

H_2-SCR, as a "green" technology, can be used for stationary sources as well as mobile applications. For instance, it can be used for NO_x control at power plants, industrial boilers, furnaces and biomass incinerators (stationary), where hydrogen can be produced on-site through steam reforming of hydrocarbons. Regarding mobile applications and in particular, for diesel-powered vehicles, on-board hydrogen generation can be achieved by autothermal reforming (ATR) of diesel fuel. Finally, H_2-SCR could be ideal for hydrogen-fueled vehicles, due to the on-board availability of hydrogen [72], [121].

For the reaction mechanism of H_2-SCR, different interpretations appear in the literature, due to the different catalyst formulation and experimental conditions examined. Currently, the reaction mechanism can be classified into two phases: NO adsorption/dissociation phase and oxidation-reduction phase. It is clear that for the first mechanism, the adsorption and dissociation of NO and H_2 are important. For the oxidation-reduction mechanism, the formation of reaction intermediates, e.g. nitrates and NH_3 (or NH_4^+), is crucial for the reduction of NO_x. The latter mechanism has a more complicated reaction pathway [72], [155]. During the H_2-SCR process, the main reaction network that occurs is described by the following six equations [72].

$$2NO + 4H_2 + O_2 \rightarrow N_2 + 4H_2O \tag{2.20}$$

which is the reaction that leads to the formation of the desirable product (N_2).

$$2NO + 3H_2 + O_2 \rightarrow N_2O + 3H_2O \tag{2.21}$$

$$2NO + H_2 \rightarrow N_2O + H_2O \tag{2.22}$$

where, N_2O can be formed as a by-product.

$$NO + {}^5/_2H_2 \rightarrow NH_3 + H_2O \tag{2.23}$$

where, NH_3 could be produced, even though the presence of oxygen can inhibit its formation over some catalyst formulations.

$$NO + \tfrac{1}{2}O_2 \rightarrow NO_2 \qquad\qquad\qquad (2.24)$$

where the formation of NO_2 may play an important role in NO_x reduction due to its higher activity compared to NO.

$$H_2 + \tfrac{1}{2}O_2 \rightarrow H_2O \qquad\qquad\qquad (2.25)$$

where the combustion reaction of H_2, competes with the first reaction and leads to the low utilization of the reducing agent for NO_x removal.

At present, mostly supported noble metal catalysts, such as Pt, Pd, Rh have been examined for the H_2-SCR process. The nature of the noble metal plays a crucial role in the high activity and selectivity of H_2-SCR catalysts. Regarding the Pt catalysts, which have been found to be among the most active noble metals for the particular reaction at hand, the oxidation state of Pt is the controlling factor for the H_2-SCR activity. It should be noted that the metallic Pt species are much more active than the oxidized Pt ones [72]. Moreover, the function of the noble metal is related to the dissociation of NO to adsorbed N and O, and the formation of active nitrate and NH_x^+ species [72], [74], [156].

For instance, the $La_{0.5}Ce_{0.5}MnO_3$ perovskite is inactive for H_2-SCR of NO_x, but Pt supported on $La_{0.5}Ce_{0.5}MnO_3$ is highly active. During the same research, Costa et al. [157] suggested that the dissociation of the N–O bond mainly proceeded on Pt active sites but not on the support. Mihet et al. [158] examined Pt, Pd and Rh supported on alumina catalysts, with 1 wt.% metal loading. All their catalysts proved to be active for H_2-SCR at low temperatures, with $X_{NO} > 95\%$ and $S_{N2} > 80\%$ at 200°C, and specifically, Pd/Al_2O_3 proved to be the most efficient since even at 100°C it showed high catalytic performance ($X_{NO}=93.5\%$ and $S_{N2}=81.39\%$).

During H_2-SCR of NO_x, the catalyst support plays a significant role in the activity of the catalyst, as it can disperse the active noble metals but also promote the reaction in many aspects through special structures. For instance, a basic support can absorb NO_3^- or NO_2^- species as intermediates [75], whereas an acidic support can stabilize the active metal and store ammonia as reaction intermediates [159]. Li et al. [160] studied the H_2-SCR of NO_x over Pt/MgO, Pt-γAl_2O_3, Pt/ZrO_2 and Pt/HZSM-5 catalysts. They found that conversion efficiency of catalysts was greatly depended on Pt content and NO_x adsorption capacity of substrates. Moreover, they proposed that higher acidity supports contributed to the formation of NH_3 or NH_4^+, which then reacted with NO and O_2 to form N_2, leading to

higher N_2 selectivity. The possible formation mechanisms of N_2 and N_2O during H_2-SCR over supported Pt catalysts are schematically presented in Figure 2.6.
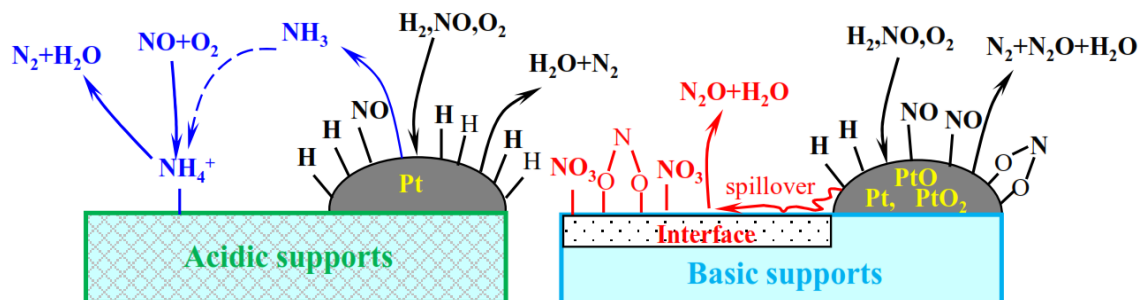
Figure 2.6: Suggested mechanism of H_2-SCR reaction over supported Pt catalysts, according to Li et al. [160].

H_2-SCR of NO_x might be considered as a breakthrough technology against the existing SCR technologies that use NH_3 or hydrocarbons as reductants. The high NO_x conversion efficiencies of H_2-SCR at low temperatures have increased the attention of H_2-SCR systems, as well as the advantages of using H_2 as a reducing agent. Hydrogen is non-corrosive, non-toxic and less processed reductant for SCR applications, compared to NH_3 [153]. Moreover, it can be produced from a variety of sources (renewable, nuclear) without CO_2 emissions. Hydrogen can also be utilized in a variety of applications (transportation, electricity production, etc.), without producing any pollutants after its combustion, just water [121].

2.3. Inkjet Printing (IJP)

Inkjet printing (IJP) is a method of digital, non-impact dot-matrix printing technology in which droplets of ink are jetted from a small aperture directly to a specified position on a media (substrate) to create an image. Each small droplet, with a typical diameter of 10-100µm which corresponds to a drop volume from 0.5-500pl, is created and deposited under digital control [161], [162]. Lord Rayleigh described in 1878 [163] the mechanism by which a liquid stream breaks up into droplets and in 1951 Elmqvist patented the first practical Rayleigh break-up ink-jet device [164]. Twenty years later IBM launched a massive development program to adapt continuous inkjet technology for their computer printers and in 1976 they introduced the IBM 4640 ink-jet printer as a word processing hardcopy-output peripheral application [165]. As can be seen in Figure 2.7 the applications of inkjet technology have developed in three waves: initially for marking and coding, followed by desktop printing of text and graphics in the home and small office

environment, and currently, increasing use in commercial printing and manufacturing [162].
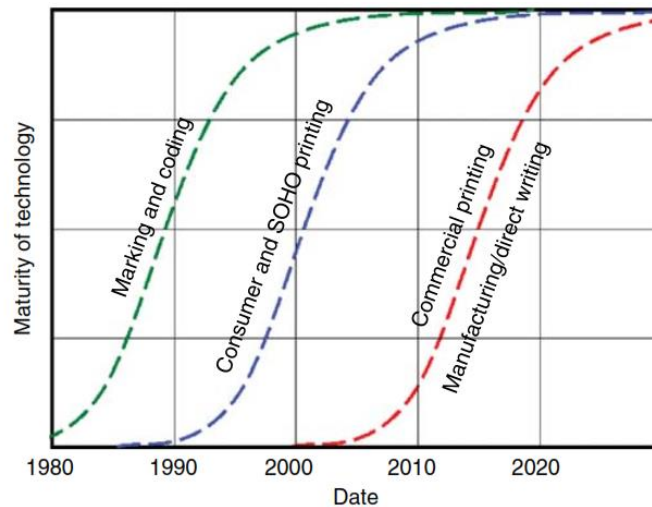
Figure 2.7: The development of inkjet technology.

Consequently, IJP is emerging as an attractive patterning technology for a wide variety of industrial and scientific applications. It has been generating increased interest due to its mildness, simplicity, low-cost and scalability of production. Moreover, IJP is a reliable method for micro- and nano-fabrication and is applicable for a wide variety of deposited metals and substrates, including flexible low-cost substrates such as paper [166], [167]. IJP technology can be used to build three-dimensional objects in a direct way by depositing droplet patterns on top of each other at a well-defined position onto a substrate [168]. In addition, the IJP method has been used beyond its traditional application in the fields of industrial manufacturing and has evolved to print macro-molecules, nanoparticles, solar cells, therapeutic drugs, catalysts, transistors, medical devices and many more [169]–[172].

2.3.1. Principles of Inkjet Printing

2.3.1.1. Categories of Inkjet Printing Technology

IJP technology can be divided into two categories, i.e. continuous and drop-on-demand, as seen in Figure 2.8 [161], [166]. The essential difference between the two categories lies in the nature of the flow through the nozzle. Continuous inkjet printing (CIJ), supplies a continuous stream of ink droplets that are charged upon leaving the nozzle and then deflected by voltage plates. The applied voltage determines whether the droplet will be deposited onto the substrate, or if the drops are undesirable and thereby the fluid is recycled through the system, as can be seen in Figure 2.9. It is noted that even if the printer is not actually printing anything onto a substrate, a stream of droplets is still being

ejected from the nozzle and recycled through the gutter [166], [170], [173]. While continuous inkjet printers are still used, the development of drop-on-demand (DoD) printing in the 1990s, and the resulting increase in achievable resolution, the outstanding control on homogeneity and thickness of the system, and also the high displacement accuracy which together allow 2D and 3D pattern printing, led to the widespread consumer and business use of inkjet printing [162], [166].
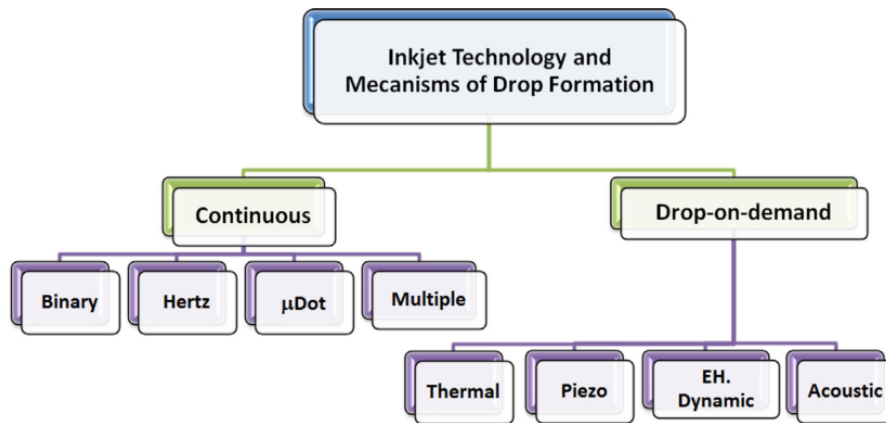
Figure 2.8: Categories of inkjet technology and mechanisms of drop formation.
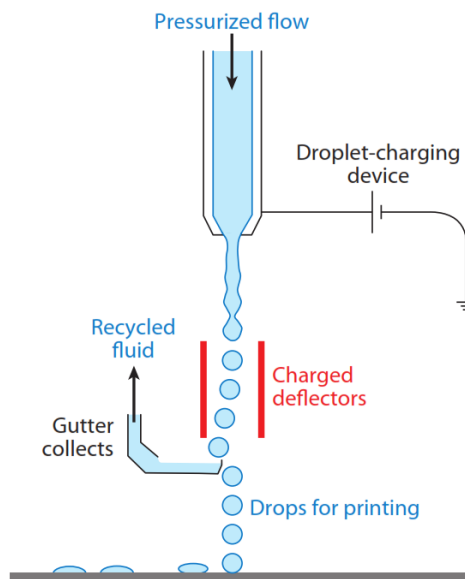
Figure 2.9: Schematic diagram showing the principles of operation of a CIJ printer.

On the other hand, a drop-on-demand inkjet printer ejects a droplet of ink only when required. Therefore, when the printer is not actually printing anything onto a substrate, there are no droplets being ejected from the nozzle [166]. Depending on the mechanism used in the drop formation process, DoD technology can be categorized into four major methods: thermal, piezoelectric, electrostatic, and acoustic ink-jet (Figure 2.8). Therefore, the ejection of ink droplets from the nozzle is generated by pulses of a thermal resistor,

piezoelectric transducer, thermal buckling or acoustic wave. Most, if not all, of the drop-on-demand ink-jet printers on the market today, are using either the thermal or piezoelectric principle [161], [166].

During the thermal jetting printing, which is also referred to as bubble printing, a small electric heating element on the thermal printhead raises rapidly the temperature of a thin layer of ink liquid to 300-400°C. This causes the ink in the nozzle to vaporize, creating a fast-expanding bubble (within μs) and a large increase in pressure which discharges the ink droplet out of the nozzle. When the droplet ejects through the nozzle, ink fills back the ink chamber to cover the occurring emptiness, and the process is ready to create the next droplets. In thermal DoD, the pressurized droplet can be ejected from the nozzle with two ways (Figure 2.10). Depending on the configuration, a thermal ink-jet can be a roof-shooter or a side-shooter, where the orifice is located on top of the heater or on a side located nearby the heater, respectively [162], [166], [173], [174]. The roof-shooter design is used in the printheads from Hewlett-Packard, Lexmark, and Olivetti. The side-shooter design is implemented in the Canon and Xerox printheads [161].
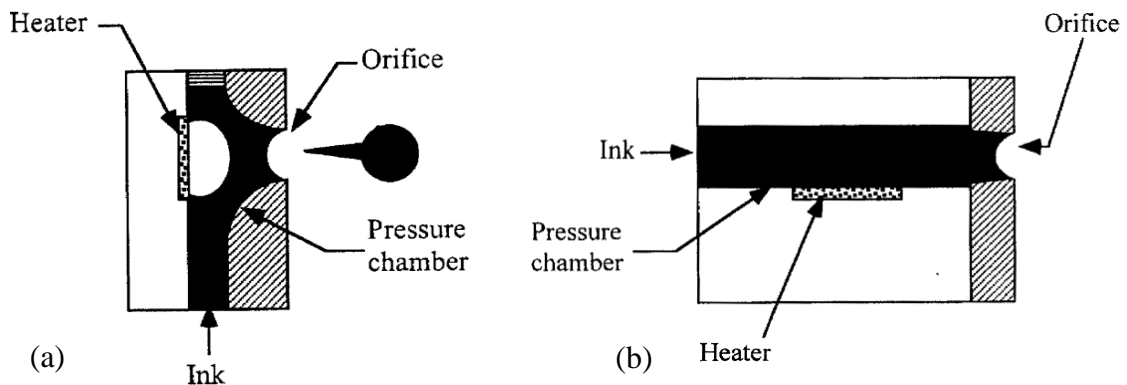
Figure 2.10: Types of thermal DoD ink-jet: (a) side shooter, (b) roof shooter.

Piezoelectric inkjet printers contain a piezoelectric transducer in the nozzle, as a key active component within the inkjet printhead. Piezoelectric printheads incorporate PZT (Lead Zirconate Titanate), which is a manufactured and propelled piezoelectric material. All piezo printheads work in practically the same way, where a terminating pulse in the form of a voltage waveform is applied to the piezoelectric transducer [173], [174]. This excitation proliferates an increase in pressure through the ink which is enclosed in the ink compartment and when the pressure surpasses at the edge of the outlet, it forces the ink droplets out of the nozzle (orifice). Simultaneously, the remaining ink stays inside the ink compartment due to the surface tension and static pressure that balances out the meniscus

phenomenon, which is the curved upper surface of a non-turbulent fluid, at the orifice [170], [175]. The voltage applied for piezo-ceramic deflection, the pulse duration, and the diameter of the nozzle are the critical parameters that define the size of the ink droplets in this type of printing [173], [174].

It is noted that between the two technologies of piezoelectric and thermal DoD inkjet printers, the piezoelectric printheads can handle a wider range of liquids than thermal printheads since they are restricted to inks which satisfactorily vaporize. Usually, in thermal DoD, aqueous solutions are used as a solvent, since they are able to vaporize and also withstand ultra-high temperatures. Therefore, since the fluids may be functionality damaged due to the high temperature, thermal inkjet printers impose limitations on the quantity of polymers, which could be printed utilizing this procedure, despite the fact that non-fluid thermal inks are accessible. On the other hand, piezoelectric printheads and supplementary hardware are costly, whereas the thermal printheads are cost-efficient and simple in design [162], [166], [170].

Regarding the piezoelectric inkjet technology, it can be classified into four main types depending on the piezoceramic deformation mode. It can be squeeze, bend, push, and shear technology, with the latter three being illustrated in Figure 2.11 [166], [173]. The squeeze-mode ink-jet can be designed with two ways; either with a thin tube of piezoceramic surrounding a glass nozzle or with a piezoceramic tube cast in plastic that encloses the ink channel. In a bend-mode design, the piezoceramic plates are bonded to the diaphragm forming an array of bilaminar electromechanical transducers used to eject the ink droplets. In a push-mode design, as the piezoceramic rods expand, they push against the ink so as to eject the droplets. In addition, in practical implementations, a thin diaphragm between piezodrivers and ink is incorporated in order to prevent the undesirable interactions between ink and piezodriver materials. As far as the shear-mode printhead, the electric field is designed to be perpendicular to the polarization of the piezodriver, which becomes an active wall in the ink chamber. The shear action deforms the piezoplates against the ink to eject the droplets. In this case, the interaction between ink and piezomaterial is one of the key parameters of a shear-mode printhead design [161].

By using any of the above modes in a commercial printing system, certain advantages arise [161], [174]. The most important are the control of speed, size, and shape of the droplets by adjusting the waveform of the voltage applied to the nozzles; the droplet formation and impact can be observed by a video camera. Moreover, the spacing of

droplets can be controlled by angling the line of nozzles along the printhead and the printheads are heat resistance.
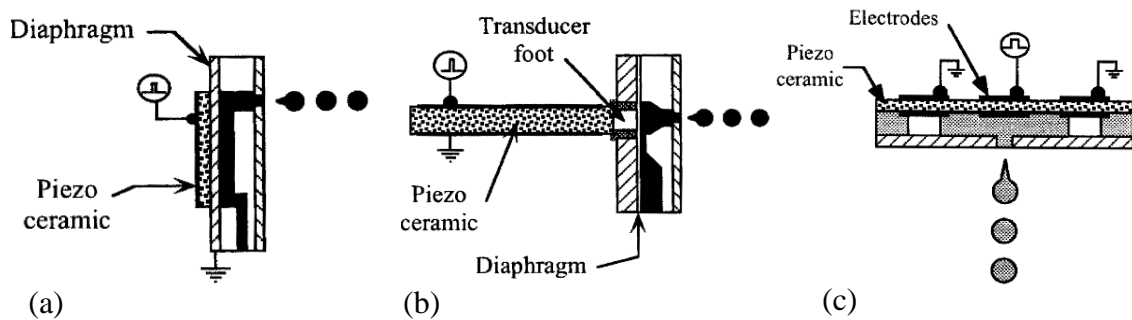
Figure 2.11: (a) Bend-mode, (b) push-mode, (c) shear-mode piezoelectric ink-jet design [161].

Examples of the commercial printers that use these modes are, for instance, the Gould's impulse ink-jet and the Siemens PT-80 inkjet printer which use the squeeze-mode ink-jet technology. The printheads in Tektronix's Phaser 300 and 350 and Epson's Color Stylus 400, 600, and 800 ink-jet printers are based on the bend-mode design. Also, the printheads from companies such as Dataproducts, Trident, and Epson have successfully implemented the push-mode piezoelectric ink-jet in their printheads. Companies such as Spectra and Xaar are pioneers in the shear-mode printhead design [161]. In terms of consumer printers, specific emphasis is given on the EPSON and FUJIFILM Dimatix printers that have been used in this dissertation.

- **Printers used in the Present Work**

  ➢ Epson Inkjet Printer

According to Le [161], in 1993, Epson introduced the Stylus 800 piezoelectric inkjet printer in order to compete directly with thermal inkjet technology in the low-end home and small office printer market. This product was very significant as it was the first time a reliable low-cost piezoelectric inkjet with a permanent printhead was successfully introduced in a low-end printer. Additionally, this Epson printhead is based on a push-mode design with a multi-layer piezoactuator [176]. Later, Epson introduced in 1997 the Color Stylus 400, 600, and 800 with a bend-mode design piezoelectric printhead, as mentioned before. The Color Stylus 800 employs two printheads; 128 nozzles for black and 192 nozzles for colour (CMY). The technological breakthrough lies in the unique fabrication method for the thick film PZT sintered on top of the zirconia diaphragm to make piezoelectric drivers. The significant reduction in the thickness of the driver

structures allows Epson to miniaturize the 192-nozzle printhead to about 18×34.8 mm with a nozzle density of 180 dpi (dots per inch)[161].

Predominantly, Epson is a consumer printer manufacturer who is employing the drop-on-demand technology on its inkjet printers. Specifically, they employ piezoelectric DoD technology [166]. The Epson L800 inkjet printer (Figure 2.12) was used for the purposes of printing solid catalysts. The L800 is equipped with Epson's Micro Piezo printhead technology that delivers unrivalled durability, quality and reliability. The minimum droplet size is 1.5pl and the printing resolution reaches 5760x1440 dpi. The high-capacity ink tank is fully integrated into the printer, providing the options of six CMYK colours (cyan, light cyan, magenta, light magenta, yellow and black). Each ink bottle can be filled up to 70 ml and when the ink level drops, the bottles can be refilled. Epson L800 also provides 180 nozzles from which 90 is for black ink and the rest are for colour. Moreover, it provides the option of printing directly onto CDs/DVDs with fast print speeds, since it can produce a 10x15cm photo in 12s [177], [178].

Figure 2.12: Epson L800 printer.

However, Epson L800 has some drawbacks like the fact that the nozzle for Epson printer cartridges is built into the printer itself and cannot be easily removed for cleaning. Moreover, its most prominent disadvantage is the overall lack of control. In particular, the drop volume and spacing cannot be adjusted, and the resolution is relatively low [173]. Furthermore, the specific model is not designed for printing solid catalysts, therefore a number of modifications were performed in order to finally print a supported-Pt catalyst [179], [180].

➤ FUJIFILM Dimatix

The company was initially founded in 1984 as Spectra, Inc. and was renamed as Dimatix in 2005 to reflect its expansion into digital materials deposition, and was acquired by

FUJIFILM Corporation in 2006. FUJIFILM Dimatix is the world's leading supplier of piezoelectric drop-on-demand inkjet products. The piezoelectric DoD inkjet printheads are recognized for their ability to sustainably jet ink and many other fluids at high frequencies with exceptional drop placement accuracy [181].

FUJIFILM Dimatix offers the Dimatix Material Printer (DMP) for material deposition. The DMP is a bench-top materials deposition system designed for high-resolution, micro-precision and non-contact jetting of functional fluids in a broad range of applications. It can use a variety of functional fluids onto virtually any surface, including plastic, glass, ceramics, and silicon, as well as flexible substrates from membranes, gels, and thin films to paper products. It can also be used for low-volume manufacturing of products from flexible circuits, RFID tags and displays to DNA arrays, and wearable electronics [181]. In 2016 it was announced that a new material printer, DMP-2850 would be launched (Figure 2.13a) [182].

The DMP-2850 provides cartridge-based inkjet print-head which uses 1pl drop volume and is designed for high-resolution and micro-precision jetting of a wide range of fluids onto virtually any surface, as mentioned before. Also, the cartridge is a piezo-driven jetting device with an integrated reservoir and heater, which can reach up to 70°C and has 16 nozzles with 254μm spacing (Figure 2.13b). It also has a heated vacuum platen (up to 60°C) and provides a large printable area of 210x315mm (if the substrate has less than 0.5mm thickness). It has an updated Drop Manager software, with pre-loaded patterned templates and it provides editing for the pattern, the piezo drive waveform, the cleaning cycles, the substrate settings, including the temperatures for the platen and the cartridge. For instance, if the fluid is too viscous to jet, the viscosity can be lowered with the increase of the cartridge temperature so as to get the desired jetting performance [183].

The DMP-2850 has two high-speed cameras which are located on the print carriage (Figure 2.13c). The cameras have finer resolution optics that provide superior images for drop watching and print inspection functions (fiducial camera). The drop watcher camera system allows direct viewing of the jetting nozzles, the faceplate surrounding the nozzles and the actual jetting of the fluid. The fiducial camera provides many advantages to the current technology, as it allows substrate alignment using reference marks, it allows positioning a print origin or reference point to match substrate placement and allows matching drop placement to the previously patterned substrate. In addition, it provides inspection and image capture of the printed pattern or drops [183].
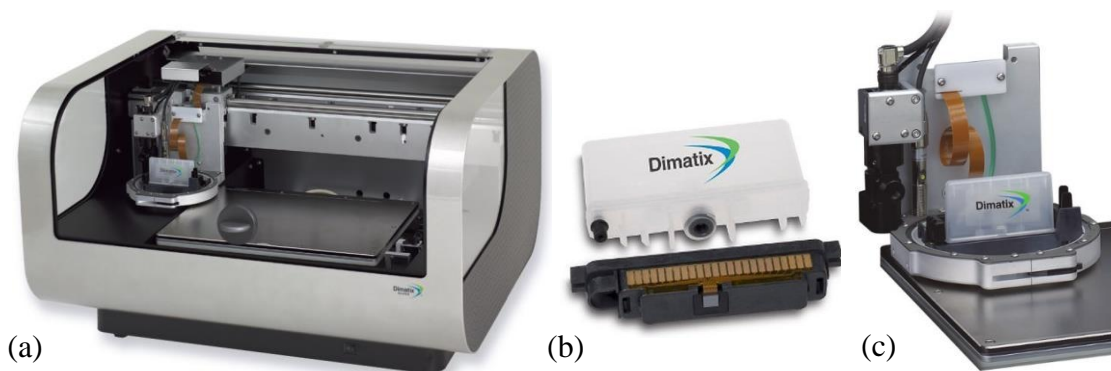
Figure 2.13: (a) DMP-2850, (b) cartridge and (c) print carriage.

Although these specialized inkjet printers can be expensive, and they have a generally small ink capacity of 1.5ml, they have a great deal of control over drop volume and spacing and they provide better resolution than other commercial inkjet printers [173], [183]. Compared to Epson L800, the DMP-2850 gives the opportunity to study and evaluate some important printing parameters such as ink composition and printing patterns. Moreover, the ease of preparation, execution and operation of the printer and software, make the printing technique an excellent alternative in fabricating functional metal/oxide heterogeneous catalytic systems.

2.3.1.2. Ink Composition and Properties

- **Ink Composition**

The ink composition is one of the most important decisions so as to achieve successful IJP operating parameters. There are currently four main types of inkjet inks; phase-change solvent-based, water-based and UV curable, although hybrid versions of these types also exist like water-based inks containing some amount of solvent. Oil-based and liquid toner inks have been found less successful and are less prevalent [184], [185]. Some of the main types of inks are discussed below.

As for the solvent-based inks, which can be formulated with either pigments or dyes (or even both), they have been used for many years and have traditionally been the formulation of choice for grand format and wide format applications. Their advantages include low cost, excellent print quality, image robustness, and range of compatible substrates. Moreover, they can adhere to different types of substrates and dry rapidly, which can be accelerated by heating. However, they have some disadvantages, such as environmental concerns and a requirement for high maintenance, since the solvent-based inks can potentially block the print head nozzles with the dried pigment or dye [184], [185].

Regarding the water-based or aqueous inks, they have the advantages of being relatively inexpensive, environmentally friendly (low toxicity of the waste materials) and are prevalent on the desktop. On the other hand, the aqueous-based inks have relatively slow drying rates, especially when they are deposited on non-paper substrates, e.g., glass, ceramic, or steel. The water-based inks tend to require porous or specially treated substrates or even lamination to impart durability since this type of ink tends not to adhere to non-porous substrates [184]–[186].

It is noted that only a few inorganic materials can be inkjet printed, due to the dissimilar condensation kinetics and chemistry of the precursors of metal species leading to difficulty in preparing inkjet-printable precursors. Therefore, the IJP synthesis of functional inorganic materials (metal oxides) has had only sporadic success, which is opposed to the successful research that is performed with respect to organic materials [186], [187]. According to Liu et al. [186], the functional inks for IJP synthesis of metal oxides are colloidal systems that are typically composed of a metal species precursor (1-30%), a liquid carrier medium (50-60%) and additives (1-10%).

The metal species precursors can be metal salt solutions, colloidal nanoparticles based on sol-gel chemistries, and colloidal suspensions of metal oxide nanoparticles. These three different metal oxide precursors are likely to lead to differences in the mechanism of fabrication of the material. The liquid carrier medium which is typically used for ink formulations is solvent-based (non-aqueous-based) and aqueous-based or water-based inks. The solvent-based inks are based on organic solvents (e.g. toluene, cyclohexanone, and acetylacetone), as well as single alcohol or mixtures of different alcohols (e.g. methanol, ethanol, isopropanol, ethylene glycol). The aqueous-based inks have either single or multiple metal colloidal nanoparticles or metal precursor solutions dissolved in water. The liquid carrier medium is really important as it determines the basic properties of the ink (e.g., viscosity, surface tension, density), and dissolves or disperses the metal species precursor [186].

The additives usually bring a specific function (e.g. surfactant, preservative, binding of the functional molecules) and enhance the printability and longevity of the ink. Specifically, the surfactant species are used to stabilize the dispersed pigment particles and prevent agglomeration. The viscosity modifiers (e.g. ethylene glycol), can be added to enhance ink jettability and reduce spreading on a substrate. Also, the addition of propanol to water can modify the surface tension which contributes to droplet formation

and droplet spreading. Defoaming agents, like tributyl phosphate, are added to inhibit the formation of bubbles and humectants, while diethylene glycol, can inhibit the evaporation of water for aqueous inks, thereby extending the time an ink can be successfully jetted from seconds to days and weeks [185], [188].

- **Ink Properties**

The goal of ink formulation is to take the active functional or structural materials (e.g. polymers, metal oxides, metals, carbons), and transform them into stable and jettable fluids. The inkjet printing process is very complicated and requires delicate tailoring of the chemical and physicochemical properties of the ink in order to have reliable and consistent results. The physical properties of the ink such as viscosity, surface tension and density, affect strongly the fluid dynamics of the droplets. Moreover, the particle size should be monitored to avoid the agglomeration of ink components that would clog the print head reservoir [174], [185], [189], [190]. The general property requirements for fluids to be used in inkjet printers were gathered by Liu et al. [186] and are listed in Table 2.4.

Table 2.4: Fluid properties requirements.

		Particle Size (μm)	Viscosity (cP)	Surface Tension (dynes/cm)	Density (g/cm³)
Continuous Inkjet Ink		<1	1-10	25-70	~1
DoD Inkjet Ink	Thermal	<1	5-30	35-70	~1
	Piezoelectric	<1	1-20	35-70	~1

Regarding the viscosity parameter, the inks may behave as Newtonian or non-Newtonian fluids, but in most inkjet inks the fluids are Newtonian. In this case, the viscosity is constant with the applied shear rates, whereas in a non-Newtonian ink, the viscosity changes over a range of the shear rate. Inks with high viscosity, reduce the droplet ejection speed, leading to aggregation and agglomeration of the inks in the print head channels. Ink viscosity can be influenced by ink temperature during the inkjet printing process. In addition to viscosity, the surface tension is the other important parameter of inks. They have a major influence on the drop formation mechanism in DoD printers and the resulting inkjet drop characteristics such as drop size, drop ejection velocity, satellite drop formation, droplet morphology upon impact and drop relaxation time. If the surface tension is high, it makes drop generation difficult and it becomes easy to form satellite droplets rather than a single drop of ideal size. If the surface tension of the ink is too low, then it can lead to pollution of the droplets and consequently make the liquid ink drip

towards the substrate at random, during the printing process. Some solvents like acetone and alcohol have lower surface tension and can be used as a co-solvent in water-based inkjet inks to reduce surface tension [174], [186], [191].

Another critical property of inkjet ink is the particle size because the nozzle of the printer would be clogged with larger particles or due to the aggregation of nanoparticles. For piezo-electric printers, a good rule of thumb for maximum particle size is 1% of the nozzle diameter, otherwise, the clogging of the nozzles will inevitably occur, requiring replacement of the printhead and process interruption. Filtering the fluid before jetting helps to remove any agglomerated particles that may block the nozzles. For DMP-2850 material printer, microfilters in the range of 0.2-0.45μm have been found to be adequate. Moreover, adjusting the pH of ink will avoid not only the particle agglomeration but also printhead and cartridge damaging, which can lead to nozzle clogging [174], [183], [191].

Ink stability is defined as the constancy of the ink characteristics over time. In most cases, for inks which do not contain undissolved materials, instability is caused by interactions between the ink components, precipitation and phase separation due to changes in solubility. The formulation characteristics which determine ink stability depend on whether the active species is a polymer (which forms an ink solution) or a particle (which forms an ink dispersion). If it is a polymeric ink, for instance, printing solid polymer electrolytes in batteries or supercapacitors, the primary requirement for stability is compatibility between the carrier solvent and the polymer. When the ink is a dispersion of particles, for instance, printing carbon-based supercapacitor electrodes, stability is defined by the particles remaining homogeneously distributed in the carrier solvent. Stoke's Law, which is indicated below (equation 2.26), defines the general conditions for creating a stable particle-based ink [185], [189], [192].

$$v = \frac{2}{9} \frac{R_s^2 (\rho_2 - \rho_1) g}{\eta} \qquad (2.26)$$

where, v is the steady-state velocity of settling, R_s is the radius of the spherical particle, ρ_2 and ρ_1 are the densities of the particle and fluid, respectively, η is the viscosity of the fluid, and g is the gravitational constant. From Stoke's law, it can be concluded that higher solvent viscosity and closer matching between particle and ink densities lead to more stable inks [189], [192].

2.3.1.3. Mechanisms of Droplets Formation

- **Drop Formation and Drop Delivery**

The fluid rheological requirements for printable inks are determined by the physics and the fluid mechanics of the drop generation process. The behaviour of liquid drops can be characterized by a number of dimensionless groupings of physical constants. The most useful are the Reynolds (Re), Weber (We), and Ohnesorge (Oh) numbers which are calculated through the following equations [162], [175], [186].

$$\text{Re} = \frac{\text{fluid inertia}}{\text{viscous forces}} = \frac{\rho V d}{\eta} \tag{2.27}$$

where, ρ is the density, V is the velocity, η is the viscosity of the fluid, and d is a characteristic length: typically, the diameter of the jet, nozzle, or drop.

$$\text{We} = \frac{\text{fluid inertia}}{\text{surface forces}} = \frac{\rho V^2 d}{\gamma} \tag{2.28}$$

where γ is the surface tension. It is noted that for a spherical drop travelling at velocity V, the ratio between its kinetic energy and the energy of its free surface is We/6. The typical fluidic parameters of ink drop ejection from thermal IJ and piezoelectric IJ print heads can be summarized as; drop weight from 2-50ng, the drop ejection velocity can vary from 5-15m/s, the Re number between 50-100 and the We number between 20-300 [185].

On the other hand, the Ohnesorge number (Oh) removes the influence that velocity has on the previous dimensionless groups and is defined by equation 2.29 [162], [175], [186]. If the Oh number is too high (Oh>~1), then viscous forces will prevent the separation of a drop, whereas if the Oh number is too low (Oh<~0.1), then the jet will form a large number of satellite droplets. Figure 2.14 indicates the operating regime for stable operation of DoD inkjet printing, in terms of the Ohnesorge and Reynolds numbers [162].

$$\text{Oh} = \frac{\sqrt{We}}{Re} = \frac{\eta}{\sqrt{\gamma \rho d}} \tag{2.29}$$

The printability of an ink is connected with the Z number, which is equivalent to the inverse of the Ohnesorge number and describes the ratio of the surface forces to the inertial forces during drop formation in DoD print heads. Therefore, the Z parameter depends on the nozzle diameter, the density, the surface tension, and the viscosity [162], [175], [186]. Fromm [193], developed the Z number based on a simple model of fluid flow in a generator with simplified geometry, which provides a dimensionless analysis of drop

formation mechanics in DoD printheads. In his research, he reported that limitations in printability occur if the Z-number is lower than 2.
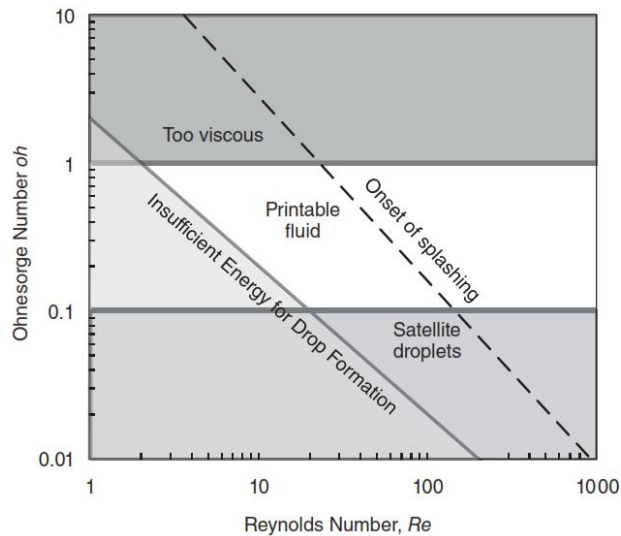
Figure 2.14: Schematic diagram showing the operating regime for stable operation of DoD IJP.

Later, Reis and Derby [194], extended this result through numerical simulations and proposed the range of 10>Z>1 for stable drop formation. Recently, Jang et al. [195], redefined the printable range as 4≥Z≥14. If the Z values are not in this region then the fluid is inappropriate for ink-jet printing, due to their inability to form a single droplet. Specifically, at low values of Z, viscous dissipation prevents drop ejection, whereas at high values the primary drop is accompanied by a large number of satellite droplets, that can be seen in Figure 2.15 [190], [195]. This shows that the ink formulation is a crucial step for a successful application of IJP.

Rapidly after ejection (~10-50μs), the drop is formed from an initial liquid column that thins to define a leading droplet and the elongated tail or ligament; the final rupture of the ligament can lead to the formation of smaller satellite drops [175], [185]. Figure 2.15 illustrates the sequence of drop formation via a DoD printer, where the tail breaks up into a trail of satellite droplets behind the primary drop. When the satellite drops catch up and merge with the leading large drop, prior to impact, then their presence is irrelevant. However, if they are still present at impact, then they lead to noncircular impact footprints of the drop, influencing negatively the deposit precision, resolution, and accuracy [175]. The printing accuracy as well as productivity, increase with drop velocity, but the generation of satellite droplets also increases with drop velocity. It is, therefore, a challenge to find nozzle geometries and actuation signals in DoD inkjet printing that result in fast drops without satellite droplets [196].
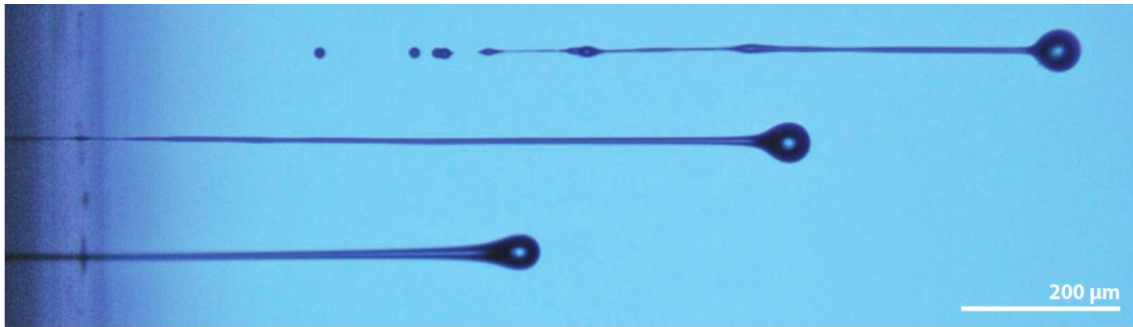
Figure 2.15: High-speed photographic image showing three drops ejected from a DoD printer at different stages of drop formation.

- **Drop Impact and Spreading**

The behaviour of a liquid drop on impacting a solid surface is controlled by several physical processes and can be driven by inertial forces, capillary forces, and gravitational forces. The important dimensionless groupings that affect drop generation are the Reynolds, Weber, and Ohnesorge numbers, that were mentioned before [175]. Schiaffino and Sonin [197] proposed that drop behaviour on impact can be divided into two rules; impact-driven, in which the inertial forces dominate, and capillarity-driven, in which initial drop velocity is unimportant and the transition in behaviour occurs at a critical value of the Weber number.

Once the ink droplet contacts the substrate, the ink wettability determines the relationship between the substrate surface energy and the ink surface tension, according to Young's modulus (equation 2.30). The ink's wetting behaviour on the substrate is an important factor on the printed film morphology and is expressed as the contact angle of a printed droplet on the substrate. Figure 2.16 illustrates an ink drop on a solid substrate with the surface free energy and contact angle as described by Young's modulus [174].

$$\gamma^{sv} = \gamma^{sI} + \gamma^{Iv} \cdot \cos\theta \qquad (2.30)$$

where γ^{sv} is the solid surface free energy, γ^{sI} is the solid/liquid interfacial free energy, γ^{Iv} is the liquid surface free energy and θ is the contact angle.
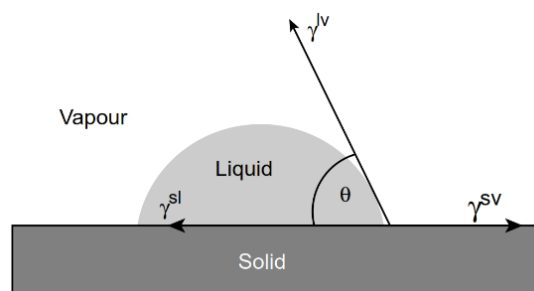
Figure 2.16: Schematic illustration of a liquid drop showing the quantities in the Young equation.

The contact angle (θ) is defined as the angle between the liquid/vapour interface as it meets the solid surface and it describes essentially the extent to which a drop wets the surface [198]. Moreover, the contact angle is a very important factor in controlling the final shape of a printed drop and the patterns that built up from the interaction of drops. Figure 2.17 illustrates the sequence of events that occur after droplet impact on a substrate, where D_i is the initial droplet diameter, D_m is the maximum radius to which a droplet spreads during impact, and V_i is the droplet velocity at impact. The initial impact has a duration of t*<1µs and is governed by kinematic behaviour, it is then followed by impact-driven spreading, recoil, and oscillation. Furthermore, at small values of t*, viscous forces mitigate the spreading and oscillations, and surface tension forces become more important in controlling behaviour. When t* ranges between 0.1-1ms, the capillary forces dominate to the point where spreading is fully controlled by capillarity, and further extension occurs. Afterwards, spreading continues and approaches true equilibrium at t*>10ms, with complete wetting occurring at $\theta=0^o$ [175], [198], [199].
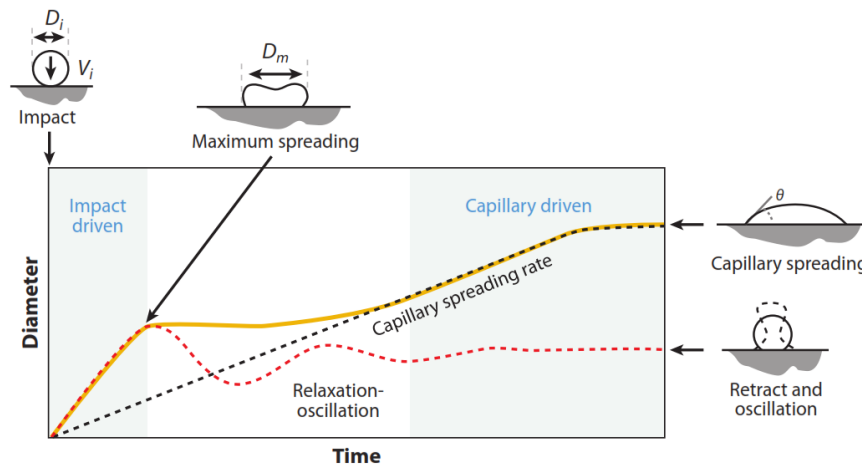
Figure 2.17: Schematic illustration of the sequence of events that occurs after a droplet impact on a substrate.

In addition, there are six possible consequences of a droplet falling on to a dry surface; deposition, prompt splash, corona splash, receding breakup, partial rebound, and complete rebound [198], [200]. These morphologies are presented in Figure 2.18. Pesach and Marmur [201], noted that for the excellent spreading of the ink droplet onto the substrate, good wetting behaviour (wet film formation) or low contact angle of the ink on the substrate is necessary, and is obtained when the ink surface tension is lower than the substrate surface energy. Additionally, the morphology of deformity upon impact with the substrate also depends on the ink droplet speed, the voltage waveform of the printer, and the nature of the substrate. Specifically, the substrate nature (e.g. hydrophobic,

hydrophilic, thermal conductivity) and the substrate temperature, influence the droplet ink behaviour on the substrate [174].
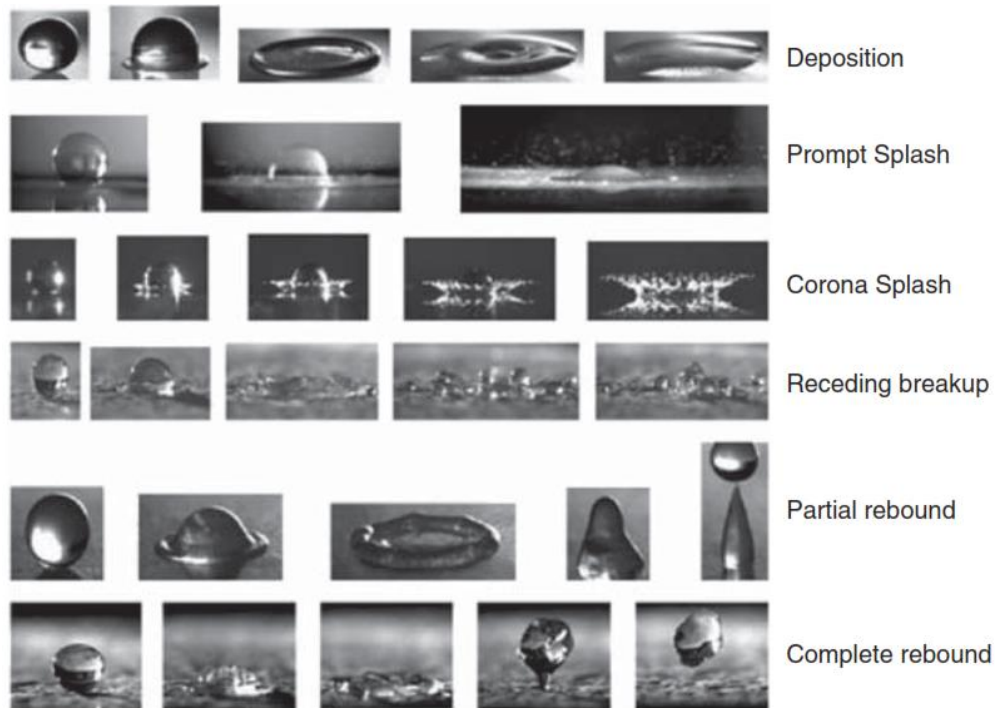
Figure 2.18: A variety of morphologies of liquid drop impact on a dry surface [198].

- **Drop Solidification**

As a drop spreads after impact, it advances over a dry surface and it transits from a liquid deposit to the final desired solid material which is the final step in the printing process. For a droplet that is solidifying, the Stefan number, which is indicated in equation 2.31, is important. Moreover, the droplet solidification process is almost always accompanied by a reduction in volume and in case the solidification occurs via solute evaporation, the volume change may be particularly great [175], [185].

$$S = \frac{c\,[T_f - T_t]}{L} \tag{2.31}$$

where c is the specific heat, T_f is the solidification temperature, T_t is the substrate's temperature and L is the latent heat of melting.

In addition, drying droplets (especially from polymer solutions) often show contact line pinning from solute deposition; this, combined with increased solvent evaporation rate toward the edge of the droplet, can lead to solute deposition in a ring at the contact line. Specifically, when a droplet contacts the surface, precipitation occurs initially at the contact line and then, fluid flow occurs from the centre of the drop, in order to replace the

evaporating fluid from close to the contact line. Also, this peripheral flow continuously feeds the solidification at the contact line. The final deposit shows a characteristic ring (like a coffee stain) where the solute has segregated during the drying process. Furthermore, the solute distribution during drying can strongly influence the shape of a printed drop through the coffee stain effect, when solute strongly segregates to the initial contact line [175], [202].

This phenomenon of ''coffee staining'' was explained by Deegan et al. [203], who observed that the rate of solvent evaporation is greatest toward the contact line due to the easy vapour transport in the surrounding "dry" substrate. Deegan et al. [204] further researched this phenomenon and concluded that coffee staining is the normal behaviour for a drying drop over all length scales studied for both solute and suspended particles. Moreover, they reported that the coffee stain effect is not caused by the surrounding dry surface, as originally proposed by them [203], but it occurs when the next two conditions are obeyed, i.e. the edge of the drying drop (the contact line) is pinned and evaporation is possible from the edge of the drop [202], [204]. The particular effect can be influenced by a number of parameters such as spacing of droplets, local partial pressure of the solvent, and even the impact velocity of the drops. The coffee staining is not significant when a liquid drop solidifies through a phase change on impact, while it is a problem when the liquid solidifies through evaporation [202].

- **Consolidation**

The final step in transforming the ink into a functioning device is the consolidation of the wet printed layer. For instance, for electrochemical devices, the consolidation process may entail removing any additives that were present in the ink like solvents, surfactants, dispersants, but should not be present in the device. Also, it may entail sintering of the ceramic materials. It is noted that the highest platen temperature of most inkjet printers is ~100°C. Therefore, the consolidation typically occurs as a separate processing step. Applying the right processing conditions for two dissimilar materials whose desired characteristics are quite different is the challenge for the consolidation step. For example, a printed electrolyte film should be dense and pinhole-free, but a printed electrode should be porous [189].

2.3.2. Inkjet Printing of Solid Catalysts

The inkjet printing technology has already been adopted in catalysis research, in a broad spectrum that includes printing metal-supported catalysts, metal oxide catalysts, carbon nanotubes, fuel cells etc. IJP is a promising tool and an attractive and alternative approach to the development/synthesis of catalysts at a nanoscale level, even though limited references exist in the literature [186], [205].

- **Metal Supported Catalysts**

Liu et al. [205], examined the IJP of Pt catalyst patterns for low-temperature catalytic combustion. They used the Microdrop Technologies GmbH (Germany) inkjet printer system that was equipped with a piezoelectric printer head with an inner nozzle diameter of 70 µm and a drop volume of 268pl (Figure 2.19a). Different Pt catalysts patterns such as dots array (180x110) and films were successfully fabricated by directly inkjet printing of 0.05M chloroplatinic acid solution onto Si substrate. The dot distance of the catalyst dot arrays onto the silicon substrate is 160µm and is indicated in Figure 2.19b. The authors investigated the performances of printed Pt patterns (area of 5cm^2) in the catalytic combustion of methanol. The highest conversion of methanol that was observed reached 85% at 100°C. They concluded that the drying behaviours of catalyst micro drop have important effects on the morphology of the catalyst, the size and shape that result in distinct activity performances of printed catalysts.
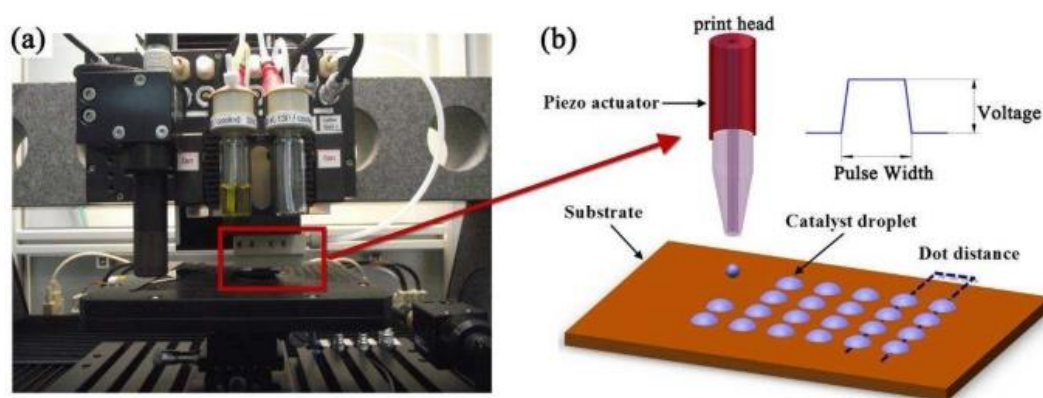
Figure 2.19: (a) Photograph of the inkjet printer heads and position system used in the experiment; (b) Schematics of IJP the catalyst precursor ink on the substrate.

Siebert et al. [206], researched the DoD IJP of GaPd$_2$ catalyst as thin and uniform wall coatings into micro-channels for selective hydrogenation of acetylene. The authors examined three different printing approaches; (a) direct printing of GaPd$_2$ into the bare micro-channels, b) printing of an α-Al$_2$O$_3$ layer first and subsequent printing of GaPd$_2$

and c) pre-immobilization of GaPd$_2$ on α-Al$_2$O$_3$ and printing of the GaPd$_2$/α-Al$_2$O$_3$. They used the commercial computer-operated printing system Autodrop Compact (microdrop technologies GmbH) which was equipped with a piezoelectric dispenser head (MD-K-140) containing an ink reservoir of 5 ml and a nozzle with 100 μm diameter. After the preparation of the catalysts, a specific activation step occurred and then the catalysts were exposed to the feed gas composition of 0.5vol.% C$_2$H$_2$, 5vol.% H$_2$, 50vol.% C$_2$H$_4$ and He at 523K. Between the three approaches, the printed GaPd$_2$/α-Al$_2$O$_3$ showed the best catalytic results with an activity of 480 mol(C$_2$H$_2$)·mol(Pd)$^{-1}$·h^{-1} and a selectivity of 76% for the semi-hydrogenation of acetylene to ethylene.

- **Metal Oxide Catalysts**

Catalysts printing is a modern method that may be used for the accurate manipulation and tuning of the properties of catalytic materials since the conventional synthesis methods for mesoporous metal oxides (MMOs) are complex and lack high-degree control over different compositional/structural parameters. For instance, the complex surface chemistry and porous structures of MMOs sometimes limit the diffusion of metal-active species during the conventional preparation processes leading to a non-uniform distribution of metal nanoparticles [207].

Liu et al. [187] proposed an inkjet printing assisted cooperative-assembly (IJP-A) method for ultrafast exploration of multi-component mesoporous metal oxides catalysts as outlined in Figure 2.20. The IJP-A synthetic platform was set up to reproducibly generate a continuous landscape of candidate catalysts at a rate of 1000000-formulations/hr containing up to eight different metal species. The IJP synthesis of the catalysts was achieved through a modified EPSON Stylus Photo 4880 piezoelectric inkjet printer. They used a nanoparticle sol-gel cooperative-assembly system to formulate the inorganic precursor inks for IJP-A synthesis. Extended reference will be given to the ink formula that was used by Liu et al. [187], as a version of it was used to prepare some of the catalysts that were synthesized for the purposes of this dissertation.

Their ink system is composed of an amphoteric nonaqueous solvent, metal species, and block-copolymers to optimize the performance of the ink. The amphoteric solvents such as alcohols or acetic acid ensure appropriate solubility, viscosity, and surface tension for all species. Acetic acid acts as a complexing agent to modify the condensation kinetics of metal alkoxides and along with isopropanol (traditional non-aqueous solvent), the ink

solutions can form stable colloidal nanoparticles that are monodispersed in size for most common metal precursors. These colloidal nanoparticles are used as building blocks and can be cooperatively assembled with each other, with elemental inorganic species, and with appropriate cosolvents, block copolymers, or surfactants to form the desired mesostructured library. Additionally, block-copolymers (e.g., F127) co-assembled with metal ions and nanoparticles are used as structure-directing agents, as binders to template a variety of high surface area mesoporous structures of metal oxides (2−50nm) and also to formulate a high quality "ink" solution. Also, the controlled addition of a strong aqueous acid such as HCl or HNO_3 partially hydrolyzes and charges the modified inorganic precursor so as to enhance the affinity for the hydrophilic block of the block-copolymer. These strong acids may act as charge intermediates between surfactants and inorganic species and inhibit condensation of certain metal ions [187], [208], [209].
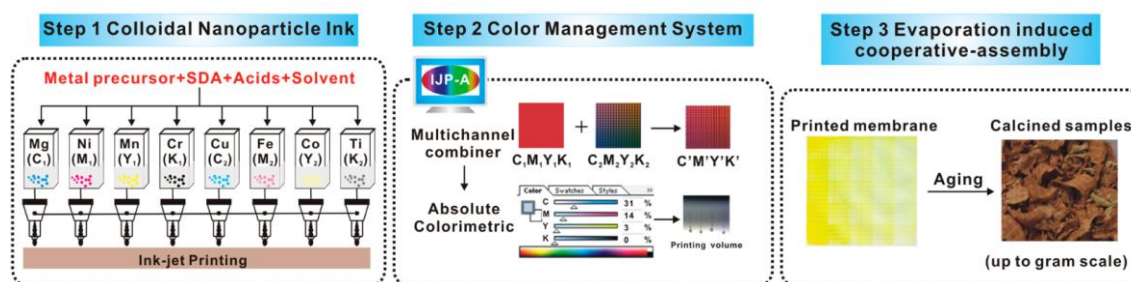
Figure 2.20: Scheme of MMMO syntheses using inkjet printing assisted cooperative-assembly method. Step 1: a stable colloidal nanoparticle "ink" system consists of nonaqueous solvents, structure-directing agents (SDA), acids, and suitable metal precursors. Step 2: the colour-management system includes an "Absolute Colorimetric" profile to create a one-to-one output between the "percent value" of each colour in an image and the "printing volume" of each ink and a "Multichannel Combiner" to extend the printable space. Step 3: an evaporation-induced cooperative-assembly process is used to generate the desired mesoporous structures of printed libraries (up to gram-scale) [187].

Woodhouse et al. [210], used a Hewlett-Packard 1220C DeskJet inkjet printer for IJP metal oxide precursors (simple nitrate salts) onto conductive glass substrates. By varying the gradient pattern of each element, a variety of stoichiometric compositions and combinations of metal oxides was produced that were capable of the photoelectrolysis of water. They concluded that the IJP is an inexpensive, rapid, and versatile method of patterning metal oxide precursors onto a conductive glass substrate. Their later research [211], reported a ternary oxide containing Co, Al and Fe in a Co_3O_4 spinel structure with Fe and Al substituted into Co sites with a nominal stoichiometry of $Co_{3-x-y}Al_xFe_yO_4$ where x and y are about 0.18 and 0.30, respectively. They used the previous inkjet printer

(Hewlett-Packard Deskjet 1220C) and the Fujifilm Dimatix DMP-2800 model. Their new materials are useful for the photoelectrolysis of water.

Lee et al. [190], used alumina-based inks that were prepared from a commercial stable aqueous colloidal nano-suspension of Al_2O_3 (particle size of 100nm) and further modified them with water, ethylene glycol and polyethylene glycol-600 creating four different inks. The authors used a commercial printer (microdrop Technology GmbH), which was equipped with a print head (MD-K-140) containing a 100μm diameter nozzle. After the calcination of the inkjet printed alumina layers, rhodium nitrate was used to impregnate them with Rh. The final microchannel reactors were used for methane steam reforming (MSR) to examine the activity of the catalyst layers. The formed catalyst layer performed well in MSR with a maximum methane conversion of 98.9% at 973 K, as seen in Figure 2.21. The specific activity was sustained for more than 60 h.
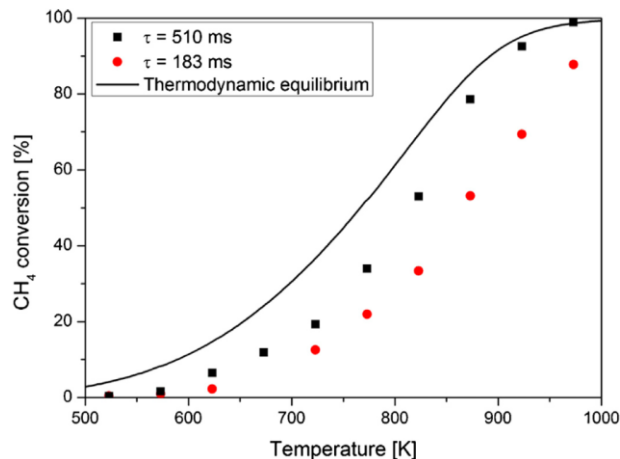
Figure 2.21: Methane conversion in MSR as a function of temperature for two different residence times and constant molar ratios at ambient pressure (C_{CH4}= 10 vol.% and C_{H2O}= 40 vol.%, corresponding to a steam to carbon ratio of 4) [190].

- **Photocatalytic Applications**

One example of IJP synthesis of a photocatalytic thin film is the deposition of photocatalytically-active transparent titanium oxide from a colloidal suspension. TiO_2 is one of the most studied photocatalysts for application to the degradation of organic pollutants [186], [212]. Arin et al. [213], printed a transparent, homogeneous thin TiO_2 film (85nm) on a glass substrate by inkjet printing and tested its photocatalytic activity. They used a chemical solution deposition using water (primary solvent), citric acid (non-toxic) and triethanolamine as stabilizing agents. For inkjet printing of the precursor solutions, a modified single Domino Macrojet electromagnetic nozzle with 90μm jewel orifice mounted on a Roland x–y plotter was used. The authors concluded that TiO_2 layers

preparation with ink-jet printing can be a suitable alternative to current photocatalytically active self-cleaning glasses coated by TiO_2 using expensive techniques like chemical vapour deposition, thermal methods, and sputtering.

He and Parkinson [214], investigated the effects of incorporating Ti, Si and Al on the performance of α-Fe_2O_3 photoanodes that can efficiently photoelectrolyze water in an inexpensive thin film device. Fujifilm Dimatix model DMP-2800 piezoelectric inkjet printer, with 10pl drop volume, was used. They printed films with combinations of Ti, Si and Al, simultaneously added to α-Fe_2O_3, which was produced by spray pyrolysis. The authors confirmed that the photoactivity of α-Fe_2O_3 was improved by the incorporation of trace amounts of Si, Al or Ti and observed synergistic effects.

- **Fuel-Cell Applications**

Taylor et al. [215], researched the IJP of carbon supported platinum 3-D catalyst for fuel cell applications. They used a Lexmark Z32 thermal ink-jet printer with a drop size of 28pl and maximum resolution of 1200x1200dpi. IJP was used to deposit catalyst materials onto gas diffusion layers that are made into membrane electrode assemblies for polymer electrolyte fuel cell. The high precision of IJP allows for controlled catalyst deposition, especially for ultra-low Pt loadings ($0.020mgPt/cm^2$), which are not easily attained using conventional methods (spray painting or screen printing).

Wang et al. [216], investigated the IJP of Ni-Gd:CeO anodes for low-temperature solid oxide fuel cells. They used a modified Domino MacroJet printer and the jetting was performed by electromagnetically (EM) driven single-nozzle print head with a 100μm orifice. It was demonstrated that the anode microstructure could be successfully nanoengineered by inkjet printing infiltration. DoD inkjet printing enabled high precision infiltration of a $Gd_{0.1}Ce_{0.9}O_{2-x}$ (GDC) sol ink, allowing the formation of GDC nano-decoration on the existing composite anode scaffold.

Sukeshini and Cummins [217], studied a versatile method for multilayer solid oxide fuel cells. They used a Dimatix DMP-2831 inkjet printer for printing all layers, including the anode interlayer, electrolyte, cathode interlayer, and cathode current collection layer. The inkjet head operated at a temperature above ambient and was chosen based on the drying rates of the printed layers. The SEM analysis conducted on the printed layers revealed a dense electrolyte and porous anode interlayer. Also, cells tested in H_2, produced a stable voltage of 1.1 V.

- **Inkjet-assisted Carbon Nanotubes Fabrication**

Tortorich and Choi [173], examined the IJP of carbon nanotubes, as they can be used in many applications, such as transistors, radio-frequency identification (RFID) tags, sensors, photonics, biological sensing labels, and more. Table 2.5 provides a comparison of recent reports on carbon nanotube inkjet printing.

Table 2.5: Comprehensive comparison of carbon nanotube printing [173].

Printer	Solvent	Dispersant and Concentration	CNT Type and Concentration	Preparation	Best Sheet Resistance	Notable Feature
Canon	Water	Functionalized	MWCNT-COOH 0.26 mg/mL	Sonication Stirring Centrifuge	40 kΩ/□ 90 prints	One of the first reported
Dimatix	Water	Functionalized	SWCNT-COOH 0.1 mg/mL	Sonication Centrifuge	Not reported	FET-like behavior
Dimatix	Water	Functionalized	SWCNT-COOH (carboxylic acid) SWCNT-CONH$_2$ (amide) SWCNT-PEG (polyethylene glycol) SWCNT-PABS (polyaminobenzene sulfonic acid) 0.13 mg/mL	Sonication Centrifuge	Estimated 2 kΩ/□ (for COOH and PABS) 14 prints (Assumed)	Fully inkjet printed FET
HP	Water	Gellan gum or xanthan gum <1 mg/mL	SWCNT or MWCNT Concentration not reported	Sonication	Not reported	Water vapor detection
Epson	Water	SDS 10 mg/mL	SWCNT 0.2 mg/mL	Sonication Centrifuge	78 Ω/□ 200 prints	Supercapacitors
Epson	Water	Combination of 3 different dispersants 150 mg/mL	MWCNT 0.15 mg/mL	Mixing Ball-milling Centrifuge	760 Ω/□ 12 prints	Low sheet resistance
Microfab	Water	Solsperce® 46000 5 mg/mL Byk 348 1 mg/mL	MWCNT 10 mg/mL	Sonication	Not reported	Electroluminescent device

Also, Zhang et al. [218], demonstrated a method to pattern catalyst via inkjet printing for the controlled growth of single-walled carbon nanotubes (SWNTs). They printed water solutions of cobalt acetate on hydrophilic Si substrates, using a regular office printer (EPSON K105). The patterns were designed on a computer and printed directly on pieces of Si substrates (~ 1cm×1cm) which were cut and stuck on printer papers for printing. During the progress of IJP, the droplets gradually dried, the metal salts hydrolyzed and precipitated, forming patterned catalyst precursors on substrates. After patterning, the Si substrates were then transferred to the furnace to grow the nanotubes by chemical vapour deposition.

Kordás et al. [219], examined the IJP of electrically conductive patterns of carbon nanotubes. They used a desktop bubble-jet printer (Canon BJC 4550) for printing the nanotube patterns (aqueous ink) on commercial office paper and transparency foil (Canon

BT-400). The narrowest lines that were printed had 70μm width, which corresponded to a printing resolution of ~360 dpi. Also, thin (~50nm) contact pads (3mm in diameter) of Pt were sputtered on the samples in order to ensure good electrical contact with the deposited nanotubes.

2.3.3. Advantages and Challenges of Inkjet Printing

Inkjet printing offers advantages that make it ideal in applications of non-traditional manufacturing. If achievable, high resolution and high printing speed would open up the possibilities for competitive production of quality objects by the extension of existing inkjet-based additive manufacturing processes. Additionally, the advantages of IJP over traditional methods of printing include the production of little or no waste and the versatility of having several different methods. Also, the IJP is non-contact and does not require a master template so that printed patterns can be readily modified on demand. Specifically, the opportunity to modify the printed design effectively on a computer is one of the most important benefits of the inkjet printing procedure, as it does not need to make a physical printing structure (i.e., it is a whole digital process) [170], [184], [220].

The main advantages of the IJP technology can be summarized as achieving excellent control of material's micro/nano-structure, using different substrates, producing variable film thickness and printing with variable speeds at high efficiency [184]. IJP of catalysts compared to other methods of preparing catalysts proves to be more advantageous as it provides a homogeneous mix at the molecular level in the liquid state. Moreover, IJP can allow a uniform distribution of material onto the surface of the substrate and provide picolitre precision and control of the deposition of each print [186].

Inkjet-printing has a great future ahead, however, the challenges of utilizing the inkjet printing technique need to be addressed. The common challenges that need careful approach are nozzle clogging, wetting behaviour, film homogeneity, viscosity limitations, limitation of printability, complex drying behaviour in order to form a uniform printed films and others [170].

One major problem of inkjet printing is nozzle clogging since IJP inks contain insoluble micro- or nanoparticles that can agglomerate and precipitate during the printing process. Also, a fast evaporating solvent at the nozzle tip is likely to quicken nozzle clogging due to the agglomeration of the remaining solid particles. It is, therefore, necessary to consider some precautions to avoid precipitation or aggregation of dispersion-based nanomaterials

in the ink. Tremendous effort has been put by researchers to control the ink flow from the printhead onto the substrate while preventing nozzles clogging due to dried ink. Nozzle clogging can be diminished by pre-printing cleaning, stirring and filtering of the ink as well as purging the ink to clear potentially clogged nozzles [166], [174], [183], [206].

In addition, the coffee ring effect is one of the fundamental difficulties, which is to achieve control over the resultant film homogeneity throughout the drying process. The coffee ring phenomenon is undesirable as it may affect the performances of inkjet-printed devices. It is reported that for avoiding the coffee ring effect as well as the nozzle clogging in the inkjet print head the inkjet inks should have a high boiling point. Another solution is to expand the vapour pressure throughout the drying process, as well as to print with a solvent-blend that has high surface tension [166], [170], [221].

Moreover, one of the challenges of IJP is the resolution, where the resolution of a printed object is constrained by the volume of the drop, as well as the temperature of the substrate and the molten liquid, as this dictates the rate at which heat is removed from the molten ink and therefore at which phase change occurs [170], [188]. Higher resolution and substrate handling at higher speed is a very demanding task. While approaching the fundamental limits of increased jetting frequency, the productivity needs to be improved in other creative ways such as increasing the number of nozzles, although this increases the cost of the printer [185].

Additionally, the drop placement accuracy plays an important role when determining the quality of the inkjet-printed material. The exact drop landing position is commonly characterized by uncertainty. Various parameters affect the drop placement like jet-to-jet variations, sensitivity to nozzle straightness, nozzle and surface wetting, nozzle plate contamination, ink formulation and condition, and drop velocity. Also, for very small dot spacing, bulging effects could appear due to excessively deposited material [170], [185].

Besides the challenges that concern the process of printing, the development of jettable materials is also a challenge as a universal ink does not exist. Specifically, a simple, general, stable and inexpensive formulation of the necessary precursor inks for printing synthesis mesoporous metal oxides has not been proposed to date [187]. Therefore, preparing the right ink is a challenging issue for researchers, as well as delivering it sufficiently rapidly, and controlling its final form [174], [185], [220].

CHAPTER 3: THEORETICAL BACKGROUND

3.1. Traditional Methods for Catalyst Preparation

The preparation techniques of supported catalysts are very diverse, and a catalyst may be produced through different methods. The preparation method of a catalyst involves several successive steps and the properties of a heterogeneous catalyst depend on them. There are three fundamental stages when preparing a catalyst; preparation of the primary solid, processing of that solid to obtain the catalyst precursor and activation of the precursor to produce an active catalyst [222]. Several innovative and cost-effective preparation methods have been developed and the most common are discussed further below.

3.1.1. Impregnation

Among the many methods to prepare supported metal catalysts, impregnation is the simplest and most widespread method for heterogeneous catalysts, such as supported Pt catalysts which are examined in this dissertation. The impregnation method consists of an interaction occurring between the surface of the support and the species of the active phase in solution. The object of this method is to fill the pores of the support with a solution containing the precursor of the supported phase, e.g., a metal salt of sufficient concentration so as to achieve the desired loading. If the volume of the impregnation solution introduced is equal to or less than the volume of the pores, then the impregnation method is known as ''incipient wetness impregnation'' or ''dry impregnation'', because the impregnated material keeps a dry character at a macroscopic scale. On the contrary, if the volume of the solution is in excess of that required to fill the pores, the technique is known as "wet impregnation" [27], [223].

The uptake of the liquid into the pores of the support, occurs due to the capillary pressure difference (Δp) across a hemispherical meniscus in a pore with radius r_p, according to the Young-Laplace equation (eq. 3.1) [224], [225].

$$\Delta p = (2\gamma_{lv}/r_p) \cos\theta \tag{3.1}$$

where, γ_{lv} is the surface tension between the liquid and vapour interface and θ is the wetting angle between the solid and the liquid.

If $\theta < 90°$, the liquid is considered as wetting and will penetrate the support spontaneously, which is the case with water in combination with most oxidic supports. If the liquid is nonwetting ($\theta > 90°$), the capillary pressure becomes negative and external pressure is needed to force the liquid into the pores [224], [225].

In addition, the pressure difference, as seen in the Young-Laplace equation, depends inversely on the pore size, so that the liquid is preferentially absorbed by the smallest pores. Moreover, the rate at which the liquid fills the pores is generally fast and is often not considered critical for catalyst synthesis. The infiltration of a wetting liquid into a porous particle can occur in seconds to minutes. However, when the support is prewetted with the same solvent before loading of the precursor via wet impregnation, capillary forces do not play a role and the only driving force for the precursor to enter the support is diffusion, which can take significantly longer [225], [226].

- **Dry Impregnation (DI)**

The method is best suited for deposition of species which interact very weakly with the surface, and for deposition of quantities exceeding the number of adsorption sites on the surface. The advantage of dry impregnation is that the weight of the added component incorporated in the catalyst can easily be controlled. On the other hand, the resultant material may not be as uniform as that prepared by wet impregnation. For instance, there may be regions of the catalyst with larger pores in which there will be larger concentrations of catalytically active material than in others. Consequently, the larger pores will take up larger volumes of solution and as a result, larger crystallites of the precursor are likely to be found in these pores. Also, redistribution inside the pores is very slow [27], [222].

- **Wet Impregnation (WI)**

In wet impregnation, the amount of the precursor solution is larger than the pore volume of the support, yielding a thin slurry, where the excess liquid is eliminated by evaporation or by draining. During the wet impregnation procedure, the deposition of the active phase is never quantitative and the quantity deposited depends on the solid/liquid ratio and the method's conditions. It is worth mentioning that deposition is slow, requiring several hours or days [222], [227]. Compared to dry impregnation, WI is more difficult to control. For instance, if the concentration of solute ions is low, then all of the solute ions may be taken up at the mouth of the pores and none will be found in the bulk of the support. In case of an expensive component (e.g. Pt, Rh), the formation of an "eggshell catalyst" (Figure 3.1) with a high concentration of the active component in a thin layer of a few tenths of a millimetre to the external surface of the support may be desirable. Additionally, if the reaction occurs predominantly near the outer surface of the catalyst

as a result of pore diffusion limitations, the same metal distribution is required. Given that the reaction is totally kinetically controlled and all of the bulk of the catalyst is utilized, it is desirable that the catalytically active component is spread throughout the support [27], [225], [227].

In industrial application, supported metal catalysts are generally used as macroscopic spheres or cylindrical extrudates. With special impregnation procedures, metal concentration profiles within the pellet can be created in a controlled way. Figure 3.1 indicates the four main categories of macroscopic distribution of metal within the support. Homogeneous distribution (Fig. 3.1a) is only preferential for relatively slow catalytic reactions, to provide reactants time to diffuse to the active sites. In the case, the reactants contain poisons, an egg-yolk distribution (Fig. 3.1b) may be favourable so that the poison can be captured at the edge of the catalyst body, where few active sites are present. Apart from the reasons stated above, an eggshell distribution (Fig. 3.1c) might be preferred if the reaction is fast or if secondary reactions are problematic. An egg-white distribution (Fig. 3.1d) is also preferred if the catalyst is prone to attrition [29], [225].
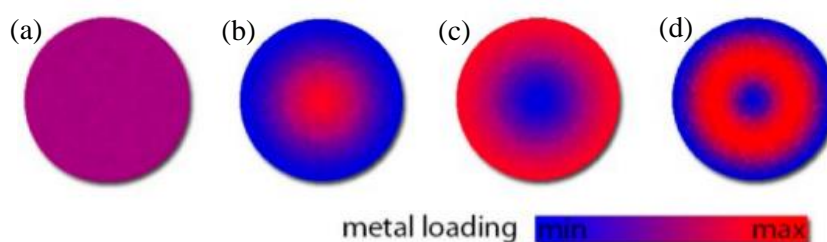
Figure 3.1: Different types of macroscopic metal distributions across a support particle: (a) homogeneous distribution, (b) egg-yolk distribution, (c) eggshell distribution, (d) egg-white distribution (red, high concentration of metal; blue, low concentration of metal) [225].

It is noted that the choice of the appropriate concentration profile may be crucial for the selectivity of a process because of the interplay between transport and reaction in the porous mass of the catalyst [29], [225]. Moreover, according to Che et al. [84], the careful selection of metal precursors and competitors helps to obtain a large number of metal distribution profiles on the support surface between the periphery and the grain centre, depending on the strength of their interaction with the support.

For both techniques (WI and DI), the main operating variables are the nature and concentration of both components (the liquid and the solid surface), the nature of the solvent and the reaction conditions (temperature, time). The most commonly used solvent for inorganic salts is water because of the high solubility of many precursors, whereas

organic solvents are mainly used for organometallic precursors. Also, in order to prevent premature deposition of the metal precursor in bulk solution, concentrations below (super)saturation are required. The temperature affects the precursor solubility as well as the solution viscosity and as a consequence the wetting time. By increasing the impregnation temperature, the solubility of the precursor compound increases, which largely solves the deposition problem of poorly soluble salts. In addition, the increase in temperature results in a reduction in the viscosity of the solution. This results in easier diffusion of the solution into the pores of the carrier [33], [228], [229]. However, increased temperatures also lead to the faster evaporation of the solvent, resulting in the formation of larger crystallites of the deposited substance [33].

- **Deposition-Precipitation (DP)**

The method of preparation termed "deposition-precipitation" was first developed by Hermans and Geus for the production of highly loaded and highly dispersed metal/oxide catalysts [80], [230]. Deposition-precipitation is performed when an insoluble form of the supported active phase is generated in solution, and deposited onto the support, whereas nucleation in the solution itself should be avoided. For instance, an active element (e.g. Ni) can be deposited onto a carrier (e.g. SiO_2) in suspension in the precipitating solution (e.g. $Ni(NO_3)_2$) by slow addition, or in situ formation, of a precipitating agent (e.g. NH_4^+)). This method is excellent if the primary particles of the carrier are not porous since for porous supports deposition takes place preferentially in the external parts of the pores [222], [223], [231].

This process is achieved through the change of solution's pH (urea, HNO_3, etc. can be utilized to increase the pH of the suspension), the addition of a precipitation agent, the addition of a reducing agent, or change in the concentration of a complexation agent. The complexing agent keeps the active precursor in solution under conditions where the (hydrated) metal ion alone precipitates. Moreover, DP can be achieved through deposition from a precursor solution by a change of temperature, or evaporation, so that metal compounds with a low solubility are formed, often metal hydroxides. The precipitation should occur only on the support and not in the solution. For that to happen, two main conditions must be fulfilled; strong interaction between the soluble metal precursor and the surface of the support, as well as controlled concentrations of the precursor in solution to avoid spontaneous precipitation [84], [222], [225], [227].

It is noted that in the presence of the support, the solubility limit shifts to lower concentration compared to the solubility limit in solution, a fact that favours deposition on the support. This is achieved, by decomposition of a suitable substance which releases the precipitating agent continuously, or by controlled and progressive addition of the precipitating agent. In practice, the support is slurried in the solution containing the soluble precursor [84], [225], [227].

Deposition-precipitation is traditionally used to produce highly loaded metal catalysts, but recently shows an increased usage for the preparation of low-loaded, noble metal catalysts. However, the most important drawback of this method is the poor control of metal distribution and surface composition, which also makes it difficult to prepare true bimetallic catalysts with controlled compositions [225], [227]. Figure 3.2 shows a schematic representation of the preparation procedure of a Pt-Au/CeO$_2$ catalyst through the deposition-precipitation technique [227].
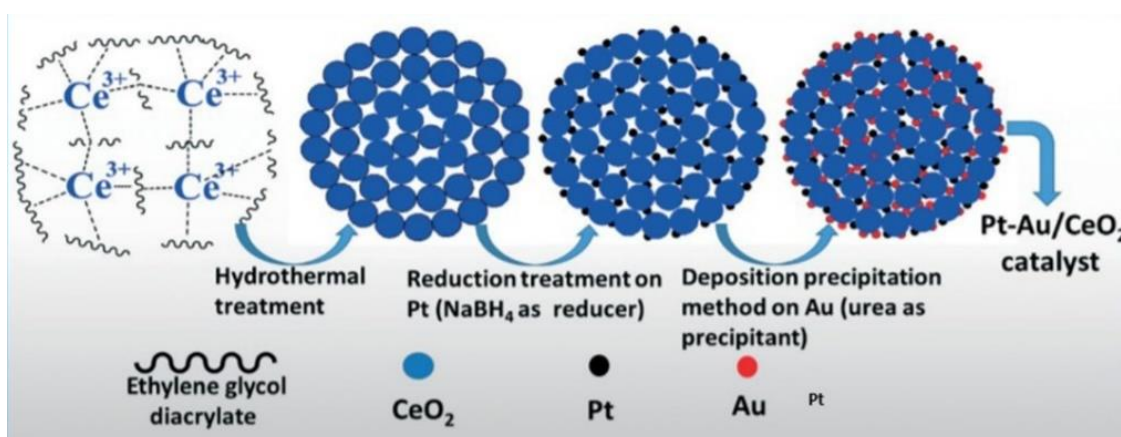
Figure 3.2: Schematic representation of the preparation procedure of a Pt–Au/CeO$_2$ catalyst by deposition-precipitation [227].

3.1.2. Sol-Gel

Sol-gel is another method for preparing supported metal catalysts. Oxidic supports are commonly produced via sol-gel chemistry, where a metal precursor is polymerized in solution. With further condensation, small particles are formed, which are links between particles, and eventually, the formation of a gel is achieved [225], [232]. Specifically, a sol, or a colloidal suspension with solid particles in a liquid, arises from hydrolysis and polymerization of a precursor. The metal precursor for the oxidic supports is usually silicate dissolved in water, or metal alkoxides dissolved in an organic solvent. During this step, the pH and the reaction temperature are carefully controlled. As hydrolysis and

polymerization occur, colloidal particles or micelles with an approximate diameter of 10nm are formed [223], [225], [233]. These colloidal particles are merged during the subsequent gelation stage into polymeric chains by chemical bonding between local reactive groups at their surface. It is noted that this, prevents flocculation which is a result of isotropic micelle aggregation [234].

The next stage in the sol-gel synthesis is referred to as the "postgelation" step. During this step, where drying and calcination of the gel are completed, a lot of changes can occur; desorption of water, evaporation of the solvent, desorption of organic residues, dehydroxylation reactions and structural changes. By completing the polymerization and removal of the solvent, which is usually obtained via evaporation under normal conditions, the sol converts into a gel (xerogel). The ambient pressure in these conditions rises the capillary pressure and causes shrinkage of the network. In case the wet gel is dried in an autoclave under supercritical conditions, thus avoiding capillary stress, the product is called an aerogel [223], [225], [233]. Figure 3.3 illustrates the general steps of the sol-gel process for the preparation of solid materials [234].
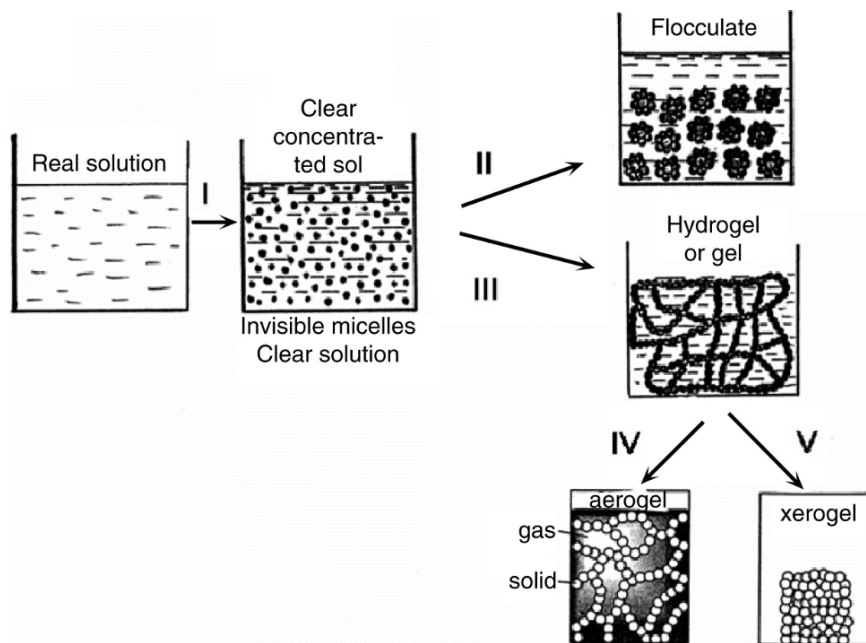
Figure 3.3: General steps of sol-gel processing in the preparation of solid materials, where: I-colloidization, II-flocculation, III-gelation, IV-supercritical fluid processing and V-drying by evaporation.

The important variables which must be considered in the synthesis of supported metals by the sol-gel method include; nature of precursors, pH, reactant stoichiometries, gelation temperature, metal loading, presence of salts, solvent removal and pretreatment condition

[225], [233]. It should be mentioned that this procedure has many advantages compared to the traditional methods of catalyst preparation. A well-defined pore size distribution, controlled porosity combined with the ability to form large surface area materials at low temperatures, purity and homogeneity. Moreover, the resulting catalysts have higher BET surface area, high thermal stability and resistance to deactivation [233], [235]. However, the sol-gel method has not been applied industrially yet, mainly due to its complexity and relatively high cost.

3.1.3. Post-treatment procedure

The characteristics of the final catalyst strictly depend on the post-treatment conditions (rate of heating, time, final temperature, atmosphere) and, obviously, on the type of supporting materials. It should be noted that different conditions can lead to different metal-support interactions, which are of fundamental importance and usually define catalytic properties [223].

- **Drying**

After impregnation, drying is carried out to remove the liquid solvent, which is usually water, from the support. During this process, the liquid solvent is transported towards the external surface of the support due to capillary flow, and the dissolved metal components are transported by diffusion and liquid convection. The drying process is very important, and the conditions used during this step, such as heating rate, temperature, duration, or gas flow rate can change the physical properties of the resulting material. Therefore, it is important to record and keep these parameters constant. If the drying process is not carried out carefully and is completed quickly, then the liquid contained in the pores may be driven out of them by vapour forming deep in the pores. As a result, it can change the distribution of active components since the catalytically active material may become concentrated at the mouth of the pores or may even move onto the exterior surface of the support [27], [29], [226], [228].

- **Calcination**

After drying, the calcination of the catalyst is carried out, as a further heat-treatment. The calcination temperature should be slightly higher or equal to the catalyst's operating temperature. Calcination, which is the thermal treatment in oxidizing atmosphere, aims to stabilize the physical and chemical properties of the catalyst or its precursor. During this step, several processes take place; loss of the chemically bonded H_2O or CO_2,

modification of the structure (e.g. pore structure) and stabilization of physical and mechanical properties. Moreover, the thermally unstable compounds (carbonates, hydroxides, or organic compounds) decompose and are usually converted to oxides, amorphous material can become crystalline and various crystalline modifications can undergo reversible or irreversible changes [29], [228].

The calcination process is also very important and even the elimination of any water vapour formed should be carefully controlled since water vapour can cause sintering in some oxides. In fact, during the calcination step, sintering of the precursor and reaction between the metal precursor and the support usually occurs [27], [223].

- **Pretreatment procedure (oxidation, reduction)**

The pretreatment procedure is performed in order to activate the catalyst surface. The pretreatment consists of several steps that must be repeated carefully between successive analyses in order to assure the best reproducibility of the analytical results. Initially, the catalyst undergoes oxidation by flowing air or pure oxygen over the sample. This step oxidizes all the metal atoms on the surface and also eventually removes carbon and other residuals [26], [27], [29].

The next step is the reduction of the catalyst, where during this process the metal nuclei are formed. This step is essential, as the nature of a noble metal is crucial for the high activity and selectivity of H_2-SCR catalysts, which are examined in this work. In particular, the state of Pt sites is of great significance, since NO can not dissociate rapidly on completely oxidized Pt sites [236]. The reduction is most frequently carried out in the reactor where the catalyst is to be used, as then there are no problems of re-oxidation prior to use [27]. The sample is reduced by flowing pure hydrogen over the catalyst, where the H_2 reacts with the metal oxide forming hydrides and water. The formed water is in part carried away by the gas stream but in part can be adsorbed by the porous structure of the support during reduction. The reduction is best carried out slowly, often with a gradually increased temperature of reduction [26], [27], [29]. The rate of this process depends on the temperature and the nature of the substrate. It is mentioned that at lower temperatures ($T<300^oC$), a narrow distribution of small metal crystallites is achieved, whereas at higher temperatures ($T>400^oC$) a broader distribution and larger metal crystallites are observed [26], [29].

In some cases, further pretreatment is required where chemisorbed hydrogen from the previous step, has to be removed. Hydrogen removal can be performed under high vacuum or in flow of an inert gas resulting in zero valence state surface metal, ready to react with the measuring gas in the analytical cycle. The temperature chosen for hydrogen removal should usually be a little higher than the reduction temperature [26].

3.2. Characterization Techniques

3.2.1. Mass Spectroscopy (MS)

Mass Spectrometry is a powerful technique for identifying and determining elements, isomers, molecular weights, and molecular structures, and probing the fundamental principles of chemistry. It is a method for ionizing the sample, separating the ionized ions by the mass difference, and estimating them [237], [238]. The first MS was designed by JJ Thompson in 1912 and was mainly used to study the atomic weight of elements and to monitor the abundance of elemental isotopes [239], [240]. Figure 3.4 shows the main components of a mass spectrometer (MS); inlet of the sample, ionization source, analyzer detector and data processor/digitizer. The mass spectrometry technique requires the injection of the sample in the instrument through the inlet, the ionization of it in the ionization chamber, the extraction of the ionized species into the analyser which resolves the ions based upon their mass to charge ratio (m/z) and finally the detection of the ions by the detectors. The relative abundance of each resolved ionic species is recorded in the form of mass spectra [239].
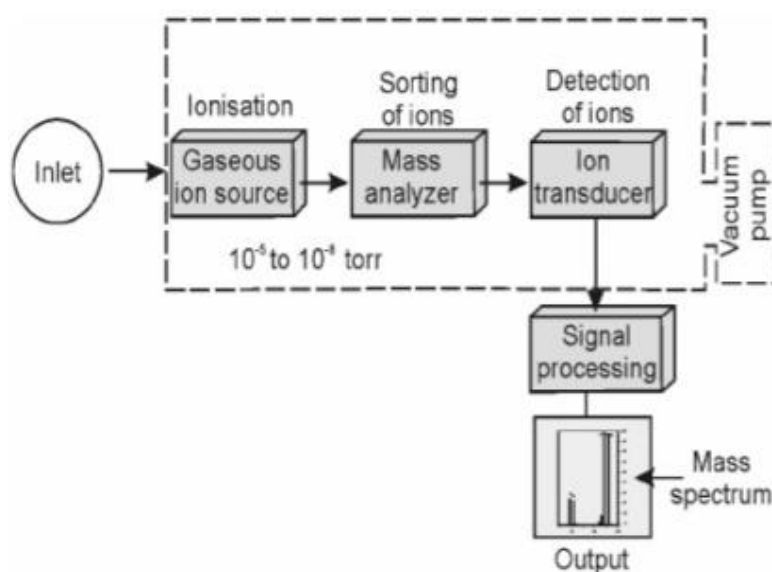
Figure 3.4: Schematic diagram of the components of a mass spectrometer.

- **Inlet system**

The purpose of the inlet system is to transfer the sample into the vacuum of the mass spectrometer. Depending on the state of the sample, a variety of inlets are available. The gas samples and samples with high vapour pressure are introduced directly into the source region, while liquids and solids are usually heated to increase the vapour pressure for analysis. In most cases, the sample to be analyzed needs to be in gaseous form. In these cases, the sample enters the MS through a short capillary at the end of a heated sleeve. This sleeve is then inserted through a vacuum lock, so the sample is inside the source region. The capillary tube is necessary to adjust the pressure of the gaseous sample from an atmosphere to 10^{-6}Pa, which is the pressure prevailing in both the ionization chamber and the remaining parts of the MS [33], [237].

- **Ionization System**

Different types of ionization methods are employed depending on the type of samples, polarity, volatility, thermal stability, and molecular weight of the compound concerned. Volatile samples are subjected to either electron or chemical ionization, while non-volatile samples can be ionized by fast atom bombardment, secondary ion mass spectrometry, matrix-assisted laser desorption ionization and electrospray techniques. The ionization energy is significant because it controls the amount of fragmentation observed in the mass spectrum [238], [239].

Electron Ionization (EI) is the most common ionization technique used for mass spectrometry and works well for many gas phase molecules. The electrons used for ionization are produced by passing a current through a wire heated filament (usually made of tungsten). An electric field with a potential difference of 40-100eV (usually 70eV), accelerates these electrons across the source region to produce a beam of high energy electrons, that are controlled by the amount of current. The emission current (that is, the current of ionizing electrons) is monitored at the source electrode and is regulated by controlling the heating current that flows through the filament. When an analyte molecule passes through this electron beam, a valence shell electron can be removed from the molecule to produce positively charged ion species. Specifically, as the electron passes close to the molecule, the negative charge of the electron repels and distorts the electron cloud surrounding the molecule. This distortion transfers kinetic energy from the fast-moving electron to the electron cloud of the molecule. If enough energy is transferred by

the process, the molecule will eject a valence electron and form a radical cation (M^+) [237]–[239].

The distribution of energy transferred during ionization and the large number of fragmentation pathways results in a variety of products for a given analyte, as seen in equations 3.2−3.4. Other electron voltages may be used to vary the amount of fragmentation produced during ionization. Intact molecular ions are observed from ions produced with little excess energy. Other molecular ions have more energy and undergo fragmentation in the source region. The abundance of the resulting fragments often called product ions, is determined by the kinetics of the fragmentation pathways and the ionization energy. Changing the ionization energy changes the observed distribution of fragment ions. This distribution provides structural information for interpreting mass spectra [33], [237].

$$\textbf{M} + \textbf{e}^- \rightarrow \textbf{M}^+ + \textbf{e}^- + \textbf{e}^- \tag{3.2}$$

$$\textbf{M} + \textbf{e}^- \rightarrow \textbf{M}^{++} + \textbf{e}^- + \textbf{e}^- + \textbf{e}^- \tag{3.3}$$

$$\textbf{M} + \textbf{e}^- \rightarrow \textbf{M}^{n+} + \textbf{e}^- + \textbf{ne}^- \tag{3.4}$$
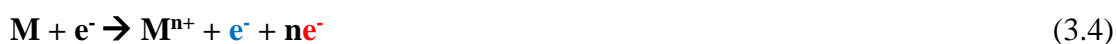
where the bombardment electron (black colour) is not captured by the positive ion that is generated but continues its course with different energy and orbit (blue colour). The electrons emitted by the ionization of the molecule (red colour) have different energy between them as well as with the bombardment electron [33].

- **Analyser**

The following component of a mass spectrometer is the analyser. After ions are formed in the source region, they are accelerated into the mass analyser by an electric field. The mass analyser separates these ions according to their m/z value. The selection of a mass analyser depends upon the resolution, mass range, scan rate and detection limits required for an application. The most common analysers are; magnetic deflection analyser, time-of-flight analyser, radio frequency mass analyser, cycloidal mass analyser, monopole mass analyser and quadrupole mass analyser (QMS). The latter analyser was used for the current dissertation [237], [239].

The Quadrupole MS (Figure 3.5) consists of four rods parallelly arranged in a hyperbolic section. The four electrodes are connected in pairs where the first two rods are connected to direct current (DC) and the other two opposite rods are linked to radio frequency (RF) alternate current (AC). Opposite rods have DC voltage and other two have RF voltage,

180 degrees out of phase, thus, generating an electrically oscillating field that functions as a bandpass filter to transmit the selected m/z value. When ions are pulsed from the ionization chamber towards the quadrupole, the positive ions will move toward the negative rod but due to changing polarity, the ions take up a complex trajectory. Thus, the trajectory of ions is regulated by varying the DC/RF voltage [237]–[239], [241].
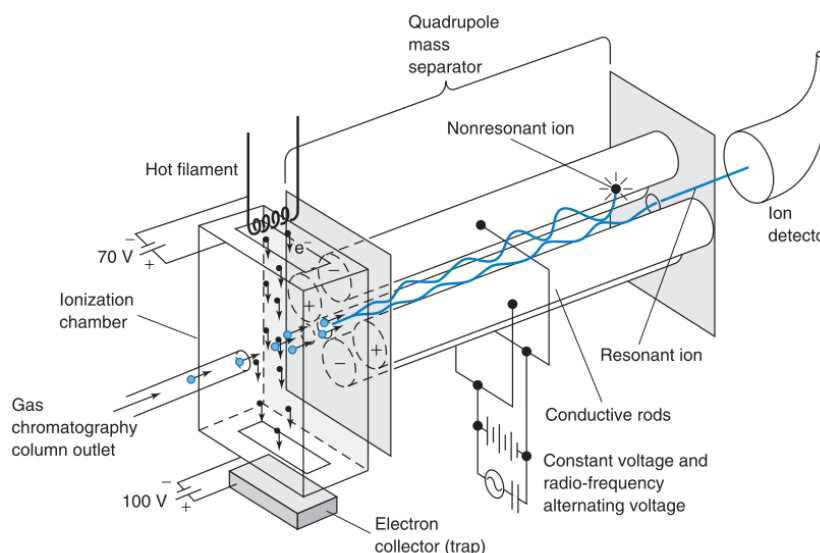
Figure 3.5: Quadrupole mass spectrometer (QMS) [49].

The ions are vibrationally moved, keeping the amplitude corresponding to m/z by the electric field. Since the ions with too large amplitude collide with the electrodes, the ions with a certain value of m/z pass through the electric field undetected. Specifically, the ions within a narrow range of m/z will take up a stable trajectory in the quadrupole ultimately reaching the detector. Ions with improper trajectory collide with the rods and will not reach the detector. By manipulating the voltage and frequency, the ions with different m/z ratios can be transmitted to the detector. In the RF mode where DC is zero, most ions acquire stable trajectory and pass through the quadrupole. In the scanning mode, RF and DC simultaneously vary to permit ions with different m/z ratio to pass through the quadrupole sequentially. The third mode is to stabilize the voltages thus permitting stable trajectory for ions with predetermined m/z ratio [237]–[239], [241].

Consequently, by selecting an appropriate RF frequency and potential, the quadrupole acts as a high pass filter, transmitting high m/z ions and rejecting low m/z ions. The combination of high and low pass filters produced by the RF and DC potentials is adjusted to only transmit the selected m/z value. All ions above or below the set m/z value are

rejected by the quadrupole filter. The RF and DC fields are scanned (either by potential or frequency) to collect a complete mass spectrum [237].

- **Detection**

The analyzer and detector are kept in a vacuum so that the ions produced do not collide with air molecules and the ion trajectories are maintained at a particular speed. Mass spectrometry can detect molecular ions at a detection sensitivity of an order of magnitude of picogram (10^{-12}g). Ions are detected by a mechanism capable of detecting charged particles (e.g. Secondary Electron Multiplier, Faraday Cup) [238].

The Faraday Cup (Figure 3.6) is a mass spectrometric ion detector in which each arriving cation is neutralized by an electron. The current required to neutralize the ions is proportional to the number of cations arriving at the Faraday cup. The dynode in a Faraday Cup consists of secondary emitting materials such as GaP, BeO, and CsSb. During the detection with a Faraday Cup, the incident ions or ion beam strikes the dynode, electrons are emitted that induce current, which is amplified and recorded. Such detectors are suitable for isotope analysis for which high signal stability is important for precise ratio measurements [49], [239], [242].
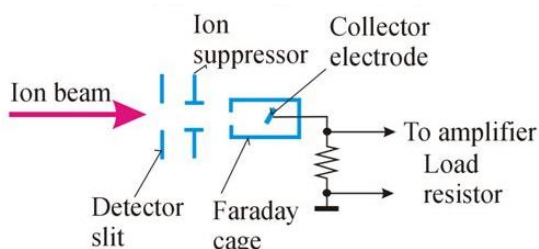
Figure 3.6: Faraday Cup.

The secondary electron multiplier is the most common ion detector (Figure 3.7). Secondary electron multipliers are especially useful when both positive and negative ions have to be detected. Ions striking the surface at the detector entrance produce secondary electrons that, in turn, cascade down the channel, causing additional electron emission. This cascade of current is finally amplified a million times or more and is recorded. The degree of multiplication depends on the composition of the individual dynode surface (usually copper-beryllium), acceleration per stage (bias voltage), number of dynodes (6–20), and bias current circuit design [239], [242]. Characteristics that make the secondary electron multiplier an excellent MS detector in the current (analog) or pulse-counting modes, are the high gain (10^3–10^7), relatively low noise (>1 count/s), and relatively large

linear dynamic range (10^4–10^6). They can also be operated in a dual analog and pulse-counting mode, thus achieving an operative dynamic range of $\geq 10^8$ [242].
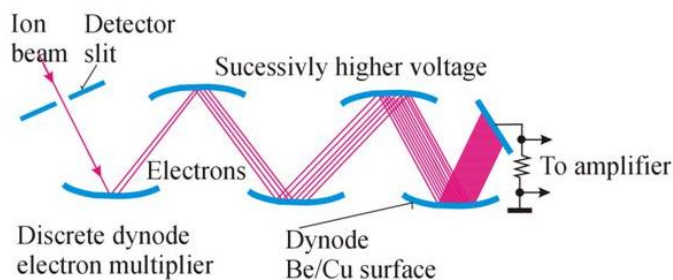
Figure 3.7: Secondary Electron Multiplier

- **Processing/Data System**

The final component of a mass spectrometer is the processing/data system. Most modern mass spectrometers are controlled by a computer via an interface (Ethernet or USB) that converts the data from the analyser (m/z) and the detector (intensity) in a mass spectrum. The mass spectrum can be displayed as a scanned mass spectrum (peak shape can be examined and optimised), as a bar chart (where the signal is recorded only at each nominal mass), or only at selected masses. The data are generally displayed in arbitrary units, proportional to the number of ions detected in % of the most abundant one, and often indicated as being the "relative abundance" as a function of its m/z ratio [237], [241], [243]. Furthermore, each gas molecule has its own characteristic cracking pattern (spectral fingerprint), which is caused by the molecule fragmenting when it is ionized. Therefore, the spectra produced can be interpreted by identifying these patterns [244].

3.2.2. Gas Chromatography-Mass Spectrometry (GCMS)

Gas Chromatography-Mass Spectrometry, GCMS, is the synergistic combination of two powerful microanalytical techniques; the gas chromatograph separates the components of a mixture in time, and the mass spectrometer provides information that aids in the structural identification of each component. The GCMS technique has the advantage of separating components of a complex mixture providing a mass spectra for qualitative purposes, as well as quantitative information on these same compounds [245], [246]. In 1952, James and Martin [247] introduced the technique of gas chromatography (GC).

The basic operating principle of GC involves the injection of a volatile liquid or gaseous sample through a septum (a rubber disk) into a heated port, in which it rapidly evaporates. Vapour is swept through the column by the carrier gas, usually He, Ar or N_2, where a

separation of the components of the mixture is followed in a specially prepared column. The separated analytes flow through a detector, in this case, mass spectrometer, whose response is displayed on a computer [49], [238], [245]. Figure 3.8 indicates the schematic diagram of a GC [49].
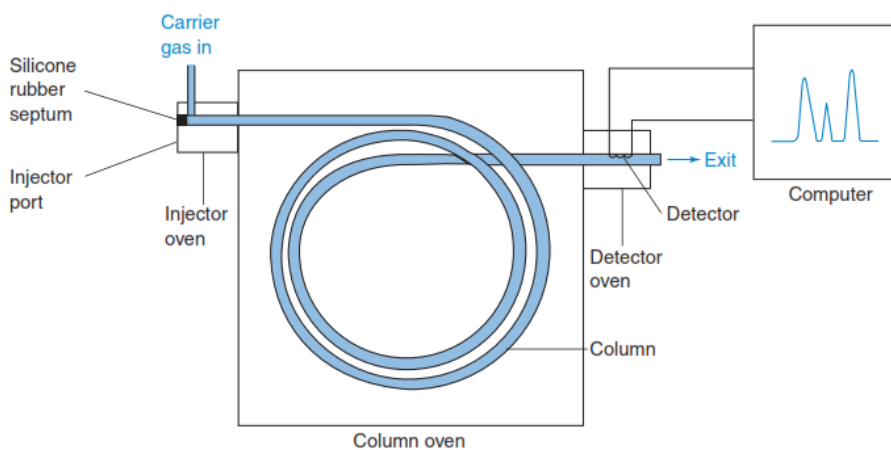
Figure 3.8: Schematic diagram of a gas chromatograph.

- **Injection System**

Regarding the injection system of a GC, there are several types of injectors that can be used, such as split/splitless injectors, programmable-temperature vaporizing injectors, on-column injectors, etc. The most common injector for capillary columns is the heated split/splitless injector, that can operate in both modes. For neat samples that are not dissolved in a solvent, or for samples where the analytes are dissolved in a solvent at relatively high concentrations, the split mode is used. Samples that contain analytes at a trace level are injected through the splitless mode. The specific injector is set at a temperature that is hot enough to vaporize the solvent and the analytes in the sample. This temperature is constant throughout the GC run. Moreover, the gas samples (typical volume of 1ml) may be introduced into the carrier gas stream through a gas sampling valve or with a gas-tight syringe [248].

- **Carrier Gas**

The carrier gas or mobile phase of the GC, which is usually N_2, He, Ar or H_2 is used to transfer the injected sample onto and down the column where the separation occurs and then out into the mass spectrometer interface. The carrier gas must be inert and of very high purity (99.999–99.9999%) in order to maximize the life of the column and assure a quiet baseline for most detectors. The selection of the gas is based on its gas chemistry, for instance, N_2 has relatively high viscosity and H_2 needs proper venting due to its

explosive nature. Helium is the most common carrier gas and is compatible with most detectors. The carrier gas must be purified before it is connected to the GC, thus the gas passes through a hydrocarbon trap, then a moisture trap, and finally an oxygen trap [245], [246].

- **Column**

The components are separated in the column, where the majority of them are capillary tubes with a stationary phase coated on the inner wall (Figure 3.9). The typical column used for GCMS is a narrow open tubular column which is a long, coiled capillary tube made of fused silica (SiO_2) and coated with polyimide (a plastic capable of withstanding 350°C) for support and protection from atmospheric moisture [49], [246]. The injected sample in the carrier gas interacts with this stationary phase and equilibrium is established between the concentration of each component in the gaseous and solid phases. It is noted that as fresh carrier gas flushes down the column, each compound comes off the stationary phase at its own rate, e.g. a component that spends little time in the stationary phase will elute quickly [245], [246].
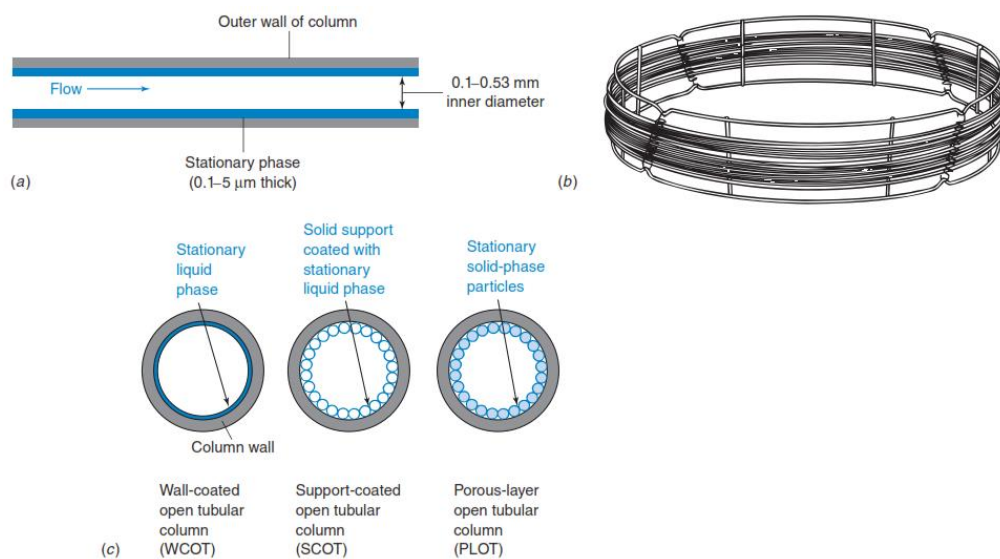
Figure 3.9: (a) Typical dimensions of open tubular gas chromatography column, (b) Fused silica column with a cage diameter of 0.2m and column length of 15–100m, (c) Cross-sectional view of wall-coated, support-coated, and porous-layer columns [49].

After elution from the column, each component is carried to the detector/MS by the carrier gas. The separations increase after many interactions (diffusion and wall interactions) down the length of the column and the separation is determined by the distribution (partitioning) of each component between the mobile phase (carrier gas) and the stationary phase. Also, the column oven temperature must be enough to provide sufficient

vapour pressure for analytes to be eluted in a reasonable time (retention time), while the detector is maintained at a higher temperature than the column so that all analytes will be gaseous. The length of the column, the thickness of the stationary phase, temperature conditions, as well as the carrier gas affect the actual retention time of a compound on a specific phase [245], [246].

- **Detector and Data Interpretation**

The detector of a GCMS analytical instrument is the mass spectrometer. The MS can separate ions according to their mass-to-charge ratio (m/z) values; therefore, because virtually all of the ions have a single charge, the m/z value of ions formed in GCMS is considered to be also the mass of the ion. The outcome of the detection is a complete mass spectrum that can be provided from a few femtomoles of an analyte. The mass spectrum provides a characteristic fragmentation pattern that can be used as the basis for identification along with the retention time of the gas chromatograph. Specifically, either a single mass spectrum can be displayed, or a series of spectra averaged together can be displayed as a single spectrum. The x-axis of such a display relates to time because the spectra are acquired at a constant rate and the y-axis is related to the abundance of each ion in the mass spectrum. This is basically a chromatographic output representing a summation of the signal strength of all the ions produced by the MS at a given time [49], [245], [246].

A mass chromatogram is, therefore, a plot of the amount of analyte as a function of time (chromatographic peaks) and is sometimes called an extracted ion chromatogram. It is noted that some instrument manufacturers' data systems have automated background subtracting routines. When the background is subtracted, the intensity of each individual m/z value in the background spectrum is subtracted from the intensity of the corresponding m/z value in the sample spectrum. Moreover, if compounds of similar chemical structure and physical solubility coelute, then they appear as overlapping or unresolved peaks. In this case, careful deconvolution should be applied [245].

By identifying the peaks through a comparison of the retention time of an authentic sample with the suspected compound, qualitative analysis can be achieved. A quantitative analysis is based on the area of a chromatographic peak since in the linear response concentration range, the area of a peak is proportional to the quantity of that component

[49], [245]. Figure 3.10 illustrates the selected ion monitoring that can happen for data interpretation [49].
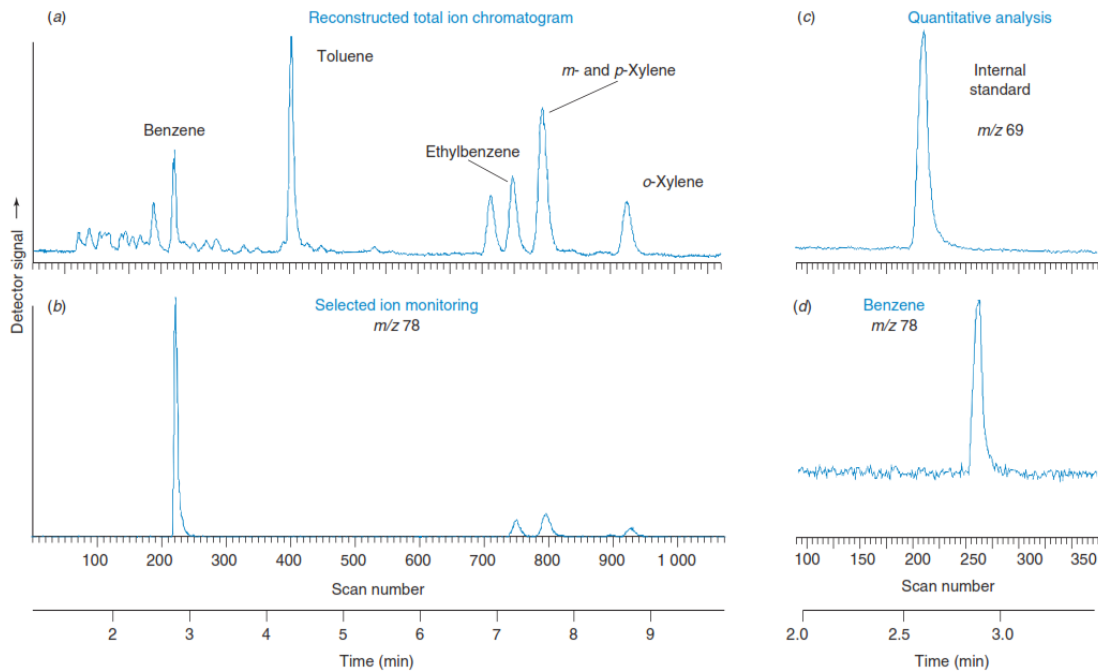
Figure 3.10: Selected ion monitoring in GCMS. (a) Reconstructed total ion chromatogram of automobile exhaust with electron ionization, (b) selected ion monitoring at m/z 78, (c) and (d) quantitative analysis of benzene after adding an internal standard with a prominent ion at m/z 69.

3.2.3. Inductively Coupled Plasma Mass Spectrometry (ICPMS)

Inductively Coupled Plasma Mass Spectrometry, ICPMS is an analytical technique used for elemental determinations and was commercially introduced in 1983. An ICPMS generally combines a high-temperature ICP (Inductively Coupled Plasma) source with a mass spectrometer, where the ICP source converts the atoms of the elements in the sample to ions and the MS separates and detects these ions [249]. An ICPMS system contains many components, such as sample introduction area (nebulizer and spray chamber), plasma torch, interface region, ion focusing, quadrupole MS and vacuum chamber. Figure 3.11 illustrates the interface between inductively coupled plasma and mass spectrometer [49]. Moreover, ICPMS requires several services in order to function properly. It needs electrical power, cooling water (for cooling the plasma coil, the ICP interface region, the turbo pump and the RF Generator), argon gas (for maintaining the ICP, to actuate pneumatic controls and to flush the vacuum chamber when the pumps are switched off) and an active exhaust system (exhaust heat and vapors generated by the plasma) [250].
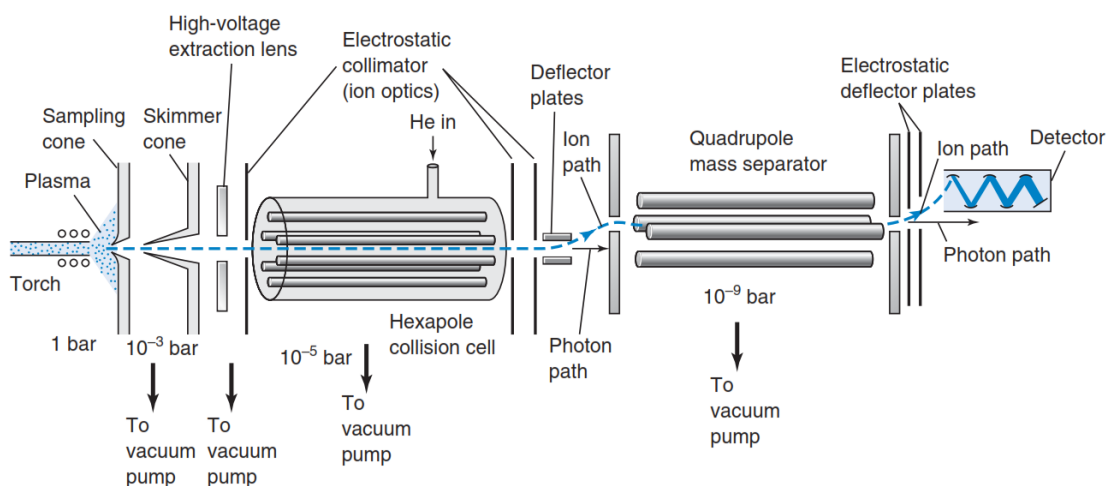
Figure 3.11: Interface between inductively coupled plasma and mass spectrometer.

- **Sample Introduction**

The liquid sample is pumped with a peristaltic pump which ensures the constant flow of the liquid, regardless of the differences in viscosity between samples, standards and blanks. The sample is pumped into a nebulizer, where it is converted into a fine aerosol (tiny droplets) with Ar gas. The fine droplets of the aerosol, which represent only 1–2% of the sample, are separated from larger droplets by means of a spray chamber. The fine aerosol then emerges from the exit tube of the spray chamber and is transported into the plasma torch via a sample injector [251].

- **Plasma Source and Interface region**

The plasma is formed by the interaction of an intense magnetic field, produced by radio frequency (RF) passing through a copper coil, on a tangential flow of Ar gas flowing through the torch. The plasma torch consists of three concentric tubes (outer, middle and sample injector), which are normally made from quartz. Once the sample aerosol is introduced into the ICP torch, it is completely desolvated and the elements in the aerosol are converted first into gaseous atoms and then ionized towards the end of the plasma. The formed ions are typically positive (M^+ or M^{+2}), thus, the elements that form negative ions, such as Cl, I, F, etc., are very difficult to determine via ICP-MS. The ICP torch provides temperatures of approximately $5500^{\circ}C$ that no material can withstand, resulting in rupturing of all bonds. Therefore, the data acquired from a plasma ion source correspond to the total content of an element in the sample [249], [251].

Once the ions are produced in the plasma, they are directed into the QMS through the interface region, which is maintained at a vacuum of 1–2 Torr with a mechanical roughing

pump. The interface region contains two nickel cones (sampler and skimmer) that have a small orifice (0.8-1.2mm and 0.4-0.8mm, respectively) which allow the ions to pass through to the ion optics, where they are guided into the mass separation device. Since the cone's orifice is really small, the total dissolved solids of the samples should be below 0.2% to avoid the deposition of the components around the sampler cone orifice. Hence, the samples must be filtered prior to their introduction in the system [49], [251].

- **Ion Focusing and QMS**

Once the ions have been successfully extracted from the interface region, they are directed into the main vacuum chamber by a series of electrostatic lenses, called ion optics. The operating vacuum in this region is maintained at about 10^{-3} Torr with a turbomolecular pump, while at the MS the vacuum is kept at 10^{-6} Torr with a second turbomolecular pump. The purpose of the ion optical region is to electrostatically focus the positively charged ion beam toward the entrance aperture or slit of the mass separation device. Another design of the optical region is to stop photons, particulates, and neutral species from reaching the detector [251].

The mass analyzer (QMS) is positioned between the ion optics and the ion detector. As the ions are emerging from the ion optics at the optimum kinetic energy, they are ready to be separated according to their mass-to-charge (m/z) ratio by the QMS. Further analysis of the QMS is provided at subchapter 3.2.1. It is noted that the quadrupole mass filter can separate up to 2400 amu (atomic mass units) per second, which is why the quadrupole ICP-MS is often considered to have simultaneous multi-elemental analysis properties [249], [251].

- **Ion Detector and Data Interpretation**

The final process is to convert the ions into an electrical signal once they have been separated by their mass-to-charge ratio. The fundamental purpose of the ion detector is to convert the number of ions striking the detector into an electrical signal. This signal can be measured and related to the number of atoms of that element in the sample, as well as, convert it into analyte concentration using ICP-MS calibration standards. Commonly, the detectors use a high negative voltage on the front surface of the detector so as to attract the positively charged ions. Once the ion hits the active surface of the detector, a number of electrons are released which then strike the next surface of the detector, amplifying the signal. The majority of ICP-MS systems use ion detectors that are based on the active

film or discrete dynode electron multiplier, which contain a series of metal dynodes along the length of the detector. The latter design converts the ions into electrons on the first dynode and the next dynode attracts the electrons and multiplies them; which results in very high steam of electrons emerging from the final dynode [249], [251].

It is noted that prior to the experiment, a full range of calibration standards (external standardization) and blanks have been run, the software creates a calibration curve of the measured intensity as a function of concentration for each element in the standard solutions. Additionally, during the ICPMS run, the examined samples and the calibration standards are often spiked with a small group of elements, which are not present in the samples, in really small quantities (μl). This method is known as internal standardization (IS), which is the classic way to compensate for a physical interference and to correct for any variations in the response of the elements caused by the matrix [251].

In a typical ICPMS run, repeated scans are made over the entire suite of analyte masses, in order to reduce the relative standard deviation. In addition, the signal pulses are continually collected as the quadrupole is swept across the mass spectrum. After a fixed number of sweeps, the total number of signal pulses in each channel is counted, resulting in the final spectral peak. Once calibration data are acquired, the unknown samples are analyzed and compared to the calibration curves. The software then calculates the concentrations (usually in ppb) for the analytes in the unknown samples [251].

3.2.4. BET Method

The total surface area of a porous material is given by the sum of the internal and external surface areas. The Brunauer-Emmett-Teller (BET) gas adsorption method has become the most widely used standard procedure for the determination of the surface area of porous materials [29], [252]. In 1938, Brunauer, Emmett and Teller, developed a simple model isotherm to account for multilayer adsorption and used this model to extract the monolayer capacity and hence the specific surface area [253].

The BET theory is based on the physisorption of chemically inert gas (N_2), on the free surface site (support) without dissociation. When physisorption occurs on the solids, a monolayer is formed on the external and internal surfaces at relatively low values of P/P_o (where: P is the measured pressure of the gas and P_o is the saturated vapour pressure of the N_2 gas at the temperature of adsorption), since each molecule is adsorbed on one site. As the pressure increases, multilayer formation begins to occur on top of that layer, as

can be seen in Figure 3.12. These subsequent layers also behave according to the Langmuir model [27].
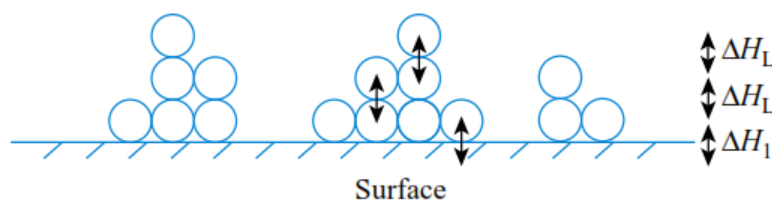
Figure 3.12: Schematic representation of the formation of first and subsequent layers.

The specific surface area of a catalyst or support (m^2/g) is determined by measuring the volume of gas, usually N_2, needed to provide a monomolecular layer according to the BET method. In this approach, the determination of the monolayer capacity is based on the physisorption of the test gas. The volume adsorbed at a given equilibrium pressure can be measured by static methods, namely, volumetric or gravimetric measurements. It should be noted that the samples prior to analysis must be free of moisture and other contaminants [29], [254].

The standard BET procedure requires the measurement of at least three and preferably five or more points in the appropriate pressure range on the N_2 adsorption isotherm at the normal boiling point of liquid nitrogen at 77 K under vacuum. Nitrogen is considered to be the most suitable adsorptive for surface area determination and it is usually assumed that the BET monolayer is close-packed, giving a_m (N_2) = 0.162nm^2 at 77 K [252]. On subsequent adsorption of N_2, the completion of the physisorbed monolayer is usually reached at $P/P_o \approx 0.1$. During the procedure, the pressure is linearly increased at a series of precisely controlled pressures until the saturation is reached (P/P_o = 1), i.e., when all the pores on the surface are filled with N_2. It is noted that when the pressure is decreased the adsorbed nitrogen molecules desorb from the sample in reverse way as they were adsorbed, thus, larger pores are emptied first [45], [252]. The adsorption and desorption of N_2 desorption can be seen in Figure 3.13 [255].

During the pressure region of $0.05 < P/P_o < 0.35$ the linearity of the BET equation is applied as shown in equation 3.5. The amount of nitrogen molecules adsorbed on the sample is measured as a function of N_2 pressure ratio over the sample. The calculation of the specific surface area is the second stage in the application of the BET method and can be calculated via equation 3.6 [45], [253], [254], [256].

$$\frac{P}{(P_0-P)\cdot V}=\frac{1}{V_m\cdot C}+\frac{(C-1)}{V_m\cdot C}\cdot\frac{P}{P_0} \tag{3.5}$$

where, V_m is the volume of adsorbed N_2 gas in a monolayer and C is a constant which is related exponentially to the enthalpy (heat) of adsorption in the first adsorbed layer.

$$S\left(m^2\right)=\frac{V_m\cdot N_{Av}}{V}\cdot A \tag{3.6}$$

where, S is the specific surface area (m^2), N_{Av} is Avogadro's number ($6.023\cdot10^{23}$mole^{-1}), V is the volume of gas in STP (cm^3/mole) and A is the molecular area of N_2 (16.2 Å^2).
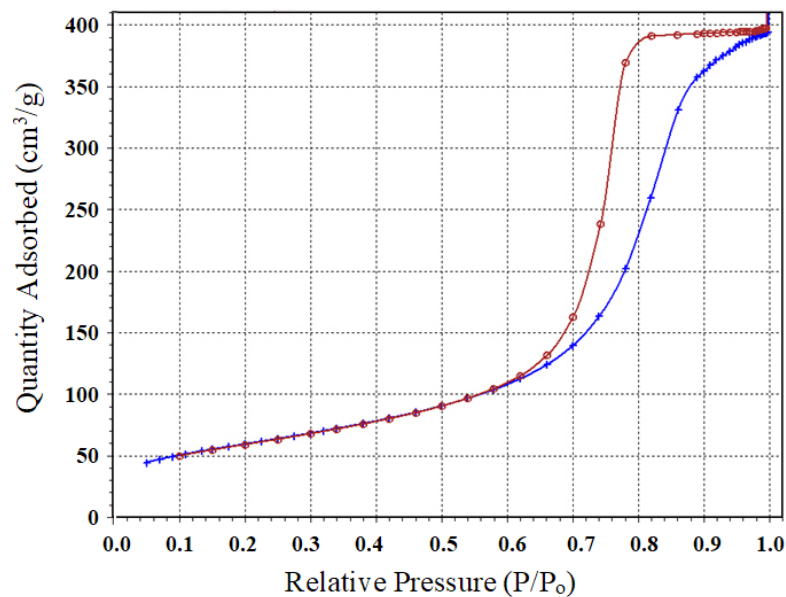
Figure 3.13: Isotherm linear plot, where adsorption is indicated with blue and desorption with red.

3.2.5. Scanning Electron Microscopy (SEM)

The scanning electron microscope (SEM) is one of the most versatile instruments available for the examination and analysis of the physical texture, microstructure morphology and chemical composition characterizations of a catalyst or its precursor(s) [27], [257]. Specifically, it offers the unique opportunity to observe catalyst morphologies over the entire range of relevant particle sizes, as well as estimate the particle shapes and sizes of the support or active phase and their size distributions. Also, SEM is most useful for studying sample topographies with resolutions approximately at 1nm. The produced SEM images are derived from scanning a finely focused probe beam in a raster pattern across the specimen surface. The emitted signals (backscattered and secondary electrons) are used for image formation [29].

- **SEM apparatus**

The SEM consists of an electron beam generating and accelerating system (electron gun), a high vacuum system, a focusing and scanning system, a specimen stage, an electron detecting and multiplying system, preamplifiers and amplifiers, and cathode ray tubes for visual observation and photography [258]. The SEM apparatus is presented in Figure 3.14.
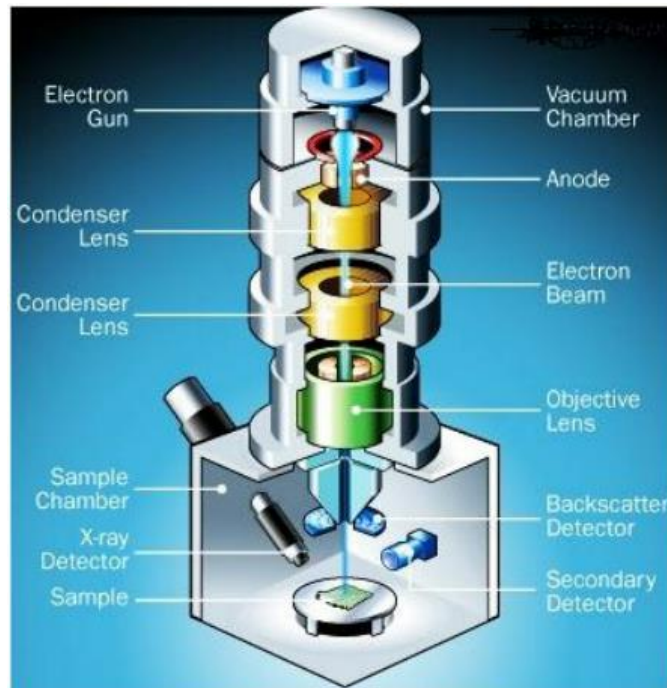
Figure 3.14: Schematic diagram of SEM.

The electron gun is the beam generating system that produces a stable electron beam with high current, small spot size, adjustable energy, and small energy dispersion. The primary electrons by which the specimen is bombarded, result from a cathode that can be either a thermionic cathode made from a piece of tungsten wire (hair-needle cathode), which is heated directly (conventional SEM), or from a single crystal of lanthanum hexaborate (LaB$_6$; conventional SEM) or tungsten, the former being heated indirectly or non-heated (field emission SEM). The most widely used electron gun is composed of three parts: a V-shaped hairpin tungsten filament (the cathode with 100μm diameter), a Wehnelt cylinder, and an anode. The filament is heated to a temperature of more than 2500°C by applying a filament current so that the electrons can escape from the surface of the filament tip. The Wehnelt-cylinder (gridcup) is a metal cup with a central hole that has a slightly more negative potential compared to the cathode and thus accelerates the electrons toward the anode. The potential difference (1-50kV) created between the

cathode (negative) and the anode (grounded) accelerates the electrons emitted from the tip of the filament towards the specimen [257], [258].

The scanning electron microscopes need a high vacuum system due to various reasons; the heated filament for electron emission would burn out under atmospheric conditions. Also, if poor vacuum conditions exist, then the gas molecules greatly enhance collisions between electrons and gas molecules, resulting in electron scattering and break-down of the focused, small-diameter straight-lined electron beam. The air moisture as well as the dust particles, contaminate the microscope column and deteriorate working conditions [258].

In addition, the SEM instrument requires a focusing and scanning system. Most SEM have two sets of condenser lenses that are electrostatic or electromagnetic. As the electron beam passes through the anode, the lenses focus the electron beam by converging and collimating it into a relatively parallel stream. The scanning generator consists of a set of deflection coils, which make the focused electron beam scan a certain area of the specimen surface with a defined frequency. The magnification unit of the SEM works closely with the scanning generator. The final lens of the microscope is the objective lens which is used to focus the electron beam into a probe point at the specimen surface and to supply further demagnification. It is noted that an appropriate choice of lens demagnification and aperture size, results in a reduction of the diameter of the electron beam that hits the specimen surface (spot size) and enhances the image resolution [257], [258].

The examined sample is placed in the specimen holder inside the specimen stage. Because of the importance of the angle between the incident electron beam and the specimen surface, the specimen stage has one or two horizontal tilting axes. Besides the specimen stage, the specimen chamber also contains the electron detecting and multiplying system, i.e., signal detector(s) consisting of a collector, scintillator and light pipe. The most common detectors are for the emission of secondary electrons as well as the backscattered electrons [257], [258].

As for the secondary electrons (SE), they produce the most widely used signal through the interaction of the primary electron beam with the specimen. When the primary electron beam strikes the specimen's surface, the atoms of the surface are ionised, which causes the emission of loosely bound electrons (secondary electrons). These electrons have low energy (~3–5eV) and they can only escape from a region within a few

nanometres of the material surface. Therefore, the SE accurately mark the position of the beam and give topographic information with good resolution. Due to their low energy, the Everhart–Thornley (ET) detector, which is the standard collector for secondary electrons in most SEMs, applies a positive bias by creating an electrostatic magnetic field in order to attract them towards the scintillator. The scintillator converts the energy of the electrons into photons (visible light), that travel down a Plexiglas or polished quartz light pipe. Then, they move out through the specimen chamber wall, and into a photomultiplier tube (PMT) which converts the quantum energy of the photons back into electrons. The output voltage from the PMT is further amplified (up to 10^6-10^8) before being output as brightness modulation on the display screen of the SEM [257], [258].

Regarding the backscattered electrons (BSE), they are defined as electrons that have undergone a single or multiple scattering event and which escape from the surface with an energy greater than 50eV at an angle of more than 90º. The elastic collision between an electron and the sample atomic nucleus causes the electron to bounce back with wide-angle directional change. It is considered that roughly 10–50% of the beam electrons are backscattered toward their source, and on an average, these electrons retain 60–80% of their initial energy. A higher backscattered signal results from elements with higher atomic numbers that have more positive charges on the nucleus, and as a result, more electrons are backscattered. Therefore, the percentage of BSE that is reemitted by the sample, depends upon the atomic number of the sample, providing atomic number contrast in the SEM images [257].

Another detector which is used in a SEM analysis is the x-ray detector. The x-ray signals are typically produced when a primary beam electron causes the ejection of an inner shell electron from the sample. The outer shell electron makes the transition to fill this vacancy and produces an x-ray whose energy can be related to the difference in energies of the two electron orbitals involved. With the emission of an x-ray photon, the ionized atom returns to ground state. Some portion of the x-rays generated in the sample will escape from the sample and travel toward the energy dispersive x-ray spectroscopy detector, known as EDS [259].

- **Data Interpretation**

The secondary electrons (SE) are used principally for topographic contrast in the SEM, that is, for the visualization of surface texture and roughness. A secondary electron signal

can resolve surface structures down to the order of 10nm or better and the topographical image depends on how many of the SE actually reach the detector. Another method of producing an image in SEM is by the detection of BSEs, which provide both compositional and topographic information in the SEM. The backscattered electron imaging enables an image to be formed by material contrast and allows elemental mappings and the study of the distribution of these elements. Furthermore, since the BSEs have large energy, which prevents them from being absorbed by the sample, the region of the specimen from which BSEs are produced is considerably larger than it is for SEs. Thus, the lateral resolution of a BSE image is considerably worse (1.0µm) than it is for a SE image (10nm). On the other hand, with a fairly large width of escape depth, BSEs carry information about features that are deep beneath the surface [257], [258].

Additionally, another class of signals produced by the interaction of the primary electron beam with the specimen is the characteristic x-rays. The analysis of characteristic x-rays provides chemical information/composition of the sample. The x-ray signal determines the elemental composition of the sample, via detailed measurements for the elements of the periodic table, resulting in an EDS spectrum with the elemental peaks. Consequently, a combined SEM-EDS analysis provides a better understanding of phase identification and microchemical analysis [259], [260].

3.2.6. X-Ray Diffraction (XRD)

The phenomenon of x-radiation was discovered by Wilhelm Conrad Röntgen in 1895. Based on his research he understood that the X-rays are sufficiently energetic to penetrate solids and therefore posse small wavelengths in the angstrom range [261], [262]. Specifically, x-rays are relatively short wavelength (0.01-10nm), high energy electromagnetic radiation (100eV-100keV), where all electromagnetic radiation is characterized by either its energy E, wavelength λ (i.e., the distance between peaks) or its frequency v (the number of peaks which pass a point per second). The energy and wavelength can be measured through the following relationships [263].

$$\lambda = \frac{c}{v} \tag{3.7}$$

$$E = hv \tag{3.8}$$

where, c is the speed of light and h is Planck's constant.

- **Basic Principle**

XRD was first observed by Max von Laue in 1912 [262] and it can be employed to study the surface in bi- and multimetallic catalysts from the position and shape of diffraction peaks [81]. The examined sample is in the form of finely divided polycrystalline powder, but depending on the nature of the application, the sample can also be a thin film or bulk material [261], [262]. The XRD as the name implies is a diffraction pattern obtained by the interaction of X-rays (usually monochromatic) with a surface, which are statistically oriented in all possible crystallographic directions satisfying the Bragg condition:

$$n\lambda = 2d \sin\theta \tag{3.9}$$

where, n is an integer called the order of reflection, λ is the wavelength of x-rays, d is the characteristic spacing between the crystal planes of a given specimen and θ is the angle between the incident beam and the normal to the reflecting lattice plane [261]. By measuring the angles, θ, under which the constructively interfering x-rays leave the crystal, the interplanar spacings, d, of every single crystallographic phase can be determined [261], [262], [264].

- **Diffractometer**

The basic components of an X-ray diffractometer are the X-ray source or generator, goniometer, the specimen holder and the detector, which can be seen in Figure 3.15. The specimen should be grinded to reduce the particle size to 10–50µm, in order to ensure sufficient particles will occupy each of the many possible orientations equally. The sample is then cast out on a glass slide, resulting in small flat layer sample. It is noted that the thinner the layer, the more accurately the position of the peaks recorded. The specimen is held at the centre of a circle, termed the diffractometer circle, and the x-ray source, as well as the x-ray detector, are fixed on the circumference of that circle. When the detector is at zero, the source, the specimen, and the detector are in the same plane with the angle between source and detector 180° [262].

When analyzing a sample in a typical run, x-ray beams interact with the sample and a part of the beam is absorbed, refracted, scattered and diffracted by the plane of atoms in the sample. The specimen rotates at an angle θ, while the detector rotates an angle 2θ, which is popularly termed the ''θ-2θ'' method, that follows the condition of Bragg's law. This θ-2θ motion implies that the radius of the focusing circle is continually changing throughout a diffraction pattern scan. By changing the 2θ angle, the possible diffraction

peaks which can be produced from the differently oriented crystallites in the sample can be acquired. Depending on the applications, the system can be equipped with a scintillation counter, a proportional counter, a position-sensitive detector, or with a semiconductor detector [261]–[263].
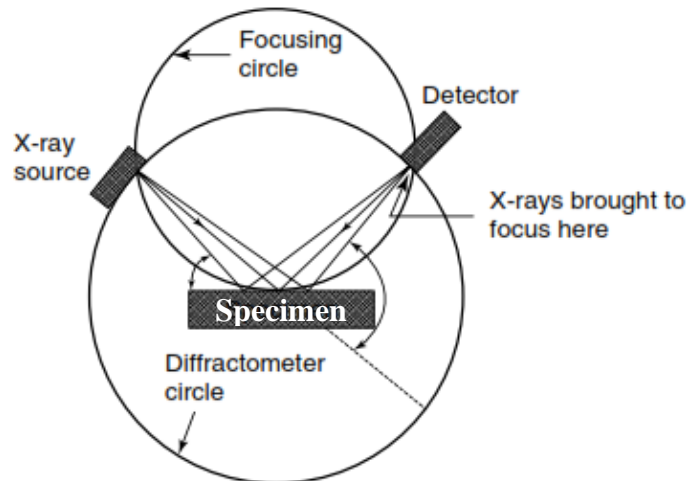
Figure 3.15: Schematic representation of the geometry of an X-ray diffractometer.

- **Data Interpretation**

The diffracted beam is detected to determine the crystallography of the sample and each mineral diffracts differently depending upon the atoms in the crystal lattice. The crystallographic measurements are used for surface and interface structure determination. The data acquisition is completed through a software that collects the data and produces the XRD pattern (peaks) based on calibrated original samples maintained by the International Centre for Diffraction Data (ICDD) [265]. Moreover, the software provides various analysis tools such as automatic phase identification, quantitative analysis, crystallite-size analysis, lattice constants refinement. Furthermore, the XRD technique helps to find the physio-chemical characteristics and crystallographic structure of the material, including chemical characterization, amount of crystallinity in the material, residual stress, and texture analysis [260], [262]. Figure 3.16 indicates an example of an XRD spectrum for a fresh Fe-ZSM5 catalyst, where the low-intensity diffraction lines at $37.65°$ and $40.85°$ (denoted by * in the figure) are attributed to traces of hematite (Fe_2O_3) particles [266].
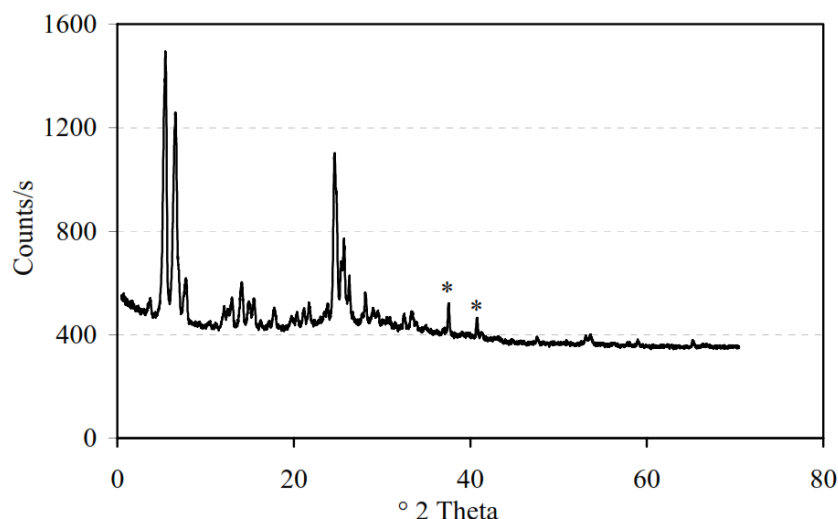
Figure 3.16: XRD of fresh Fe-ZSM5 catalyst.

3.2.7. Temperature Programmed Techniques

The most well-known temperature-programmed techniques are the temperature programmed desorption (TPD) and the temperature programmed surface reaction (TPSR).

3.2.7.1. Temperature Programmed Desorption (TPD)

A temperature programmed desorption (TPD) technique has been developed especially in the field of catalysis since it allows the study of the interaction between the reaction gases with the solid surfaces. This method can be useful in the extraction of very important information, such as the evaluation, identification and characterization of active sites on catalyst surfaces and the understanding of the mechanisms of catalytic reactions including adsorption, surface reaction and desorption. Moreover, it can be used in the study of binding energies, surface concentration and desorption kinetics [267], [268].

- **Basic Principle**

The TPD technique can generally be described as the measurement of the rate of desorption of adsorbed molecules, as a function of temperature. The gaseous molecules of interest are adsorbed at the surface of a catalyst, at a constant temperature, which is very often at ambient temperature but sometimes at sub-ambient or at elevated temperature. The events that take place at the surface of the solid substance are monitored, while the temperature of the investigated sample is increased linearly with time at constant rates ($\beta(t) = dT/dt$). The most common detector in modern implementations of TPD techniques is the quadrupole mass spectrometer (QMS). The application of QMS

enables simultaneous acquisition of single or multiple masses desorbed during heating. In this case, the detector enables the distinction between different species desorbed at the same time from the surface [267], [268].

- **Methodology**

The first steps prior to a TPD run is the appropriate pretreatment of the catalytic sample, to obtain a clean surface and to eliminate undesired contaminants. The pretreatment procedure depends on the characteristics of the investigated sample and the purpose of the TPD experiment. Then, the sample is exposed to the adsorbate gas (reaction or probe gas) and the adsorption is performed isothermally on the catalyst surface, at an appropriate temperature. Specifically, the solid surface is exposed to the adsorbate until saturation is achieved. Afterwards, the excess physiosorbed part of the adsorbed gas is removed from the surface, either by evacuation or by inert gas flow, usually He, Ar or N_2, at the same temperature of the saturation. This step is essential as the weakly chemisorbed gas and the gas present in the lines of the reactor need to be removed. The sample is therefore submitted to a linear heating rate under a carrier gas flow, where the residual chemisorbed adsorbate is desorbed in the carrier gas. The change of the desorbed gas from the surface is monitored with a downstream detector (MS) as a function of temperature, in order to establish the identity (qualitative studies) and amount (quantitative studies) of the evolved gas. It is noted that the whole procedure is performed in situ and the experimental conditions should be prepared in a standardized manner to obtain reproducible results [26], [267], [268].

As far as the quantitative measurements, the detector signal has to be properly calibrated in order to consider the results accurate. For that purpose, dilute gas streams of known concentrations are used. The gas streams can be passed through the empty reactor or bypass the reactor and simultaneously monitor their signal intensity. Furthermore, the intensity of the signal obtained as a result of the same gaseous species evolved from the TPD run can be considered as proportional to the value obtained from the known mixture. Once the detector is calibrated, the intensity of the detector signal can be given in concentration units and the measurement of evolved gas concentration becomes possible. The calibration of a detector signal enables the precise determination of both adsorbed and desorbed amounts. Regarding the adsorbed gas, its precise amount can be obtained by passing it bypass the reactor, and subsequently, through the sample (Figure 3.17a). Since the detector signal is properly calibrated, the monitoring of the two signals (bypass

and through the sample) provides the true adsorption amount of respective gas at a given temperature. The precise amount of desorbed gas can be attained from the surface under the TPD profile (Figure 3.17b) [267], [268].
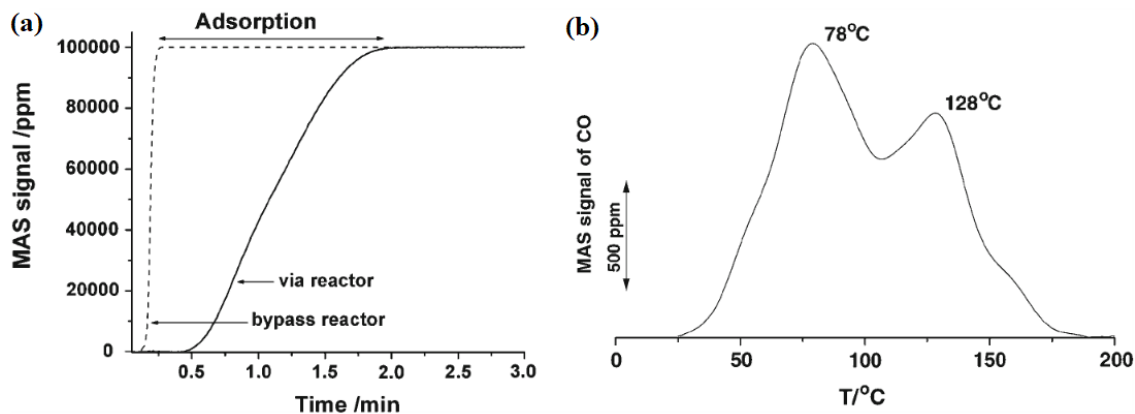
Figure 3.17: (a) Time dependence of adsorbate concentration upon exposing the solid sample, (b) example of a TPD profile (signal of detector versus temperature) [268].

- **Data Interpretation (TPD Profiles)**

The data obtained from a TPD run are presented as the variation of a detector signal intensity (y-axis) as a function of time (x-axis). Consequently, as the detector signal is proportional to the concentration of the species desorbed from the surface, y-axis values can be presented in terms of concentration (ppm). Also, since the heating ramp is based on a linear rate ($\beta(t)= dT/dt$), the x-axis can be presented in terms of temperature. The usual TPD profile indicates the gas evolution changes with the increased temperature, where the type of the gas desorbed and the peak temperatures are affected by the chemical form of the catalyst surface, the surface reactions, etc. Particularly, in the case of a catalytic system, many different chemical species can evaporate from the sample in the same temperature region [26], [267].

The desorption profile indicates two main classes of data. Initially, the area under the TPD profile, which is proportional to the amount of adsorbate originally adsorbed. If the limitations such as diffusion and/or readsorption can be neglected, then the TPD technique can be employed for determination of surface coverage. Moreover, from the TPD profile, the position of the peak maximum (along the temperature scale, T_{max}), is related to the activation energy for desorption. It is mentioned that the higher the value of the temperature of peak maximum is, the desorption is more difficult. This acts as an indication of stronger interaction between the adsorbate species and the active site on the

catalyst surface, i.e., increased strength of adsorbate binding to the surface [26], [268]. Also, as seen in the TPD spectrum of Figure 3.17b, the desorbed gas can produce more than one peaks, since very often there is more than one binding state for the adsorbate molecules on a surface, therefore significantly different activation energies for desorption. In the case of multiple peaks, the determination of T_{max} positions demands particular attention in the deconvolution procedure [268].

- **Temperature Programmed Desorption of Hydrogen (H$_2$-TPD)**

An important example of TPD experiments is the H$_2$-TPD, where the gas adsorbed on the catalytic surface is H$_2$ and it is desorbed at a linear heating rate. The H$_2$ molecule as mentioned before (subchapter 1.3.6) can be adsorbed dissociatively and therefore occupies two surface sites upon adsorption. This selective chemisorption uses the probe gas of H$_2$ which forms a strong chemical bond to the surface metal atoms of the supported crystallites, while it interacts negligibly with the support at the chosen temperatures and pressures. Regarding the Pt supported catalysts, the H$_2$ chemisorption that happens at 1 atm pressure in a plug flow reactor, which was used in this dissertation, can be shown in the following figure [269].

$$2Pt_{surface} + H_2 \implies 2Pt_{surface}H$$
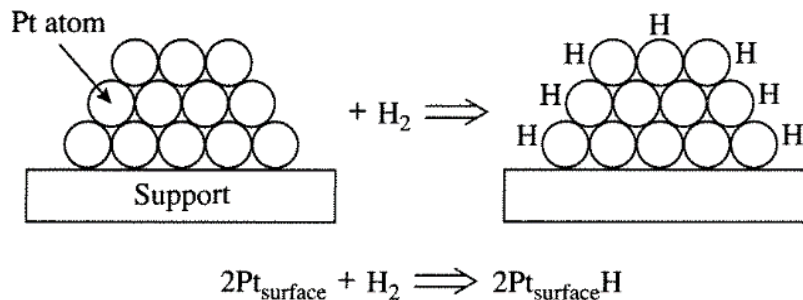
Figure 3.18: H$_2$ chemisorption on Pt supported catalysts.

In this case, the H$_2$ molecule dissociates into two hydrogen atoms and reacts with two active surface atoms of Pt. The surface area of active metals (Pt) dispersed on a support can be calculated through the TPD spectrum of a H$_2$-TPD run. Specifically, the area under the H$_2$-TPD profile indicates the saturated amount of adsorbed H$_2$ on the surface. Therefore, since the hydrogen atoms are chemisorbed on a 1:1 stoichiometry (H:Pt), the results can be used to calculate the amount of Pt crystallites exposed on the catalytic surface [28], [269]. Consequently, the number of adsorptive molecules (N_m) taken up by the active surface must be multiplied by a stoichiometry factor F_s, where in this case is equal to two (H/Pt$_s$ is 1:1), so as to arrive at the number of surface atoms N_s or "sites".

Mathematically, this translates to the following equation, where, N_s and N_m are determined per gram of sample [26], [28], [74].

$$N_s = F_s \cdot N_m = 2 \cdot N_m \qquad (3.10)$$

In addition, a variation of the normal H_2-TPD run, which uses a known mixture of H_2/He (usually 2%H_2/He) to adsorb on the active metal, is the introduction of Ar as a tracer gas in the gas stream, where 1%He is replaced with Ar (usually, 1mol% H_2/ 1mol% Ar/ 98mol% He). The outcome of the specific experiment is illustrated in Figure 3.19. The y-axis is expressed in terms of the dimensionless concentration, Z, which represents the fraction of the ultimate change (giving Z= 0) as a function of time. The Z term is calculated via the following equation.

$$Z\ (t) = \frac{y(t) - y_\infty}{y_0 - y_\infty} \qquad (3.11)$$

where the subscripts 0 and ∞ refer to the values of y (mole fraction) just before (t= 0) and long after the switch from pure He to the gas mixture (t $\rightarrow \infty$) [74].

The area between the H_2 curve and the y-axis represents the amount of hydrogen required to fill the piping (lines) and the reactor, known as the gas phase hold-up of the system, as well as the adsorbed amount on the surface of the catalyst. The area between the curve of Ar and the y-axis represents the amount of hydrogen required to fill the piping and the reactor (in the presence of the catalyst). Therefore, the difference in the areas of the two curves (shaded part of the graph) provides the amount of hydrogen adsorbed to the catalyst [33].
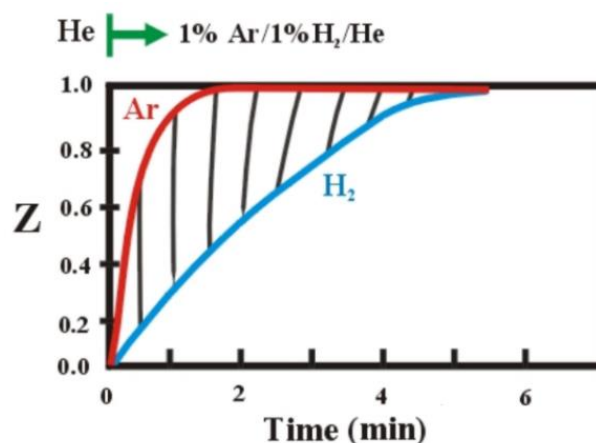
Figure 3.19: Dynamic response of the H_2 and Ar signals obtained in QMS during the change of gas stream from He to 1% H_2/ 1% Ar/ 98% He [33].

Using this data, the metal dispersion (D, %) of Pt, can thus be determined through equation 3.12. The dispersion of Pt can be estimated if the number of metal atoms exposed

at the surface is experimentally available (through H_2-TPD experiments) as well as the total number of metal atoms in a given amount of catalyst (usually via ICPMS experiments).

$$D \, (\%) = \frac{N_S}{N_T} \cdot 100 \tag{3.12}$$

where, N_S is the number of metal atoms exposed at the surface and N_T is the total number of metal atoms in a given amount of catalyst [29].

Furthermore, the dispersion is directly linked to the particle size and particle size distribution. Assuming reasonable model shapes for the metal particles (sphere), average particle sizes can be calculated from the chemisorption data. The average size of a spherical metal particle (d_{cr}) can be calculated through the following equations [33]:

$$a_m = 4\pi r_{cr}^2 \tag{3.13}$$

where, a_m is the area of a spherical metal particle (m^2) and r_{cr} is the radius of the metal crystallite (m).

$$N_T = \frac{m_{cr}}{AW} = \frac{\rho V_{cr}}{AW} = \frac{\rho \frac{4}{3}\pi r_{cr}^3}{AW} \tag{3.14}$$

where, m_{cr} is the mass of the metal crystallite (g), AW is the atomic weight of the metal (g/mol), and ρ is the density of the metal (g/m^3).

Therefore, by combining the previous equations 3.12-3.14, the relationship for the r_{cr} can be determined:

$$r_{cr} = \frac{3 \, AW N_S}{a_m \rho D} \tag{3.15}$$

The particle size of a metal crystallite is expressed in terms of the particle's diameter (d_{cr}). The d_{cr} (m) of a single metal particle (thereby N_s=1) is determined as the multiplication of the previous relationship by number two, combined with the Avogadro number ($N_a = 6.022 \times 10^{23}$ mol^{-1}).

$$d_{cr} = \frac{6 \, AW}{a_m \rho D N_a} \tag{3.16}$$

It is noted that the surface area of active metals dispersed on support deserves particular consideration since the metal surface area and particle size determine the catalytic properties of supported metal catalysts [27], [29].

3.2.7.2. Temperature Programmed Surface Reaction (TPSR)

Regarding the TPSR technique, it is a relatively simple and sensitive technique that finds application in both the field of catalysis and the field of surface chemistry. As the name states, a surface reaction takes place on a catalytic surface and after a temperature programmed process where the temperature increases under a non-inert gas atmosphere (eg, H_2, O_2, CO, He, etc.), on a solid that has adsorbed species on its surface, then in addition to desorption, a surface reaction is observed. The specific reaction occurs between the adsorbed species on the surface of the solid and the gas that is being used, either from the gas phase or after adsorption of the latter [270]. This technique can provide important mechanistic information for a reaction, such as determining the activity of various adsorbed species in a particular gas (e.g. H_2, O_2, etc.) and the monitoring of the surface reaction products is usually done using a mass spectrometer [33].

In a typical TPSR run, the examined catalyst follows usually the same pretreatment procedure as the one mentioned in the TPD experiments. The following step involves the introduction of a gas mixture on the catalytic surface until steady-state conditions are observed. Therefore, a particular gas is introduced at a constant flow on the sample and then a gradual linear increase of the temperature is applied on the solid in order to carry out the TPSR experiments. It is also noted that the whole procedure is performed in situ and the experimental conditions should be prepared in a standardized manner to obtain reproducible results [26], [267], [268]. The desorbed reaction products are continuously monitored via a MS and the TPSR spectra/profiles that arise can give qualitative and quantitative results of the evolved gas. The same procedure for interpreting the spectra is followed as the one mentioned in the TPD profiles.

3.2.8. Diffuse Reflectance Infrared Fourier Transform Spectroscopy (DRIFTS)

DRIFTS is the Diffuse Reflectance Infrared (IR) Fourier Transform Spectroscopy and is essentially a reflection sampling technique that makes use of the phenomenon of diffuse reflectance and is used primarily on powders and other solid samples. It is an in-situ method for the study of the nature and dynamics of surface intermediates contributing to a deeper understanding of the catalysis mechanism [271], [272]. One of the advantages of this technique is the very short preparation time that is needed for the examined samples (powder), as well as the small amount of sample required to produce a strong spectrum [271], [273].

- **Basic Principle**

In-situ DRIFTS studies are characterized by the use of infrared (IR) electromagnetic radiation. IR encompasses all the wavelengths between the visible and microwave regions of the electromagnetic spectrum from 700nm-1mm. In the context of infrared spectroscopy, the wavelength is measured in wavenumbers, which have the unit's cm^{-1}. The wavenumber is represented as $1/\lambda$, where λ is the wavelength (cm). In the case of IR, the portion of the electromagnetic (light) spectrum that represents the infrared radiation is 14000 to 10cm^{-1} [274]–[276].

During the experiment, the IR beam is directed onto a powder material which gives rise to scattering due to the rough surface of the sample. Depending on the nature of the sample, a variety of processes can occur, i.e., reflection, diffraction, refraction, transmission, and absorption. The scattered radiation distributes itself diffusely over the whole hemisphere above the sample as can be seen in Figure 3.20a [271], [272]. Also, the reflection on rough surfaces or powdered samples is sometimes subdivided into three different categories which are illustrated in Figure 3.20b. The first category is the regular, directed reflection of the incident radiation on the boundary layers parallel to the ''macroscopic'' surface of the sample or the powder. It is noted that analogous to a smooth surface, the angle of incidence and the angle of reflection are equal (specular reflection) and this type of isotropic reflection represents the regular proportion of the so-called Fresnel reflection. However, in DRIFTS experiments the main concern is aimed at the non-Fresnel reflection. Reflection can also occur at the boundary layers that are not oriented parallel to the ''macroscopic'' surfaces. The IR radiation penetrates the powder, interacts via various processes (e.g., transmission and reflection) with the sample material and finally escapes as diffuse radiation (Kubelka–Munk path) [272].
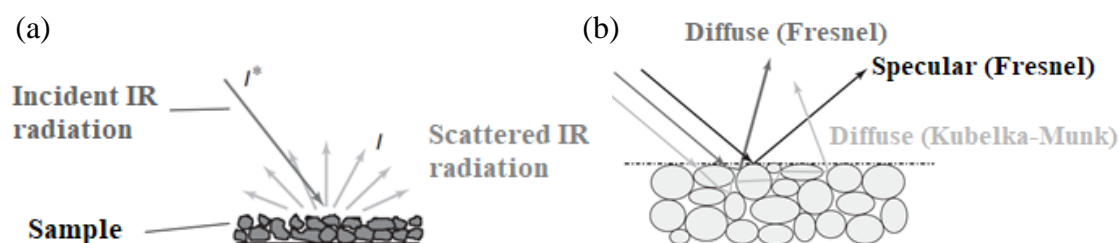
Figure 3.20: (a) Scattered radiation, (b) Scheme with different types of reflection.

The interpretation of the diffuse reflectance spectra is based on the phenomenological theory of Kubelka and Munk [277], who defined the so-called Kubelka-Munk (K-M)

function (equation 3.17), which relates the reflectance of a supposed infinitely thick layer $R\infty$ (2-3mm) to the ratio of the absorption coefficient (absorption module) k and the scattering coefficient (scattering module) S [272], [278].

$$f(R_\infty) = \frac{(1 - R_\infty)^2}{2R_\infty} = \frac{k}{S}$$
(3.17)

For most cases, the scattering module S is taken as constant and the absorption module k is proportional to the concentration c and the molar extinction coefficient ε, similar to the absorbance E, where $E = \varepsilon \cdot d \cdot c$, according to the Lambert-Beer equation [272].

$$k = ln(10) \cdot \varepsilon \cdot c = 2.303 \cdot \varepsilon \cdot c$$
(3.18)

If the previous two equations are combined then, the final K-M relationship is revealed:

$$K - M = 2.303 \cdot \varepsilon \cdot c/s$$
(3.19)

It is worth noting that the K-M function is only valid if both the sample and the reference material (KBr) fulfil the criterion of an infinitely thick layer, which means that the IR radiation should not penetrate to the bottom of the sample holder. Also, the IR penetration depth depends on the scattering and absorption properties of the sample and in the case of IR transparent powders, it can be several millimetres [271].

- **Experimental Set-Up**

The set-up for carrying out DRIFTS analyses is indicated in Figure 3.21. In-situ DRIFTS experiments require an appropriate optical system to direct a sufficiently high proportion of the diffusely reflected radiation to the detector. This special mirror arrangement is placed in the sample chamber of the spectrometer and it allows the IR radiation to focus on the sample and to collect a part of the emerging diffuse reflected radiation. The most common mirror system contains two ellipsoid mirrors (Fig. 3.21f), whose arrangement reminds one of the arm position of a mantis and thus led to the name ''Praying Mantis^{TM} system''. Furthermore, the IR beam is directed into the sample chamber and is focused on the sample via three mirrors and a part of the diffusely reflected radiation is again directed by the three mirrors to the exit of the sample chamber, which is connected to the detector. It is important to note that the mirrors are made from IR transparent materials, such as ZnSe (Fig. 3.21i) [272].

The solid powdered sample can be dispersed in a finely powdered KBr (as it does not absorb in the IR spectrum) and afterwards it is poured carefully into a sample holder

which is substituted with a hermetically sealed reactor chamber, as can be seen in Fig. 3.21j. During a DRIFTS run; the heterogeneous catalyst can be pretreated as it could be in a reactor by directing gas mixtures through the smooth powder and apply the appropriate temperature. Moreover, by combining the electrical heating of the sample holder, IR investigations can be carried out at elevated temperatures and in the presence of reaction gas, i.e., in situ [48], [271], [272].
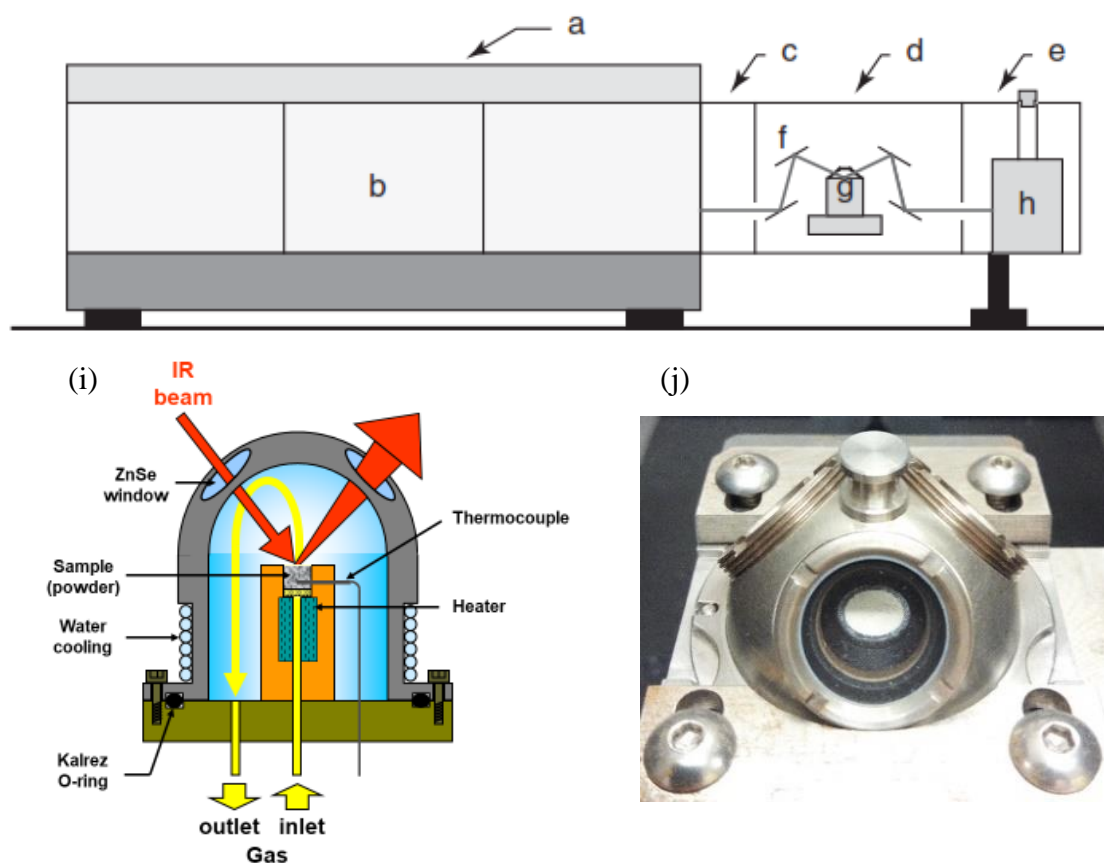
Figure 3.21: Scheme of a spectrometer with external accessories: (a) FTIR spectrometer, (b) internal sample chamber, (c) mirror chamber, (d) external sample chamber, (e) detector chamber, (f) mirror system, (g) DRIFTS measuring cell, (h) MCT-detector, (i) scheme of a typical DRIFTS measuring cell and (j) sample holder with three mirrors.

- **Data Interpretation (spectra)**

The analysis of DRIFTS spectra can generate useful information concerning the nature and concentrations of different types of intermediate species found on the surface of the sample during a specific range, such as 2500-800cm^{-1}. However, a real spectrum does not consist of infinitesimally narrow lines, but of bands whose intensities are ultimately distributed over a certain wavenumber range. After converting the transmittance to the absorbance spectra as shown in Figure 3.22, subtracting the background and smoothing the spectra, the resulting values can be analysed in order to interpret the results of the

DRIFTS run [272]. The final spectra are analysed with a software in order to apply the appropriate deconvolution in the coalesced peaks and identify afterwards the different intermediates species that were formed on the catalytic surface. The identification of the intermediate species needs a thorough literature review. For the purposes of this dissertation, the chemical structure and absorption bands (stretching mode) of all the NO_x species observed in these experiments were identified and evaluated based on the literature [60], [76]–[79] and other DRIFTS studies performed on similar catalysts [73], [75], [279], (see Table 1.2, subchapter 1.3.7.2.).
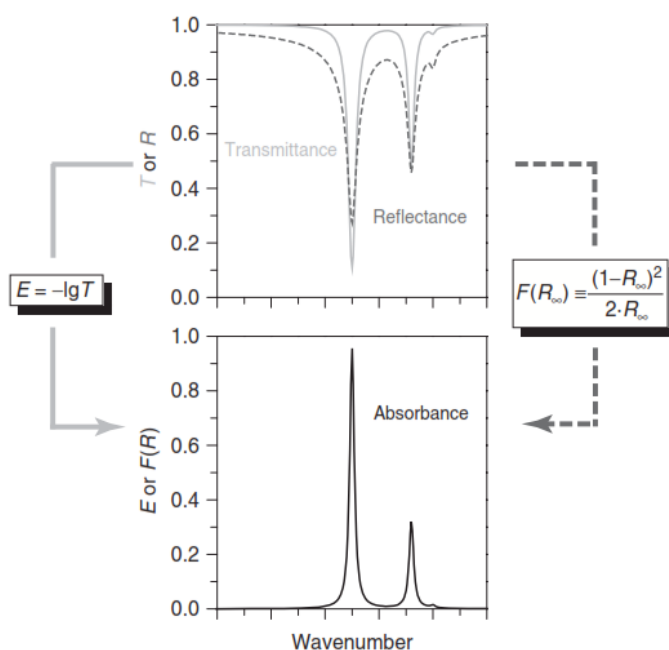
Figure 3.22: Solid path: formation of an absorption spectrum (absorbance) from a transmission spectrum using Lambert–Beer's law; dashed path: formation of an absorption spectrum from a reflectance spectrum using the Kubelka–Munk transformation [272].

3.2.9. Steady-State Isotopic Transient Kinetic Analysis (SSITKA)

The reaction rate, selectivity and stability with time-on-stream, i.e., the catalytic properties of a solid surface are determined by its chemical composition and structure on the atomic scale. Thus, a deep understanding of the microkinetics (detailed kinetics of each elementary reaction step) and mechanism occurring on the catalyst surface is required for the design and improvements of a catalyst's properties. This requirement includes the use of in-situ techniques, such as the SSITKA technique, for obtaining site reactivity and characterization data of the chemical composition and structure of the active surface catalytic sites and the accommodated adsorbed reaction intermediate species [280].

The technique known as SSITKA stands for ''Steady-State Isotopic Transient Kinetic Analysis'' and is a powerful technique for the kinetic and mechanistic study of heterogeneous catalytic reactions [27], [29], [281]. The specific technique was originally developed by Happel, Bennet and Biloen [282]–[284] and has been used in a number of studies to determine in-situ kinetic information about the reaction mechanism and the catalyst-surface reaction intermediates. Furthermore, the SSITKA method is based on isotope transfer dynamics associated with the active reaction intermediates, providing therefore in situ information about the surface concentrations of active surface reaction intermediates, as well as rate constants of elementary steps under complex steady-state catalytic reaction conditions. In addition, as an effective catalyst may have many different types of active surface species and each may be capable of catalysing either a single reaction or a whole range of related reactions, then the identification of the reaction intermediates, both the truly active and inactive (spectator) species, is an important step when evaluating a catalyst [27], [280].

- **Basic Principle**

The basic principle in a SSITKA experiment is that it involves a switch in the isotopic composition of the gas flowing over a catalyst. The isotopes are defined as ''elements having the same atomic number but different atomic weight and are divided into two categories; radioactive and stable isotopes''. Consequently, since their chemical properties are practically identical, it is possible to label particular molecules by isotopes and follow them through a sequence of chemical or physical changes [285]. Moreover, during a catalytic reaction, an atom in a certain position or group is isotopically labelled, for instance, an X-H bond is replaced by X-D, whether a kinetic isotope effect occurs or not. The outcome of this reaction provides information on whether weakening or rupture of the X-H bond is involved in a kinetically significant elementary step [29], [286].

In a SSITKA run, the isotopic switch happens without any (significant) all-over change in the gas-phase composition and it can be done in a system in which it is possible to switch from one isotope under investigation to the other while not disturbing the other flows. Furthermore, the technique is based on the detection of isotopic labels in the reactor effluent species versus time, following a step change in the isotopic labelling of one of the reactants in the reactor feed, such as switching $^{16}O_2$ flow to $^{18}O_2$ flow. It is noted that reactant and product concentrations and flow rates remain undisturbed during the step

change and in the absence of isotopic mass effects, steady-state conditions are maintained under isotopic-transient operation [27], [29].

Regarding the isotopic change, the most frequently used isotopes are ^{2}H, ^{13}C, ^{14}C, and ^{18}O. Their use can greatly aid the elucidation of catalytic mechanisms. For instance, deuterium and ^{13}C labelling can be used to determine which carbon atoms end up where or whether a reaction is inter- or intramolecular. It is noted that ever since H. S. Taylor used deuterium isotope (^{2}H) to investigate the reactions of hydrocarbons at surfaces, isotope substitution has remained a valuable approach for the catalyst scientist [270], [287]. Also, ^{18}O labelling has been applied to elucidate the relative rates of CO and CO_2 in methanol synthesis [29], [288]. Furthermore, ^{15}NO isotope can be used in order to gain significant information about the concentration of the adsorbed active intermediate NO_x species formed during reaction conditions [74], [289].

Generally, transient kinetic methods allow for assessment of the reactivity and the abundance of catalyst-bound intermediates and although catalysis can be understood through steady-state experiments, it seems clear that transient experiments will usually furnish much additional information. It is noted that on the contrary to other transient experiments, SSITKA experiments can provide steady-state kinetic and mechanistic information, including concentrations of different types of adsorbed reaction intermediates, coverages, surface lifetimes, site heterogeneity, activity distributions, and identification of possible mechanisms [29], [281], [284].

- **Combined SSITKA-DRIFTS**

Steady-state isotopic transient kinetic analysis coupled with DRIFTS is a powerful tool to investigate key mechanistic and kinetic aspects of a heterogeneous catalytic reaction [290]. Moreover, when SSITKA studies are coupled with in situ IR analysis, their combination allows the determination of rate coefficients, elementary rate constants, surface coverages, and residence times of surface intermediates [273]. Isotope switches have been utilized within situ IR spectroscopy in order to discriminate between side products and reaction intermediates [284]. For instance, SSITKA-DRIFTS studies were used to determine the chemical structure of the active NO_x species participating in the nitrogen reaction path of the H$_2$-SCR of NO [73], [291]. Figure 3.23 is an example of the combined studies, where after the isotopic switch of ^{14}NO to ^{15}NO, the IR bands shifted

to lower wavenumbers indicating the active adsorbed intermediate NO_x species formed during the $NO/H_2/O_2$ reaction that eventually lead to N_2 and N_2O gas products [73].

The SSITKA-DRIFTS studies that were performed during this dissertation involved the same experimental set-up that was used for the DRIFTS experiments, with the addition of a stable isotopic ^{15}NO gas mixture. Careful band deconvolution was also performed in order to obtain the wavenumber peak and therefore identify any IR band shifts after the isotopic switch.
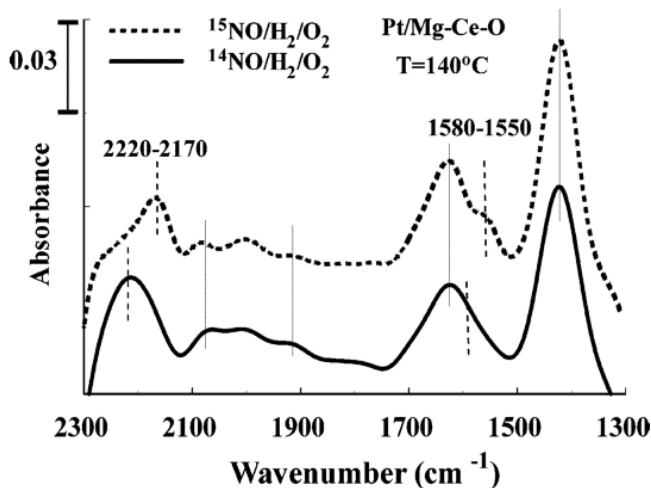
Figure 3.23: In situ DRIFTS spectra recorded over the 0.1 wt % Pt/ MgO-CeO$_2$ catalyst after 30 min of $^{14}NO/H_2/O_2/Ar$ reaction (-) at 140°C, and after 30 min following the isotopic switch $^{14}NO/H_2/O_2/Ar \rightarrow {}^{15}NO/H_2/O_2/Ar$ (---) at 140°C [73].

CHAPTER 4: EXPERIMENTAL PROCEDURE

4.1. Catalysts Preparation

The supported-Pt catalysts shown in Table 4.1 were prepared by three different methods; by the conventional wet impregnation method (WI-H_2O), by a modified wet impregnation method (ink formula, IF) and by novel inkjet printing (IJP) using two different printing devices.

Table 4.1: Prepared catalysts within the present work.

	Catalyst	Methods		Code
1		Wet	H_2O	WI
2	0.1 wt%	Impregnation	Ink formula	IF
3	Pt/Al$_2$O$_3$	Inkjet Printing	Epson	IJP-Epson
4			Dimatix Material Printer	IJP-DMP
5	0.1 wt%	Wet	H_2O	WI
6	Pt/MgO-	Impregnation	Ink formula	IF
7	CeO$_2$	Inkjet Printing	Dimatix Material Printer	IJP-DMP

4.1.1. Wet Impregnation (WI)

In order to prepare the supported catalysts, $Pt(C_5H_7O_2)_2$ (Aldrich) was used as a metal precursor of Pt. Nitrate metal precursors ($Al(NO_3)_3.9H_2O$, $Mg(NO_3)_2.6H_2O$, $Ce(NO_3)_3.6H_2O$), were supplied by BDH chemicals and Aldrich and were used in this method of synthesis due to their good solubility in water. 0.1 wt% Pt/Al$_2$O$_3$ (WI) and 0.1 wt% Pt/MgO-CeO$_2$ (WI) catalysts were prepared by placing the appropriate amounts of the solids in beakers containing de-ionized water and mixed thoroughly by stirring at 65°C. After water evaporation, the resulting solids were dried at 120°C and then the catalyst samples were calcined in air at 500°C for 2h, prior to storage for further use. The main objective of calcination is to stabilize the physical and chemical properties of the catalyst.

Also, the same procedure was followed in order to prepare 0.1 wt% Pt/Al$_2$O$_3$ (WI-isopropanol) and 0.1 wt% Pt/MgO-CeO$_2$ (WI-isopropanol) with wet impregnation but instead of de-ionized water, isopropanol was used, and the stirring was held at 55°C, following drying at 120°C and calcination in air at 600°C. These catalysts provided the lowest catalytic performance and therefore no further evaluation was performed.

Moreover, 0.1 wt% Pt/Al_2O_3 (IF) and 0.1 wt% $Pt/MgO-CeO_2$ (IF) catalysts were prepared by a modified wet impregnation method using the "ink formula", IF, suggested by Liu et al. [187], [208]. In the case of the latter catalysts, the following compounds were used to optimize the properties of the ink: 5mmole of metal precursors ($Al(NO_3)_3.9H_2O$, $Mg(NO_3)_2.6H_2O$, $Ce(NO_3)_3.6H_2O$), 0.8gr of Pluronic-F127 polymer, 30ml isopropanol, 20mmole acetic acid and 6mmole nitric acid. The liquid mixture was then stirred at 50-55°C and afterwards, the same procedure was followed as with the WI method. It must be mentioned that these catalysts were synthesized solely for the purposes of this dissertation and up to now, they have never been used for nitric oxide reduction.

Initially, all catalysts were calcined in air at 600°C for 2h and similarly oxidized in 20%O_2/He gas mixture during the pretreatment of the catalysts. However, these catalysts presented low catalytic performance and therefore the calcination and oxidation temperatures were lowered to 500°C for the newly prepared catalysts, in order to avoid sintering of the metal phase.

4.1.2. Inkjet Printing (IJP)

Inkjet printing method was implemented to produce three catalysts in order to better control (regulate) the catalyst's particle size distribution and nano-scale structure, towards an optimum interaction between various crystal phases of the catalyst. Inkjet printing (IJP) is regarded as one of the most promising techniques for the creation of functional metal oxides on various substrates because it can have an automatically controlled printing pattern with precise and flexible droplet volumes, as well as it provides a homogeneous mix at the molecular level in the liquid state [186]. For the first time ever, the catalyst of 0.1 wt% Pt/Al_2O_3 was prepared by novel IJP using two different printers; the custom-modified Epson L800 printer and the Dimatix Material Printer-2850. As for the 0.1 wt% $Pt/MgO-CeO_2$ catalyst, it was synthesized with the latter printer.

Initially, the Pt/Al_2O_3 catalyst was prepared with the Epson-L800 printer. Figure 4.1, presents the printer as it was delivered from the manufacturing company and which after several modifications resulted in the printing apparatus that successfully created the first printed catalyst for NO reduction, even though the specific printer is definitely not designed for material printing. It is worth mentioning that the modified printer was mainly comprised by an actuator, three sensors (stepper home, home position and print position sensors) and a controller (Fig. 4.1, lower image).
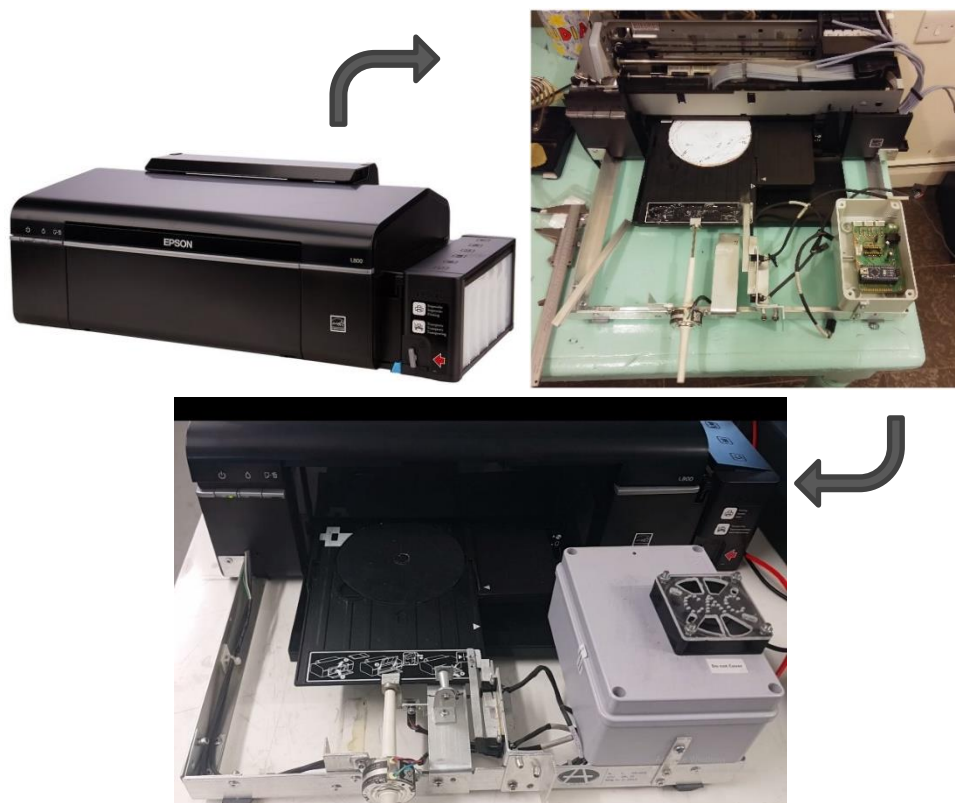
Figure 4.1: Modified Epson L800 printer apparatus.

Moreover, "CATAprint®" software was specially designed to continuously monitor the printing process and allowing maximum control of any occurring errors. The software can receive information from the external hardware and send print commands to the default printer connected on the computer. The software allowed to pause/resume the process, add/delete layers or delay the following printing layer. CATAprint was developed to meet the exact requirements of multiple layer catalyst printing. Its structure is divided into 5 sections; Connection and Feedback Status, Layers Selection, Printing Management, Printing Process and Troubleshooting (hidden), as can be seen in Figure 4.2. It must be noted that the printer modification and software development was completed by Andreou et al. [179], [180].

As far as the synthesis of the catalyst, it was achieved with the formulation of two different "inks", one containing the support of the catalyst (5mmole $Al(NO_3)_3.9H_2O$) and the other the appropriate solution so as to yield the desired loading of 0.1 wt% Pt. Each ink also contained four more compounds (Pluronic-F127 polymer, isopropanol, acetic and nitric acids). The inks were then stirred for 2-3h in order to become transparent and afterwards they were transferred to the Epson ink bottles. The original ink-jet printer driver uses multi-level colour technology (black, yellow, magenta, cyan, light magenta

and light cyan cartridges) in order to increase the quality of professional colour prints. The stable precursor "inks" were transferred into the empty ink cartridges, where the support ink (Al_2O_3) was placed in magenta and light magenta cartridges and the active metal (Pt) in cyan and light cyan cartridges. The last two cartridges (black, yellow) were filled with isopropanol.
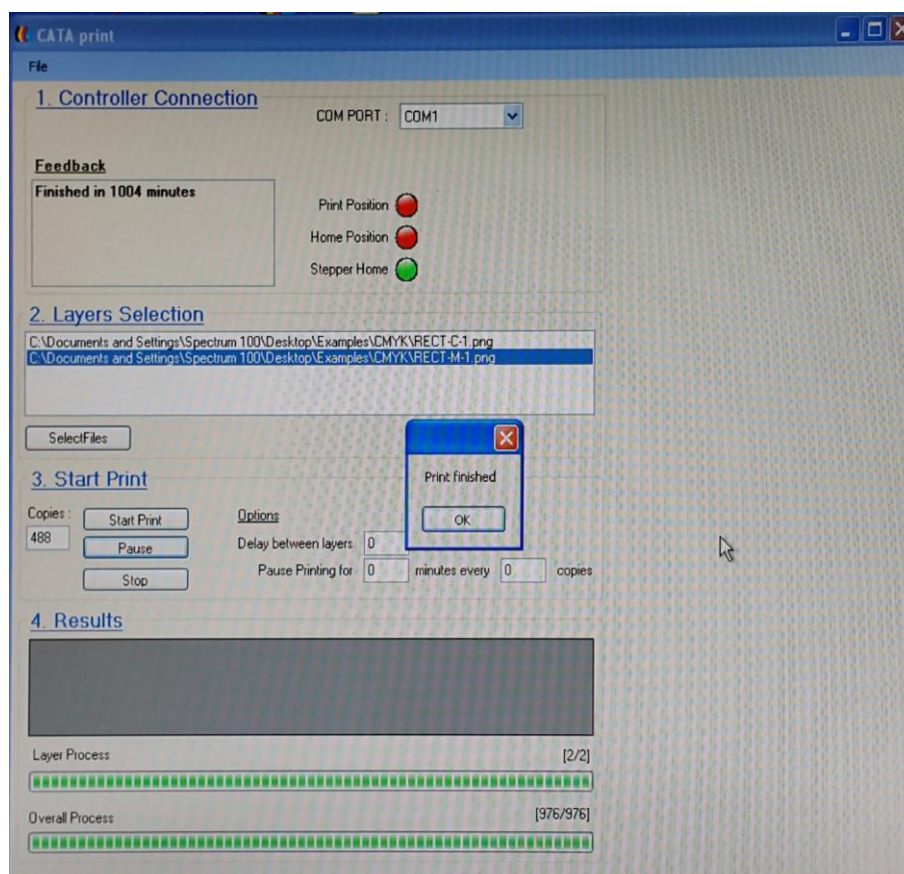
Figure 4.2: CATAprint software after finishing printing. The CATAprint software was developed exclusively for the needs of the present work.

Many colour images were designed until deciding on the final two sets, as the inner and outer diameter of the CD played an important role on the available dimensions of the printing prototype. The coloured images were produced using single colours; magenta for the support and cyan for the active phase. These images, which contained the printing prototype of magenta and cyan colour for A_2O_3 and Pt ink respectively, were selected with the help of the software. Once the number of copies (layers) was entered in the software the printing process was initiated. The droplets (1.5pl) were then ejected onto a thin stainless-steel tray (making use of the CD/DVD printing ability of the printer) and they were deposited drop by overlapping drop, and, as the carrier solvent evaporated, drops coalesced to form layers. Then, layer by layer a three-dimensional material was

produced. It is of utmost importance that the printed layers were alternated, as seen in Figure 4.3, so as to achieve uniform topography and a larger interface between the support and the metal.
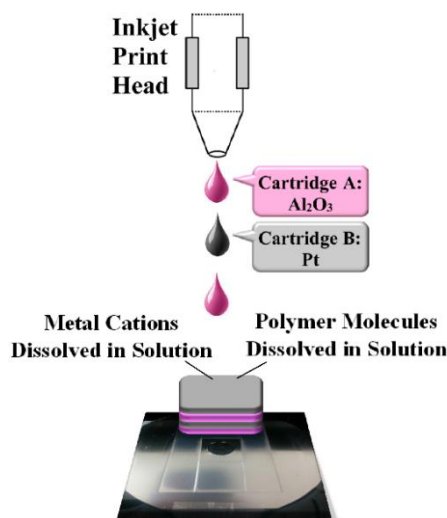
Figure 4.3: Layer-by-layer printing through the custom-designed Epson L800 inkjet printer.

Two batches of 0.1 wt% Pt/Al_2O_3 catalysts were printed; the first one was used for SEM analysis and the second one for catalytic and mechanistic studies. The first batch of catalyst had $\approx 7cm^2$ printed area and was consisted of 12266 layers (Fig 4.4a), whereas the final catalyst had $45cm^2$ printed area (543% increase in the available printing area) and ≈ 1700 layers (Fig 4.4b). After printing was completed, the catalysts were collected carefully, dried at 120^oC and calcined in air at 500^oC for 2h to remove the block-copolymer surfactants. resulting in ~0.1gr final printed solid (Fig 4.4b). Also, after the synthesis of the catalyst the printer head was cleaned several times with isopropanol (non-aqueous solvents) for avoiding clogging and erosion.
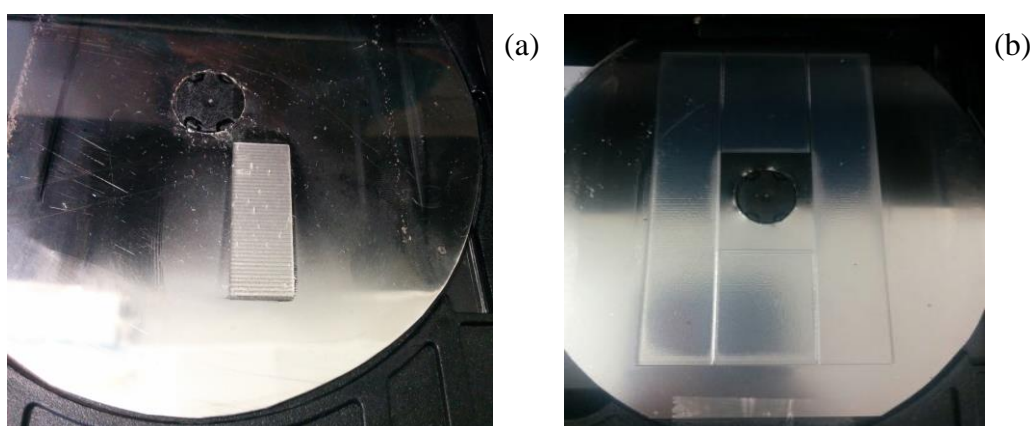
Figure 4.4: Samples (a, b) of the printed 0.1 wt% Pt/Al_2O_3 catalyst with Epson-L800.

Since Epson L800 printer endured extensive modifications and multiple repairs (until it was no longer functioning), a new Dimatix Materials Printer (DMP-2850) was employed

to continue this innovative work (Figure 4.5). This apparatus contains only one cartridge; therefore, the ink formula was prepared containing both the support and the active metal of the catalyst. Due to the smaller size of the fluid module, maximum capacity of 1.5ml compared to 70ml of the previous printer, some adjustments to the ink formula were made in order to acquire 0.1wt% Pt loading.

Figure 4.5: The Dimatix Material Printer (DMP-2850).

Various experiments were performed so as to decide the composition of the ink formula. Initially, the same composition that was used for the Epson printer was tested where the ink formula was comprised of the metal species ($Al(NO_3)_3.9H_2O$), the metal precursor ($Pt(C_5H_7O_2)_2$) diluted in isopropanol, Pluronic-F127 polymer, isopropanol, acetic acid and nitric acid. However, this composition did not work well as the pH of the formula was lower than the optimum (according to the manufacturer of the device) and the ink started drying at the nozzles, leaving a crystal-like residue and thereby, clogging the nozzles severely until they no longer jetted properly. Further tests with the ink composition were attempted, where the ink formula was diluted with either ethanol or isopropanol. However, these tests did not yield to acceptable results.

The final ink formula that was used for the examined solids was the same as the conventional wet impregnation method using de-ionized water as a solvent, i.e., $Al(NO_3)_3.9H_2O$ for the 0.1 wt% Pt/Al_2O_3 catalyst and $Mg(NO_3)_2.6H_2O$ and $Ce(NO_3)_3.6H_2O$ for the 0.1 wt% $Pt/MgO-CeO_2$ catalyst, using $Pt(C_5H_7O_2)_2$ as a Pt precursor for both catalysts. Before the inks were carefully transferred in the fluid module

the following steps took place to achieve the ink's optimum performance. The ink formulations were stirred for 2h in order to be transparent (complete dissolution of precursors) and afterwards were degassed for 30 minutes by using an ultrasonic bath to remove any dissolved gas which might inhibit jetting. Then, the pH of the fluid was measured, in order to ensure that it was within the optimum range (pH= 4-9), which was usually around 6. The density of the ink was also considered, where it is beneficial for the printing procedure if the specific gravity (SG), of the ink formulation is greater than one ($SG_{inks} > 1.06$-1.12). Finally, the fluid was filtered with Whatman HPLC certified syringe filters, with 0.2μm pore size as suggested by the manual of DMP-2850 [183]. The fluid was carefully filtered (1.5ml) and inserted in the fluid module and then it was attached to the jetting module (JM). It was really important to let the cartridge set for at least 30 minutes with the nozzles facing down, as well as, having a clean cleaning pad so that the pad adsorbed any excess fluid from the nozzle plate.

Once the cartridge was inserted into the cartridge holder, purging was initiated, where pressure was applied to the cartridge; to push fluid out of the nozzle and remove any trapped air, as well as prime the nozzles. Afterwards, the Drop Watcher (camera) feature of the Dimatix Drop Manager Software was enabled, where direct viewing of the 16 jetting nozzles (Figure 4.6), and the faceplate surrounding the nozzles was achieved, as well as the actual jetting of the fluid (1pl droplets). Then, calibration of the nozzles was performed, which automatically controls the stage motion and keeps the nozzles in line.
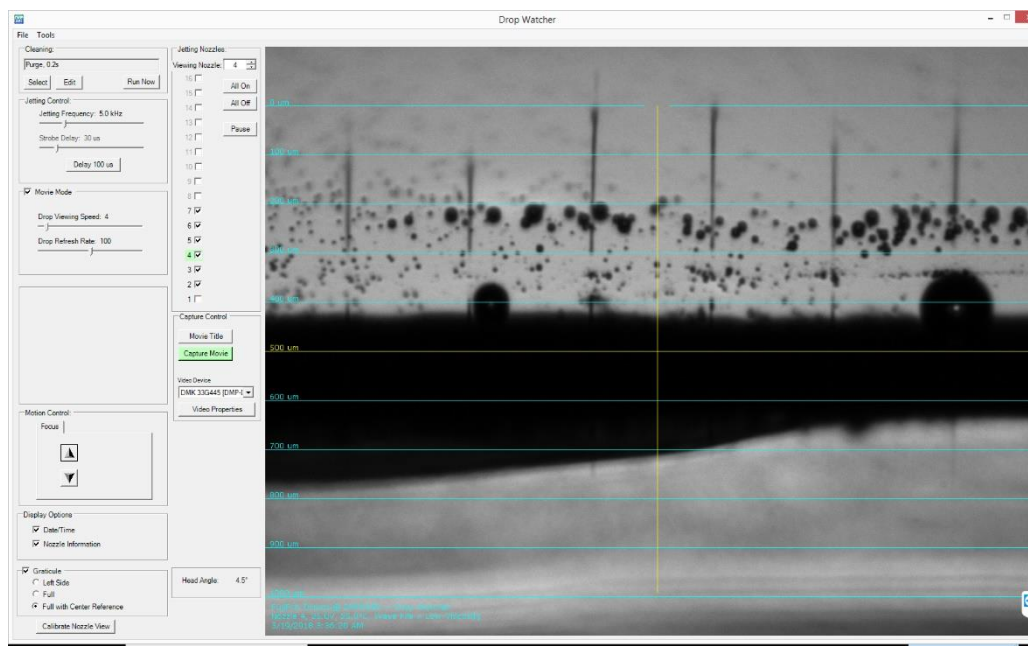
Figure 4.6: Drop Watcher image showing the jetting process.

After the evaluation of the ink and the jetting module, the following step was to select the pattern from the many options offered by the software. As can be seen in Figure 4.7, the pattern selected within the present work was the ''Dimatix 1mm Hatch'', for both catalysts (Pt/Al$_2$O$_3$ and Pt/MgO-CeO$_2$). The selected drop spacing, which is the centre to centre distance from one drop to the next in the X and Y position to create the pattern, was 20μm since it was proven to give good printing results. Moreover, the print cartridge was properly aligned at a head angle of 4.5° according to the selected pattern (suggested by the manufacturer).
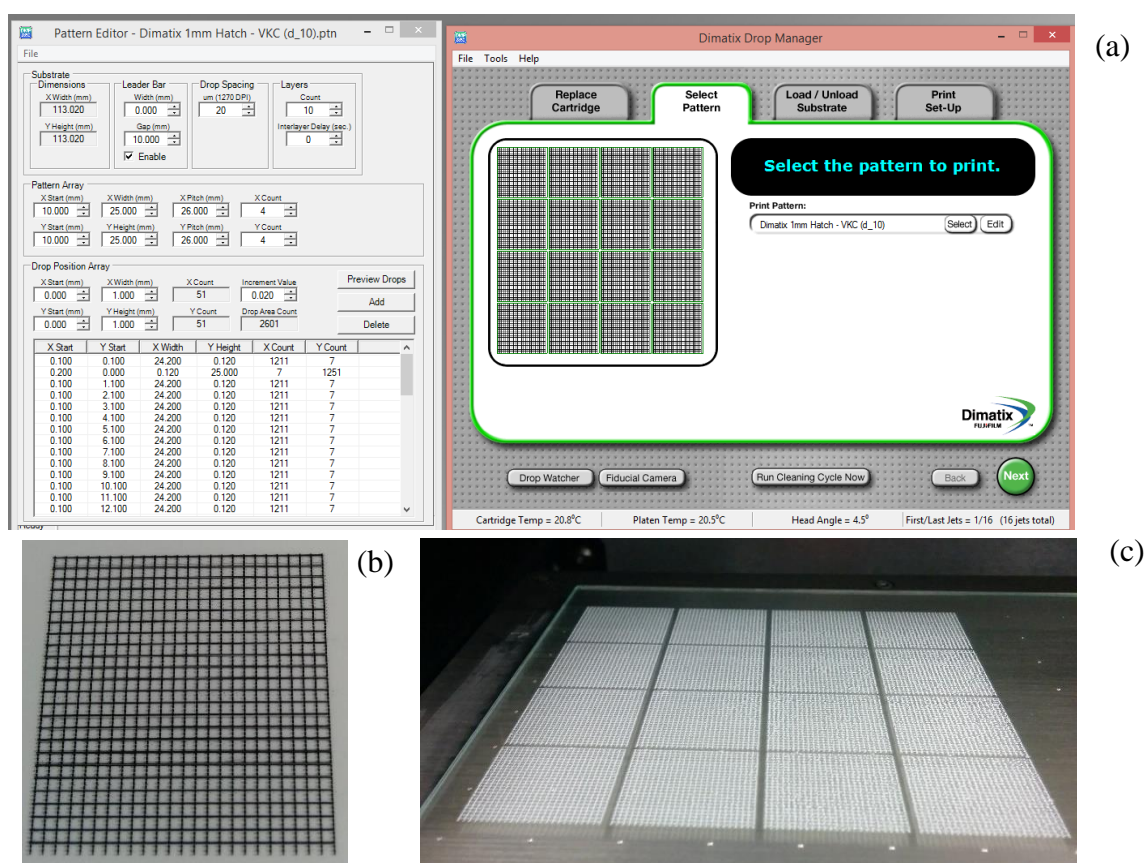
Figure 4.7: (a) Print Pattern, (b) printed Dimatix Model Fluid sample and (c) printed 0.1 wt% Pt/Al$_2$O$_3$ catalyst.

Furthermore, the cartridge settings were modified to optimize the printing procedure. During the printing process, if any nozzle did not work properly, it was eliminated through the cartridge settings. Also, the cleaning cycle (spit, purge, blot) was set at the start and during the printing process (e.g. every 20 bands). It was crucial to make sure that the cleaning pad was not saturated or clogged during the printing process to ensure good removal of the fluid from the nozzles after purging or spitting. A feature that did not exist in the previous printer and was one of the initial issues that had to be solved,

was the setting of the distance of the printhead above the substrate. The cartridge print height was automatically set to 1mm. Finally, the clear glass substrate was loaded on the platen and vacuum was enabled to keep the substrate completely still. The thickness of the glass substrate was set at 3000μm and after a number of prints, it was increased by 100μm in order to ensure that the printhead would not directly contact the substrate. The cartridge temperature was not modified. However, the temperature of the platen was maintained at 35°C and that achieved a first drying step.

The first printed catalyst was 0.1 wt% Pt/Al_2O_3, a picture of which can be seen in Figure 4.7c. It was consisted of 550 layers and used 12 JM, whereas the second printed catalyst, with the mixed substrate of $MgO-CeO_2$, had 10 available JM and lasted for 650 layers. The two catalysts had the same printed area (113.02mm x 113.02mm= 127.74cm^2) and were also evaluated through the Fiducial camera which can be seen in Figure 4.8. After printing was completed, the catalysts were scraped carefully, transferred in a crucible and calcined in air at 500°C for 2h. Since the platen was at 35°C, the catalysts were already dried. The final catalysts resulted in 0.28gr for the Pt/Al_2O_3 and 0.16gr for the $Pt/MgO-CeO_2$.
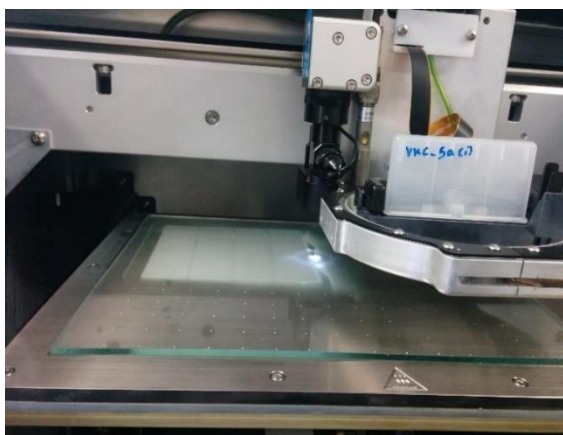
Figure 4.8: Evaluating catalyst samples with the Fiducial Camera.

4.2. Catalysts Characterization

4.2.1. Inductively Coupled Plasma Mass Spectrometry (ICPMS)

Inductively Coupled Plasma Mass Spectrometry, ICP-MS, was used for elemental determination of Pt in the examined catalysts. A Thermo Scientific XSERIES 2 Quadrupole Inductively Coupled Plasma Mass Spectrometer was used to conduct the experiments.

All catalysts that were produced through the wet impregnation method using H_2O or ink formula, as well as the IJP Pt/Al_2O_3 catalyst that was printed by DMP, were analysed by ICPMS. Sample preparation included acid digestion of 40mg of each catalyst in 100ml of a mixture of acids; HNO_3 (72ml, Riedel-deHaen), HCl (24ml, Riedel-deHaen) and HF (4ml, Scharlau) in a spherical flask. During digestion, the spherical flask was sonicated to ensure particle solubility and held for at least 72h under continuous heating at 55°C with reflux. Furthermore, when the samples were ready, the proper dilutions with 2% HNO_3 were made in order to end up with a concentration within the analytical range of the instrument.

Also, a series (0-25-50-75-100ppb) of Pt standard samples, were prepared and used for the calibration curve of Pt (external standardization). The latter samples were prepared with specific calibration ICPMS standards. All the samples (catalysts and standards) were filtered with a 0.2μm pore filter and an internal standard solution (Indium standard for ICP) was added for internal standardization (50ppb internal standard in 100ml sample). The instrument's cooling system was activated and Argon gas (99.999%) was used throughout the procedure. In addition, once the instrument was activated an autotune was performed, following a performance check for checking the ICPMS ability to identify a variety of elements and afterwards the calibration standards were run. Then, the examined samples were analyzed having also quality control samples before and after the catalytic samples, where the quality control was one of the calibration standard samples. Finally, acquired data were processed with the software "Thermo PlasmaLab".

4.2.2. Surface Area and Pore Size Analysis

The specific surface area (m^2/g) and the total pore volume (cm^3/g) of the metal oxide supports of Al_2O_3 and $MgO-CeO_2$ catalysts were checked by N_2 adsorption at 77K (Brunauer-Emmett-Teller (BET) method) using a multi-point Micromeritics Gemini V System (Gemini Model: 2380). BET experiments were conducted on the four catalysts (0.5gr) that were prepared with the wet impregnation method (WI and IF), as well as, on a reference material of silica-alumina sample in order to ensure that the Micromeritics Gemini V System was working properly. Unfortunately, BET analysis was not conducted on the printed catalysts since the catalyst quantity produced by inkjet printing was not enough for the performance of a reliable BET measurement. Prior to the experiments, the samples were pretreated in a flowing-gas degassing unit (SmartPrep™ 065) which removes adsorbed contaminants (especially water) obtained from atmospheric exposure

before the analysis. The degas conditions included flowing N_2 gas at 180ºC (453K) for 12h (overnight). After degassing, each sample was weighed again to calculate the remaining mass of the catalyst and then the sample tube was attached to the system. Throughout the experiment, the samples were kept at 77K using a container filled with liquid nitrogen and they were analyzed under vacuum. Then, the catalysts were admitted to N_2 gas at a series of precisely controlled pressures.

The starting relative pressure was $0.01P/P_o$ and by linear progression (8 points) the pressure increased until the final relative pressure was $0.35P/P_o$, (where: P is the measured pressure of the gas and P_o is the saturated vapour pressure of the N_2 gas at the temperature of adsorption). During this pressure region (P/P_o) the linearity of the BET equation (equation 3.5, subchapter 3.2.4) is applied. The amount of nitrogen molecules adsorbed on the sample is measured as a function of N_2 pressure ratio over the sample [255]. The equipment automatically calculates the BET-surface area and the C-constants for the samples using the multipoint BET method on 8 points of the adsorption isotherm near monolayer coverage.

4.2.3. Scanning Electron Microscopy (SEM)

In order to examine the surface morphology of the catalysts, scanning electron microscopy (SEM) studies were performed at "The Biomechanics and Living System Analysis laboratory" of the Department of Mechanical Engineering and Materials Science and Engineering of CUT. The experiments were carried out with a Quanta 200 SEM (FEI, Hillsboro, Oregon, USA), equipped with Energy Dispersive X-ray Spectroscopy (EDS). The Quanta 200 SEM is equipped with standard SE (Secondary Electron) and BSE (Back-Scatter Electron) detectors.

SEM studies, using SE and BSE, were performed on all fresh solid catalysts after calcination in air at 500ºC for 2h and some on used samples after conducting catalytic and transient experiments (e.g. IF Pt/Al_2O_3 and IJP-DMP $Pt/MgO-CeO_2$ catalysts). The powder samples were deposited on the SEM stubs and then inserted in the specimen chamber, which is kept under vacuum. Since all the substrates are conductive, it was not required to coat the samples with a thin layer of a conductive material such as Au (ion sputtering). However, the IF $Pt/MgO-CeO_2$ catalyst was analysed with and without Au sputtering of 1.5nm thickness since the sample was very soft (foamy) and the SEM images were not representative. Moreover, choosing the right accelerating voltage is critical for

obtaining a good clear image. Sometimes the most suitable voltage level depends mostly on the type of material being examined. Most imaging was done using a voltage of 20kV and 30kV.

The electron microscope images were captured using different magnification (such as 100000, 50000, 24000, 6000, 2000, 200) and show the sample's surface topography, properties, and composition. Also, the exposure time of each sample point in the electron beam was 1-10μsec depending on the sample. If the sample was exposed for a long period of time (e.g. 10μs), the image was clear, but then the sample was deformed by the beam, and the imaging was not usable (acceptable). Usually, an exposure time of 3μs gave the best possible SEM images. It should be mentioned that specific areas of interest in the catalysts were selected in the SEM image at the same magnification (x6000) and then EDS was activated for all the samples in order to identify the surface chemical composition of the sample (SEM-EDX images).

4.2.4. X-Ray Diffraction (XRD)

X-Ray Diffraction (XRD) analysis was used to probe the presence or difference in the presence of the crystalline phases of MgO, CeO, CeO_2, Ce_2O_3 within two catalyst samples. Specifically, the catalysts chosen for this analysis were the 0.1 wt% Pt/MgO-CeO_2 catalysts prepared with IJP using the DMP, as well as, the modified WI method using the "ink formula". It is worth mentioning that these catalysts were also examined with in-situ Drifts and combined SSITKA-DRIFTS experiments. The XRD experiments were performed at the "Characterization lab" of the Department of Mechanical Engineering and Materials Science and Engineering of CUT.

The powdered samples were deposited on a glass substrate and afterwards, it was inserted in the sample holder of the Rigaku Ultima IV X-Ray Diffractometer. The system had a 285mm radius goniometer operating in θ/θ mode and was equipped with a 3kW X-ray generator with a copper tube (CuKαl radiation). Also, the system was equipped with a multilayer mirror for parallel x-ray beam geometry and operated at 40 kV and 40 mA. The sample patterns were collected over the 20°–80° 2 Theta range (º), in a sample holder without rotation. The 2theta were calculated with 1.54056Å wavelength for all measurements.

4.2.5. Temperature Programmed Desorption of Hydrogen (H₂-TPD)

The average dispersion of Pt on all the examined catalysts was determined by H_2 chemisorption according to the following procedure. After oxidation at 500°C for 2h in a 20%O_2/He gas mixture, the catalyst samples were reduced in pure H_2 at 300°C for 2h. Following this step, the feed was changed to He (inert gas) and the temperature was increased to 400°C in He flow and kept at this temperature until no hydrogen desorption was observed so as to avoid any possible hydrogen spillover that might have taken place at 300°C. Then, the reactor was quickly cooled under He flow to 25°C (not activated hydrogen adsorption) or 200°C (activated hydrogen adsorption) and the feed was changed to a 2%H_2/He gas mixture (50cc) for 30min for saturation of the active sites of the catalyst samples. In the case of the activated adsorption, the reactor was then cooled to 25°C under 2%H_2/He gas mixture. Afterwards, the feed was changed to He and kept at 25°C for 15min, where the remaining adsorptive molecules were flushed out by the inert gas. Then, the temperature of the catalyst was increased linearly to 500°C, since desorption is an endothermic process, at the rate of 30°C/min while a constant flow of He (50cc) was maintained over the sample in order to carry out the TPD experiment.

For the determination of the hydrodynamic response of the experimental apparatus used, i.e., the gas phase holdup of the system, some H_2-TPD experiments were performed using Ar in the gas mixture (2%H_2/4%Ar/He). In the latter case, the mass number of Ar (40) was also monitored by the mass spectrometer, along with hydrogen (2) in order to record Ar desorption as well as that of H_2.

4.3. Catalytic and Transient Studies

The flow system used for conducting catalytic studies and various kinds of transient experiments was consisted of a quartz plug-flow reactor (PID, Eng & Tech, Microactivity Reference). In particular, the system consisted of a custom made flow measuring control system, a fixed bed quartz micro-reactor (2ml nominal volume), an on-line Quadrupole Mass-spectrometer (QIC-20 Gas Analysis System, Hiden Analytical) and an on-line Gas Chromatograph-Mass Spectrometer (GC-MS, Agilent 5975C–7890A). A schematic diagram of the system is described in Figure 4.9. Thermal mass-flow control valves (MFC, Bronkhorst High-Tech) are used to prepare a given gas mixture in situ. Good mixing of the gas streams was achieved by using small chambers of about 3 ml, the

entrances of which were machined in such a way as to create local mixing (based on Peclét number) [292].
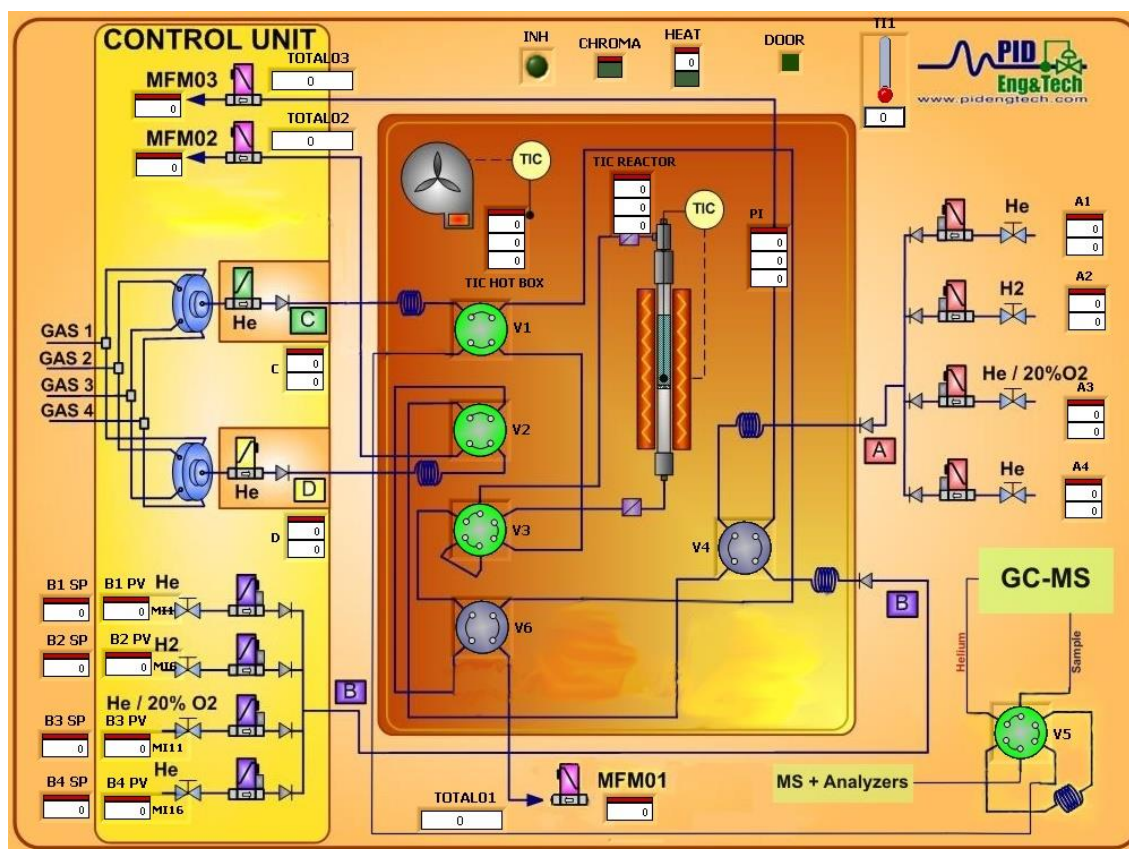
Figure 4.9: Schematic diagram of the transient flow system: reactor oven, quartz reactor, TIC (thermocouple), PI (pressure sensor), chromatographic valves, mass flow control valves, fan, mass flow meter (MFM), Quadrupole-MS and GCMS.

As can be seen in Figure 4.9, the 6-port switching valve, V_3, provides two alternative routes for the gas mixture, one through and one bypass the reactor. In addition, the 4-port chromatographic switching valve V_6 is used to create step concentration functions to the reactor and direct the gas stream towards V_3 valve. Specifically, a step change of the feed gas via V_6 valve diverts the gas mixture to bypass the reactor and forwards it to the mass spectrometer or a mass flow meter, depending on the rest of the valves. This option describes the forcing function of the system and accounts for all the back-mixing and electronic delays outside of the reactor. Moreover, the 6-port chromatographic switching valve V_5 is used to inject a pulse sample to the Gas Chromatography-Mass Spectrometry system (GCMS). Also, all valves are driven by electric actuators with 0.2s response time [292], [293].

Additionally, the microreactor used in the present work consists of a quartz cell (cylindrical shape) of 9.8mm (internal diameter). Also, a small furnace (cylindrical shape,

Therm-craft, Inc.) controlled by a programmable temperature controller allows heating of the reactor. The temperature of the catalyst is measured by a "K"-type thermocouple placed within a quartz capillary well at the entrance of the catalyst bed. Quartz wool was placed at both sides of the catalyst bed to keep the solid sample in place [292], [293].

For catalytic and transient measurements, ~0.1-0.15g of catalyst in powder form was loaded into the reactor. In particular, 0.0981g were used in the case of the IJP-Epson Pt/Al_2O_3 catalyst, 0.14g were used in the case of the IJP-DMP $Pt/MgO-CeO_2$ catalyst and 0.15 were used in the case of the rest of the catalysts. Before any experiment was conducted, the catalysts were additionally pretreated despite the former calcination in air at 500°C for 2h. The pretreatment procedure is very important, and it consists of several steps that must be repeated for successive experiments in order to guarantee reliable and reproducible results. The solids were first pretreated in 20% O_2/He at 500°C for 2h, cooled down in He and then reduced in pure H_2 at 300°C for 2h. Afterwards, the catalysts were cooled down to the appropriate temperature under He flow. H_2 and He gases were purified by passing through an oxygen and a universal trap (for O_2, H_2O, CO_2, CO, and hydrocarbon adsorption), while He passed through a moisture trap as well, all provided by Agilent.

Following the pretreatment, the catalyst surface is activated and ready to react with the reactive gas mixture for the catalytic experiment which consisted of 500ppm NO (0.05 vol%), 5 vol% O_2, 1 vol% H_2 and He as balance gas. The total gas flow rate was 100cc/min for the 0.15gr loaded catalysts, 65cc/min and 93cc/min, for the Pt/Al_2O_3 printed catalyst (Epson) and $Pt/MgO-CeO_2$ printed catalyst (DMP) respectively, leading to the same contact time (W/F) and gas hourly space velocity (GHSV= 80000h^{-1}) for all examined catalysts. GHSV is mathematically defined as the volume flow rate per hour divided by the volume of catalyst (GHSV=Q/V$_{cat}$), and it really shows the number of times the catalyst is swept by its own volume of gas in 1h [294].

For the present catalytic reaction system, NO reacts with H_2 and O_2 on the basis of the following reaction scheme [157].

$$2NO + 4H_2 + O_2 \rightarrow N_2 + 4H_2O \tag{4.1}$$

$$2NO + 3H_2 + O_2 \rightarrow N_2O + 3H_2O \tag{4.2}$$

$$H_2 + \tfrac{1}{2}O_2 \rightarrow H_2O \tag{4.3}$$
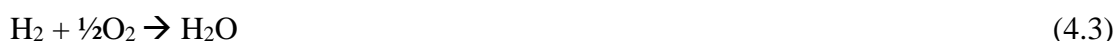
The conversion of NO (X_{NO}, %) of the H_2-SCR reaction was estimated based on the following relationship [279]:

$$X_{NO}(\%) = \frac{F_T \cdot y_{NO}^o - F_T \cdot y_{NO}}{F_T \cdot y_{NO}^o} \cdot 100 = \frac{y_{NO}^o - y_{NO}}{y_{NO}^o} \cdot 100 \qquad (4.4)$$

where, F_T is the total molar flow rate (mol/s), y_{NO}^o is the molar fraction of NO in the feed and y_{NO} is the molar fraction of NO after the reaction.

The only N-containing product species formed in the present catalytic reaction system were N_2 and N_2O. Integral N_2 and N_2O production and NO consumption rates were calculated based on the product analyses using the following relationships:

$$Rate_i \ (mole/g.s) = \frac{F_T \cdot y_i}{W} \qquad (4.5)$$

$$Rate \ NO \ (mole/g.s) = F_T \cdot y_{NO}^o \ \frac{X_{NO}}{W} \qquad (4.6)$$

where, y_i is the molar fraction of product i (N_2, N_2O) and W is the weight of catalyst (g).

Reaction selectivity was calculated as the rate of formation of the product to the rate of consumption of the reactant. N_2 and N_2O reaction selectivities were then calculated based on the following relationships, where the sum of selectivities (S_{N2} and S_{N2O}) always totalled 100%.

$$S_{N2O}(\%) = \left[\frac{2 \ Rate_{N2O}}{Rate_{NO}}\right] \cdot 100 = \frac{2 \cdot y_{N2O}}{y_{NO}^o - y_{NO}} \cdot 100 \qquad (4.7)$$

$$S_{N2} \ (\%) = \left[\frac{2 \ Rate_{N2}}{Rate_{NO}}\right] \cdot 100 = 100 - S_{N2O} \qquad (4.8)$$

The analysis of the effluent gas stream of the catalytic experiments was performed using both an on-line Quadrupole Mass-spectrometer and a Gas Chromatograph Mass Spectrometer (GC-MS, Agilent 5975C–7890A). In particular, the catalytic studies presented in the following chapter were conducted through GC-MS analysis after verifying steady-state reaction conditions through the on-line MS. It is noted that the gaseous response signals of H_2, NH_3, N_2, NO, N_2O and NO_2, were continuously monitored through the on-line MS at the mass numbers (m/z) of 2, 15, 28, 30, 44 and 46, respectively. The column that was used in the GC-MS system was the Agilent J&W Plot column (HP-PLOT/Q) and the analysis occurred at 40°C (oven) with 2.5 minutes run time and 2ml/min flow. A range of 2-80 mass numbers (m/z) was continuously recorded and the quantitative analysis was performed through multiple ion extraction from the main spectrum (2, 15, 28, 30, 44, 46). Afterwards, the peaks were integrated through the "MSD

ChemStation Data Analysis Software". Elution time and sensitivity of a given component required for quantitative analysis were also determined based on a known mixture of that component in He gas. It is noted that the catalytic experiments were run in triplicates for all the examined catalysts to rule out experimental bias or some random error and to ensure reproducible and accurate results. Error bars for NO conversion and N_2 selectivity were thereby calculated from the repeated experiments.

An example of the extraction of the ion chromatograms, as well as the integration and the elution time of the examined ions, are presented in Figure 4.10, for the 0.1 wt% Pt/MgO-CeO_2 IJP-DMP catalyst at 175ºC. As can be seen, the extracted NO is almost eliminated when the gas stream passes through the reaction, compared to the peak that is presented while passing the feed stream bypass the reactor.

Moreover, surface reactivity studies were conducted by transient methods of temperature-programmed desorption (TPD) and temperature-programmed surface reaction (TPSR). TPSR experiments were performed on all catalysts in order to quantify the intermediate species formed on the catalyst's surface during the $NO/H_2/O_2$ reaction after achieving steady-state reaction conditions. NO-TPD experiments were also performed on all the loaded samples to investigate the chemical interaction of the reaction species with the catalytic surface involved. The gas flow rate during the reaction (TPSR) was the same as the catalytic experiments (100cc/min, 65cc/min, or 93cc/min) and the gas flow rate during the desorption was at 50cc/min for He or $2\%H_2/He$ as can be seen in Table 4.2.

After pretreatment, the feed was switched to pure He and the temperature was increased to 350ºC for 30 min and then the reactor was cooled to the appropriate temperature of the experiment to be followed. For the TPSR experiments, the appropriate temperature was the temperature where the catalyst exhibited maximum NO conversion during the catalytic experiments, whereas for the NO-TPD experiments it was 25ºC. Table 4.2 summarizes the sequence of steps for each kind of transient experiment performed. The final step of the analysis was the gradual linear increase of the temperature to 500°C, using a rate of 30°C/min, while a constant flow of 50 cm^3/min of He or $2\%H_2/He$ was maintained over the sample to carry out the experiments. This step was recorded by an on-line QMS (Hiden Analytical) and is underlined in Table 4.2.
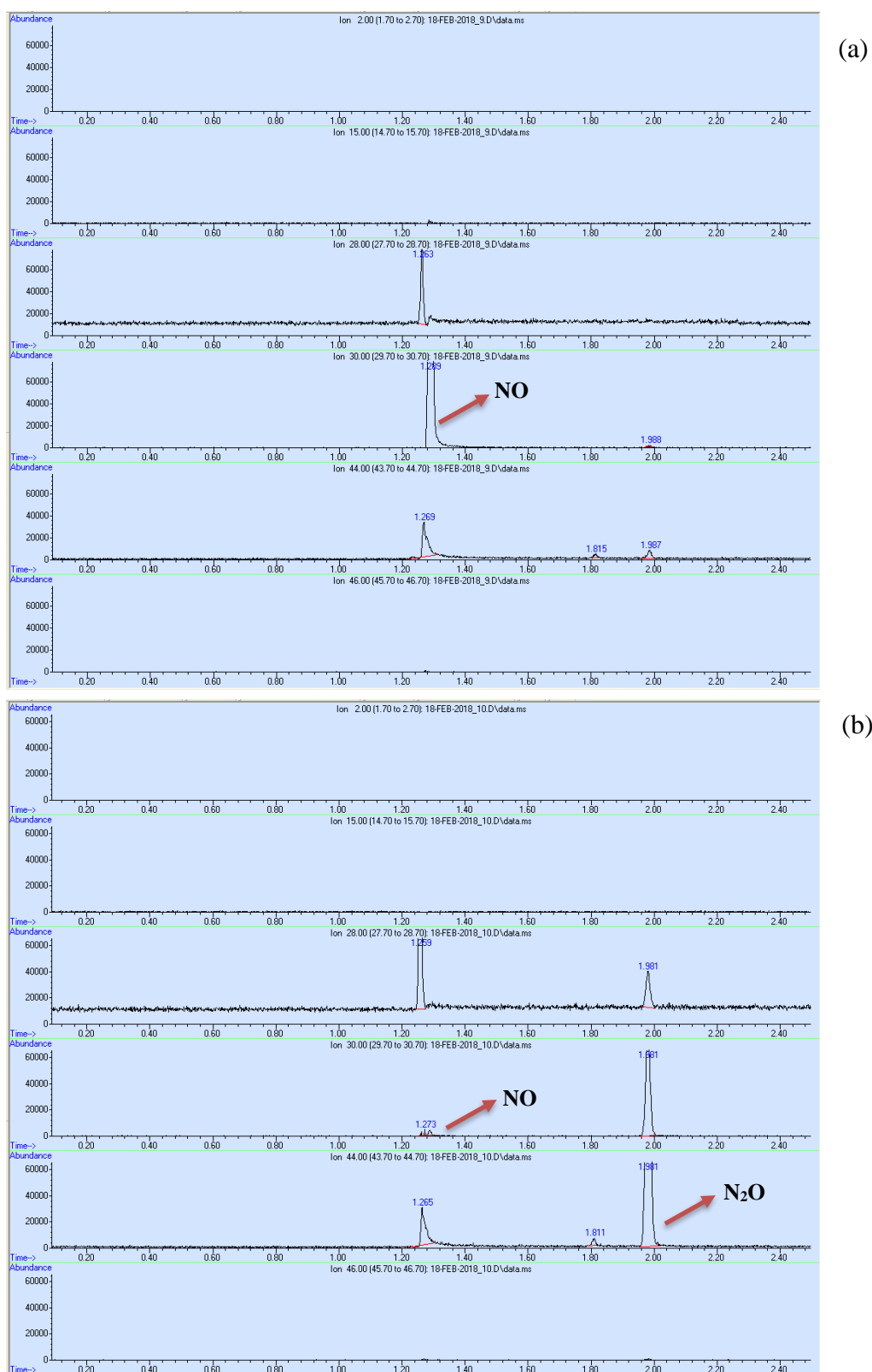
Figure 4.10: Typical multiple ion extraction (m/z = 2, 15, 28, 30, 44, 46) from the main GC–MS spectrum used for the quantitative analysis of the reaction's effluent for (a) bypass sampling and (b) through sampling for the IJP-DMP Pt/MgO-CeO$_2$ catalyst at 175°C.

Table 4.2: Description of sequential step changes in gas flow during TPD and TPSR experiments.

Experiment	Sequence of step changes of gas flow over the catalyst sample
A	0.05vol% NO/ He (25°C, 15min) → He (5min, 25°C) → <u>TPD in He flow</u>
B	0.05vol% NO/ He (25°C, 15min) → He (5min, 25°C) → <u>TPD in 2%H_2/He flow</u>
C	<u>0.05vol% NO/ 1vol% H_2/ 5vol% O_2/ He</u> ($T^{max}_{X(NO)}$, ~45 min, steady state conditions) → cool down quickly to 25°C in NO/H_2/O_2 → He (5min, 25°C) → <u>TPSR in He flow</u>
D	<u>0.05vol% NO/ 1vol% H_2/ 5vol% O_2/ He</u> ($T^{max}_{X(NO)}$, ~45 min, steady state conditions) → cool down quickly to 25°C in NO/H_2/O_2 → He (5min, 25°C) → <u>TPSR in 2%H_2/He flow</u>

The monitoring of the effluent gas stream during the transient studies including the previously mentioned H_2-TPD experiments was performed with an on-line quadrupole mass spectrometer equipped with a fast response inlet capillary/leak valve and data acquisition systems. It should be mentioned that all lines between the outlet of the reactor and the inlet capillary of MS and GCMS were held at 120°C to avoid problems associated with the condensation of water. The gaseous response signals recorded were calibrated against standard gas mixtures. The mass numbers (m/z) 2, 15, 28, 30, 44 and 46 used for H_2, NH_3, N_2, NO, N_2O and NO_2, respectively, were continuously monitored. It is worth mentioning that no gas phase reaction between NO and O_2 to form NO_2 was detected by mass spectrometry (MS). The acquired data (signals) were processed with the software "HIDEN analytical ltd MASsoft Professional'', version 6.1.

It is noted that three independent experiments (N=3) were also performed for each of the transient experiments for all the examined catalysts, in order to ensure reproducible and accurate results. After the experiments were completed, their initial analysis involved offset filtering (subtraction of a constant offset from all the values of the signal). Afterwards, the filtered signal was further processed by subtracting the overlapping components with the monitored mass numbers, as mentioned before. The MASsoft software indicated the overlapping percentage (cracking coefficient) for each monitored component. Specifically, the mass number of 15 that was used to identify NH_3, overlaps with nitric oxide by 2.4% and nitrous oxide by 0.1%. The mass number of 28 and 30 that were used to identify N_2 and NO, respectively, overlap with N_2O by 10.8% and 31.1%. For instance, for the NO analysis, after the offset filtering of the initial signal, the signal undergone further subtraction of the N_2O overlapping component, i.e., subtracting 31.1% of the filtered N_2O signal from the filtered NO signal. Finally, the signals of the monitored

mass numbers were converted to concentration units, as they were calibrated against standard gas mixtures.

The final data files were inserted in the "OriginPro 8.5'' software for further analysis, that is, baseline subtraction, position of the peak maximum (along the temperature scale, T_{max}) and area under the TPD profile. It is worth mentioning that if the peaks overlapped, then a deconvolution process was followed, which enhances the resolution of a spectrum in order to visualise spectral features that overlap to give a broad band [273]. It is noteworthy that the deconvolution of the original peaks resulted in an accuracy of up to 99.5% as was indicated by the coefficient of determination (R^2).

Furthermore, if necessary, a normalization procedure was followed for the NO-TPD and TPSR experiments that used $2\%H_2/He$ gas flow at the desorption step (B and D experiments, Table 4.2), since the total desorbed N-containing μmoles were slightly different than the A and C experiments using only He. As the total N-containing μmoles of the experiments (e.g. TPSR-He and TPSR-$2\%H_2/He$) should not differ at the same catalyst, the final values of the products concentrations were processed by normalizing the values with a stoichiometric coefficient, i.e., a normalized mole fraction of ''the total N-containing μmoles desorbed by He to the total N-containing μmoles by $2\%H_2/He$''. It is noted that the normalization scheme was necessary so as to be able to compare the results from these experiments on an equal basis, even if the details of the experimental conditions were different (desorption gas).

4.4. DRIFTS and Combined SSITKA-DRIFTS Studies

In situ DRIFTS and combined SSITKA-DRIFTS studies have been performed on selected catalysts, i.e., printed $0.1\%Pt/MgO-CeO_2$ (IJP-DMP) catalyst and $0.1\%Pt/MgO-CeO_2$ (IF) catalyst. The DRIFTS studies were conducted in order to identify and evaluate the chemical structure of adsorbed NO_x intermediate species that are formed during $NO/H_2/O_2$ and NO/H_2 reactions on the catalytic surface. The combined SSITKA-DRIFTS studies were performed in order to identify the active intermediate species as well as the spectator species during the $NO/H_2/O_2$ reaction. Moreover, these studies were performed in an attempt to gather fundamental knowledge on the intrinsic reason(s) of the large influence of oxygen feed gas composition on NO conversion for H_2-SCR of NO on the printed 0.1 wt% $Pt/MgO-CeO_2$ (DMP) catalyst, which presented impressive catalytic results without O_2 in the feed stream.

DRIFTS spectra were recorded on a PerkinElmer Spectrum 100 FTIR spectrophotometer using a high-temperature/high-pressure temperature controllable DRIFTS cell (Praying Mantis™ Diffuse Reflectance Attachment, Harrick Scientific) equipped with ZnSe IR windows. The DRIFTS cell was cooled throughout the experiment at 23°C with a cooling system that circulated water in order to prevent any damage to the ZnSe windows. The detector that was used was a CSI TGS (triglycine sulphate) [295].

The catalyst sample, which was in a fine powder form, was diluted at a 1:1 w/w ratio with dry KBr, 99+% FT-IR grade provided by Sigma-Aldrich, for improved signal-to-noise ratio, resulting in 45mg of examined powder. Additionally, KBr does not influence the acquired spectra in terms of the number and position (wavenumber) of the peaks observed. Before any measurements were taken, the catalysts were pretreated in situ in 20%O_2/He for 1h at 500°C followed by treatment with pure hydrogen gas at 300°C for 1h. The total flow rate was kept constant at 30 cc/min. The feed was then switched to pure He at 300°C for 5 min and the sample was then cooled down to 200°C, where the reactions took place. At the same time, the reaction mixture of 0.05%NO/1%H_2/5%O_2 was prepared and sent to the vent until good mixing was achieved. For FTIR single-beam background subtraction, the IR spectrum of the solid was recorded in Helium flow at 200°C, as that spectrum was taken in the absence of any adsorbed NO_x species. Figure 4.11 presents the DRIFTS panel flow diagram that was used for conducting these experiments.
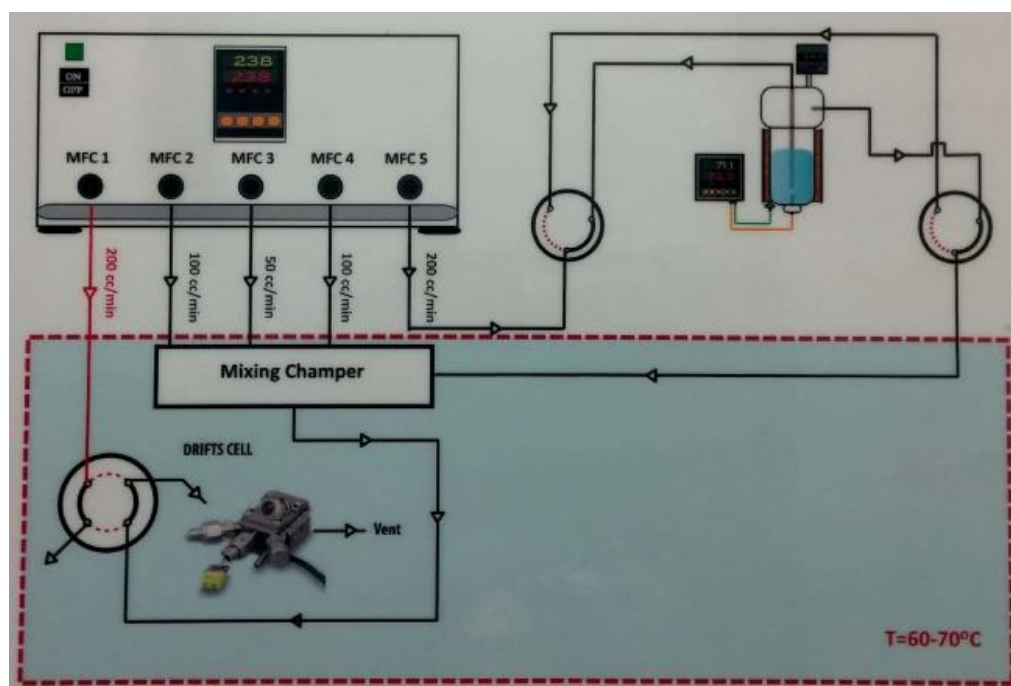
Figure 4.11: DRIFTS panel flow diagram.

After the pretreatment of the sample and recording of He background at 200°C, the feed stream was changed from He to the gas mixture of NO/H$_2$/O$_2$ for 45 minutes, until steady-state reaction conditions were achieved. Then the IR spectrum of the solid was recorded. The second step of the experiment involved the examination of the O$_2$ influence on the gas composition on the Pt/MgO-CeO$_2$ catalysts, therefore oxygen was removed from the gas mixture, resulting in NO/H$_2$ feed to the surface of the solid (0.05%NO/1%H$_2$). The IR spectrum was recorded after an hour of reaction at 200°C (steady-state reaction conditions). Afterwards, oxygen was introduced again, and that IR spectrum was recorded after 45 minutes of NO/H$_2$/O$_2$ reaction. The fourth and final experiment was the combined SSITKA-DRIFTS run which involved the isotopic switch of ^{14}NO to ^{15}NO in the reaction gas stream (^{15}NO/H$_2$/O$_2$) and the IR spectrum of the solid was recorded after 45 minutes of H$_2$-SCR of NO. The isotope used in the SSITKA experiments was 1000ppm ^{15}NO/He gas mixture (Linde).

DRIFTS spectra were recorded at a resolution of 1cm^{-1}, at the rate of 0.5cm/s in the 800–2500cm^{-1} range and the averaged spectrum (40 spectra were collected) was then recorded. All spectra were analysed using the instrument's Spectrum for Windows$^\circledR$ software which was provided. Initial analysis of the data concerned the conversion of the transmittance to absorbance spectra. Afterwards, the background of He is subtracted and then a smooth process of the resulting spectra is initiated, which is the same for all the spectra of the examined catalysts. The final values of the spectra are inserted in the "OriginPro 8.5'' software, where deconvolution procedures were applied [296]. The various observed infrared absorption bands due to adsorbed NO$_x$ species were assigned based on literature [60], [76]–[79] (see Table 1.2, subchapter 1.3.7.2.) and other DRIFTS studies performed on similar catalysts [73], [75], [279].

CHAPTER 5: RESULTS AND DISCUSSION

5.1. Catalysts Characterization

5.1.1. Inductively Coupled Plasma Mass Spectrometry (ICPMS)

The total concentration of Pt and thus the total metal loading (wt% Pt) of the supported-Pt catalysts was measured via ICPMS analysis. Table 5.1 presents the loading obtained for all the Pt/Al_2O_3 and $Pt/MgO-CeO_2$ catalysts that were prepared through the wet impregnation method, using H_2O or ink formula as solvents, as well as the IJP-DMP Pt/Al_2O_3 catalyst. As seen in Table 5.1, the loadings of the catalysts are not significantly different from the theoretical value of 0.1 wt%. A slight difference can be seen for the IF $Pt/MgO-CeO_2$ catalyst, which presented the lowest total concentration of Pt and hence the lowest loading. The differences with the theoretical value can be attributed to a variety of factors, such as the different preparation methods, minor errors during their synthesis preparation, or during the samples' acid digestion.

Table 5.1: ICPMS results for supported-Pt catalysts

Catalyst	Method	Loading (%)
Pt/Al_2O_3	WI	0.096
	IF	0.103
	IJP-DMP	0.098
$Pt/MgO-CeO_2$	WI	0.094
	IF	0.086

5.1.2. BET Surface Area Measurements

The specific surface area (m^2/g) and the total pore volume (cm^3/g STP) of each examined catalyst were measured via a Micromeritics Gemini V System-2380. Table 5.2 presents the BET results obtained on Al_2O_3 and $MgO-CeO_2$ supported Pt-catalysts which were prepared by the wet impregnation and ink formula methods. As can be seen, the Pt/Al_2O_3 catalyst prepared by ink formula showed the higher BET surface area ($35m^2/g$) and total pore volume ($8.1cm^3/g$) compared to the rest of the solids. Also, the aforementioned catalyst has almost $20m^2/g$ more surface area than the same catalyst that was prepared by WI, using de-ionized water.

As for the supported-Pt catalysts prepared with the binary oxides of MgO and CeO_2, the IF catalyst exhibited higher specific area and total pore volume compared to the WI one,

i.e., almost $27m^2/g$ more surface area. Therefore, the IF catalysts showed larger specific surface area than the WI solids. The greatest difference in the specific surface area and the total pore volume is found between the Al_2O_3 support (IF) and the $MgO-CeO_2$ sample (WI). Additionally, the C constant values that were calculated for all samples fall in the range of 80-144, a fact which based on Sing [254], indicates that the samples are consistent with the formation of well-defined monolayers on mesoporous adsorbents.

Table 5.2: BET results for Al_2O_3 and $MgO-CeO_2$ supported-Pt catalysts.

Support material	BET Surface Area (m^2/g)	Total pore volume $(cm^3/g$ STP)
Al_2O_3 (WI)	16	$Q_{m=}$ 4
Al_2O_3 (IF)	35	$Q_{m=}$ 8
$MgO-CeO_2$ (WI)	5	$Q_{m=}$ 1
$MgO-CeO_2$ (IF)	32	$Q_{m=}$ 7

5.1.3. Scanning Electron Microscopy (SEM)

Scanning electron microscopy (SEM) studies were performed on all 0.1 wt% Pt/Al_2O_3 and 0.1 wt% $Pt/MgO-CeO_2$ catalysts that were prepared by wet impregnation, using de-ionized water (WI) or the ink formula (IF), and novel inkjet printing (IJP). The SEM results were used to examine the surface morphology of the catalysts, the sample's surface topography, properties, and elemental composition.

- **0.1 wt% Pt/Al₂O₃ catalysts**

The first-ever inkjet printed catalyst produced for the reduction of NO, as mentioned before, was prepared with the Epson L800 inkjet printer and was consisted of alternating layers of 0.1 wt% Pt and Al_2O_3 formula inks. Figure 5.1, shows multiple SEM images that were taken in different magnifications from secondary electrons (Fig. 5.1a, c) and backscattered electrons (Fig. 5.1b), as well as a SEM-EDX image (Fig. 5.1d). The SEM studies on this catalyst indicate the micro-crystallinity and the relatively narrow size distribution of the catalyst's particles (d~150nm in Fig. 5.1a) with a practically spherical shape. Also, the morphology of the printed catalyst included the formation of smooth surfaces with high porosity. Moreover, a honeycomb distinct structure is observed at a closer look (Fig. 5.1c). It is suggested that the honeycomb structure occurs from the calcination of the polymer's micelles where after calcination, the freed space creates this unique structure.

It is worth mentioning that SEM-EDX analysis was also performed in order to determine the surface elemental composition of the printed catalyst. The SEM-EDX analysis consists of spectra showing peaks corresponding to the elements making up the composition (Al, O, Pt) of the catalyst (Fig. 5.1d). Specifically, the IJP-Epson catalyst presents a surface (of a few nm) dispersion of 0.68 wt% Pt and a ratio of Pt/Al of 0.012. It is noted that the elemental composition of the SEM-EDX images indicates the surface concentration of the corresponding elements at a depth of a few molecular layers. Therefore, the concentration of Pt, which is higher than the theoretical value (0.1 wt%), is considered reasonable due to the preparation method followed. The fact that Pt is concentrated on the external surface of the support (eggshell catalyst) is desirable, in order to avoid possible mass transfer phenomena.
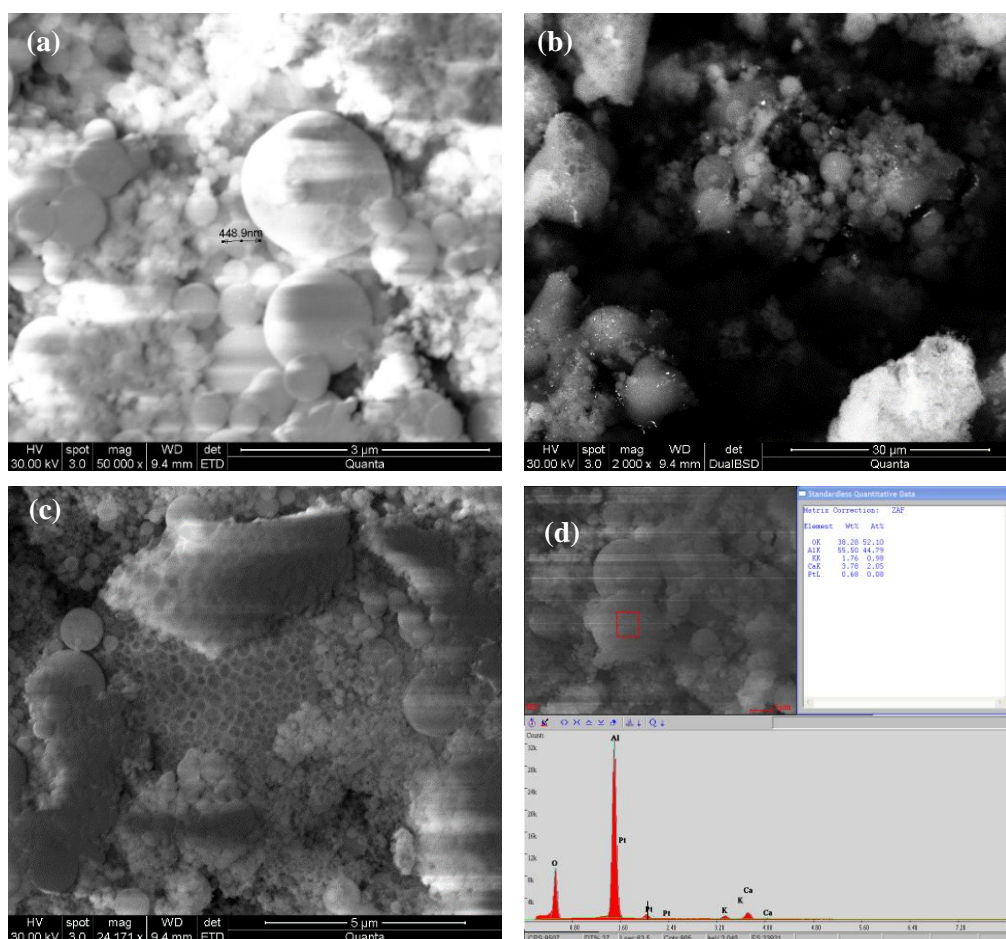
Figure 5.1: SEM (a, b, c) and SEM-EDX images (d) of the IJP Pt/Al$_2$O$_3$ catalyst (Epson).

SEM studies were performed on the fresh sample of Pt/Al$_2$O$_3$ (IF) catalyst after calcination, as well as on a used solid sample following catalytic experiments (NO/H$_2$/O$_2$) in the temperature range of 100-400°C. Figure 5.2 shows some of the SEM images that were captured for the Pt/Al$_2$O$_3$ (IF) catalyst in different magnifications (x6000 - x26000).

This SEM analysis also showed a distinct honeycomb structure, like the one seen on the printed catalyst (IJP-Epson), as well as a spongy-like structure which does not appear in the case of the catalyst that was prepared by standard WI, using de-ionised water as a solvent (Fig. 5.3). This unique structure is a consequence of the decomposition of the polymer's micelles, after catalyst's calcination, a compound that the WI catalysts do not contain. Additionally, this catalyst exhibits a highly porous structure with the size of the majority of the particles being smaller than 300nm and some up to ~700nm (Fig. 5.2c). Moreover, based on the SEM studies performed on the used Pt/Al_2O_3 (IF) solid (Fig. 5.2d), it is concluded that the catalytic surface retains its honeycomb, spongy-like structure even after several catalytic cycles.
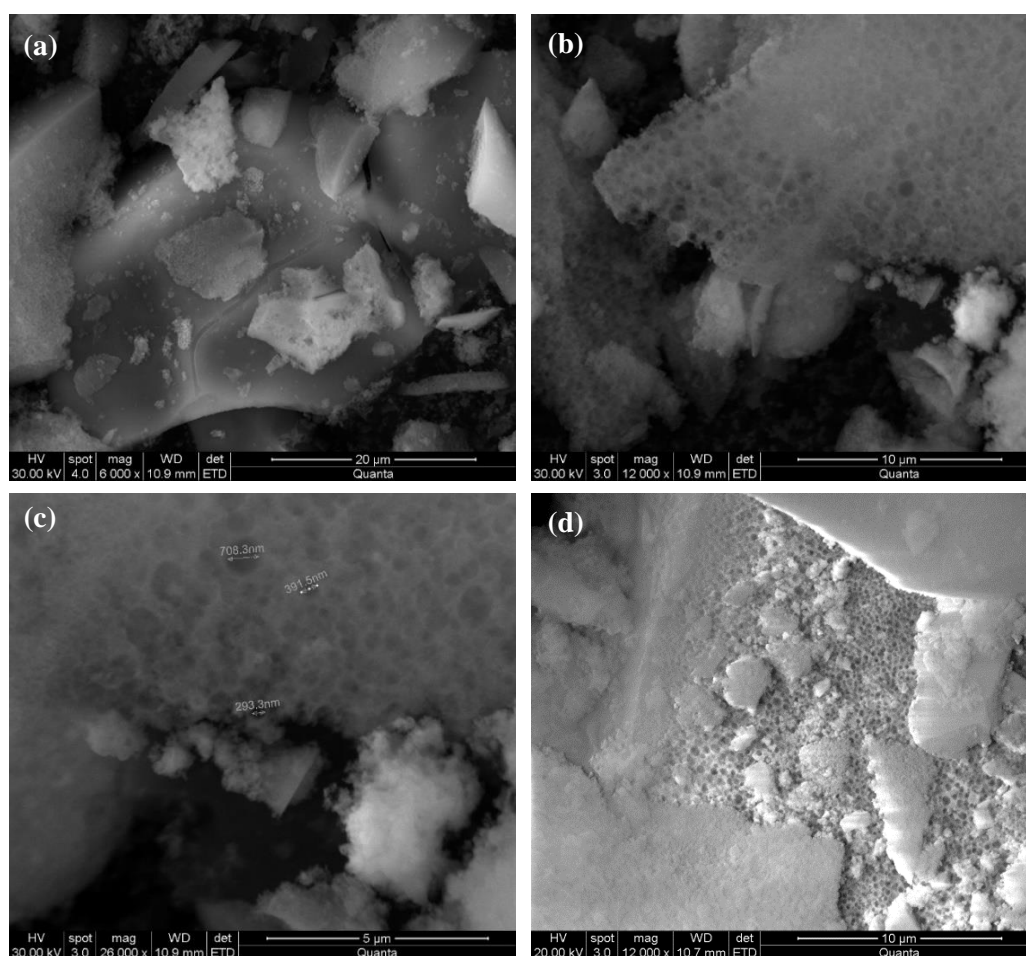
Figure 5.2: SEM images in different magnifications of the Pt/Al_2O_3 (IF) catalyst.

Figure 5.3 shows the SEM images that were captured through the ET detector using secondary electrons in different magnifications on the Pt/Al_2O_3 (WI) catalyst. The analysis of the specific catalyst which was prepared with the traditional wet impregnation method does not reveal a particularly porous structure. Additionally, compared to the previously mentioned catalysts it does not exhibit multiple spherical particles nor a

distinct porous morphology. Fig. 5.3d presents the SEM-EDX image that was captured for the WI solid and indicates the surface elemental composition of the catalyst (Al, O, Pt). It is noted that the surface concentration of Pt was found to be 0.76 wt%, which indicates that Pt is concentrated mainly on the external surface of the support.
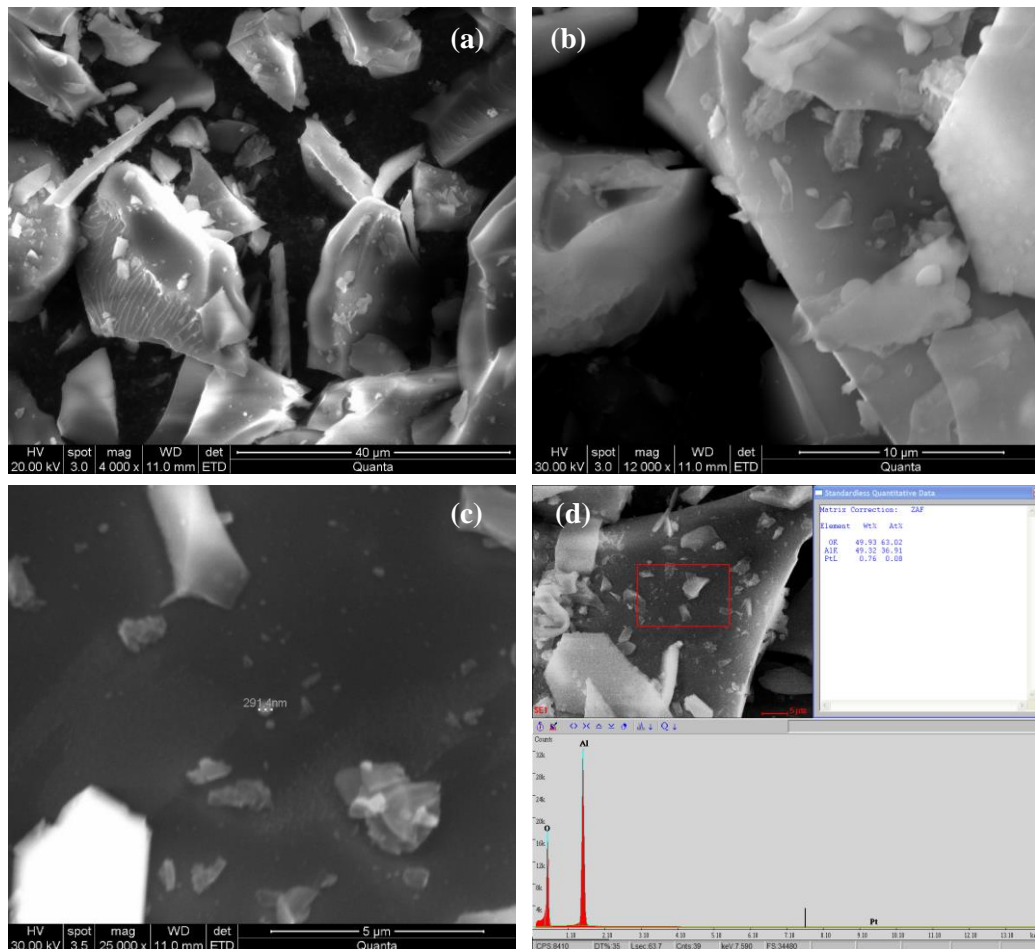
Figure 5.3: SEM (a, b, c) and SEM-EDX image (d) of the Pt/Al$_2$O$_3$ (WI) catalyst.

Figure 5.4 presents the HR-SEM images obtained on the DMP printed Pt/Al$_2$O$_3$ catalyst (IJP-DMP). As seen, the solid presents a lego-like structure, where the primary grains were joint together composing a unique and uniform morphology throughout the sample. It should be mentioned that this catalyst, which was prepared by the inkjet printer DMP, had one ink solution containing both the substrate and the active metal precursors diluted in deionized water, similar to the WI catalyst. However, even though the printed catalyst presents particles in the range of ~ 950nm as seen in Fig. 5.4b, which was measured according to the scale of 5μm after the image was captured, its larger agglomerates are consisted of much smaller particles (Fig. 5.4c). Specifically, as seen in Fig. 5.4d, at 100 000 magnification, the IJP-DMP catalyst's nanoparticles were found to be ranging 60-

90nm and have a spherical shape. These small-sized nanoparticles were not observed in the WI solid.
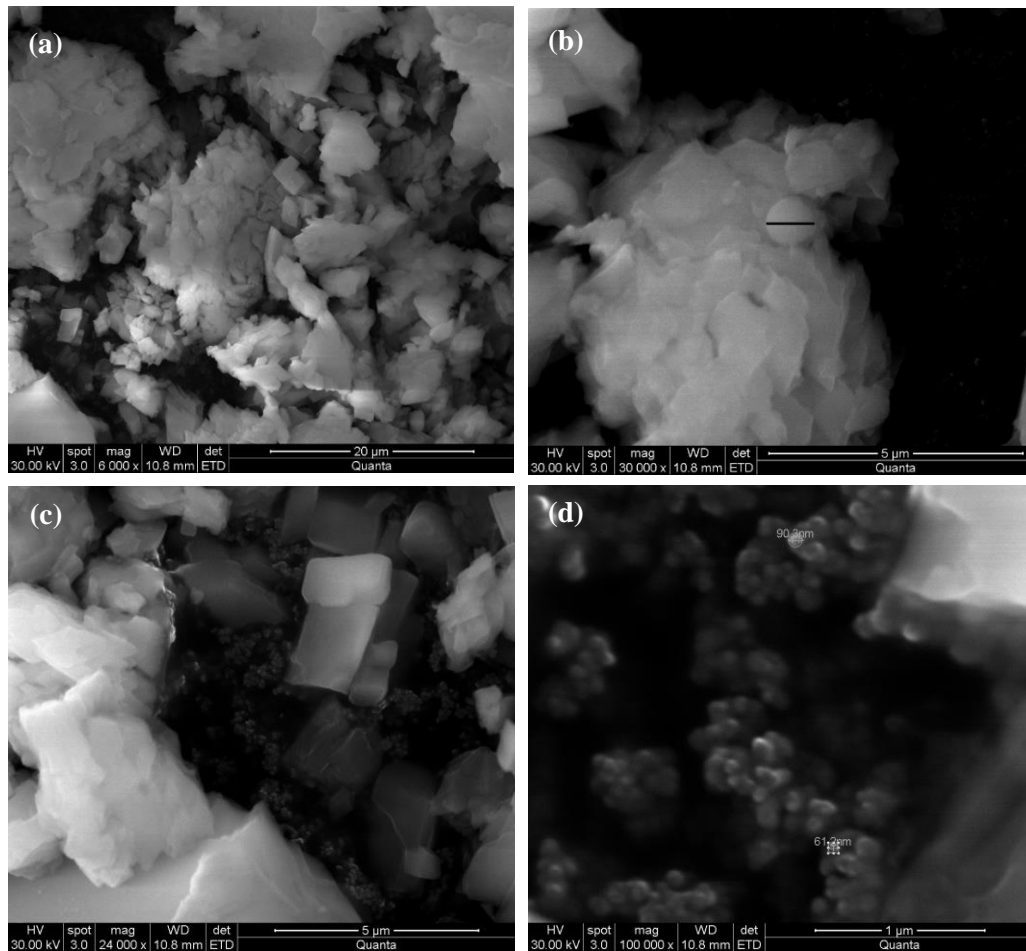
Figure 5.4: SEM images in different magnifications of the printed Pt/Al$_2$O$_3$ catalyst (DMP).

According to the images presented in Figures 5.1-5.4, one of the most significant differences between the four catalysts is the distinct spherical particles morphology (nanospheres) of the first printed Pt/Al$_2$O$_3$ catalyst (Fig. 5.1). In particular, as shown in Fig. 5.1a, the particles consisting of the printed catalyst, vary in the area of 100-800nm, with the majority of the particles appearing in the range of 100-200nm. The average size of the latter catalyst's particles was calculated to be around 150nm. Moreover, the second IJP Pt/Al$_2$O$_3$ catalyst (DMP) presented large agglomerates that are consisted of much smaller spherical nanoparticles in the range 60-90nm. On the contrary, the catalysts prepared by the wet impregnation method present rather large grains (particles) of undefined structure with rather smooth external surface morphology. The above results indicate that the nanospherical shape of the printed catalyst's particles is produced only during the printing process, and cannot be duplicated by the wet impregnation method, even when using the same ink formulation used for the preparation of the printed catalyst. Another important

difference that occurs through the SEM analysis, is the distinct honeycomb structure that is exhibited only by the IJP-Epson Pt/Al_2O_3 catalyst as well as the IF solid. This structure was explained through the unique ink formula that was used for their preparation.

- **0.1 wt% $Pt/MgO-CeO_2$ catalysts**

The microstructural features of each 0.1 wt% $Pt/MgO-CeO_2$ catalysts were also evaluated through SEM imaging, while EDS was applied to determine their surface elemental composition. Figure 5.5 shows the captured SEM images of the $Pt/MgO-CeO_2$ (WI) catalyst in different magnifications (x3000 – x24000). The first two images (Fig. 5.5a and b) present the same spot on the sample with the first one using the ET detector for the emitted secondary electrons and the second one using the DualBSD for the emitted backscattered electrons. Also, Fig. 5.5c shows that the particles are uniformly dispersed throughout the sample and Fig. 5.5d presents a wide range of particle sizes, i.e., from smaller than 90nm and bigger than 330nm. Moreover, the morphology of the $Pt/MgO-CeO_2$ (WI) catalyst included the formation of smooth surfaces and high porosity.
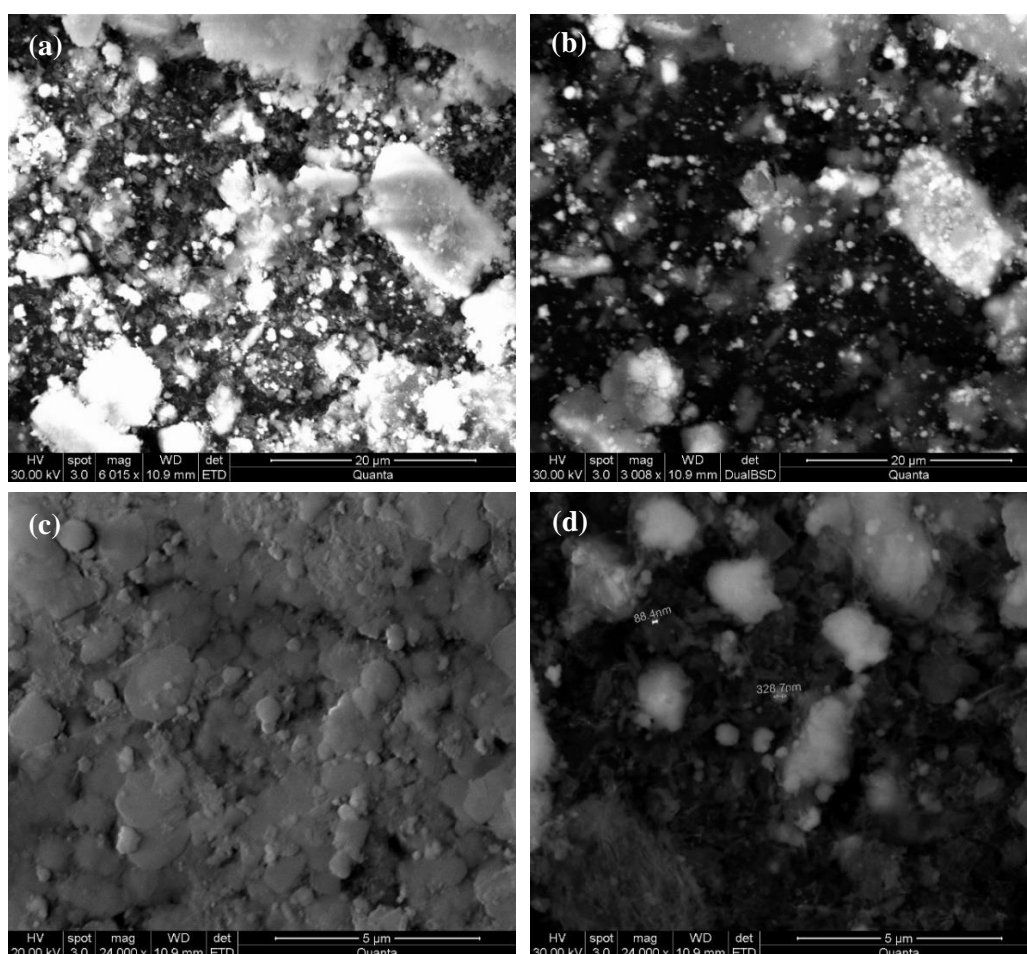
Figure 5.5: SEM images in different magnifications of the $Pt/MgO-CeO_2$ (WI) catalyst.

SEM analysis was also performed on the Pt/MgO-CeO$_2$ (IF) catalyst, however, as the sample was very soft (foamy), the first SEM images that were captured were not representative of the catalyst, therefore, the sample was coated with Au of 1.5nm. Fig. 5.6a shows the honeycomb structure which was also found on the Pt/Al$_2$O$_3$ catalysts that were prepared by the ink formula (Figs. 5.1 and 5.2). Further analysis of this catalyst was conducted again on a fresh sample (after calcination) without the Au sputtering. As seen in Fig. 5.6b the honeycomb structure is still observed, though not in the same distinct degree as the previously mentioned catalysts. The morphology of the catalyst indicates a highly porous structure with a wide range of sizes, e.g. smaller than 500nm and up to 2.2μm. In higher magnifications of x50000 (Fig. 5.6c), spherical particles morphology (nano-spheres) is observed with particles exhibiting 100nm diameter, which indicates the fine porous structure of the catalyst. Also, Fig. 5.6d shows the surface elemental composition of the latter sample, without Au sputtering, which was found to be 0.95 wt% Pt, 34.10 wt% Mg, 28.64 wt% Ce and 36.31 wt% O.
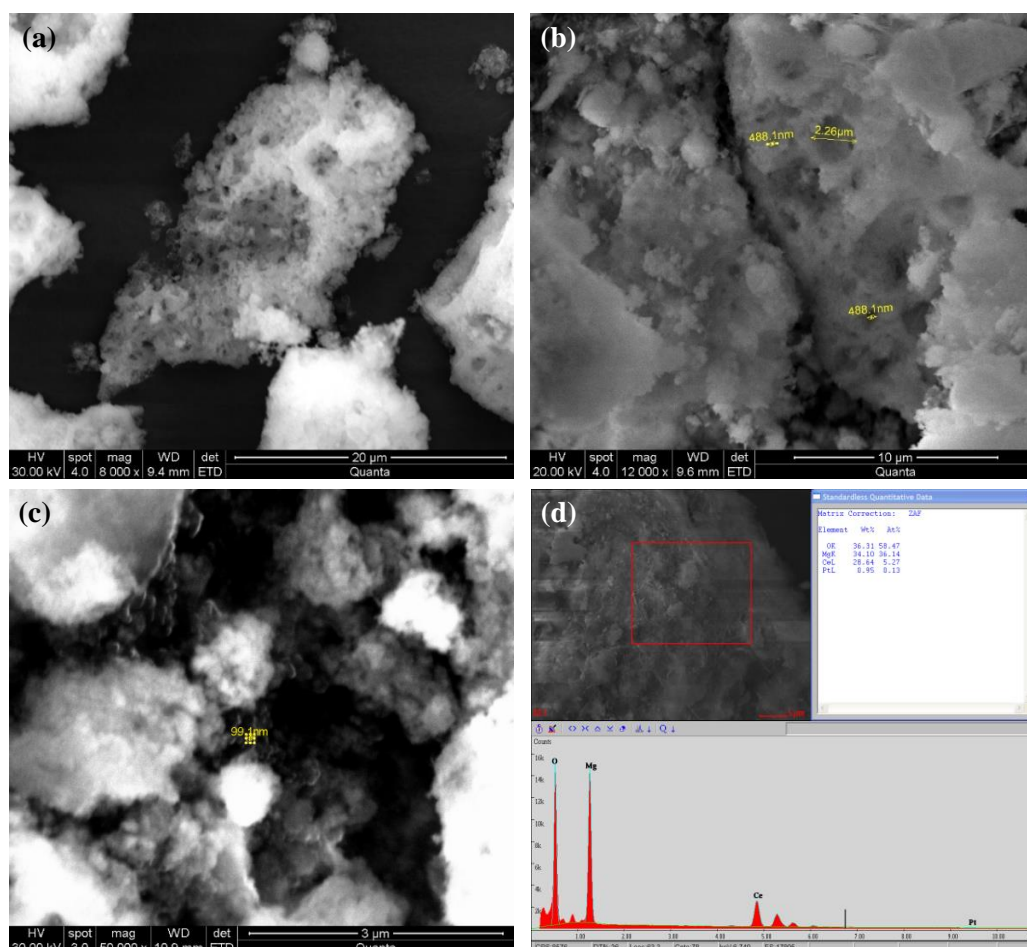
Figure 5.6: SEM (a, b, c) and SEM-EDX (d) images of the Pt/MgO-CeO$_2$ (IF) catalyst.

High-resolution SEM analysis was also employed for microstructural characterization of the first IJP Pt/MgO-CeO$_2$ (DMP) catalyst on a fresh sample (Fig.5.7a), as well as on a used sample after conducting several catalytic and transient experiments (Fig.5.7b, c).
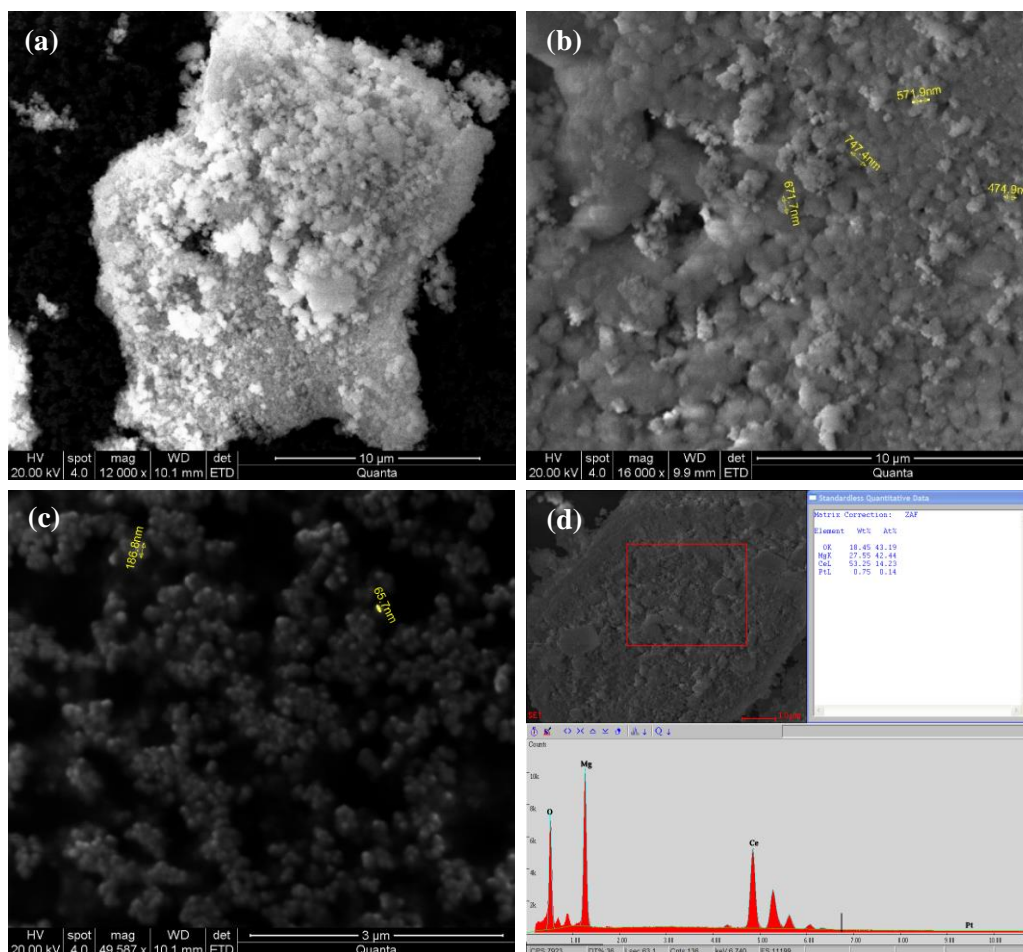
Figure 5.7: SEM (a, b, c) and SEM-EDX (d) images of the IJP Pt/MgO-CeO$_2$ catalyst (DMP).

As can be seen in Figure 5.7, the printed Pt/MgO-CeO$_2$ catalyst showed a uniform distribution of the catalyst crystallites, even after performing various experiments. It also presented with a lego-like structure as the Pt/Al$_2$O$_3$ catalyst that was prepared with the same inkjet printer (DMP). In particular, as shown in Fig. 5.7b, the particles consisting of the printed catalyst have a spherical shape, and vary in the area of 300-800nm, with the majority of the nanoparticles being less than 300nm. On a closer look though (50 000 and 100 000 magnification), the IJP-DMP Pt/MgO-CeO$_2$ catalyst exhibited spherical nanoparticles in the range of 65-200nm, with the majority of them being less than 100nm as seen in Fig. 5.7c. Regarding the porosity of the examined catalyst, when compared to the other Pt/MgO-CeO$_2$ catalysts, the IJP solid seems to has higher porous morphology than the WI catalyst but lower than the IF sample.

Moreover, the surface elemental composition of the used catalyst, was found to be 0.75 wt% Pt, 27.55 wt% Mg, 53.25 wt% Ce and 18.5 wt% O as seen in Fig.5.7d. It is noted that the increased (compared to the theoretical value) surface concentration of Pt, indicates that Pt is deposited, via the printing protocol that was followed, mainly on the external surface of the support, creating an eggshell catalyst.

5.1.4. X-Ray Diffraction (XRD)

XRD analyses were conducted on two 0.1 wt% Pt/MgO-CeO$_2$ catalysts; the IF and the IJP-DMP solids. The specific experiments were used to probe the presence or difference in the presence of the crystalline phases of MgO, CeO, CeO$_2$, Ce$_2$O$_3$ within the two catalyst samples. Figure 5.8 compares the XRD patterns for both catalysts. As can be seen, CeO, and Ce$_2$O$_3$ were not present in either sample. The crystalline phases of MgO and CeO$_2$ are present in both MgO-CeO$_2$ catalysts. The XRD patterns of both samples demonstrate distinct peaks located at the major crystalline phase at 28.6º, 33.2º, 47.6º, 56.5º, 59.2º, 69.8º and 77.1º. All aforementioned peaks correspond to CeO$_2$, whereas 36.9º, 42.9º, 62.3º and 74.6º correspond to MgO. The CeO$_2$ phase, indicated with # in the figure, was identified with a crystalline constant of α=0.54nm and crystallized in the cubic close-packed array (face centred cubic, fcc). In addition, MgO, which was marked with * in the figure, was also identified in the cubic system with α=0.42nm.
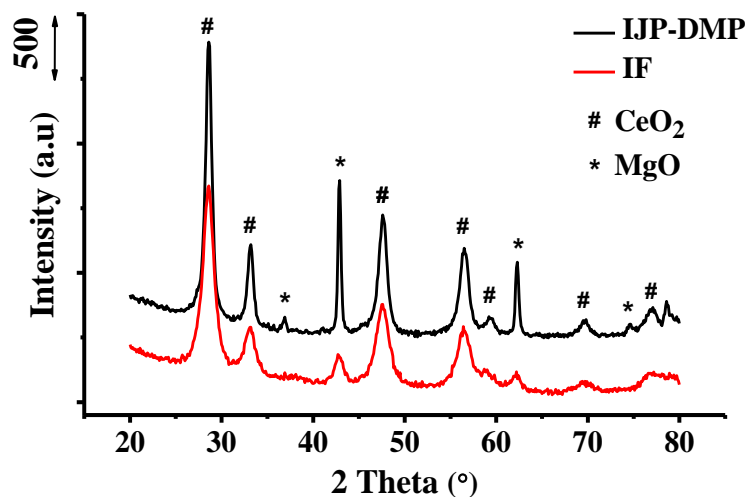
Figure 5.8: X-ray diffraction pattern for IJP-DMP and IF MgO-CeO$_2$ catalysts.

By comparing the two samples, the IJP-DMP catalyst appears to have more crystallic MgO than the sample prepared with IF. In general, the crystallinity of the printed catalyst is better than the other sample (IF), since the peaks shown in the figure are sharper. It is

noted that these catalysts were also examined with in-situ Drifts and SSITKA experiments (subchapter 5.4).

5.1.5. Temperature Programmed Desorption of Hydrogen (H_2-TPD)

The temperature-programmed desorption of H_2 from the solid surface of the catalyst is widely used for the study and characterization of catalytic surfaces, particularly the heterogeneity of the catalyst's active surface. The theoretical metal dispersion of the supported catalysts was determined by H_2 chemisorption at 25°C (not activated chemisorption) followed by temperature-programmed desorption (TPD) in He flow up to 500°C at the rate of 30°C/min. During the TPD, when the temperature increases, the dissociated adsorbed hydrogen atom becomes re-associated with another hydrogen atom to form a hydrogen molecule and then desorbs to the gas phase [27]. The area under the desorbed peaks is proportional to the amount of hydrogen originally adsorbed to the exposed surface of metal clusters. Since the hydrogen atoms are chemisorbed on a 1:1 stoichiometry (H: Pt), the results can be used to calculate the amount of Pt atoms exposed on the catalytic surface, which are involved in the catalytic reduction of NO [28], [269].

Pt dispersion (%) is presented in Table 5.3 for all Al_2O_3 and MgO-CeO_2 solids. In particular, all four Pt/Al_2O_3 catalysts showed similar dispersion of Pt, in the range of 88-91%, whereas the dispersion found on the MgO-CeO_2 catalysts varied between 63-93% during H_2 chemisorption at 25°C. These results are in agreement with the dispersion values found in literature, i.e., Costa et al. reported 90% dispersion for 0.1wt% Pt/Al_2O_3 [157] and 0.1wt% Pt/MgO-CeO_2 [73] catalysts, while Xue et al. [297] measured a dispersion of 72% for the 0.1wt% Pt/Al_2O_3 solid. Also, Table 5.3 presents the amount of surface Pt atoms (μmolPt/g_{cat}) for all the catalysts, which is the maximum concentration (monolayer, θ=1) of H species that can be accommodated on the surface of the catalysts. Moreover, the fact that almost all of the examined catalysts presented similar dispersions indicates that the differences in the catalytic behaviour, observed over the solids examined (subchapter 5.2), cannot be attributed to the effects of Pt dispersion and are solely due to the different chemical structure/morphology of the catalysts examined (as a consequence of their different preparation method).

Table 5.3: H_2-TPD results of examined Pt/Al_2O_3 and $Pt/MgO-CeO_2$ catalysts.

Catalysts		μmol Pt/g_{cat}	Dispersion D (%)	Particle size d_c (Å)
0.1 wt% Pt/Al_2O_3	WI	4.5	88.2	18.3
	IF	4.7	91.1	17.7
	IJP-Epson	4.6	90	17.9
	IJP-DMP	4.5	88.4	18.2
0.1 wt% $Pt/MgO-CeO_2$	WI	4.8	93.1	17.3
	IF	3.2	63.3	25.4
	IJP-DMP	4.8	93.3	17.3

Also, Table 5.3 shows the particle size of the Pt clusters that was calculated based on equation 3.16. As seen, the size of the particles is inversely proportional to Pt dispersion, thus the IJP-DMP $Pt/MgO-CeO_2$ catalyst that showed relatively higher dispersion values has the smallest sized Pt particles. On the contrary, the $Pt/MgO-CeO_2$ (IF) solid presented the lowest dispersion values, thus bigger sized Pt particles. It was reported that the electronic structure of the metal-support interface region can be altered (due to metal-support interactions) for metal particle sizes less than 2.0nm (20Å), thus affecting the chemisorption and catalytic properties of active sites within that region [74], [298].

The Pt/Al_2O_3 catalysts were also examined under activated H_2 chemisorption (T_{ads}= 200°C) and resulted in similar μmol Pt/g_{cat}. Thus, since an additional uptake of H_2 was not observed in higher temperatures, then, the adsorption of H_2 on the Pt/Al_2O_3 solids is considered to be a non-activated process. In this case, the gas dissociation process can be activated without a temperature increase and the formation of a chemisorptive bond (Pt-H) does not require the overcome of a significant activation barrier [26], [299]. Therefore, the interaction of H_2 with the reduced adsorbate-free Pt/Al_2O_3 catalysts follows a dissociative adsorption process, producing weakly bound and highly mobile hydrogen species [300].

Figure 5.9a presents the TPD profiles acquired from the three $Pt/MgO-CeO_2$ catalysts, after H_2 chemisorption at 25°C. The area under the peaks provided the total amount of desorbed H_2, which is 44.8 μmolH_2/g_{cat} for the WI solid, 51.0 μmolH_2/g_{cat} and 40.3 μmolH_2/g_{cat} for the IF and printed (DMP) catalyst, respectively. In addition, Fig. 5.9b shows a representative example (WI) of the deconvolution of the complex and broad H_2 bands presented in Fig. 5.9a. After deconvolution (Origin) of the initial band of the WI catalyst, three peaks were resolved, which are centred at T_{M1}= 126°C, T_{M2}= 306°C, T_{M3}=

403°C. The resulting peaks can be correlated to three different types of active sites on the catalytic surface, as H_2 was desorbed at different temperatures [26], [301]. It is noted that the desorption temperature reflects on the strength of the Pt-H chemisorbed bond and that the bond is stronger at higher temperatures [26]. Therefore, the last desorption temperature (T= 403°C) indicates a stronger Pt-H bond.

Additionally, the first band of the IF catalyst (Fig. 5.9a), that is in the area of 25-160°C, resulted in two small peaks (T_{M1}= 66°C, T_{M2}= 106°C), while the second band was not well-resolved and corresponded to desorbed H_2 at T> 240°C. The printed catalyst resulted in five peaks, the first one centred at 132°C, whereas the other peaks were found at T > 250°C (287°C, 342°C, 394°C and 437°C). The dispersion values and thus the $\mu molPt/g_{cat}$ that are presented in Table 5.3, were based on the first peak of the H_2 desorbed profiles of the catalysts, that was desorbed at T<150°C.
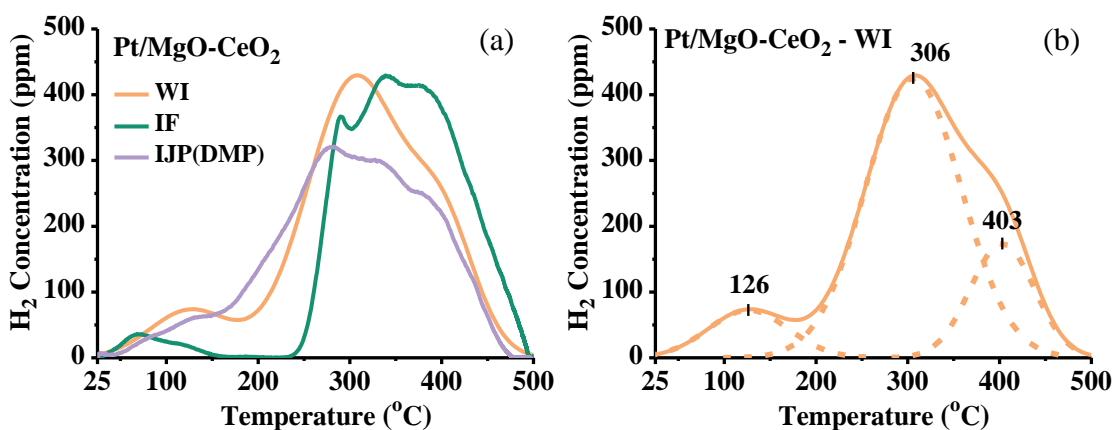
Figure 5.9: H_2-TPD profiles obtained over the examined 0.1 wt% Pt/MgO-CeO$_2$ catalysts.

The chemisorbed H_2 found in the present work was observed in both low (T<150°C) and high temperatures. According to the literature [110], [113], [302], [303], during a H_2-TPD experiment on supported Pt catalysts, multiple peaks above 100°C can occur. At low temperatures (T= 150°C), hydrogen is chemisorbed on the metal surface, while the higher temperatures (T= 300-500°C) have been assigned to spilt-over H_2, to strongly chemisorbed H_2, to H_2 in subsurface layers of the Pt, or to oxidation of the reduced metal by support protons. Consequently, the H_2-TPD profiles observed in Figure 5.9 are in excellent agreement with the existing literature for supported-Pt catalysts.

It is noted that Pt/MgO-CeO$_2$ catalysts were also examined under activated H_2 chemisorption (T_{ads}= 200°C), that resulted in higher amounts of $\mu mol\ H_2/g_{cat}$. In particular, the WI solid presented 109.6$\mu mol\ H_2/g_{cat}$, which is 2.4 times more than the H_2

desorbed during the non-activated chemisorption. The IF desorbed 200.3μmol H_2/g_{cat} (almost four times more) and the IJP-DMP catalyst presented 106.2μmolH_2/g_{cat} (2.6 times more). Therefore, the Pt/MgO-CeO$_2$ catalysts were found to adsorb much higher quantities of dissociative H_2 than the quantity that corresponds to a monolayer coverage of Pt surface (μmol Pt/g_{cat}, Table 5.3). Specifically, the WI and the IJP-DMP solids adsorbed ~45 equivalent monolayers, and the IF catalyst 124 equivalent monolayers.

This observation can be interpreted considering two factors; i.e., the adsorption of H_2 on the Pt/MgO-CeO$_2$ solids is an activated process and the rate of diffusion of atomic hydrogen from the metal to the substrate, via a spillover mechanism, is increasing. In the first case, adsorption can happen on more active surface sites, that could not adsorb at low temperatures since the formation of a chemisorptive bond (Pt-H) requires the overcome of an activation barrier [26], [299]. This, however, cannot explain the huge amount of H_2 that was found to be adsorbed on the examined catalysts. Furthermore, it is suggested that most of the chemisorbed H_2 found on the Pt/MgO-CeO$_2$ catalysts is due to a spillover effect, which is inevitable at catalysts with low metal loadings. During the spillover process, the chemisorbed hydrogen atoms migrate from the metal phase (Pt) to the support [108]. It should be mentioned that when H_2 spillover occurs, the support may serve as a "hydrogen buffer", where it can take off excess hydrogen which otherwise would block active sites. This spilt-over hydrogen can be released, through a reverse spillover mechanism, during the TPD process [304].

Hydrogen surface coverage (θ_H), is a very important parameter that determines both the activity and the selectivity of the H_2-SCR reaction on supported Pt catalysts [52], [305]. The consumption of H_2 is largely determined by the hydrogen combustion reaction (eq. 5.1), which takes place on the Pt surface [52]. The support plays also a very important role in regulating the θ_H parameter and in the case of the Pt/MgO-CeO$_2$ catalysts, the CeO$_2$ phase can have a decisive role [73], [306]. As mentioned before, CeO$_2$ can enhance the oxygen storage capacity (OSC) of the catalyst; it can store a large amount of oxygen, and subsequently, release it under reducing conditions [91]–[93]. This action has a direct effect on the regulation of surface oxygen uptake on Pt, and consequently, on the rate of hydrogen combustion. The produced OH$^-$ lead to the formation of H_2O (eq. 5.2) [52]. Also, Miller et al. [113], proposed that the quantity of spillover hydrogen depends on the number of hydroxyl groups (OH$^-$) on the support.

H-s + O-s $\rightarrow$ OH-s + s (5.1)

OH-s + H-s $\rightarrow$ H$_2$O +2s (5.2)
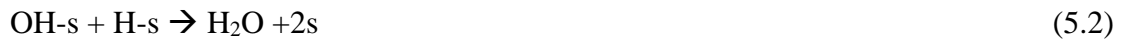
Finally, according to the research of Costa et al. [305], [306] on the 0.1 wt% Pt/MgO-CeO$_2$ catalyst, the active NO$_x$ species formed during the NO/H$_2$/O$_2$ reaction, reside on both the MgO and CeO$_2$ support phases, in the vicinity of Pt particles, where the main role of Pt is to provide active atomic H species by a spillover mechanism. Therefore, hydrogen spillover from the Pt sites to the metal-support interface is essential so that the active NO$_x$ intermediate species, which are located near the metal-support interface, be able to get reduced into N$_2$. It is noted that some of the active NO$_x$ species found on the Pt/MgO-CeO$_2$ catalysts in the current work (subchapter 5.4), are also formed on the support, thus, the hydrogen spillover effect that is observed on these catalysts is essential for the H$_2$-SCR of NO.

5.2. Catalysts Performance (H$_2$-SCR of NO)

Catalytic experiments were conducted on all 0.1 wt% Pt/Al$_2$O$_3$ and 0.1 wt% Pt/MgO-CeO$_2$ catalysts towards the selective catalytic reduction of NO with H$_2$, in excess oxygen in the feed (H$_2$-SCR), in the 100-400ºC temperature range. The highest investigate reaction temperature was 400ºC in order to avoid sintering of Pt metal. It is noted that the only N-containing product formed during the present catalytic experiments were N$_2$ and N$_2$O. Moreover, as shown in all figures (Fig. 5.10-5.12, 5.14), the standard deviation of the values presented is less than 2% throughout the whole temperature range examined.

5.2.1. 0.1 wt% Pt/Al$_2$O$_3$ Catalysts

Figures 5.10-5.13 present the results of the NO conversion (X_{NO}, %) and nitrogen reaction selectivity (S_{N2}, %) over the four 0.1 wt% Pt/Al$_2$O$_3$ catalysts examined for the H$_2$-SCR of NO. As can be observed throughout Fig. 5.10 and Fig. 5.11, there is an initial nearly linear increase in the conversion of NO, with the catalysts reaching a maximum value of NO conversion, and after which, the conversion starts to decline, following the typical volcano-shape curve. This curve is ascribed to the competitive reactions between NO and O$_2$ for the reducing agent (H$_2$), according to Savva and Costa [121]. Moreover, it is suggested that the unselective and significant combustion of H$_2$ at higher temperatures, which consequently diminishes the remaining number of reductant molecules for the SCR reaction and the partial oxidation of Pt crystallites are the main reasons for this behaviour [121].

- WI and IF Pt/Al_2O_3 catalysts

Figure 5.10a shows the temperature profiles of the NO conversion and N_2 selectivity obtained over the 0.1 wt% Pt/Al_2O_3 (WI) catalyst for the $NO/H_2/O_2$ reaction. This catalyst showed the highest NO conversion of 81% at $T_M= 200°C$ (T_M), where T_M is the reaction temperature at which maximum X_{NO} is observed. Also, the examined catalyst presented a wide temperature-window of operation ($\Delta T= 110°C$), in the range of 140-250°C, where at least half of the maximum NO conversion is observed. The N_2 selectivity of the WI catalyst had an average value of 79% within the temperature window of 140-200°C, where the maximum value was observed at 175°C ($S_{N2}= 84\%$). It is noted that Costa et al. [157] also examined the 0.1wt% Pt/Al_2O_3 catalyst, prepared by wet impregnation with H_2O, on the 0.25%NO/ 1%H_2/ 5%O_2/He reaction (five times higher NO concentration) and they reported maximum X_{NO} of 66% at 125°C and S_{N2} of 60% in the low-temperature range of 90-200°C.

Figure 5.10b presents the catalytic behaviour, in terms of NO conversion and N_2 selectivity, of the $NO/H_2/O_2$ reaction in the range of 100-400°C over the 0.1 wt% Pt/Al_2O_3 (IF) catalyst. This catalyst presented high NO conversion values ($X_{NO}= 90\%$) at 200°C. Also, at 175°C, the selectivity towards N_2 was 84% and the conversion of NO was 87%. The IF catalyst presented an operating temperature window of $\Delta T=110°C$, ranging 140-250°C, same as the WI catalyst. It is worth mentioning that the IF Pt/Al_2O_3 catalyst, which was also prepared and examined for the first time in the present work, appears to be more active (by ~10%) compared to the conventional catalyst (WI), in the 100-200°C low temperature range, as well as in the operating temperature window ($T_R= 140-250°C$). This slightly improved behaviour of the former catalyst is probably due to the use of the "ink" solution and in particular of the F127 polymer, which leads to a larger B.E.T. surface area, and in general, a different surface structure, due to its combustion during catalyst's calcination. Additionally, the selectivity towards N_2 was similar within ΔT between the two catalysts, since they presented an average value of $S_{N2}= 72\%$ (IF) and $S_{N2}= 75\%$ (WI).

(a)

(b)

Figure 5.10: Temperature profiles of NO conversion and N_2 selectivity obtained during $NO/H_2/O_2$ reaction over (a) 0.1 wt% Pt/Al_2O_3 (WI) and (b) 0.1 wt% Pt/Al_2O_3 (IF) catalysts. Reaction Conditions: NO= 0.05 vol%, O_2= 5 vol%, H_2= 1 vol%; m_{cat}= 0.15g, Q= 100 cm^3/min, GHSV= 80000 h^{-1}.

- IJP-Epson and IJP-DMP Pt/Al_2O_3 catalysts

An important contribution of this dissertation in respect to the development of efficient and innovative catalysts for the reduction of NO is achieved through the two Pt/Al_2O_3 printed catalysts that were prepared for the first time by novel inkjet printing and were compared to 0.1 wt% Pt/Al_2O_3 conventional catalysts (WI and IF). Figure 5.11 shows the temperature profiles of the NO conversion and N_2 selectivity of the $NO/H_2/O_2$ reaction over the two inkjet-printed 0.1 wt% Pt/Al_2O_3 catalysts (Epson and DMP).
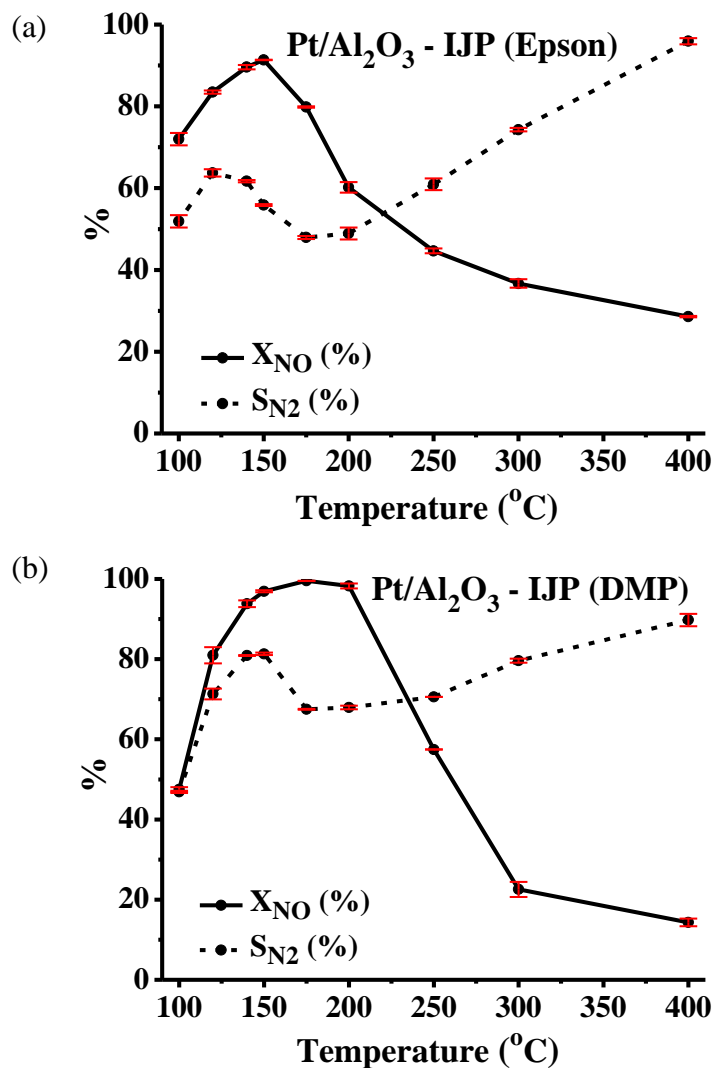
Figure 5.11: Temperature profiles of NO conversion and N_2 selectivity obtained during NO/H_2/O_2 reaction over inkjet printed 0.1 wt% Pt/Al_2O_3 catalysts; (a) IJP-Epson and (b) IJP-DMP catalysts. Reaction Conditions: NO= 0.05 vol%, O_2= 5 vol%, H_2= 1 vol%; $m_{cat\ (a)}$= 0.1g, Q_a= 65 cm^3/min, $m_{cat\ (b)}$= 0.15g, Q_b= 100 cm^3/min, GHSV= 80000 h^{-1}.

As shown in Figure 5.11a, the NO conversion behaviour of the first-ever printed catalyst (using the custom-modified Epson L800 printer), can be distinguished in two different temperature ranges. In the low 100-200°C range, the catalyst presents high activity (X_{NO}> 60%) with a maximum conversion of 91% at 150°C. In the high 250-400°C temperature range, the NO conversion varies from ~30% to 45%. Also, the IJP-Epson Pt/Al_2O_3 catalyst exhibited better catalytic performance (as compared to the conventional Pt/Al_2O_3 catalysts) in the 100-175°C low-temperature range (average X_{NO}= 83%). Another advantage of the printed solid is the achievement of a wider operating temperature window of operation (ΔT= 150°C), i.e., the catalyst retains at least half of its maximum catalytic activity within the 100-250°C range. Regarding the selectivity of the reaction,

this printed catalyst shows a slightly lower nitrogen selectivity value at the temperature of maximum conversion of NO, as compared to the catalysts prepared with the wet impregnation methods (Fig. 5.10). However, the opposite behaviour is observed at 300°C, where the printed catalyst appears to be superior to the conventional catalysts, especially in terms of N_2 selectivity. The latter results indicate that the inkjet printing method is able to lead to solid catalysts with unique catalytic characteristics.

Figure 5.11b presents the catalytic behaviour of the second novel inkjet-printed Pt/Al$_2$O$_3$ catalyst (IJP-DMP). As seen, this specific solid presented remarkable NO conversion for the low-temperature range of 140-200°C (average X_{NO}= 97%), where at 175°C it achieves practically complete conversion of NO (X_{NO}= 99.5%). It also exhibited the same wide operating temperature window (ΔT= 150°C) in the same temperature range (T= 100-250°C) as the Epson printed catalyst. The N_2 selectivity values observed during the reaction at hand were greater than 67% for the temperature range of 120-400°C, where at 140°C and 150°C the selectivity reached 81%, with X_{NO} at 94% and 97% respectively, indicating the superior performance of the printed catalyst.

Figure 5.12a compares the catalytic activity (in terms of NO conversion) of the latter four Pt/Al$_2$O$_3$ solids towards the NO/H$_2$O$_2$ reaction. As seen, the printed catalysts displayed a unique behaviour compared to the rest of the catalysts examined, namely, high NO conversion at very low reaction temperatures and wider temperature window of operation. Specifically, Fig. 5.12a illustrates the remarkable catalytic performance of the second printed catalyst (IJP-DMP) in the low-temperature range of 140-200°C, where at 175°C the solid achieved almost 100% NO conversion. Moreover, the first printed catalyst (IJP-Epson), is superior to the catalysts prepared by the wet impregnation method (WI and IF), particularly concerning the temperature of maximum NO conversion, which is 50°C lower in the case of the printed catalyst (Epson). It must also be noted that at 100°C and 120°C, which are the first two examined temperatures, the Epson printed catalyst exhibited the highest conversion values of 72% and 84%, respectively. On the contrary, the WI and IF catalysts presented X_{NO}< 40% for 100°C and 120°C, and they attained significant catalytic activity at reaction temperatures higher than 140°C.
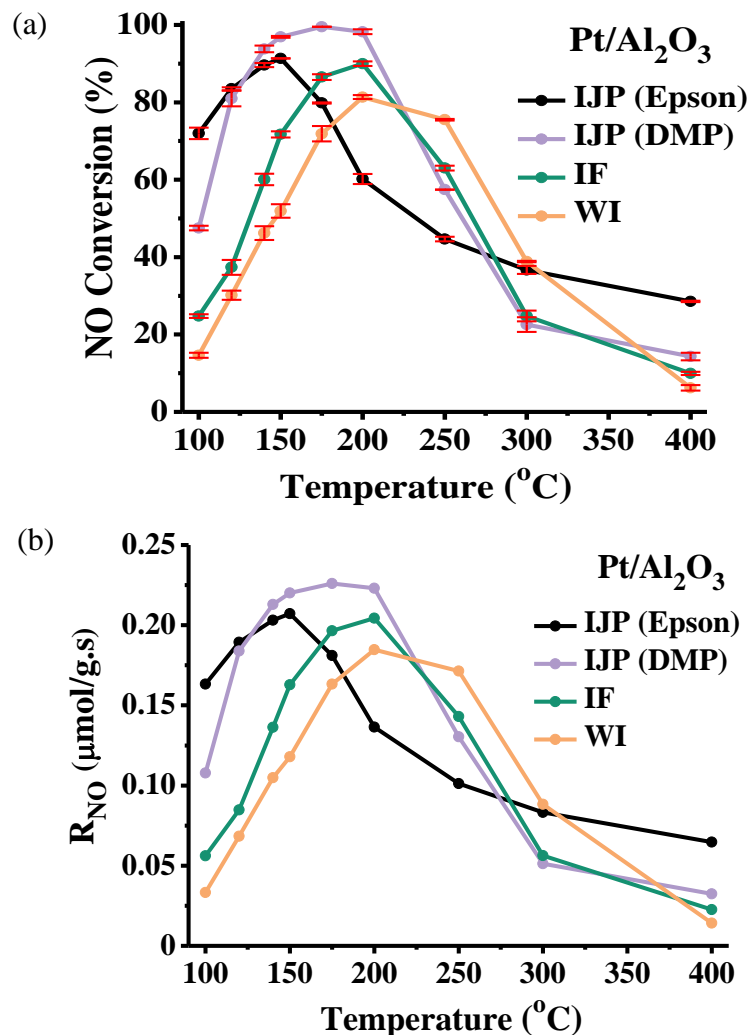
Figure 5.12: Temperature profiles of (a) NO conversion and (b) integral rate of NO consumption (μmole/g.s) obtained during $NO/H_2/O_2$ reaction over 0.1 wt% Pt/Al_2O_3 catalysts prepared by IJP and WI methods. Reaction Conditions: NO= 0.05 vol%, O_2= 5 vol%, H_2= 1 vol%; GHSV= 80000 h^{-1}.

In addition, the Epson printed catalyst retains substantial catalytic activity even at reaction temperatures as high as 400°C. This is also a unique feature of the printed catalyst since Pt/Al_2O_3 catalysts are known to lose their catalytic activity at reaction temperatures higher than 250°C, for the $NO/H_2/O_2$ reaction [307]. In particular, the rest of the Pt/Al_2O_3 catalysts (Fig. 5.12a), appear to be practically inactive at the higher temperature of 400°C, with the NO conversion found to be less than 14%. This observation can be partially explained by the oxidation of the larger part of the Pt surface as the reaction temperature increases. This behaviour affects negatively the rate of H_2 dissociation and consequently decreases further the surface coverage of H on Pt, and in turn, decreases the rate of NO reduction [305]. It is noted that these observations are in agreement with the integral rate of NO consumption (μmole/g.s) for the reaction at hand, which is indicated in Fig. 5.12b.

As seen, the integral rate of NO follows the same trend as the conversion of NO, since R_{NO} is proportional to X_{NO} based on equation 4.6.

Figure 5.13 presents the temperature profiles of the integral rate of N_2 production (R_{N2}, dotted line) and N_2 selectivity (S_{N2}, straight line), for the NO/H_2/O_2 reaction over all the 0.1 wt% Pt/Al_2O_3 catalysts examined in the present work. As seen the R_{N2} follows a similar trend to S_{N2} for the examined catalysts. It is noted that the standard deviation of the values presented regarding the selectivity towards N_2 is less than 2% throughout the whole temperature range examined. Also, at $T_R \geq 250^{\circ}C$ highest N_2 selectivity values were obtained by the catalysts prepared by inkjet printing, while the opposite is true for the lower temperature range (175-200°C). At temperatures lower than 150°C, the DMP catalyst appears to be slightly superior.
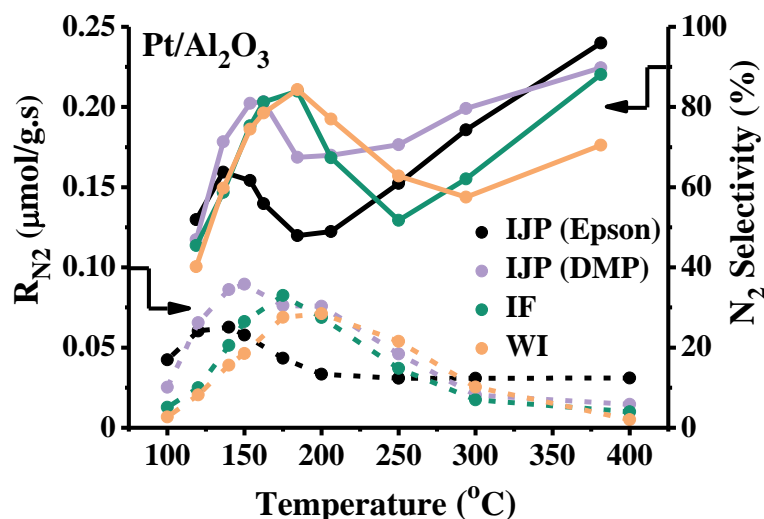
Figure 5.13: Temperature profiles of the integral rate of N_2 production (µmole/g.s) and N_2 selectivity obtained during NO/H_2/O_2 reaction over 0.1 wt% Pt/Al_2O_3 catalysts prepared by IJP and WI methods. Reaction Conditions: NO= 0.05 vol%, O_2= 5 vol%, H_2= 1 vol%; GHSV= 80000 h^{-1}.

Consequently and since all four catalysts present similar Pt dispersion (as mentioned in subchapter 5.1.5), the differences shown in Figures 5.12 and 5.13 can be safely attributed to the different surface structure (metal-support interface) of the four catalysts, which is a result of their different preparation method. In particular, it appears that the inkjet printing technology, leads to better contact between the metallic phase and the support, possibly due to the printing sequence followed (consecutive, precise, alternating layers-Epson), creating a unique structure of the final printed catalysts, as seen during the SEM analysis. It is noted at this point that the nature of the metal-support interface is of high

importance and can significantly affect the overall behaviour of Pt supported catalysts, as proven by the work of Burch et al. [70] and Costa et al. [157], [307]. In particular, it was proven that the support actively participates in the overall reaction mechanism ($NO/H_2/O_2$), through the formation of active intermediate NO_x species on the metal-support interphase, which ultimately lead to the formation of the final products (N_2 and N_2O) [157], [307]. In conclusion, the catalytic behaviour and especially the activity (X_{NO}) of the supported-Pt catalysts towards the $NO/H_2/O_2$ reaction was found to strongly depend on the catalyst's preparation technique. It can be safely claimed that the printing protocol followed in the present work, has led to a unique surface structure that favours the conversion of NO at low reaction temperatures (T= 100-200°C).

5.2.2. 0.1 wt% Pt/MgO-CeO$_2$ Catalysts

Figures 5.14 and 5.15 present the results concerning NO conversion (X_{NO}, %) and nitrogen selectivity (S_{N2}, %) obtained at 100-400°C over the three 0.1 wt% Pt/MgO-CeO$_2$ catalysts examined in the present work, for the H_2-SCR of NO.

- WI and IF Pt/MgO-CeO$_2$ catalysts

In Figure 5.14a catalytic results obtained over the Pt/MgO-CeO$_2$ (WI) catalyst are given in terms of NO conversion (X_{NO}, %) and N_2 selectivity (S_{N2}, %). The WI catalyst showed the highest NO conversion of 87.5% at 200°C and presented a wide temperature-window of operation (ΔT= 110°C), in the range of 140-250°C. This catalyst had the same T_M and ΔT with the WI and IF Pt/Al$_2$O$_3$ catalysts. The N_2 selectivity values observed on the WI catalyst were higher than 60% within ΔT (average S_{N2}= 67%), where the maximum value was observed at 250°C (S_{N2}= 74%). The same catalyst was also examined by Costa and Efstathiou [306] for the 0.25%NO/ 1%H$_2$/ 5%O$_2$/He reaction. The authors reported maximum X_{NO} of 94% at 150°C and high S_{N2} values such as 80% in the 100-200°C range and 90% for the rest of the temperature profile examined (250-400°C). The latter results are in good agreement with the ones obtained in the present work.

Figure 5.14b presents the temperature profiles of NO conversion and N_2 selectivity observed during $NO/H_2/O_2$ reaction over the 0.1 wt% Pt/MgO-CeO$_2$ (IF) catalyst, which as mentioned before has never been prepared and thus never been examined for the reaction at hand. The IF solid presented the highest NO conversion at 250°C (X_{NO}= 63%), which was the highest T_M observed in all examined catalysts, as well as the lowest X_{NO}^{max}. Moreover, the specific solid presented the narrowest temperature-window of operation

(ΔT= 100°C), in the temperature range of 200-300°C. This behaviour can be partially explained by the dispersion of Pt on the catalyst, that was determined by H_2 chemisorption at 25°C followed by TPD, and therefore by the size of Pt particles, which have a great influence on the performance of the catalyst [308]. In particular, the IF solid presented the lowest Pt dispersion (D= 63.3%), and consequently the largest Pt particles (Table 5.3). Regarding the selectivity towards N_2, the catalyst presented a relatively high average value of 78% within ΔT and S_{N2} values higher than ~70% for all examined temperatures (100-400°C).
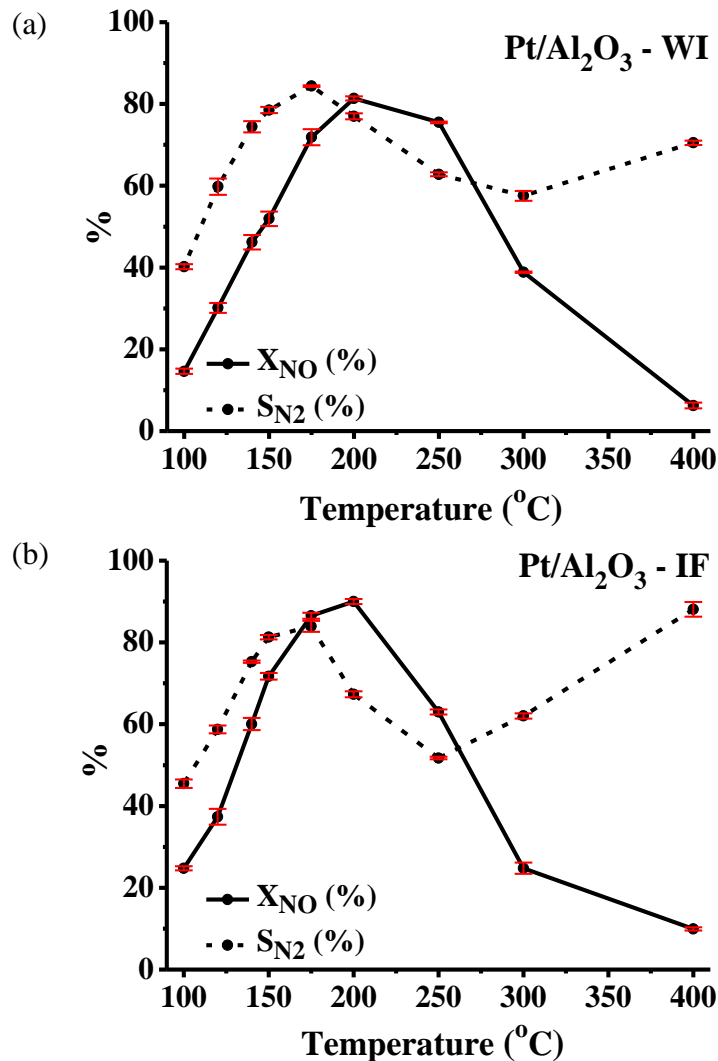
(a)

(b)
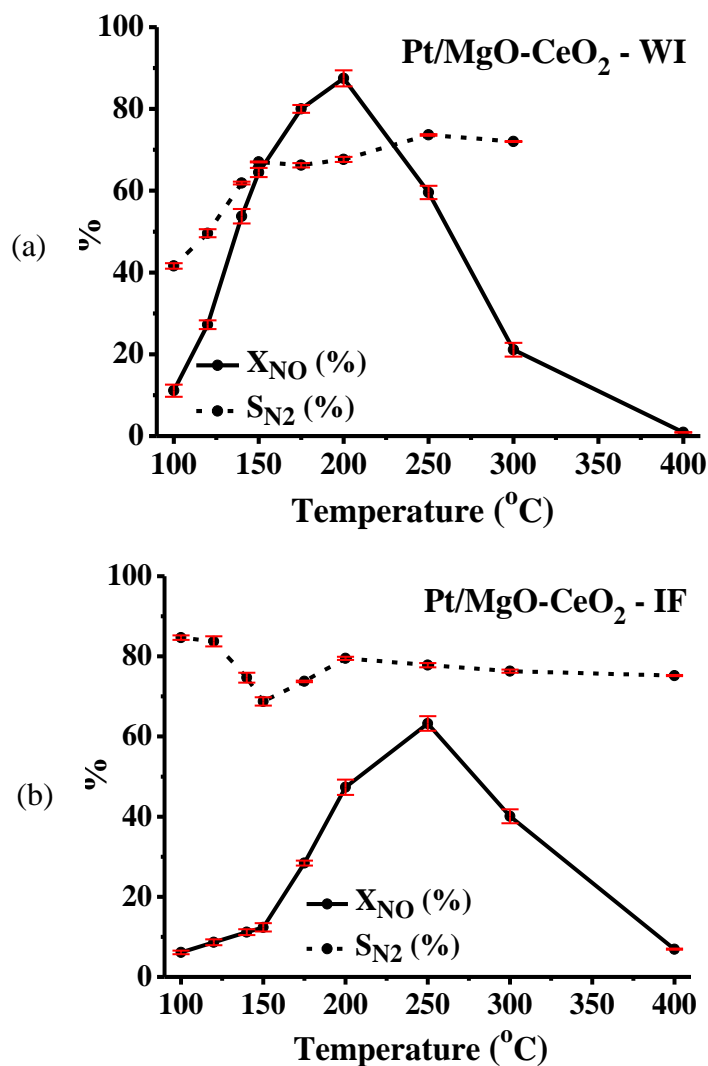
Figure 5.14: Temperature profiles of NO conversion and N_2 selectivity during $NO/H_2/O_2$ reaction over (a) 0.1 wt% $Pt/MgO-CeO_2$ (WI) and (b) 0.1 wt% $Pt/MgO-CeO_2$ (IF) catalysts. Reaction Conditions: NO= 0.05 vol%, O_2= 5 vol%, H_2= 1 vol%; m_{cat}= 0.15g, Q= 100 cm^3/min, GHSV= 80000 h^{-1}.

By comparing the catalytic performance of the two aforementioned solids, the following conclusions can be derived. The WI catalyst is superior to the IF catalyst, particularly concerning the temperature of maximum NO conversion (T_M), which is 50°C lower in

the case of the WI catalyst. Moreover, it has slightly wider ΔT (by 10°C), in a lower temperature range of 140-250°C, compared to 200-300°C of the IF solid, which is a consequence of the high T_M (250°C) of the volcano-shaped curve. It should also be noted that the larger the value of ΔT is, the better for the applicability of the catalyst under practical conditions. Although most of the Pt-based catalysts lose their catalytic activity at temperatures higher than 200°C [307], all examined catalysts in the present work kept more than half of their maximum catalytic activity at temperatures up to 250°C and the IF Pt/MgO-CeO$_2$ catalyst up to 300°C.

Regarding the activity of the Pt/MgO-CeO$_2$ catalysts within their temperature-window of operation (ΔT), the WI solid presented higher NO conversion values by ~20%, whereas regarding their behaviour to N$_2$ selectivity, the IF catalyst achieved higher S_{N2} values by 11%. In addition, the WI solid appears to be more active (by ~25%) compared to the IF catalyst at their T_M. Moreover, the WI catalyst exhibited higher NO conversion values during the low-temperature range of 100-200°C, whereas as the reaction temperature increased (250-400°C), the opposite becomes true. In particular, at 300°C, the IF catalyst presented almost double conversion of NO. It is also worth mentioning that the IF solid presented higher nitrogen selectivity values throughout the examined temperature range (100-400°C).

The fact that the WI solid presents better activity towards NO conversion but lower N$_2$ selectivity compared to the IF, may suggest that, even though the adsorbed NO$_x$ species may possess lower N–O bond strengths, are not selectively reduced to N$_2$ gas. This might be observed due to the less favoured chemical conditions encountered on the WI surface compared to the IF [33]. Therefore, it is suggested that the IF catalyst can promote the storage of higher amounts of more active NO$_x$ species that can be selectively reduced by hydrogen to form N$_2$ gas. Finally, the specific surface areas of the catalysts, does not appear to play a significant role on their catalytic activity, since the IF solid, which presented the lowest activity, was found to have the largest BET surface area (Table 5.2).

- IJP-DMP Pt/MgO-CeO$_2$ catalyst

Another innovation of this work is the synthesis of the 0.1 wt% Pt/MgO-CeO$_2$ catalyst by novel inkjet printing using a Dimatix Material Printer (DMP). The latter catalyst presented the most interesting/unique results among the Pt/MgO-CeO$_2$ solids examined. The first catalytic experiment that was conducted on the IJP-DMP catalyst showed

negligible NO conversion values ($X_{NO} < 5\%$) throughout the temperature range of 100-400°C. Therefore, the experiment was performed again within a wider temperature range as the temperatures of 60°C and 80°C were added. It is noted that the temperature of 400°C was the highest examined to avoid sintering of Pt metal. Figure 5.15 shows the temperature profiles of NO conversion and N_2 selectivity observed during $NO/H_2/O_2$ reaction ($T_R = 60$-400°C) over the printed Pt/MgO-CeO_2 catalyst. As seen the catalyst presented the lowest ever reported catalytic behaviour in terms of NO conversion. All NO conversion values were lower than 6%, whereas the selectivity towards N_2 had an average value of 82% within the temperature range of 150-400°C. It is noted that at $X_{NO} \leq 2\%$ the selectivity of the reaction cannot be defined/determined in practice.
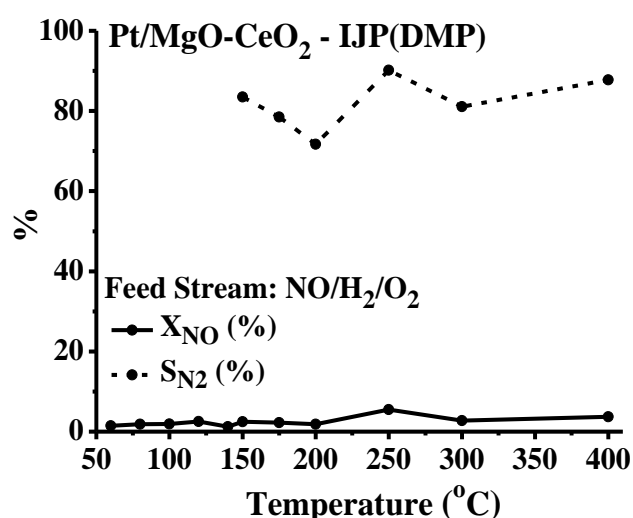
Figure 5.15: Temperature profiles of NO conversion and N_2 selectivity during $NO/H_2/O_2$ reaction over the inkjet-printed 0.1 wt% Pt/MgO-CeO_2 (IJP-DMP) catalyst. Reaction Conditions: NO= 0.05 vol%, O_2= 5 vol%, H_2= 1 vol%; m_{cat}= 0.14g, Q= 93 cm^3/min, GHSV= 80000 h^{-1}, T_R=60-400°C.

As this catalytic behaviour was never seen before in this work, further investigation took place in order to understand these unique results. Therefore, more catalytic studies were conducted, where oxygen was removed from the feed stream. It is noted that Costa et al. [306] also examined the 0.1wt% Pt/MgO-CeO_2 catalyst, prepared by wet impregnation, for the NO/H_2 reaction. The authors reported that the rate of NO conversion was increased with increasing T_R, and at 400°C the solid achieved X_{NO}= 98%. Regarding the selectivity of N_2, they reported their maximum value at 150°C (S_{N2}= 94%) and then the S_{N2} significantly decreases with increasing T_R, due to the production of NH_3. Figure 5.16a shows the temperature profiles of NO conversion and N_2 selectivity obtained during NO/H_2 reaction (T_R= 80-200°C) over the IJP-DMP Pt/MgO-CeO_2 catalyst. As shown in

Fig. 5.16a, the conversion of NO during the first two examined temperatures was below 3%, whereas as the reaction temperature increased the conversion of NO increased rapidly and at 150°C and 200°C the catalyst achieved absolute conversion (X_{NO}= 100%). It is noted that during this experiment no production of NH_3 was observed, which is a typical by-product during the reduction of NO with H_2 (in the absence of O_2), particularly at reaction temperatures lower than 200°C [306], [309], [310].
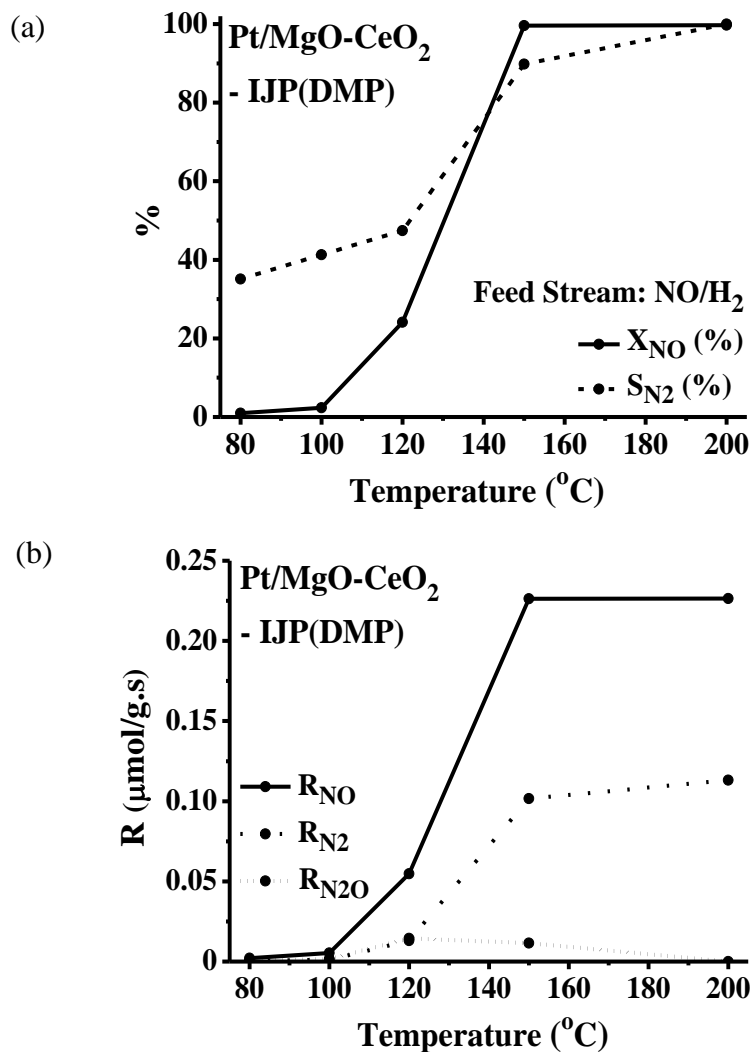
Figure 5.16: Temperature profiles of (a) NO conversion and N_2 selectivity and (b) integral rate of NO consumption, N_2 and N_2O production (μmole/g.s) observed during NO/H_2 reaction over the inkjet-printed 0.1 wt% Pt/MgO-CeO$_2$ (IJP-DMP) catalyst. Reaction Conditions: NO= 0.05 vol%, H_2= 1 vol%; m_{cat}= 0.14g, Q= 93 cm^3/min, GHSV= 80000 h^{-1}, T_R=80-200°C.

The results described above can be explained as follows: Oxygen has two main effects on the H_2-SCR process. According to Liu et al. [155], oxygen can reduce the adsorbed H on the catalyst surface, releasing active sites, and oxidize NO to form NO_x species and inhibit NH_3 generation, as well as lead to the oxidation of the active sites, which is

unfavourable to the catalytic reaction. Regarding the specific IJP-DMP catalyst, a unique behaviour has been identified as NH_3 formation is suppressed without oxygen in the feed stream. On the contrary, the reduction of NO by noble metal catalysts (Pt, Pd, Au) using only hydrogen as a reducing agent (NO/H_2) has been associated to the formation of significant amounts of NH_3 (especially at low temperatures) [309], [310]. As mentioned before, the IJP-DMP $Pt/MgO-CeO_2$ catalyst has the outstanding ability to convert NO only to N_2 and N_2O, without producing any NH_3 during the NO/H_2 reaction.

Moreover, as seen in Fig. 5.16a the N_2 selectivity profile of the IJP-DMP $Pt/MgO-CeO_2$ catalyst, during the specific catalytic studies, is remarkable. As in the case of X_{NO}, S_{N2} followed the same trend, since, at low reaction temperatures, nitrogen selectivity was below 50%, while at 150°C and 200°C the solid showed a rapid increase in N_2 selectivity achieving S_{N2}= 90% and finally S_{N2}= 100%, respectively. It is worth mentioning that these exceptional selectivity values have not been reported in the previously examined catalysts (Pt/Al_2O_3 and $Pt/MgO-CeO_2$). Therefore, it can be safely claimed that the printing protocol followed in the present work, has led to a unique surface structure that in this case favours significantly the conversion of NO at low reaction temperatures in the absence of O_2.

Fig. 5.16b indicates the integral rate of NO consumption, N_2 and N_2O production (μmole/g.s) of the NO/H_2 reaction over the printed $Pt/MgO-CeO_2$ catalyst. As seen, the R_{NO} follows the same trend as the X_{NO} (Fig. 5.16a), as the catalyst achieves the highest R_{NO} values at $T_R \geq 150$°C. In addition, the integral rate of N_2 production also follows the same trend as the S_{N2} (Fig. 5.16a), while the R_{N2O} is practically zero at 200°C as N_2 was the only product observed during the NO/H_2 reaction (S_{N2}= 100%).

In order to further examine the remarkable effect of oxygen on the catalytic behaviour of the printed solid, more catalytic studies were conducted. In particular, the effect of oxygen concentration (0-5 vol%) on the NO conversion and N_2 selectivity was examined for the $NO/H_2/O_2$ reaction at 150°C, which was the lowest temperature where X_{NO}= 100% (NO/H_2 reaction). As in the case of the previously mentioned experiments, steady-state reaction conditions were achieved (NO/H_2, $NO/H_2/O_2$) and monitored through the on-line Quadrupole Mass-spectrometer, before the O_2 concentration in the feed was changed.

Initially, 0 vol% O_2 was used, thus NO/H_2 reaction was examined, where X_{NO} was 100% and S_{N2}= 94% (S_{N2O}= 6%), as seen in Figure 5.17. Then, the concentration of oxygen was

increased to 0.5 vol% and then to 1 vol%, where X_{NO} was less than 2% (X_{NO}= 1.9% and X_{NO}= 1.4%, respectively). Afterwards, the oxygen was removed from the feed stream, where NO/H_2 reaction took place again and, as seen in Fig. 5.17, the IJP-DMP solid regained most of its catalytic activity by X_{NO}= 87% and S_{N2}= 71%. The lowest possible oxygen concentration that could be examined was 0.25 vol% O_2, which is twenty times less than the usual 5 vol% O_2 feed, and as seen in Fig. 5.17, even the slightest oxygen concentration affects drastically the catalytic behaviour of this sample (X_{NO}= 2.2%). Finally, at an oxygen concentration of 5 vol% O_2, practically zero conversion of NO was observed (X_{NO}< 1%) in accordance to Fig. 5.15. As mentioned before, at such low conversion values ($X_{NO} \leq 2$%) the selectivity of the reaction cannot be defined in practice.
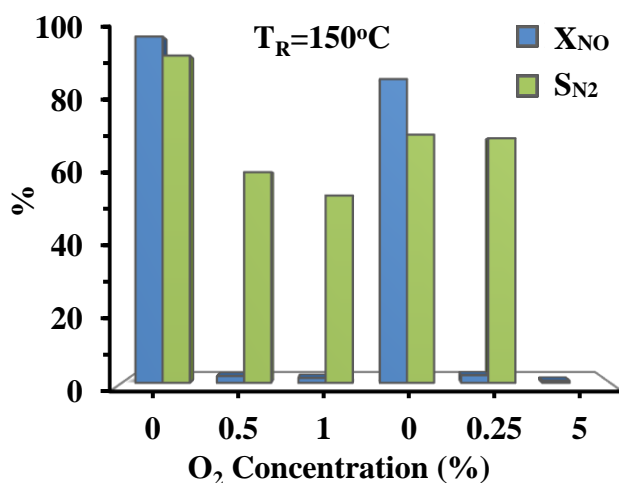
Figure 5.17: Effect of oxygen concentration on NO conversion and N_2 selectivity during $NO/H_2/O_2$ reaction over the inkjet-printed 0.1 wt% $Pt/MgO-CeO_2$ (IJP-DMP) catalyst. Reaction Conditions: NO= 0.05 vol%, H_2= 1 vol%, O_2= 0-5 vol%; m_{cat}= 0.14g, Q= 93 cm^3/min, GHSV= 80000 h^{-1}, T_R=150°C.

In addition, the concept of adding and then removing oxygen in the feed stream was further examined at 150°C using a series of NO/H_2 – $NO/H_2/O_2$ cycles. Figure 5.18 presents the effect of oxygen concentration on NO conversion and N_2 selectivity of the NO/H_2 reaction over the IJP-DMP $Pt/MgO-CeO_2$ catalyst. As seen, every time oxygen was absent from the feed the catalyst regained most of its catalytic activity in terms of both NO conversion and N_2 selectivity. As the number of cycles and O_2 concentration increased, the conversion of NO started declining to some degree and at the fifth and final cycle, NO conversion was at 51% (S_{N2}= 62%), after 22h of continuous catalytic reactions ($NO/H_2/O_2$ and NO/H_2). When oxygen was present, the same declined catalytic behaviour as Figs. 5.15 and 5.17 was observed.

Figure 5.18b shows the integral rates of NO consumption, N_2 and N_2O production (μmole/g.s), during $NO/H_2/O_2$ reaction, over the IJP-DMP $Pt/MgO\text{-}CeO_2$ catalyst, under alternating oxygen concentrations (O_2= 0-5 vol%). As in the case of X_{NO} and S_{N2} (Fig. 5.18a), when NO/H_2 reaction was taking place, R_{NO} and R_{N2} were found to be considerably high, whereas when $NO/H_2/O_2$ reaction was examined, regardless the oxygen concentration (0.25-5 vol%), R_{NO}, R_{N2} and R_{N2O} were practically zero. Higher rates of N_2 production were observed when high S_{N2} was achieved and therefore lower values of R_{N2O} were recorded.
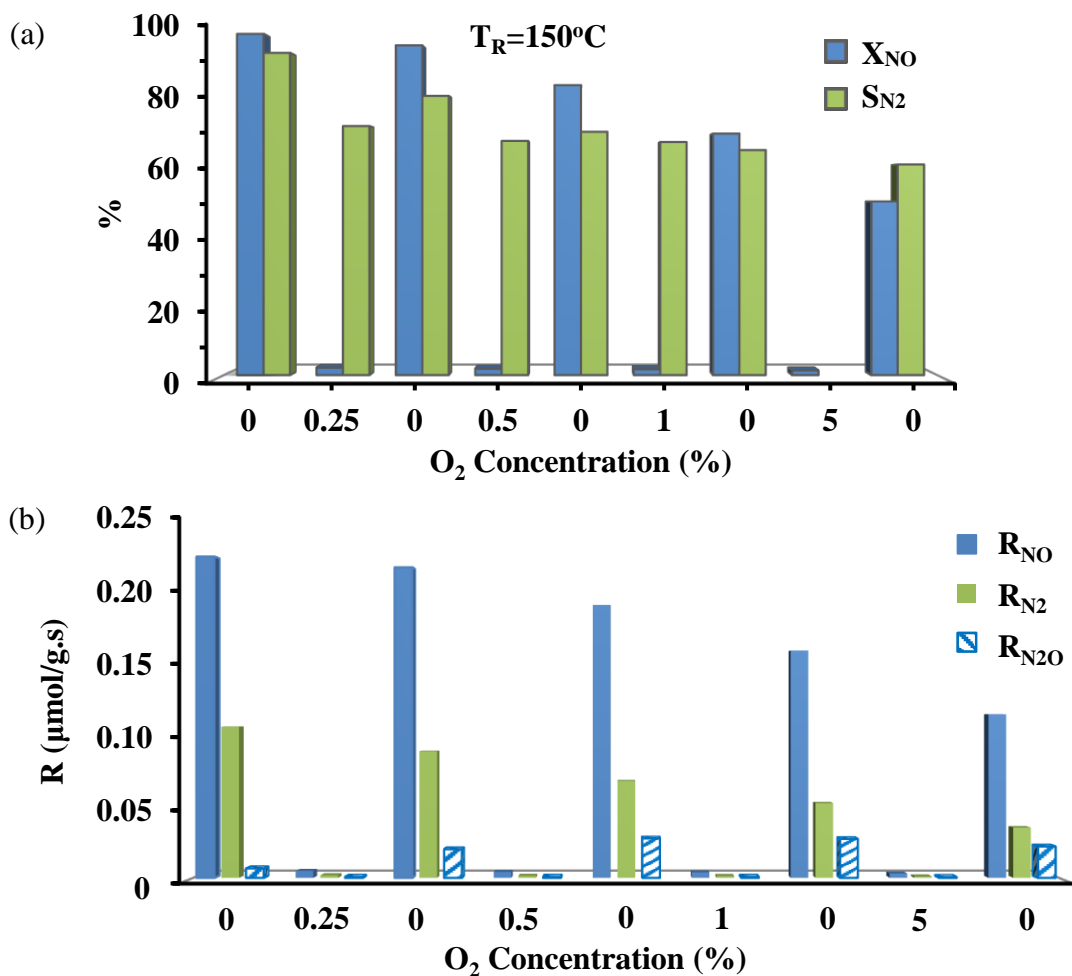
Figure 5.18: Effect of O_2 concentration on (a) NO conversion and N_2 selectivity and (b) integral rates of NO consumption, N_2 and N_2O production (μmole/g.s) during $NO/H_2/O_2$ reaction over the inkjet-printed 0.1 wt% $Pt/MgO\text{-}CeO_2$ (IJP-DMP) catalyst. Reaction Conditions: NO= 0.05 vol%, H_2= 1 vol%, O_2= 0-5 vol%; m_{cat}= 0.14g, Q= 93 cm³/min, GHSV= 80000 h⁻¹, T_R=150ºC.

By comparing the results of Fig. 5.14 to those presented in Figs 5.15-5.18, it can be safely claimed that the printing protocol that was followed in order to prepare the $Pt/MgO\text{-}CeO_2$ catalyst clearly changed the properties of the solid and created a unique surface structure (metal-support interface) that can be very easily oxidized. As it was observed, the catalyst

can be affected by even the slightest input of oxygen in the feed stream and lose its catalytic activity. The remarkable results that occur in the absence of oxygen have never been reported before according to the author's knowledge, in particular without the formation of NH_3 and limited or any N_2O. Moreover, as shown from the catalytic studies of the IJP-DMP $Pt/MgO-CeO_2$ solid, the state of Pt sites is of great significance, which is in agreement with the research reported by Burch et al. [236], since NO dissociates rapidly over reduced (metallic Pt) but not on completely oxidized Pt sites. According to Liu et al. [72], [155], the NO dissociation mechanism includes the adsorption of NO as Pt-NO and then its dissociation into adsorbed Pt-N (formation of active nitrate and NH_x^+ species) and Pt-O with a neighbouring free active site. If the active site is however covered by O_{ads} (oxidation state), then the Pt site becomes inactive for de-NO_x. Moreover, the oxidized sites can increase the density of Pt-NO, and therefore the probability to form N_2O as a secondary product. Therefore, the nature of the noble metal is crucial for the specific catalyst, as the oxidation state of Pt is of utmost importance in order to achieve exceptional catalytic behaviour in both terms of NO conversion as well as N_2 selectivity.

It should be noted that in-situ DRIFTS and combined SSITKA-DRIFTS studies were also conducted on the innovative IJP-DMP $Pt/MgO-CeO_2$ in order to further examine the influence of oxygen concentration on the adsorbed NO_x intermediate species that were formed during the $NO/H_2/O_2$ reaction on the catalytic surface (see subchapter 5.4).

5.3. Surface Reactivity Studies by Transient Methods

5.3.1. Temperature Programmed Desorption of NO (NO-TPD Studies)

The chemical interaction of NO with the surface of Pt/Al_2O_3 and $Pt/MgO-CeO_2$ solids was studied by performing adsorption of 500ppm NO at 25°C followed by TPD in He or 2%H_2/He flow as shown in Table 4.2 (Experiments A and B, subchapter 4.3). The following spectra report the number of different types of adsorbed NO species and their concentration on the catalyst surface. The peaks (some after deconvolution) presented in the figures that follow correspond to the existence of different active NO adsorption centres (heterogeneity of the surface) or different chemisorption modes of NO on the same active site [52].

5.3.1.1. 0.1 wt% Pt/Al₂O₃ Catalysts

- WI Pt/Al₂O₃ catalyst

Figure 5.19a presents the temperature-programmed desorption (TPD) profiles of NO, N_2O and N_2 in He flow obtained on the WI Pt/Al₂O₃ catalyst. In the case of NO, two peaks are observed after careful deconvolution of the original peak (straight line) and are indicated with a dotted line in Fig. 5.19b. The first peak (the numbering of desorption peaks follows the direction of increasing temperature) is centred at 162°C, while the second peak is centred at 295°C. Regarding the N_2 desorption profile (Fig. 5.19c), two main desorption peaks are observed, which are centred at 193°C and 232°C. Finally, N_2O shows a very broad band in the 30-350°C temperature range, which results in two smaller peaks at 81°C and 200°C.
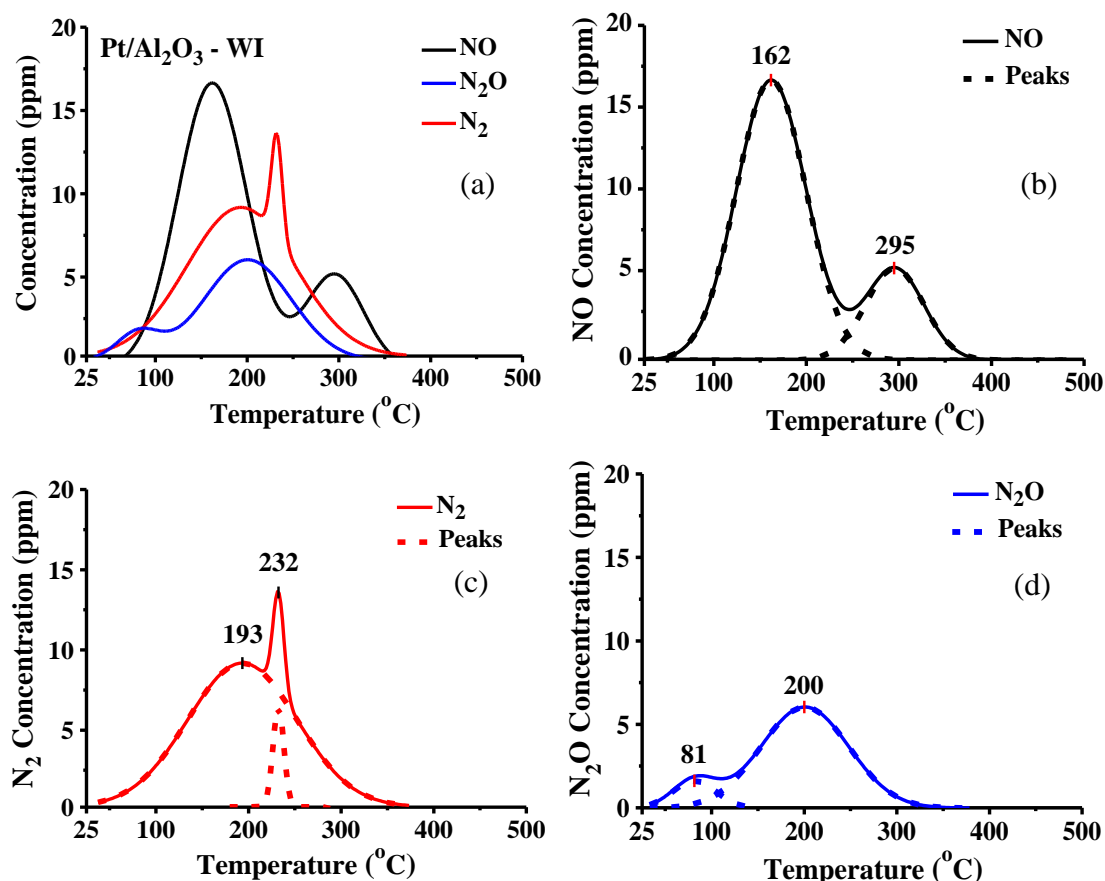
Figure 5.19: Temperature-programmed desorption (TPD) profiles of (a) NO, N_2O and N_2, (b) NO, (c) N_2 and (d) N_2O in He flow observed on the 0.1 wt% Pt/Al₂O₃ (WI) catalyst; m_{cat}= 0.15g, Q_{He}= 50 cm³/min, β= 30°C/min.

Figure 5.20, shows the TPD response curves of (a) N_2 and (b) N_2O for the same catalyst after temperature desorption under 2%H_2/He. As seen, NO was not detected during this

experiment. Two N_2 peaks were found after deconvolution at 137°C and 305°C, while N_2O was found to desorb at 98°C. The amount of N_2 desorbed during the NO-TPD under 2%H_2/He flow is considerably larger than that observed during NO-TPD in He. Moreover, N_2O was found to desorb at significantly higher temperatures during TPD in He, as compared to NO-TPD under H_2.

Since, N_2 and N_2O response curves were observed in both TPD experiments (under He and 2%H_2/He flow), it is suggested that the WI Pt/Al_2O_3 catalyst facilitates the breaking of the N-O bond even in the absence of hydrogen. It is noted that the following widely accepted elementary reaction steps (5.3-5.6) describe the formation of N_2 and N_2O on the Pt surface [311].

$$NO(g) + s \leftrightarrow NO\text{-}s \tag{5.3}$$

$$NO\text{-}s + s \rightarrow N\text{-}s + O\text{-}s \tag{5.4}$$

$$NO\text{-}s + N\text{-}s \rightarrow N_2O(g) + 2s \tag{5.5}$$

$$N\text{-}s + N\text{-}s \rightarrow N_2(g) + 2s \tag{5.6}$$

where, NO-s are adsorbed NO_x species, e.g. NO_3^-, NO_2^-, NO^+, and s is an active site where chemisorption occurs.
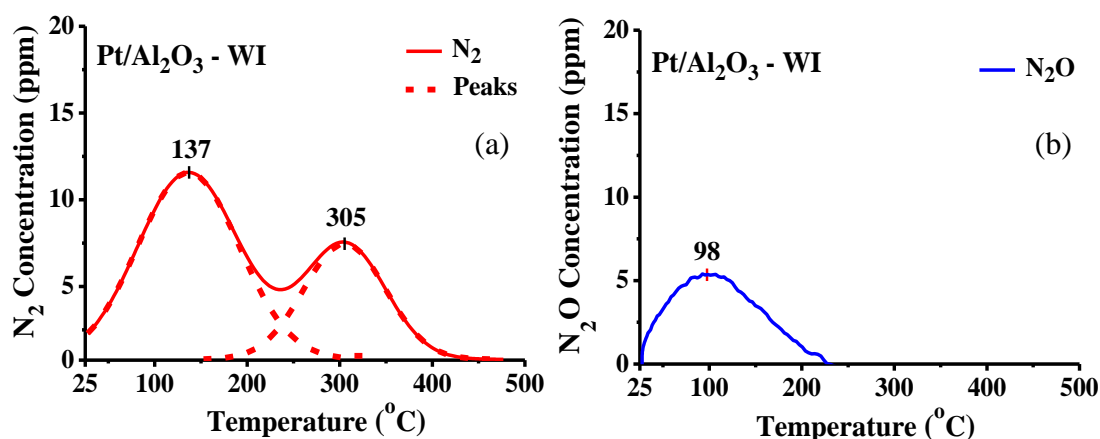
Figure 5.20: Temperature-programmed desorption (TPD) profiles of (a) N_2 and (b) N_2O in 2%H_2/He flow observed on the 0.1 wt% Pt/Al_2O_3 (WI) catalyst; m_{cat}= 0.15g, Q_{H2}= 50 cm^3/min, β= 30°C/min. [Deconvoluted peaks are presented with dotted lines].

It is worth mentioning that the total amount of desorbed N-containing species and the quantities of each product obtained (μmol/g_{cat}) over all the Pt/Al_2O_3 catalysts are presented in Table 5.4 (Exps. A and B from Table 4.2, subchapter 4.3). The total amount of N-containing species is calculated by adding the desorbed amount of NO, N_2 and N_2O, where, in the case of N_2 and N_2O, their quantities are multiplied by a factor of 2 since

they contain two N-atoms. As seen in Table 5.4, the total amount of desorbed N-containing species remains practically the same (3.2 μmol/g_{cat}) for the WI catalyst during both experiments (A and B). It can also be noticed that the quantity of desorbed N_2O has slightly increased from 0.3 μmol/g_{cat} to 0.4 μmol/g_{cat} when the TPD was carried out in 2%H_2/He flow, whereas N_2 increased significantly by ~45%. This difference can be explained through the reaction of NO_x species with adsorbed hydrogen, on the catalyst's surface, leading to the formation of N_2 and N_2O.

Table 5.4: Amount (μmol/g_{cat}) of gases desorbed during Temperature-Programmed Desorption (TPD) experiments over 0.1 wt% Pt/Al_2O_3 catalysts.

Pt/Al_2O_3	Exp.	NO (μmol/g)	N_2O (μmol/g)	N_2 (μmol/g)	Total N-containing species (μmol/g)
WI	A	0.9	0.3	0.9	3.2 (θ= 0.7)
	B	-	0.4	1.2	3.21
IF		1.9	0.4	0.7	4.0 (θ= 0.8)
IJP-Epson	A	2.1	0.9	2.0	8 (θ= 1.7)
IJP-DMP		0.8	0.2	1.5	4.1 (θ= 0.9)

At this point, it should be noted that the IF and the inkjet-printed Pt/Al_2O_3 catalysts were prepared for the first time ever during this dissertation and thus no available literature exists to compare these results. However, a comparison can be performed for the 0.1 wt% Pt/Al_2O_3 (WI) catalyst which was also studied by Costa et al. [157]. The authors studied NO chemisorption (0.5%NO/He) at room temperature followed by TPD in He flow on the same catalyst. The authors observed only NO (14.25μmol/g_{cat}) and N_2O (1.6μmol/g_{cat}) response curves, at higher amounts as compared to what was detected during the present work (Table 5.4). However, the peak maximum of all the products of the present work was observed at lower temperatures, since Costa et al. [157], observed NO desorption at 240°C, 420°C and 470°C, while a small N_2O peak was found in the range of 120-230°C and a broader one at 535°C. Furthermore, the N_2O produced in the high-temperature range of 425-625°C was justified by the authors as a result of the reaction of readsorbed NO (after being desorbed from the support, alumina) with N atoms on Pt according to 5.3 - 5.5 elementary reaction steps. Consequently, since N_2O in the present work was desorbed earlier (T< 300°C) on all Pt/Al_2O_3 solids, then it can be assumed that NO was probably not readsorbed on the catalysts' surface after desorption. Finally, it should be noted that the differences in the desorbed amounts and the peak maximum of the products are most

likely due to the difference in NO concentration during chemisorption, as the authors used ten times higher NO concentration (0.5% NO) compared to the present work (0.05% NO).

- IF Pt/Al$_2$O$_3$ catalyst

Figure 5.21 presents the Temperature Programmed Desorption profiles of NO, N$_2$ and N$_2$O obtained on the 0.1 wt% Pt/Al$_2$O$_3$ (IF) sample under He flow. As seen in Fig. 5.21b, two main NO desorption peaks are obtained, which are centred at 201°C and 264°C, with the latter appearing as a shoulder at the descending part of the initial peak. Also, very broad and small N$_2$ (T$_{M1}$= 183°C and T$_{M2}$= 292°C) and N$_2$O (T$_M$= 170°C) peaks are observed (Fig. 5.21c and Fig. 5.21d). As reported in Table 5.4, the total amount of desorbed N-containing species was found to be 4 µmol/g$_{cat}$, of which 47.4% was desorbed NO, 34.1% was desorbed N$_2$ and the rest was N$_2$O.
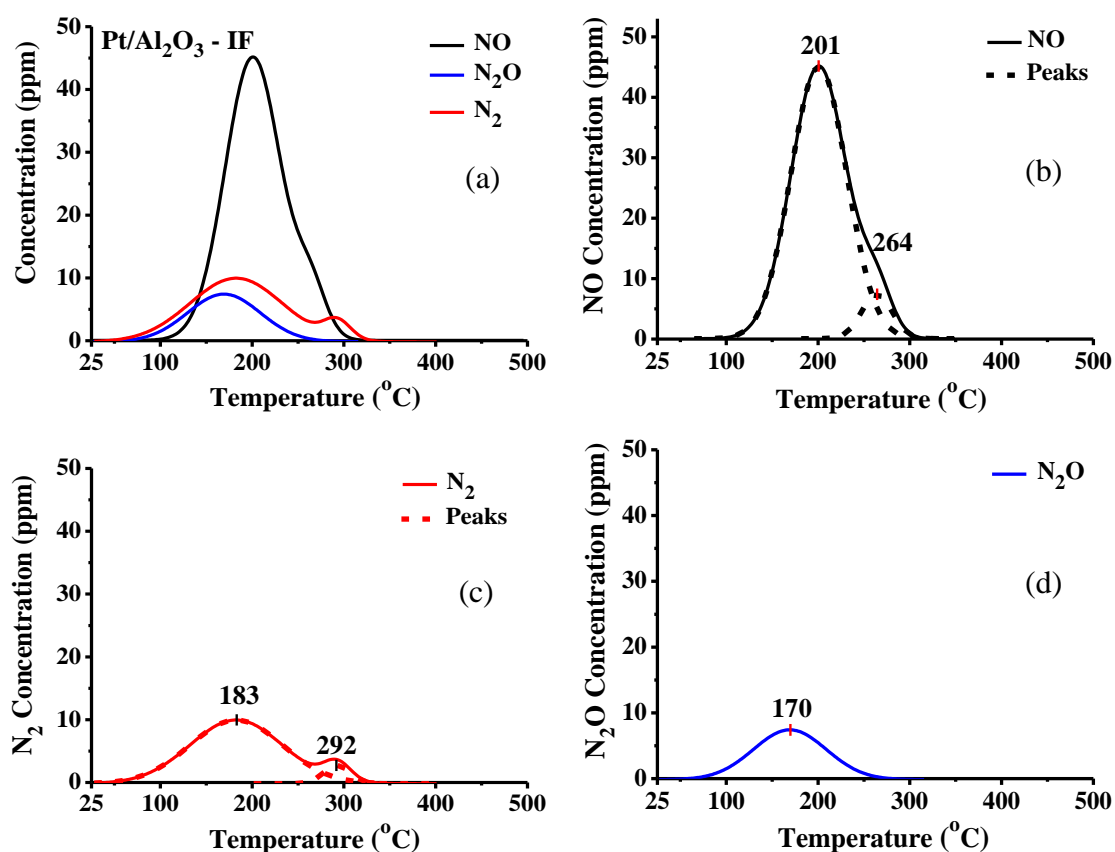
Figure 5.21: Temperature-programmed desorption (TPD) profiles of (a) NO, N$_2$O and N$_2$, (b) NO, (c) N$_2$ and (d) N$_2$O in He flow observed on the 0.1 wt% Pt/Al$_2$O$_3$ (IF) catalyst; m$_{cat}$= 0.15g, Q$_{He}$= 50 cm^3/min, β= 30°C/min.

- IJP-Epson Pt/Al$_2$O$_3$ catalyst

Figure 5.22 demonstrates the desorption profiles of NO, N$_2$ and N$_2$O after the NO-TPD experiment under He flow on the inkjet-printed 0.1 wt% Pt/Al$_2$O$_3$ (IJP-Epson) catalyst.

In the case of NO, two distinct peaks, are observed in Fig. 5.22b after deconvolution. The two peaks are centred at 146°C and 197°C. Moreover, two N_2 desorption peaks are obtained, which are centred at 73°C and 172°C, as seen in Fig. 5.22c. The first N_2 peak is observed at a significantly lower temperature (73°C) compared to the previously analyzed WI (193°C) and IF (183°C) catalysts, by 120°C and 110°C, respectively. Also, N_2O is observed in the broad range of 25-270°C, with the band centred at 130°C. As far as the desorbed total amount of N-containing species, the IJP-Epson catalyst desorbed 8 μmol N/g, which is also higher than the amount desorbed during the same experiment on WI and IF solids, as seen in Table 5.4.
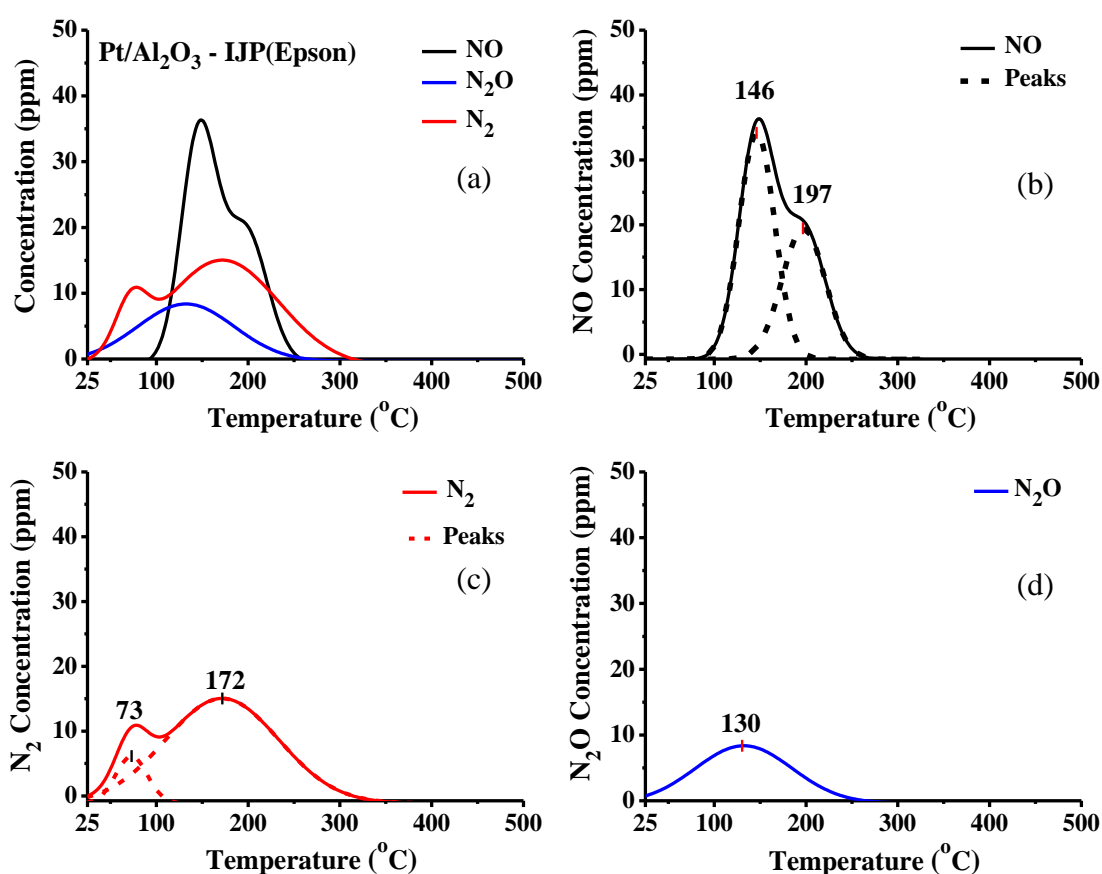
Figure 5.22: Temperature-programmed desorption (TPD) profiles of (a) NO, N_2O and N_2, (b) NO, (c) N_2 and (d) N_2O in He flow observed on the printed 0.1 wt% Pt/Al_2O_3 (IJP-Epson) catalyst; m_{cat}= 0.0981g, Q_{He}= 50 cm³/min, β= 30°C/min.

- IJP-DMP Pt/Al_2O_3 catalyst

The temperature-programmed desorption profiles of desorbed NO, N_2O and N_2 obtained on the IJP-DMP Pt/Al_2O_3 catalyst under He flow are comparatively presented in Figure 5.23a. As seen in Fig. 5.23b, NO (0.8 μmol/g) is desorbed in two broad peaks in the range of 25-185°C and 175-375°C. The first peak is analyzed into two additional peaks, after

deconvolution, which are centred at 90°C and 137°C, while the last peak is observed at higher temperatures (T_M= 269°C). On the contrary, N_2 (Fig. 5.23c) starts to desorb immediately as the temperature begins to increase from room temperature, according to experiment A (Table 4.2, subchapter 4.3). The IJP-DMP solid presented three very sharp N_2 peaks, which are centred at 28°C, 34°C and 61°C. It is noted that all N_2 peaks (1.5 µmol/g) appeared at lower temperatures, compared to the rest of the Pt/Al_2O_3 catalysts examined. Finally, the N_2O desorption profile (Fig. 5.23d) shows only one broad and small N_2O peak (0.2 µmol/g), like the majority of the Pt/Al_2O_3 solids, which is centred at 165°C. The total amount of desorbed N-species, obtained on the IJP-DMP Pt/Al_2O_3 solid, under He flow, was found to be 4.15 µmol N/g.
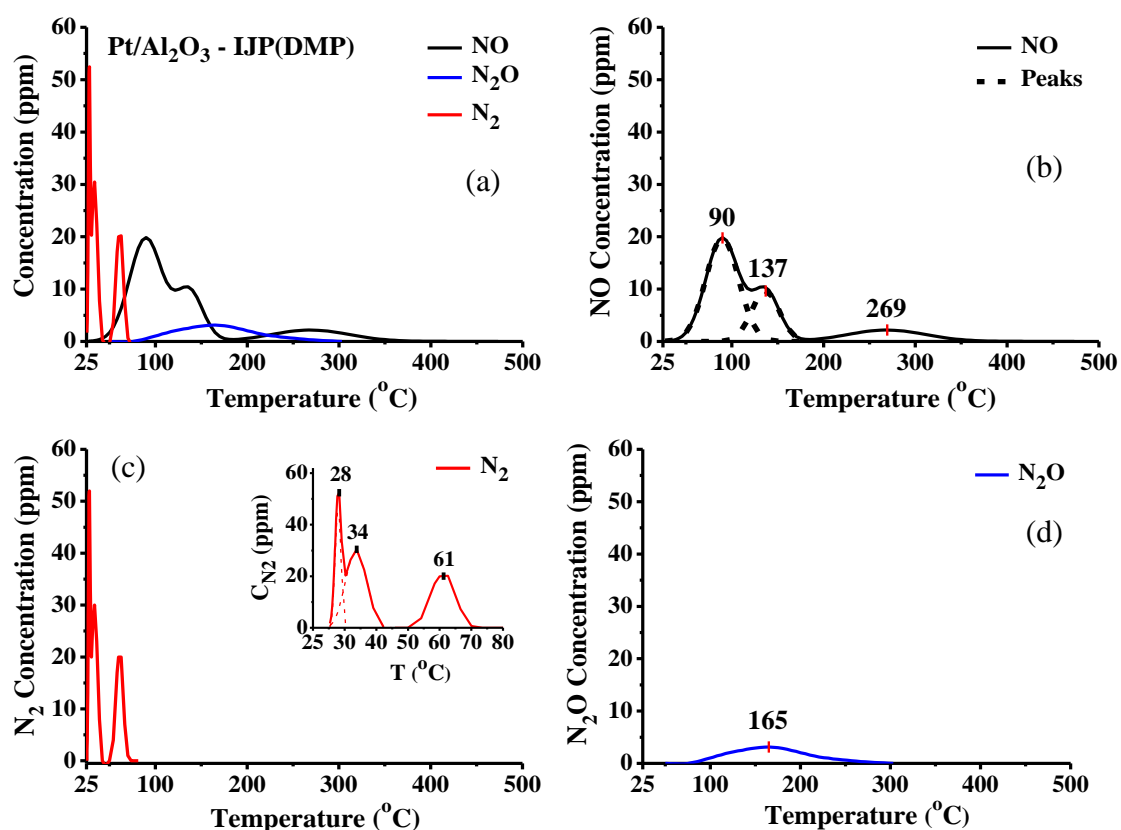
Figure 5.23: Temperature-programmed desorption (TPD) profiles of (a) NO, N_2O and N_2, (b) NO, (c) N_2 and (d) N_2O in He flow observed on the printed 0.1 wt% Pt/Al_2O_3 (IJP-DMP) catalyst; m_{cat}= 0.15g, Q_{He}= 50 cm^3/min, β= 30°C/min.

It should be noted that all Pt/Al_2O_3 catalysts were examined in both experiments, A and B, under He and 2%H_2/He flow, respectively. However, only for the WI catalyst the desorbed peaks where observed during the NO-TPD experiment under 2%H_2/He flow (Exp. B). It is noted that no observation was made for the rest of the catalysts during the

particular experiment, probably due to the fact that the products (gases) were desorbed at very low temperatures.

By comparing the TPD results obtained on the four different Pt/Al_2O_3 catalysts, several differences are noted. A distinct difference between the Pt/Al_2O_3 catalysts during the experiment under He flow is the N_2 profile observed on the IJP-DMP catalyst. The sharp N_2 peaks that were obtained on the specific catalyst, as well as the lowest T_M of the peaks have not been observed on the rest of the solids examined in the present work or any other catalysts reported in the literature. Moreover, the amount of desorbed NO, N_2O and N_2 over the four differently synthesized catalysts is substantially different. The total amount of N-containing species ($\mu mol/g_{cat}$), as well as the amount of desorbed N_2 of the Epson printed catalyst, is greater than the other catalysts. In fact, the IJP-Epson solid desorbed two and a half times more total N-containing species than the WI catalyst, two times more than the IF solid and almost two times more compared to the IJP-DMP catalyst.

Furthermore, since N_2 and N_2O desorption curves were observed during NO-TPD under He flow on all Pt/Al_2O_3 catalysts, then, it is suggested that the Pt/Al_2O_3 catalysts facilitate the dissociation of the N-O bond even in the absence of hydrogen. It is also worth mentioning that two adsorbed states of NO are expected to be formed on the surface of each Pt/Al_2O_3 catalyst, since two clear NO peaks were observed, except in the case of the IJP-DMP printed catalyst, where there are probably three states of NO on the solid due to the three NO peaks observed (Fig. 5.23b). Some of the adsorbed species are expected to have a stronger interaction with the active sites of the catalysts' surface which can be concluded from the higher desorption temperatures of the corresponding peaks, observed during the TPD experiments. Specifically, as seen in Figure 5.24, which shows the temperature of peak maximum, T_M, for all desorbed NO peaks observed on all Pt/Al_2O_3 catalysts, the WI solid presented the highest T_M (295^oC), whereas the IJP-DMP catalyst presented the lowest T_M (90^oC). In addition, NO desorbs completely by $T<280^oC$ in the case of the Epson printed catalyst, compared to the rest of the catalysts where NO desorbs completely at higher temperatures, i.e., by 350^oC (IF), 375^oC (IJP-DMP) and 400^oC (WI).
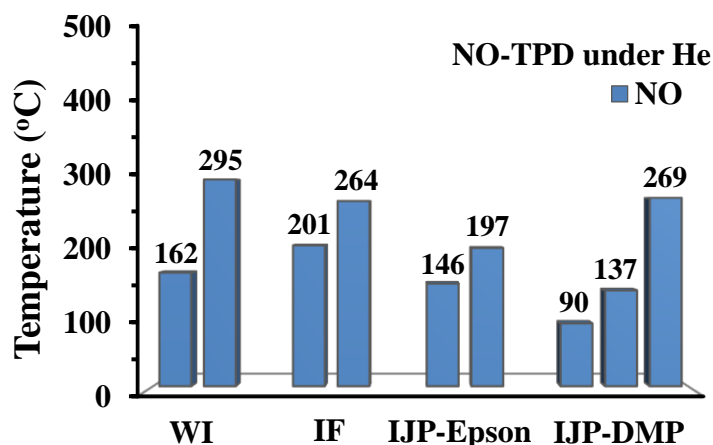
Figure 5.24: Desorption temperature of NO peaks observed under He flow on all Pt/Al_2O_3 catalysts.

Moreover, the NO peaks not only desorbed at different temperature ranges but in different concentrations as well. This outcome indicates that the synthesis process of the Pt/Al_2O_3 catalysts has a significant effect on the nature and intensity of the metal (Pt)-support interactions influencing the binding energy of certain type(s) of NO_x species and their reactivity characteristics through short-range electronic interactions, affecting the atoms of the metal or the metal-support interface [298], [306], [312]. It is really important to point out that the chemical interaction of NO with Pt is strongly influenced by the nature of Pt atoms interaction with the support [306]. This argument was invoked to explain the different shape and position of the NO and N_2 curves of the IJP-DMP Pt/Al_2O_3 solid, as compared to the rest of the catalysts. Furthermore, the NO-TPD peaks observed in Figures 5.19 - 5.23 can be justified based on the fact that NO chemisorption on metal oxides, such as Al_2O_3, proceeds with the participation of metal cations, oxygen anions, and oxygen vacant sites, which form various kinds of nitrate and nitrite structures as suggested by Costa et al. [306].

5.3.1.2. 0.1 wt% Pt/MgO-CeO₂ Catalysts

- WI $Pt/MgO-CeO_2$ catalyst

As in the case of Pt/Al_2O_3 catalysts, the chemical interaction of NO with the surface of 0.1 wt% $Pt/MgO-CeO_2$ catalysts was also studied by performing adsorption of 500ppm NO at 25°C followed by TPD in He flow (Exp. A) or 2%H_2/He flow (Exp. B) as shown in Table 4.2 (subchapter 4.3). Figure 5.25a shows the TPD profiles of desorbed NO, N_2O and N_2 obtained on the WI $Pt/MgO-CeO_2$ catalyst (Exp. A). As seen, the desorption profiles of NO (Fig. 5.25b) and N_2O (Fig. 5.25d) exhibit similar peaks which are centred

at 95°C and 105°C, respectively. In the case of N_2 spectrum, it presents multiple peaks in the range of ~30-300°C, which are centred at 83°C, 136°C, 168°C and 204°C (after deconvolution).

Figure 5.25: Temperature-programmed desorption (TPD) profiles of (a) NO, N_2O and N_2, (b) NO, (c) N_2 and (d) N_2O in He flow obtained on the 0.1 wt% Pt/MgO-CeO$_2$ (WI) catalyst; m_{cat}= 0.15g, Q_{He}= 50 cm^3/min, β= 30°C/min.

Figure 5.26 shows the TPD response curves of NO, N_2 and N_2O observed on WI Pt/MgO-CeO$_2$ after NO adsorption and desorption in 2%H_2/He. The desorption profile includes a distinct N_2 band, while the amount of desorbed N_2O (T_M= 70°C) is a lot smaller and NO (T_M= 72°C) is negligible. The absence of desorbed NO from the TPD profile implies that the majority of adsorbed NO_x species react with the carrier gas (2%H_2/He) to produce N_2 (Eq. 5.6) and N_2O (Eq. 5.5). The deconvolution of the desorbed N_2 band, which was found to range in the area of 25-250°C, resulted into three peaks which are centred at 69°C, 99°C and 117°C (Fig. 5.26b).
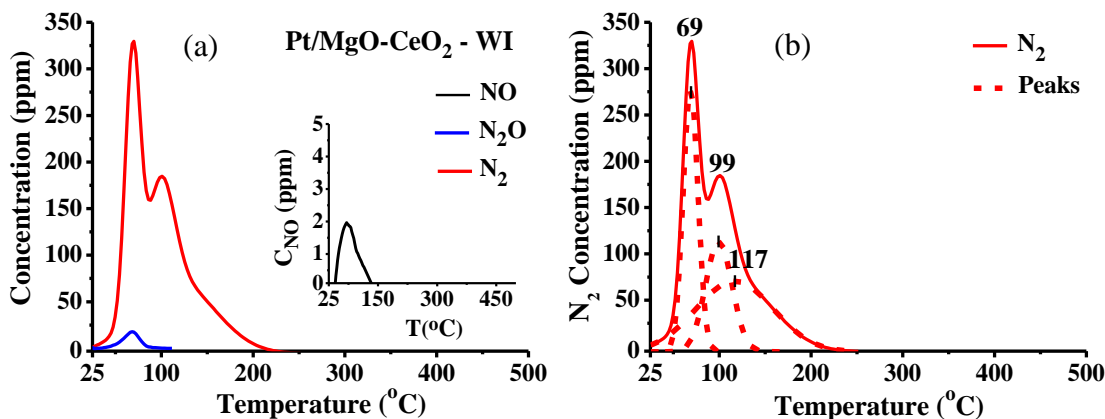
Figure 5.26: Temperature-programmed desorption (TPD) profiles of (a) NO, N_2O and N_2 and (b) N_2 in 2% H_2/He flow obtained on the 0.1 wt% Pt/MgO-CeO$_2$ (WI) catalyst; m_{cat}= 0.15g, Q_{H2}= 50 cm^3/min, β= 30ºC/min.

Comparing the above (Fig. 5.26) to the previous results (Fig. 5.25), it can be seen that during TPD in H_2/He flow, the desorption of NO and N_2O is observed at lower temperatures, i.e., ΔT= ~25ºC and ΔT= 35ºC, respectively. Furthermore, the first N_2 peak of Fig. 5.26b (T_M= 69ºC) was sharper and larger than the first N_2 peak of Fig. 5.25c (T_M= 83ºC). Moreover, similar observations are obtained when comparing the rest of the N_2 peaks obtained after NO adsorption and desorption in He or H_2/He flow. Consequently, it can be clearly stated that there is a shift of the peaks to lower temperatures when desorption is carried out in H_2/He. It is suggested that a hydrogen-assisted effect takes place on the dissociation of NO, as it can lower the strength of the Pt-NO bond [157], [311]. By combining the reaction steps of 5.3 and 5.4 with 5.7, the reaction step of 5.8 is facilitated, which is the hydrogen-assisted N-O dissociation step [313], [314].

$$H_2(g) + 2s \leftrightarrow 2H\text{-}s \tag{5.7}$$

$$NO\text{-}s + H\text{-}s \rightarrow N\text{-}s + OH\text{-}s \tag{5.8}$$

It is noted that the total amount of desorbed N-containing species and the specific quantities obtained (μmol/g_{cat}) for each desorbed gas on all Pt/MgO-CeO$_2$ catalysts examined are presented in Table 5.5 (Exps. A and B). As stated before, the total amount of desorbed N-containing species remains the same (20.9 μmol/g_{cat}) for the WI catalyst during both experiments (A and B). It can also be noticed that the quantity of desorbed NO and N_2O has decreased significantly when the TPD was carried out by 2% H_2/He flow, whereas the amount of N_2 increased by 35%.

Table 5.5: Amount (μmol/g$_{cat}$) of gases desorbed during Temperature-Programmed Desorption (TPD) experiments over 0.1 wt% Pt/MgO-CeO$_2$ catalysts.

Pt/MgO-CeO$_2$	Exp.	NO (μmol/g)	N$_2$O (μmol/g)	N$_2$ (μmol/g)	NH$_3$ (μmol/g)	Total N-containing species (μmol/g)
WI	A	1.4	2.2	7.5	-	20.9 (θ= 4.4)
	B	0.1	0.3	10.2	-	20.9
IF	A	1.0	7.2	23.9	-	63.2 (θ=19.5)
	B	0.6	0.1	28.9	4.77	63.3
IJP-DMP	A	14.4 (θ= 3)	3.5	7.0	-	35.4 (θ= 7.4)
	B	6.1	7.0	7.6	-	35.3

As with the case of Pt/Al$_2$O$_3$ catalysts, the IF and IJP-DMP Pt/MgO-CeO$_2$ catalysts were prepared for the first time during this dissertation and thus no available literature exists to compare these results. The only comparison can be made for the WI 0.1 wt% Pt/MgO-CeO$_2$ catalyst, which was also studied by Costa et al. [306]. NO-TPD experiments under He flow were also conducted on the 0.1 wt% Pt/MgO-CeO$_2$ solid, where 0.5%NO was adsorbed at 25°C (10 times higher NO concentration than the one used in this work). It is reasonable to expect that both the adsorption and desorption kinetics would have been significantly different in the work of Costa et al., due to the high concentration of NO used during adsorption. The authors reported only two large NO desorption peaks, one centred at 370°C with a shoulder at the rising part of it, and the second peak at 515°C. On the contrary, during this work, only one NO peak was observed at T$_M$= 95°C, as well as N$_2$ and N$_2$O response curves, which were not reported by the authors [306]. However, the Pt/MgO-CeO$_2$ catalyst of the literature desorbed about 4.5 times more total N-containing species compared to the WI catalyst within this work. In addition, the authors examined the support of the catalyst (MgO-CeO$_2$) and reported that it desorbs 7 μmole NO/g$_{cat}$, as well as 5.4 μmol N$_2$O/g$_{cat.}$ This result was justified by the fact that NO chemisorption on metal oxides proceeds with the participation of metal cations, oxygen anions, and oxygen vacant sites, which form various kinds of nitrate and nitrite structures as previously discussed.

- IF Pt/MgO-CeO$_2$ catalyst

NO-TPD experiments under He and 2%H$_2$/He flow were also conducted on the IF Pt/MgO-CeO$_2$ catalyst. Figure 5.27a presents the spectrum of NO, N$_2$ and N$_2$O obtained under He flow on the latter catalyst. As seen in Fig 5.27b, the profile of NO presents only

one peak (1 µmol/g) in the low-temperature range of 50-160°C which is centred at 98°C. N_2 was desorbed in a very broad band (T= 40-400°C), which was deconvoluted into three peaks that are centred at 149°C, 183°C and at 279°C. The IF catalyst resulted in the highest desorbed amount of N_2 (23.9 µmol/g) compared to the rest of the Pt/MgO-CeO$_2$ catalysts, as seen in Table 5.5 (Exp. A). Moreover, this quantity attributes to 75.5% of the total amount of N-containing species (63.2 µmol/g). Fig 5.27d shows the response curve of N_2O (7.2 µmol/g), which after deconvolution revealed two peaks, one small peak at T_M= 81°C and a broader one at T_M= 124°C (25-225°C).
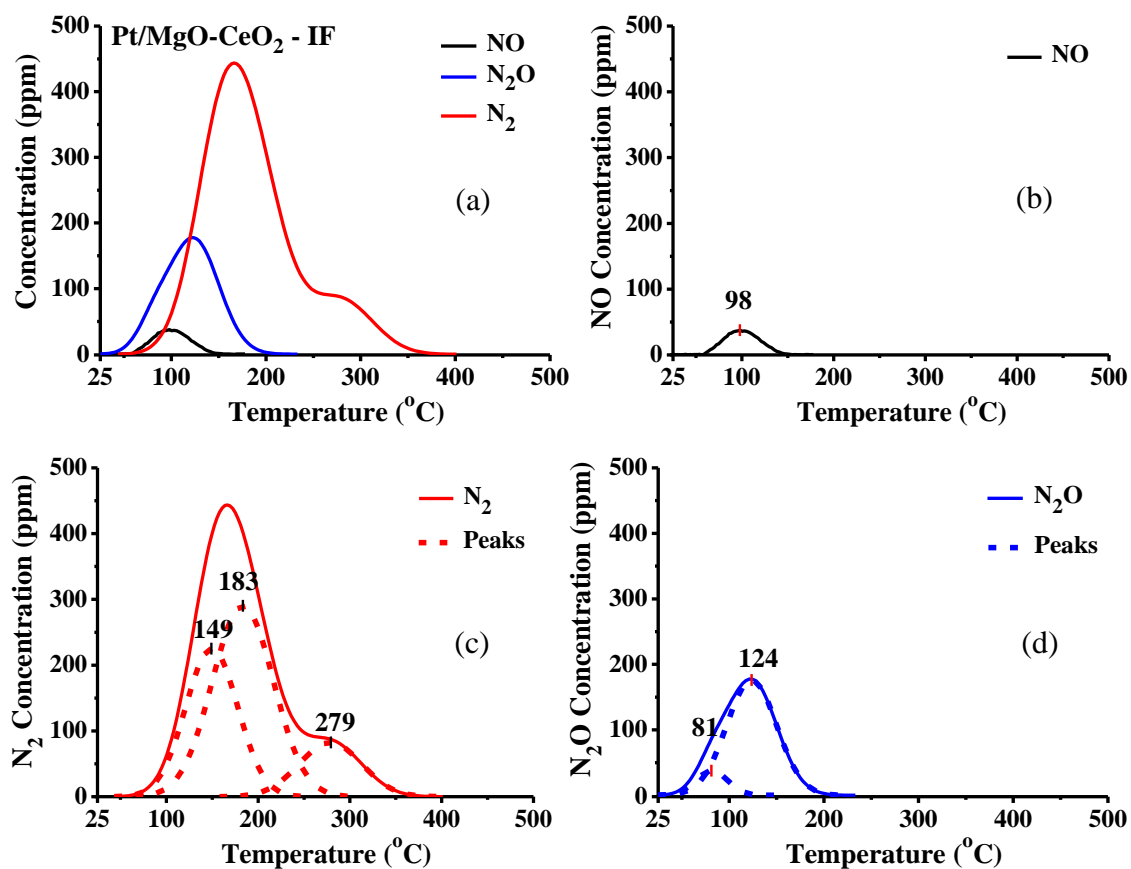
Figure 5.27: Temperature-programmed desorption (TPD) profiles of (a) NO, N_2O and N_2, (b) NO, (c) N_2 and (d) N_2O in He flow obtained on the 0.1 wt% Pt/MgO-CeO$_2$ (IF) catalyst; m_{cat}= 0.15g, Q_{He}= 50 cm^3/min, β= 30°C/min.

Figure 5.28 shows the TPD profiles that were obtained on the IF solid under 2%H$_2$/He flow. As seen in Fig. 5.28a, the NO desorption profile shows initially a small peak (T_M= 90°C) and afterwards a relatively broad peak ranging between 100°C and 300°C, which is analysed in two smaller peaks at 141°C and 180°C. N_2O is desorbed at lower temperatures with a small peak at T_M= 68°C (Fig. 5.28a), which is the same temperature of which the first N_2 peak (Fig. 5.28b) is observed. In addition, the desorption profile of

N_2 presents two more peaks at 93°C and at 122°C. Nitrogen is observed at much higher concentrations (Fig. 5.28b), compared to NO and N_2O, which translates to the highest amount (28.9 μmol/g) observed during the NO-TPD studies of the present work, as seen in Tables 5.4 and 5.5. It is worth mentioning that this amount consists of 91% of the total amount of N-containing species (63.3 μmol/g) of the IF solid.

In addition to NO, N_2O and N_2, the specific catalyst desorbed a significant amount of NH_3 at relatively high temperatures with T_M= 398°C (Fig. 5.28b). The desorbed amount of NH_3 attributes to 7.5% of the total amount of N-containing species. It is noted that NH_3 has not been observed in any of the NO-TPD experiments (He or 2%H_2/He flow) of this work (Pt/Al_2O_3 or Pt/MgO-CeO_2). It is suggested that NH_3 may have been produced through the reaction of the excess and not fully converted hydrogen (2%H_2/He flow) with the N-containing species [314], according to the following elementary reaction steps (5.9-5.12) combined with Eq. 5.3, 5.4 and 5.7 [33].

$$NO\text{-}s + H\text{-}s \rightarrow NH\text{-}s + O\text{-}s \qquad (5.9)$$

$$O\text{-}s + H\text{-}s \rightarrow OH\text{-}s \qquad (5.10)$$

$$NH\text{-}s + OH\text{-}s \rightarrow NH_2\text{-}s + OH\text{-}s \qquad (5.11)$$

$$NH_2\text{-}s + OH\text{-}s \rightarrow NH_3(g) + O\text{-}s + s \qquad (5.12)$$
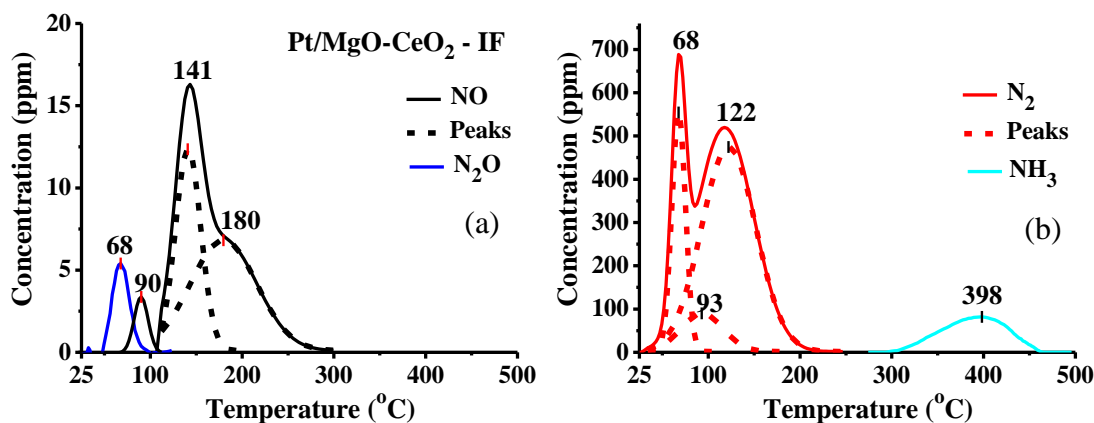
Figure 5.28: Temperature-programmed desorption (TPD) profiles of (a) NO and N_2O and (b) N_2 and NH_3 in 2%H_2/He flow obtained on the 0.1 wt% Pt/MgO-CeO_2 (IF) catalyst; m_{cat}= 0.15g, Q_{H2}= 50 cm^3/min, β= 30°C/min.

- IJP-DMP Pt/MgO-CeO_2 catalyst

The chemical interaction of NO with the surface of the IJP-DMP Pt/MgO-CeO_2 catalyst was also studied by adsorption of NO at room temperature followed by TPD in He and 2%H_2/He flow. Figure 5.29a presents the TPD response curves of NO, N_2O and N_2 under

He flow. As seen in Fig. 5.29b, two NO desorption peaks are obtained at T_M= 114°C and T_M= 156°C, in the range of 40-275°C. Two smaller N_2 peaks appear in the temperature range of 25-280°C and are centred (after deconvolution) at 121°C and at 189°C (Fig. 5.29c). Fig. 5.29d shows the N_2O response curve which (after deconvolution) shows two relatively small peaks centred at T_M= 73°C and T_M= 134°C. These peaks are smaller than the respective NO and N_2 peaks, which is also verified by the desorbed amount of NO (14.4 μmol/g) and N_2 (7 μmol/g) which is four times and two times more than the amount of desorbed N_2O (3.5 μmol/g), respectively. It can be assumed that since the majority of the adsorbed NO is desorbed without dissociation, then probably Eq. 5.4 (NO dissociation) is the slow step in the reaction of NO dissociation in order to form the NO_x intermediates [33].
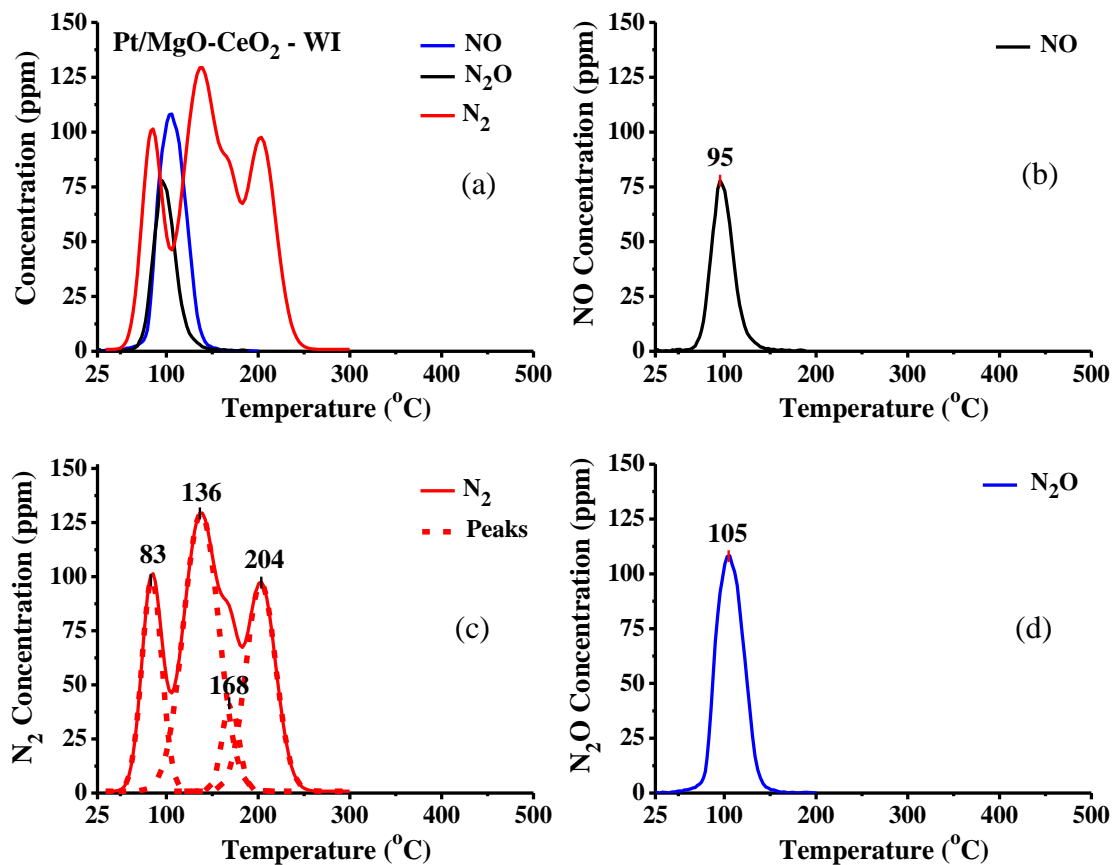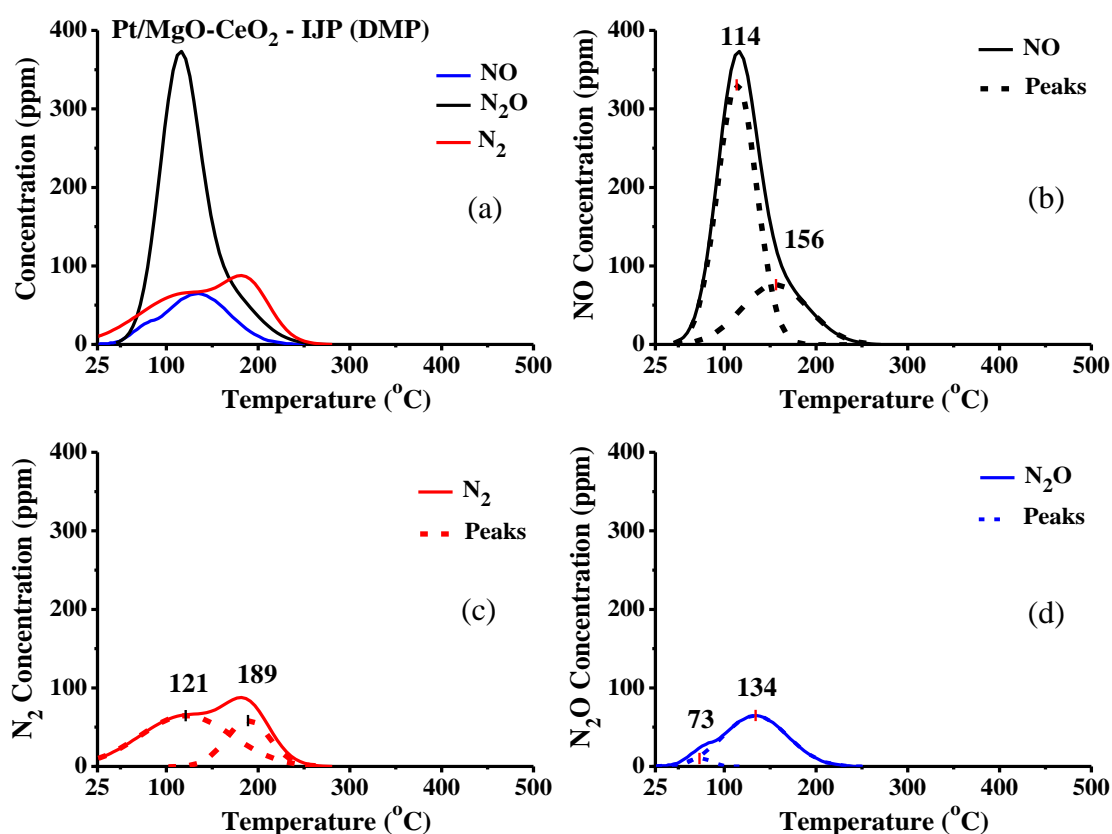

Figure 5.29: Temperature-programmed desorption (TPD) profiles of (a) NO, N_2O and N_2, (b) NO, (c) N_2 and (d) N_2O in He flow obtained on the printed 0.1 wt% Pt/MgO-CeO$_2$ (IJP-DMP) catalyst; m_{cat}= 0.14g, Q_{He}= 50 cm³/min, β= 30°C/min.

In the case of NO-TDP under 2%H$_2$/He (Figure 5.30a), all N-containing species, were desorbed by the temperature of 130°C, which is ~140°C lower compared to the NO-TPD experiment under He flow. Therefore, a hydrogen assisted effect is invoked to explain the significant shifts of the desorbed peaks to lower temperatures. As seen in Fig. 5.30b, the

NO desorption profile presents two peaks centred at $T_M = 80^oC$ and $T_M = 96^oC$. Fig. 5.30c shows a distinct N_2 peak in the low-temperature range of 45-110^oC with a shoulder at the rising part. After deconvolution, two N_2 peaks are obtained, a small one at $T_M = 65^oC$ and a bigger at $T_M = 82^oC$. Finally, the N_2O desorption profile (Fig. 5.30d), shows two peaks which are centred at $T_M = 91^oC$ and at $T_M = 106^oC$ and are similar, in shape, to the desorbed NO peaks, with $T_M^{N2O} > T_M^{NO}$ by 10^oC for both peaks. Regarding the desorbed amount of N-species, which is reported in Table 5.5, the IJP-DMP Pt/MgO-CeO$_2$ catalyst, desorbed the same total amount of N-containing species (35 μmol/g) during both experiments (A and B). The main difference between the two experiments is mainly the decrease of the amount of desorbed NO by more than two times, and the increase of the amount of N_2O by two times when the desorption was performed under 2%H$_2$/He flow.
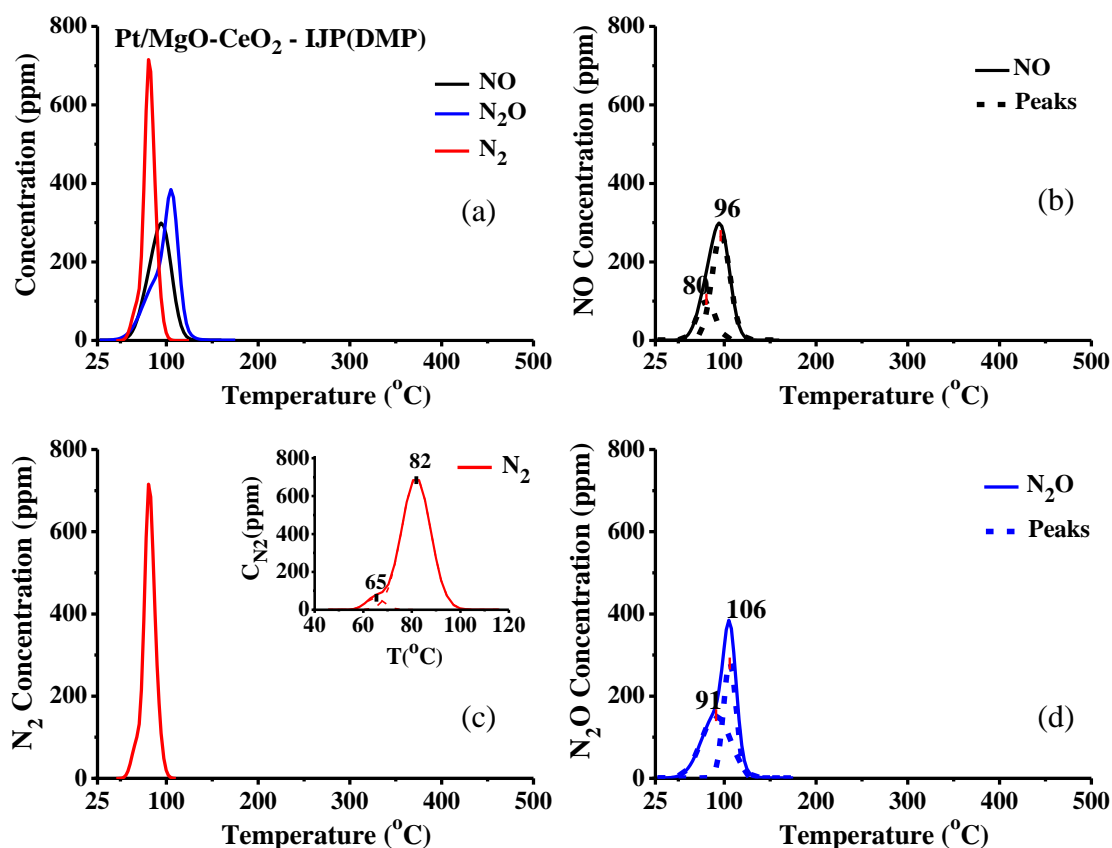
Figure 5.30: Temperature-programmed desorption (TPD) profiles of (a) NO, N_2O and N_2, (b) NO, (c) N_2 and (d) N_2O in 2%H$_2$/He flow obtained on the printed 0.1 wt% Pt/MgO-CeO$_2$ (IJP-DMP) catalyst; $m_{cat} = 0.14g$, $Q_{H2} = 50$ cm^3/min, β= 30^oC/min.

The NO-TPD results obtained over the three Pt/MgO-CeO$_2$ catalysts can be summarized as follows. The amount of desorbed NO, N_2O and N_2 over the three catalysts is substantially different. The total amount of N-containing species (μmol/g$_{cat}$), as well as the amount of desorbed N_2 on the IF solid, is greater than the amount obtained on the

other two catalysts. In particular, the IF catalyst desorbed three times more total N-containing species than the WI Pt/MgO-CeO$_2$, and almost two times more than the IJP-DMP catalyst. Also, the IF solid was the only one to desorb NH$_3$ during the NO-TPD under 2%H$_2$/He flow. In fact, NH$_3$ was not detected in the NO-TPD profiles of any other catalyst and was probably produced through the reaction of the excess and not fully converted hydrogen (H$_2$/He flow) with the N-containing species at relatively high reaction temperatures [314].

It should also be noted that the IJP-DMP catalyst was the only catalyst that was found to desorb much higher quantities of NO (3 equivalent monolayers based on Pt$_s$) during the TPD under He flow (Table 5.5), while the rest of the Pt/MgO-CeO$_2$ catalysts presented $\theta_{NO} \leq 0.3$. An explanation for this result could be based on the fact that additional sites for NO chemisorption, besides those on Pt and MgO-CeO$_2$ surfaces alone, may have been formed at the periphery of metal-support [157]. In addition, a spillover process of NO$_x$ species from Pt to the support (Fig. 5.31) during the adsorption of NO at room temperature could be invoked to explain this observation [306]. Burch et al. [70], also suggested a spillover mechanism to describe the reactions between C$_3$H$_8$ and NO$_x$ on Pt/Al$_2$O$_3$. As seen in Figure 5.29, N$_2$ was found to desorb at 25°C and NO by 40°C, which suggests a reverse spillover mechanism, where NO is transferred from the support to the metal and then it is desorbed.
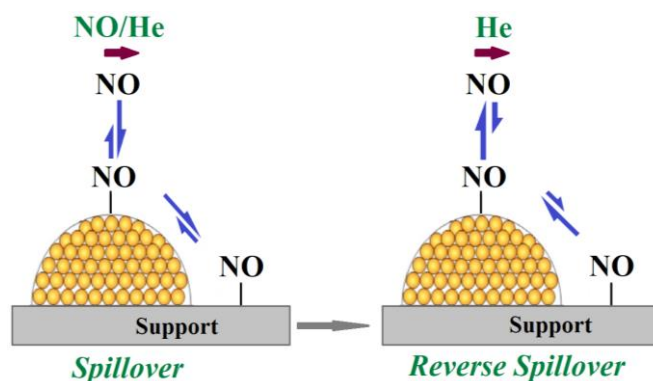
Figure 5.31: Schematic representation of the spillover and reverse spillover mechanism of NO between the active metal and support.

In addition, all the samples presented sharper N$_2$ peaks during Exp. B, whereas the response N$_2$ curves for Exp. A were broader. It is noted that the IJP-DMP solid presented N$_2$ desorption peaks at the lowest T$_M$ (65°C) during temperature desorption under 2%H$_2$/He flow. This hydrogen-assisted effect was also observed in the desorption spectrum of NO observed on the WI and IJP-DMP Pt/MgO-CeO$_2$ catalysts during Exp.

B, where the NO response curves shifted to lower temperatures compared to those obtained during Exp. A. In particular, under H_2/He flow, NO desorbed completely by $130^{\circ}C$ for both catalysts (WI and IJP-DMP), whereas under He flow, NO desorbed completely by $150^{\circ}C$ and $270^{\circ}C$, respectively. It is noted that the presence of hydrogen, shifts the desorbed peaks significantly to lower temperatures since it can lower the bond strength of Pt–NO [157], [311]. Specifically, according to Hecker and Bell [314], the activation energy of the N–O bond dissociation step (Eq. 5.4) is higher than that of the H-assisted N–O bond dissociation step given by Eq. 5.8. However, this effect was not detected for the IF solid, since the opposite outcome was observed. As seen in Figure 5.32, the only catalyst that presents higher T_M during Exp. B (2%H_2/He flow) is the IF Pt/MgO-CeO_2 solid.

Furthermore, since N_2 and N_2O desorption was observed in both experiments, where TPD occurred under He or 2%H_2/He flow on all Pt/MgO-CeO_2 catalysts, then, it is suggested that the Pt/MgO-CeO_2 catalysts facilitate the breaking of the N-O bond even in the absence of hydrogen. The same observation was noted for all Pt/Al_2O_3 catalysts.
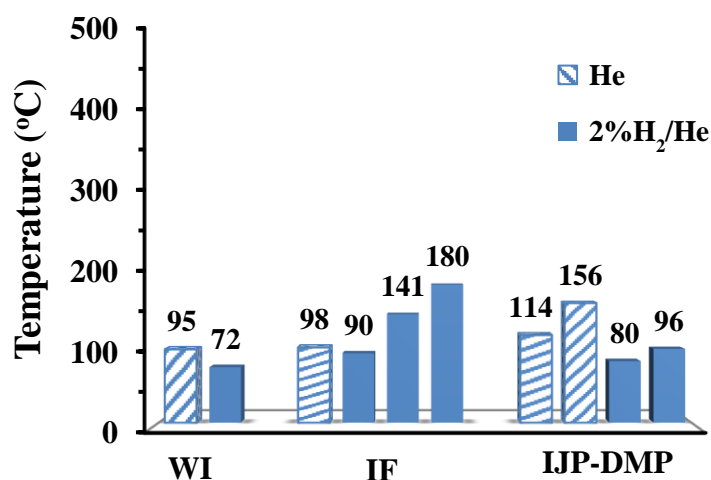
Figure 5.32: Desorption temperature of NO peaks observed under He and 2%H_2/He flow for all Pt/MgO-CeO_2 catalysts.

In addition, based on these results (Fig. 5.32), it can be said that there is probably one adsorbed state of NO, which is likely formed on the Pt-clusters of the WI and IF Pt/MgO-CeO_2 catalysts since only one NO peak was observed during Exp. A, while in the case of the IJP-DMP catalyst, there are probably two states of NO on the solid's surface, since two NO peaks were observed (Fig. 5.29b). It is also noted that, although the IJP-DMP solid desorbed higher amounts of NO (Table 5.5), most of it is desorbed at higher temperatures compared to the rest of the catalysts, which have a T_M= 95-98$^{\circ}C$ (Fig. 5.32).

Therefore, it can be assumed that the adsorbed species on the IJP-DMP solid have a stronger interaction (bond) with the active sites on the catalyst surface and that the chemical interaction of NO with Pt is strongly influenced by the unique surface structure that was created via the printing process. Finally, the NO desorption profiles observed on the Pt/MgO-CeO$_2$ as well as on the Pt/Al$_2$O$_3$ catalysts during the dynamic experiments analysed above, strongly support the view of the existence of various kinds of NO$_x$ species formed during NO chemisorption at room temperature (25°C).

5.3.2. Temperature Programmed Surface Reaction (TPSR) Studies

The TPSR experiment is essentially a TPD experiment carried out under reactive conditions (NO/H$_2$/O$_2$) at the temperature where the catalyst exhibited maximum NO conversion during the catalytic experiments (see subchapter 5.2). By using a mass spectrometer, the detection of the desorbed species evolving as a function of temperature is possible. The transient response curves of NO, N$_2$, N$_2$O and NH$_3$ obtained during TPSR in He or 2% H$_2$/He flow (Exps. C and D, Table 4.2, subchapter 4.3) following H$_2$-SCR on NO reaction on all the solid samples of Pt/Al$_2$O$_3$ and Pt/MgO-CeO$_2$ are illustrated in the Figures 5.33-5.48. In a TPSR experiment, the evolution (reaction, desorption) of the products of the NO/H$_2$/O$_2$ reaction may be observed. Specifically, during the reaction with the catalytic surface, the intermediate adsorbed NO$_x$ and N-containing species are formed. These intermediate species can either desorb without reaction or react on the catalyst's surface towards the production of final products of the reaction such as N$_2$, N$_2$O and NH$_3$.

5.3.2.1. 0.1 wt% Pt/Al$_2$O$_3$ Catalysts

- WI Pt/Al$_2$O$_3$ catalyst

Figure 5.33 shows the TPSR profiles in He flow, recorded as a function of temperature on WI Pt/Al$_2$O$_3$ catalyst. As shown in Fig. 5.33b, two broad NO desorption peaks were obtained (solid line). The first complex peak appears at around 82°C with a distinct shoulder at its descending part. After deconvolution of the initial peak (Origin), two peaks were resolved, one centred at 78°C and another at 114°C (dotted line). A second broad desorption band is also observed in the area of 340-490°C. The latter band can be resolved in two peaks, one centred at 411°C and another at 443°C. It is noteworthy that the deconvolution of the original peaks resulted in an accuracy of up to 99.5% as was indicated by the coefficient of determination (R^2). The formation of large amounts of NO

during the TPSR experiment (especially at high temperatures) illustrates that not all of the adsorbed NO_x species are able to react with O_2/H_2 towards N_2 or N_2O, therefore, these species could be considered as inactive (or spectator) [315].

The TPSR profile also includes two N_2 desorption bands, as seen in Fig. 5.33c. The first large band can be deconvoluted into three peaks (T_{M1}= 131°C, T_{M2}= 214°C and T_{M3}= 259°C), while a second peak appears in the range of 375-490°C with a maximum at 434°C. The nitrogen peaks are taken as a good measure of the active intermediate species of the catalyst. Therefore, this might indicate the presence of three different active intermediate species of adsorbed NO_x, which are reduced to N_2. It is also noted that WI Pt/Al_2O_3 exhibited S_{N2}> 50% (X_{NO}> 60%) at the temperature range of 175-250°C, where most of the N_2 was desorbed (Fig. 5.33c). Finally, two small N_2O desorption bands were also observed. The first band appears in the range of 100-330°C (T_{M1}= 217°C, T_{M2}= 259°C) and the second very small one is centred at 411°C.

Figure 5.33: Transient response curves of (a) NO, N_2O and N_2, (b) NO, (c) N_2 and (d) N_2O, obtained during TPSR in He flow following $NO/H_2/O_2$ reaction at 200°C, on the 0.1 wt% Pt/Al_2O_3 (WI) catalyst; m_{cat}= 0.15g, Q_{He}= 50cm^3/min, β= 30°C/min.

As mentioned in subchapter 5.3.1.1., the WI Pt/Al$_2$O$_3$ catalyst facilitates the breaking of the N-O bond even in the absence of hydrogen, since, N$_2$ and N$_2$O response curves were observed in both TPD experiments after NO chemisorption at 25°C (under He and 2%H$_2$/He flow). Therefore, the formation of N$_2$ and N$_2$O on the Pt surface is indicated by the previously mentioned reaction steps (5.6: N-s + N-s → N$_2$(g) + 2s and 5.5: NO-s + N-s → N$_2$O(g) + 2s). The quantities (μmol/g$_{cat}$) of all desorbed gases (NO, N$_2$, and N$_2$O) are reported in Table 5.6. The last column of the table reports the total amount (μmol/g) of N-containing species formed in the TPSR experiments for all the Pt/Al$_2$O$_3$ solids.

Table 5.6: Amount (μmol/g$_{cat}$) of N-containing gases desorbed during Temperature-Programmed Surface Reaction (TPSR) experiments over 0.1 wt% Pt/Al$_2$O$_3$ catalysts.

Pt/Al$_2$O$_3$	Exp.	NO (μmol/g)	N$_2$O (μmol/g)	N$_2$ (μmol/g)	NH$_3$ (μmol/g)	Total N-containing species (μmol/g)
WI	C	13.7	1.6	9.3	-	35.4 (θ= 7.8)
	D	4.9	0.4	9.8	10.0	35.4
IF	C	39.1	2.4	11.4	-	66.8 (θ= 14.3)
	D	19.1	1.3	12.8	19.4	66.8
IJP-Epson	C	17.6	0.6	5.4	-	29.4 (θ= 6.4)
IJP-DMP	C	2.1	0.3	3.1	-	8.8 (θ= 1.9)
	D	0.1	-	2.9	2.8	8.8

Figure 5.34 presents the response curves of NO, N$_2$O, N$_2$ and NH$_3$ obtained in 2%H$_2$/He flow on the same catalyst following H$_2$-SCR of NO at 200°C for 45 min (steady-state). The desorption spectrum obtained, shows two distinct peaks of NO at 71°C and 324°C (in the broad range of 170-480°C). It is noted that the numbering of desorption peaks follows the direction of increasing temperature. In addition, two N$_2$ peaks were observed as shown in Fig. 5.34c. The first peak is centred at 116°C, while the second desorption band has a peak at 308°C and a distinct shoulder at its descending part (T$_M$= 387°C). Also, a very small N$_2$O peak is observed at 81°C, while a large NH$_3$ peak is found at 331°C, as seen in Fig. 5.34d. The NH$_3$ peak may have been produced by the stepwise hydrogenation of N-atoms, due to excess and not fully consumed hydrogen (2%H$_2$/He flow) at high temperatures [314].

Figure 5.34: Transient response curves of (a) NO, N_2O, N_2 and NH_3, (b) NO, (c) N_2 and (d) N_2O and NH_3, obtained during TPSR in 2% H_2/He flow following NO/H_2/O_2 reaction at 200°C, on the 0.1 wt% Pt/Al_2O_3 (WI) catalyst; m_{cat}= 0.15g, Q_{H2}= 50cm^3/min, β= 30°C/min.

By comparing the results presented in figures 5.33 and 5.34, some significant differences arise. The desorption profile of NO, during Exp. D, shows two peaks (Fig. 5.34b) compared to the four peaks obtained during Exp. C. In addition, the second peak of Fig. 5.34b appeared earlier by almost 100°C compared to the last NO peak of Fig. 5.33b (highest desorption temperature). As for the N_2O spectra, only one peak (81°C) was obtained during the TPSR in H_2/He flow and its peak maximum shifted to a significantly lower temperature as compared to the case of TPSR in He. Specifically, the single N_2O peak of Fig. 5.34d appeared earlier by 178°C than the major N_2O peak of Fig. 5.33d. Moreover, it is noteworthy that during Exp. C (He-TPSR) on the WI solid, NH_3 was not desorbed, whereas in Exp. D (H_2-TPSR), a very large NH_3 peak is observed at relatively high temperatures (Fig. 5.34d).

It is worth mentioning that the total amount of desorbed N-containing species observed in both experiments (C and D) remains the same (35 μmol/g_{cat}) for the WI catalyst, as shown in Table 5.6. It is noted that the total amount of N-containing species is calculated

by adding the desorbed amount of NO, N_2, N_2O and NH_3. In the case of desorbed N_2 and N_2O, their quantities are multiplied by a factor of 2 since they contain two N-atoms. As seen in Table 5.6, the quantity of desorbed NO and N_2O has significantly decreased by 64% and 72%, respectively, when the TPSR was carried out by H_2/He flow. As for nitrogen desorption, there is a slight increase of about 6% in the case of the H_2-TPSR experiment.

The results obtained in the present work on the WI catalyst can be compared, to some extent, to the TPSR (0.25%NO/1%H_2/5%O_2) experiment under He and H_2/He flow conducted by Costa et al. [157] on a 0.1 wt% Pt/Al_2O_3 catalyst synthesized by wet impregnation. During their first experiment (He-TPSR) two large and intense N_2 and NO peaks were observed at T_M= 305°C and T_M= 470°C, respectively, and also a small N_2O peak was centred at 310°C. These peaks corresponded to 12.43 µmol/g_{cat}, 13.12 µmol/g_{cat} and 0.81 µmol/g_{cat}, respectively. Comparing these results with the ones presented in Table 5.6, the current work showed a decrease of 25% in the amount of N_2 desorbed, an increase of 92% for N_2O, while the amount of NO was practically the same. It is worth mentioning that the peak maximum of all the products in this work, with the exception of the last peak of N_2 and N_2O, were observed at lower temperatures. Regarding the second experiment (H_2-TPSR), the authors reported only a large N_2 response curve with four peaks in the 125-425°C range. The amount of desorbed nitrogen was 18.83 µmol/g_{cat} which was almost twice the amount that was observed during this work. Finally, the total amount of N-containing species was 37.7 µmol/g_{cat} which is similar to what was observed in the present work (Table 5.6).

The larger quantities of desorbed N_2 observed in the work of Costa et al. [157] (compared to the present work), can be attributed to the higher partial pressure (molar ratio) of NO used during the H_2-SCR reaction of NO, which is five times higher than that used in the present work. The higher gaseous concentration of NO is expected to lead to higher surface concentrations of NO_x species on the catalyst and thus, will increase the probability of recombination of two such species (same or different to each other) towards the production of N_2. In fact, this result indicates that such an interaction, might be essential, or at least favourable, for the production of N_2.

- IF Pt/Al_2O_3 catalyst

TPSR experiments were also carried out on the IF Pt/Al_2O_3 catalyst, using exactly the same experimental conditions described previously (Exps. C and D). The results obtained during the TPSR studies under He flow are presented in Figure 5.35. The NO response curves obtained on the IF catalyst, which are shown in Fig. 5.35b, are very similar to the ones obtained on the WI catalyst (Fig. 5.33b). The first broad peak is observed in the range of 25-215°C and the second in the range of 320-480°C. After deconvolution of the initial bands, the resolved peaks were centred at 84°C and 118°C for the first desorption band and 401°C and 430°C for the second one. Moreover, all the NO peaks desorbed from the IF catalyst are found in much higher concentrations compared to the WI catalyst. As shown in Table 5.6, the amount of NO desorbed from the IF catalyst is almost three times the amount obtained on the WI Pt/Al_2O_3 catalyst.

Fig. 5.35c shows the response curves of desorbed nitrogen which are obtained in the range of 25-275°C and 350-500°C. The first N_2 peak consisted of practically two peaks, a broad peak centred at 139°C and a sharper one at 237°C. The final peak of N_2 is centred at 423°C. These three N_2 peaks indicate that there are probably three different active intermediate species of adsorbed NO_x which are reduced to N_2, as the obtained peaks are observed in quite different temperatures. Furthermore, a direct association with N_2 selectivity and NO conversion can be made through the N_2 peaks desorbed during the TPSR in He flow. Regarding the IF Pt/Al_2O_3 solid, S_{N2} had an average value of 71% and X_{NO} presented an average of 78% at 150-250°C, where most N_2 was desorbed (Fig. 5.35c). As for N_2O desorption, two bands were observed as seen in Fig. 5.35d. The first complex band is in the temperature range of 100-260°C, which resulted in three peaks after deconvolution (T_{M1}= 142°C, T_{M2}= 176°C and T_{M3}= 240°C). The second band appears in the range of 340-485°C and is centred at 412°C.
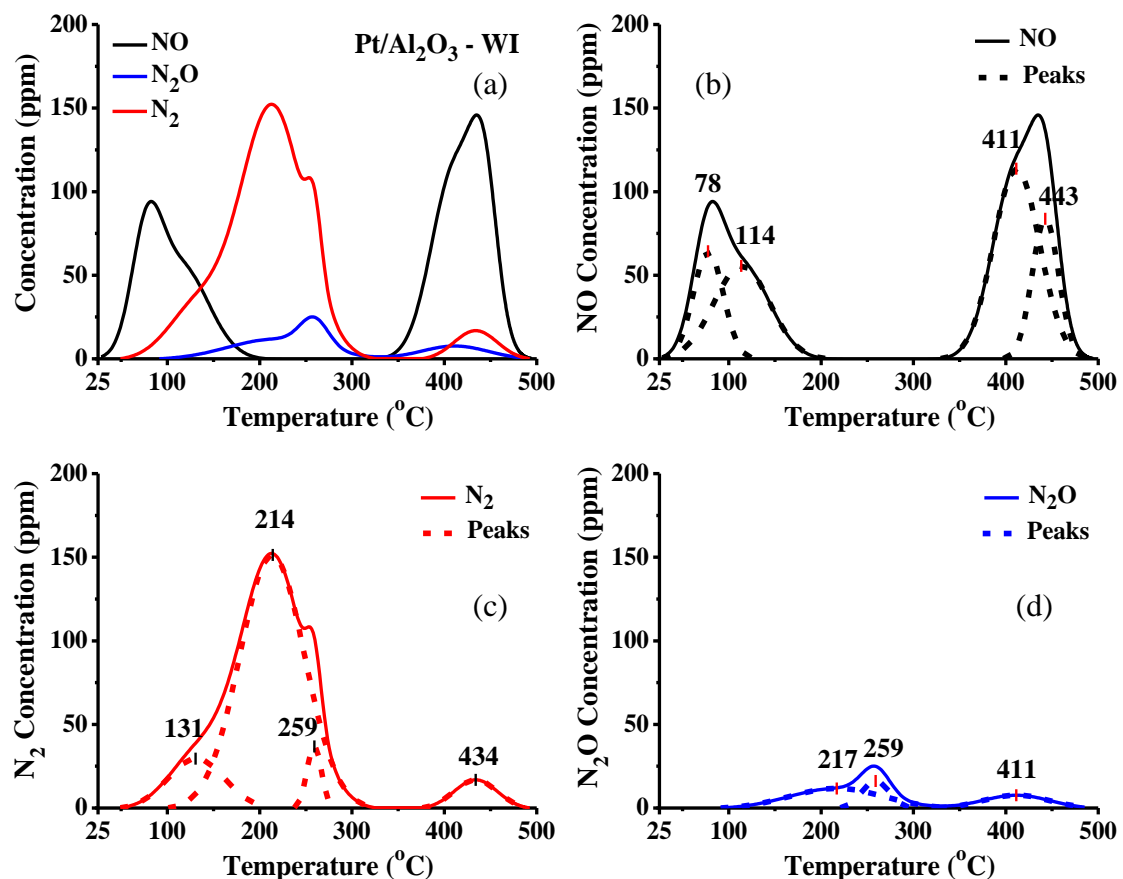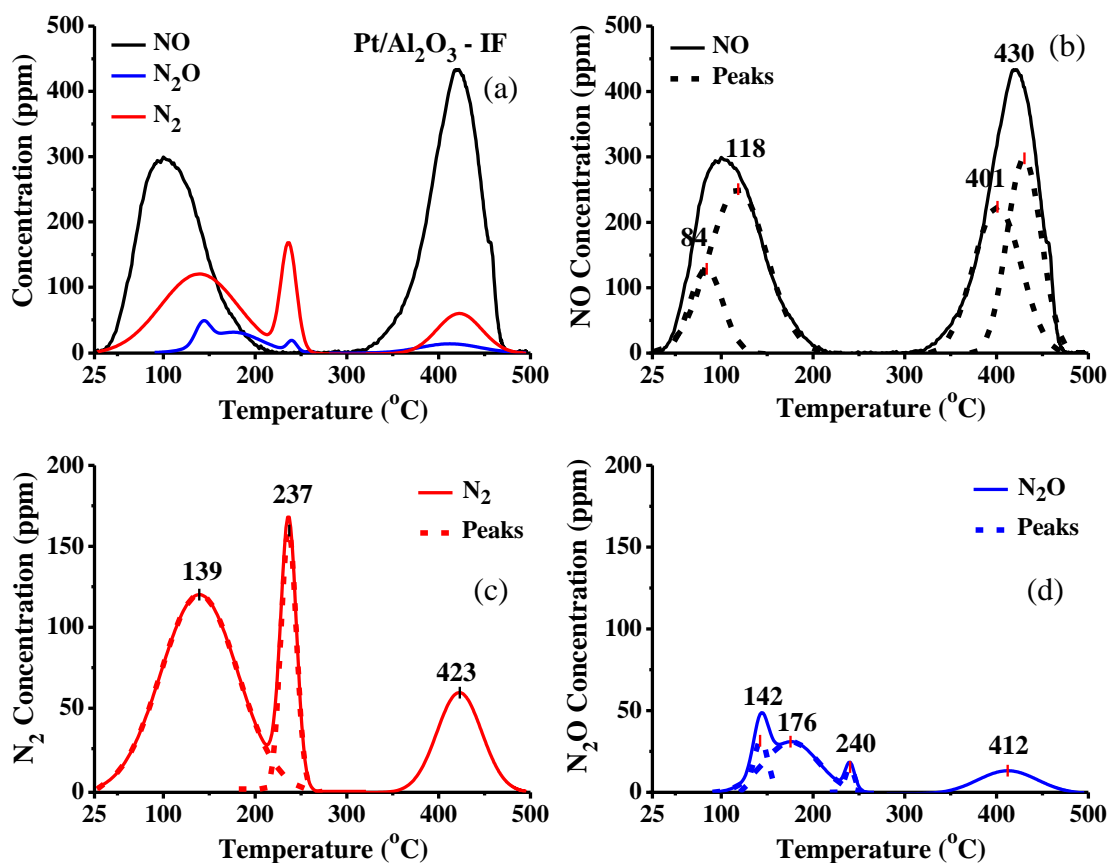
Figure 5.35: Transient response curves of (a) NO, N_2O and N_2, (b) NO, (c) N_2, and (d) N_2O, obtained during TPSR in He flow following $NO/H_2/O_2$ reaction at 200°C, on the 0.1 wt% Pt/Al_2O_3 (IF) catalyst; m_{cat}= 0.15g, Q_{He}= 50cm³/min, β= 30°C/min.

Figure 5.36 shows the results of the TPSR experiment under 2% H_2/He obtained on the IF Pt/Al_2O_3 catalyst. The NO spectrum shows one peak centred at the low temperature of 78°C, as well as a broad band (160-450°C) which consisted of two peaks; one broad peak centred at 279°C and a smaller at 368°C at the descending part of the initial peak. The N_2 desorption profile is presented in Fig. 5.36c and shows also two broad bands, where the first one is resolved in two individual peaks (dotted line), at T_{M1}= 101°C and T_{M2}= 141°C. The last N_2 peak is observed at T_M= 278°C. In addition, the H_2-TPSR experiment resulted in a small N_2O peak (T_M= 97°C), as well as a broad NH_3 peak centred at 281°C (Fig. 5.36d). As seen in Table 5.6, the desorbed amount of NO and NH_3 is practically the same and each gas attributed to 29% of the total N-containing species, while the desorbed amount of nitrogen (12.8 μmol/g_{cat}) constitutes 38% of the total N-containing species. The small desorbed N_2O peak which is shown in Fig. 5.36d corresponds to just 1.3 μmol/g, as shown in Table 5.6.
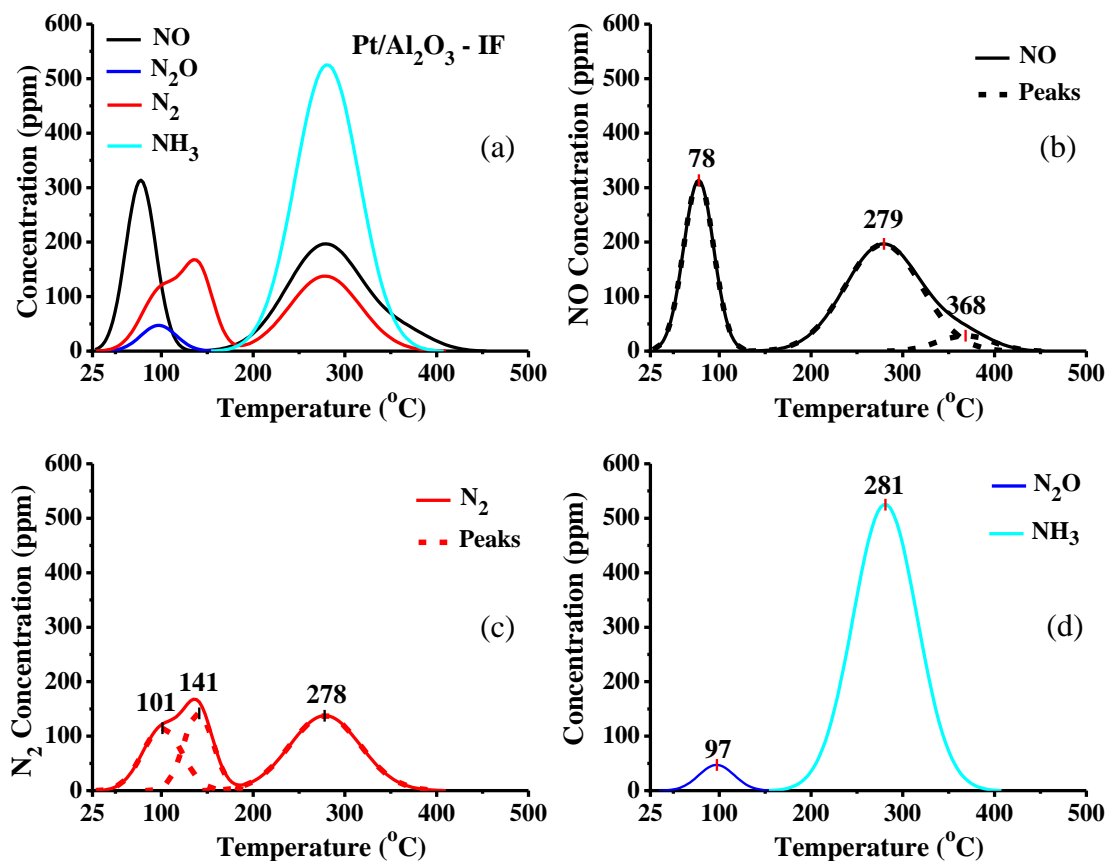
Figure 5.36: Transient response curves of (a) NO, N_2O, N_2 and NH_3, (b) NO, (c) N_2 and (d) N_2O and NH_3, obtained during TPSR in 2% H_2/He flow following NO/H_2/O_2 reaction at 200°C, on the 0.1 wt% Pt/Al_2O_3 (IF) catalyst; m_{cat}= 0.15g, Q_{H2}= 50cm^3/min, β= 30°C/min.

A direct comparison can be made for the results of the H_2-TPSR and He-TPSR experiments. As mentioned before, the total desorbed amount of the N-containing species is the same between the two experiments (~67 μmol/g_{cat}). However, there is a significant reduction in the desorbed amount of NO (105%), as well as N_2O (81%), while there is a slight increase in the desorbed amount of N_2 (12%) in the H_2-TPSR experiment. In addition, NH_3 was desorbed only during the H_2-TPSR experiment. This is due to the easier hydrogenation of N-atoms (during the H_2-TPSR exp.) as suggested by Hecker and Bell [314] and according to the reaction step 5.12.

Regarding the other species (NO, N_2 and N_2O), there is a clear shift of the peaks to lower temperatures when the desorption step is carried out in H_2/He. This hydrogen-assisted effect, which is due to the lowering of the bond strength of Pt-NO, was expected as it has been previously reported in the literature for Pt [157], [311], as well as for Rh supported catalysts [156]. In particular, it is reported that the activation energy of the N-O bond dissociation step (Eq. 5.4: NO-s + s → N-s + O-s) is higher than that of the H-assisted N-

O bond dissociation step (Eq. 5.8: NO-s + H-s → N-s + OH-s) [156], [306], [314]. The most noticeable shift is observed in the case of the N_2 peaks where there is a difference of $38^{\circ}C$ (for the first peak), $96^{\circ}C$ (for the second peak) and $144^{\circ}C$ (for the third peak) between the peaks desorbed under He and H_2/He flow. A significant shift is also observed in the desorption temperature of N_2O.

- IJP-Epson Pt/Al_2O_3 catalyst

The temperature-programmed surface reaction studies described above were also performed on the first inkjet-printed (Epson) Pt/Al_2O_3 catalyst and the results obtained are shown in Figure 5.37. In the case of NO (17.6 $\mu mol/g_{cat}$, Table 5.6), two desorption bands were obtained, a complex band in the area of $25\text{-}250^{\circ}C$, which resulted in two peaks after deconvolution ($T_{M1}= 77^{\circ}C$, $T_{M2}= 140^{\circ}C$) and another well-resolved band in the range of $250\text{-}460^{\circ}C$ ($T_M= 359^{\circ}C$). Moreover, three similar in shape but smaller desorption peaks of N_2 are also noticed in Fig. 5.37c (after deconvolution). The first peak appears relatively early, at $65^{\circ}C$, the second at $136^{\circ}C$, while the final peak is centred at $345^{\circ}C$. These different N_2 peaks indicate that there might be three different active intermediate NO_x species adsorbed on the surface of the printed catalyst, which may differ from those observed on the previous catalysts since these N_2 peaks were found to desorb at considerably different temperatures. It is noted that these N_2 peaks correspond to a relatively low amount of N_2 as seen in Table 5.6, which is in agreement with the average selectivity values of N_2 that were obtained during the catalytic studies on the same catalyst (average $S_{N2}= 56\%$, for T=100-250°C, Fig. 5.11a). Also, a relatively broad and small N_2O peak appears in the range of $25\text{-}225^{\circ}C$ ($T_M= 117^{\circ}C$).

Finally, the IJP-Epson Pt/Al_2O_3 catalyst was also examined in both experiments, C and D, under He (Fig. 5.37) and 2% H_2/He flow, respectively, as all the examined catalysts (Pt/Al_2O_3 and $Pt/MgO\text{-}CeO_2$) in the present work. However, this specific catalyst was the only one where the products were not observed during the H_2-TPSR experiment, probably due to the fact that they desorbed at very low temperatures.
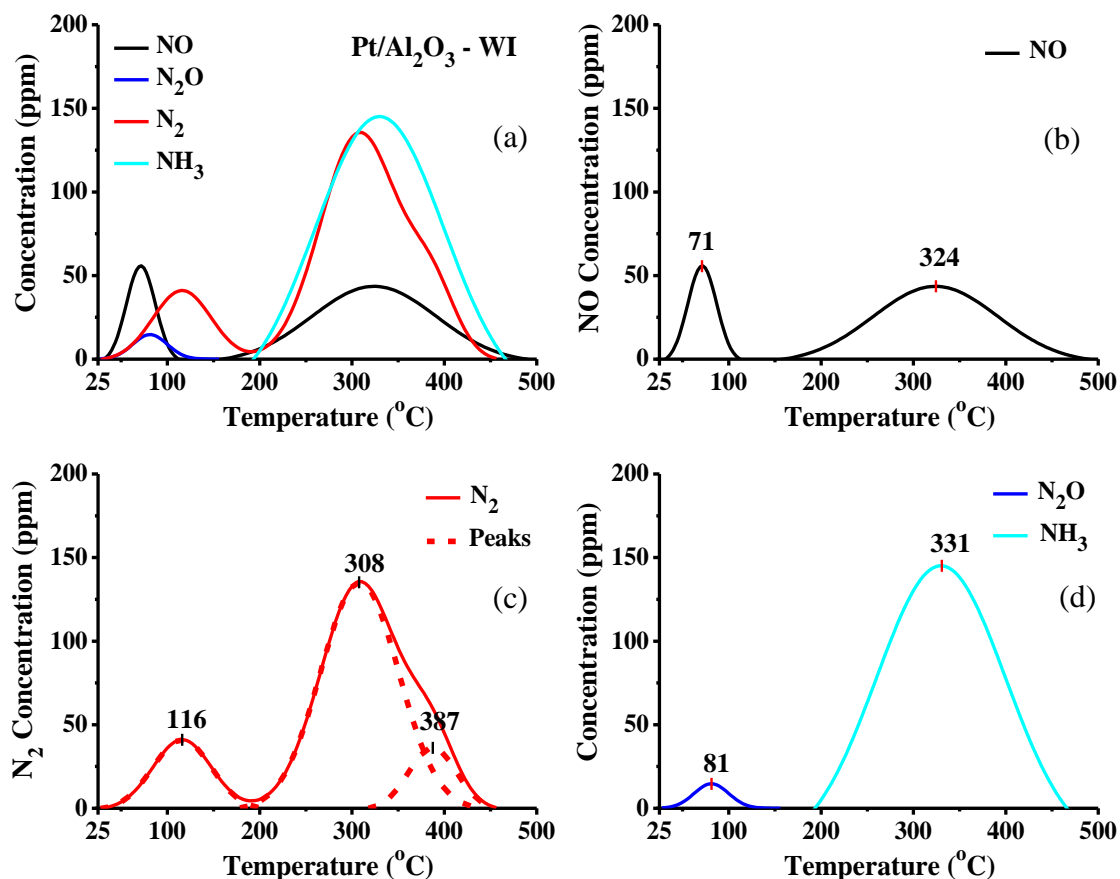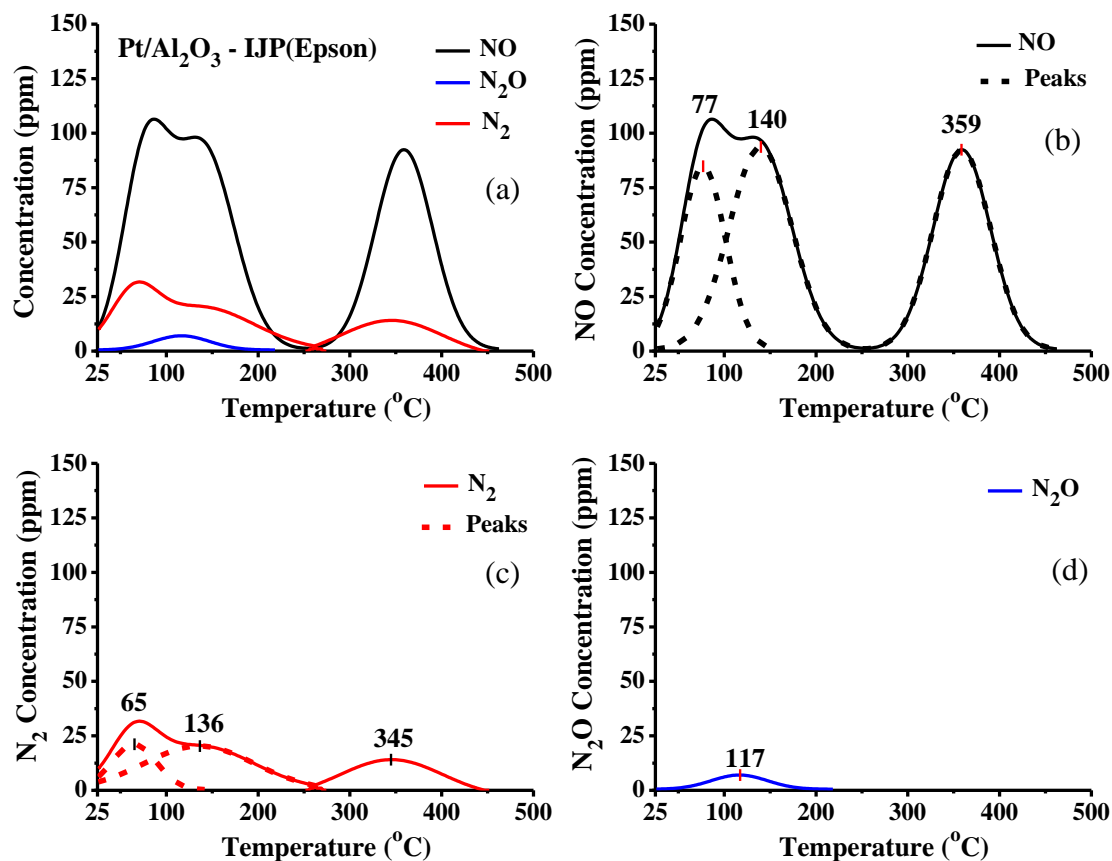
Figure 5.37: Transient response curves of (a) NO, N_2O and N_2, (b) NO, (c) N_2 and (d) N_2O, obtained during TPSR in He flow following $NO/H_2/O_2$ reaction at 200°C, on the printed 0.1 wt% Pt/Al_2O_3 (IJP-Epson) catalyst; m_{cat}=0.0981gr, Q_{He}= 50cm³/min, β= 30°C/min.

- IJP-DMP Pt/Al_2O_3 catalyst

Figure 5.38 presents the transient response curves of NO, N_2O and N_2, obtained during TPSR in He flow, following $NO/H_2/O_2$ reaction at 175°C on the IJP-DMP printed Pt/Al_2O_3 catalyst. Fig 5.38b shows the evolution of NO which generates two desorption bands; one in the 25-140°C range and another in the 230-450°C range. The first band resulted in two peaks after deconvolution, which are centred at 73°C and 95°C, and the second band contained two more peaks at T_{M1}= 341°C and T_{M2}= 404°C which appears as a shoulder of the initial peak. In the case of N_2 (Fig 5.38c), three desorption peaks are observed. The first one is centred at the very low temperature of 36°C, while the other two peaks are eluted from the same desorption band (100-330°C) and are centred at 162°C and 217°C. These nitrogen peaks could be taken as a good measure of the active intermediate species formed on the IJP-DMP Pt/Al_2O_3 catalyst under reaction conditions. Regarding the N_2O profile which is shown in Fig 5.38d, two small peaks are obtained at T_{M1}= 142°C and T_{M2}= 177°C in the narrow temperature range of 115-215°C. These small

peaks, as also seen in Table 5.6, correspond to the lowest amount (0.3 $\mu mol/g_{cat}$) compared to the rest of the N-containing species produced. The total amount of desorbed N-containing species was 8.8 $\mu mol/g_{cat}$, of which 24% was desorbed NO, 69% was desorbed N_2 and the rest was N_2O. It is noted that the desorbed amount of NO reached a 46% of monolayer coverage ($\theta_{NO} \sim 0.46$), based on the Pt exposed surface, whereas, the rest of the Pt/Al_2O_3 catalysts showed a much larger coverage ($\theta_{NO} \geq 3$).

Figure 5.38: Transient response curves of (a) NO, N_2O and N_2, (b) NO, (c) N_2 and (d) N_2O, obtained during TPSR in He flow following $NO/H_2/O_2$ reaction at 175°C, on the printed 0.1 wt% Pt/Al_2O_3 (IJP-DMP) catalyst; m_{cat}=0.15gr, Q_{He}= 50cm^3/min, β= 30°C/min.

H_2-TPSR experiments were also conducted on the IJP-DMP Pt/Al_2O_3 catalyst and are presented in Figure 5.39. The formation of NO during this specific experiment is negligible (Fig. 5.39b), as also seen in Table 5.6 (0.1 $\mu mol/g_{cat}$). Furthermore, N_2 is obtained in one complex desorption band; which resulted in three peaks after deconvolution (T_{M1}= 33°C, T_{M2}= 135°C, T_{M3}= 300°C) in the broad temperature range of 25-450°C. Fig. 5.39d presents the response curve of NH_3, which shows a single broad band peak which is centred at 323°C. As reported in Table 5.6 the total amount of N-containing species desorbed during Exp. D is 8.8 $\mu mol/g_{cat}$, which is practically the same

as the total amount desorbed during Exp. C. The amounts desorbed by N_2 and NH_3 species attributed to 67% and 31.5% of the total amount of N-containing species, respectively.
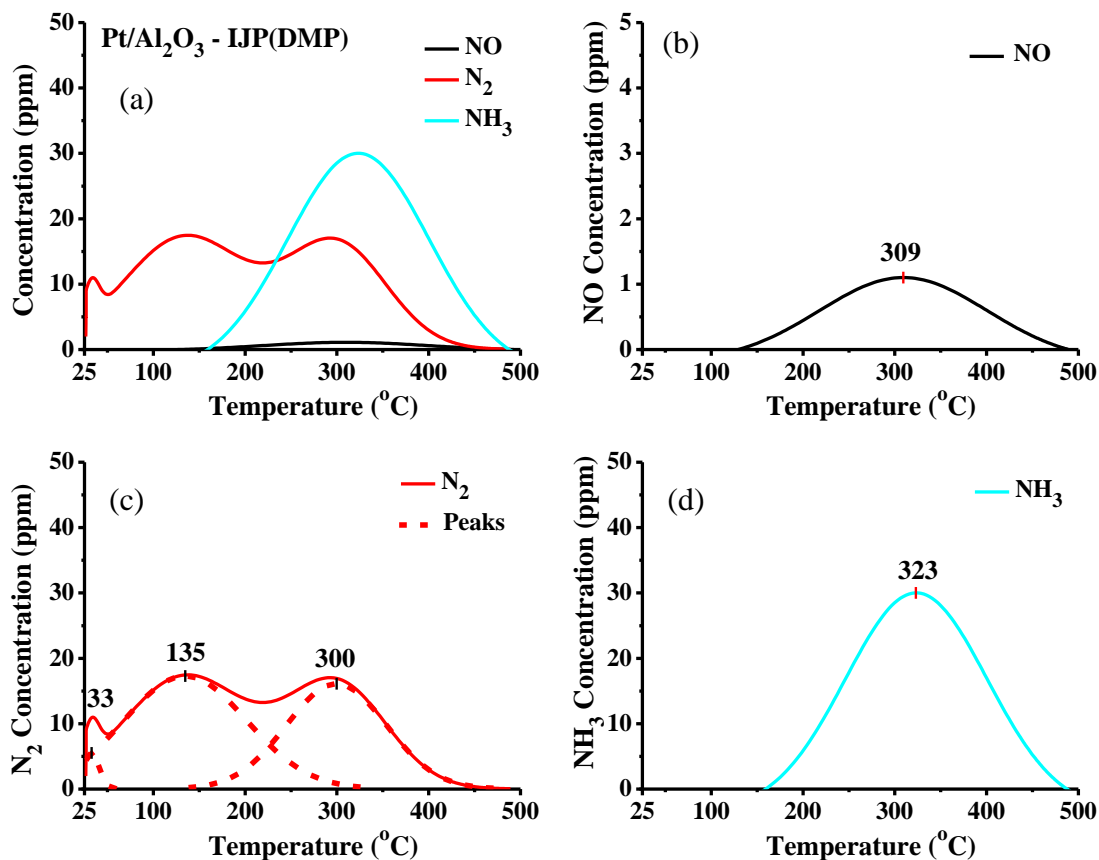
Figure 5.39: Transient response curves of (a) NO, N_2 and NH_3, (b) NO, (c) N_2 and (d) NH_3, obtained during TPSR in 2% H_2/He flow following $NO/H_2/O_2$ reaction at 175°C, on the printed 0.1 wt% Pt/Al_2O_3 (IJP-DMP) catalyst; m_{cat}=0.15gr, Q_{H2}= 50cm^3/min, β= 30°C/min.

By comparing the TPSR results of the IJP-DMP Pt/Al_2O_3 catalyst (Figs. 5.38 and 5.39), the following conclusions can be reached. During the H_2-TPSR experiment, the desorbed amount of NO was significantly reduced by 17 times, while N_2 was slightly decreased by 3%. It is also worth mentioning that N_2O was not desorbed during the TPSR under H_2/He flow. The IJP-DMP solid is the only catalyst among all Pt/Al_2O_3 and $Pt/MgO-CeO_2$ catalysts examined where the latter phenomenon was observed.

As clearly seen by the comparison of the results presented in Figs. 5.33 (WI), 5.35 (IF), 5.37 (IJP-Epson) and 5.38 (IJP-DMP), the four examined Pt/Al_2O_3 catalysts present significantly different He-TPSR profiles, in the whole temperature range of 25-500°C. In particular, the WI, IF and IJP-DMP catalysts do not show any desorption of N_2O at desorption temperatures lower than 100°C, while the IJP-Epson printed catalyst shows some desorption. Also, at T< 100°C, the catalysts prepared by wet impregnation, i.e., WI

and IF solids, show less N_2 desorption compared to the printed catalysts (Epson and DMP). The latter result explains (at least partially) the superior catalytic activity of the printed catalysts at very low reaction temperatures, as at 100°C the IJP-Epson catalyst presented X_{NO}= 72%, and at 120°C the IJP-DMP showed X_{NO}= 81%, while the rest of the catalysts presented X_{NO} < 25 at T= 100°C.

Moreover, the very broad desorption profile of N_2 obtained on the printed catalysts explains in an adequate degree the very large temperature window of operation of these catalysts (ΔT= 150°C). Finally, the temperatures where maximum N_2 and N_2O desorption is observed, over all the examined catalysts, comes in a good agreement with the maximum NO conversion obtained over the solids. Since the desorption profiles obtained on the catalysts are highly linked to the nature of the adsorbed intermediate NO_x species on their surface during $NO/H_2/O_2$ reaction [157], one can safely claim that the surface of the printed catalysts favours the formation of such intermediate NO_x species that ultimately lead to improved catalytic activity, particularly at very low reaction temperatures.

It should be noted that the amount of NO that was desorbed during the He-TPSR experiments is quite different between the catalysts. The IJP-DMP catalyst presented the lowest amount (2.1 $\mu mol/g_{cat}$), while the IF solid the highest (39.1 $\mu mol/g_{cat}$). The same pattern was observed regarding the total amount of N-containing species. It is worth mentioning at this point that the most important information that can be obtained from the TPSR profiles is not the total amount of desorbed species, but the amount and percentage of active species, particularly desorbed at low reaction temperatures (preferably at T≤ 150°C). As shown in Figs. 5.33 and 5.35 the percentage of N_2 and N_2O desorbed from the WI and IF catalysts, respectively, is not significant at temperatures lower than 150°C. On the contrary, a significant amount of N_2 and N_2O is desorbed from the two printed catalysts at such low temperatures (Fig. 5.37, IJP-Epson and 5.38, IJP-DMP). It is noted that N_2 and N_2O are both formed by active intermediate species during the TPSR process.

As for the H_2-TPSR experiments, all the catalysts exhibited a decrease in the amount of desorbed NO, as seen in Table 5.6, due to the excess hydrogen which reacted with the adsorbed NO_x species on the catalyst's surface. Noteworthy, the IJP-DMP Pt/Al_2O_3 solid did not exhibit any N_2O desorption in the area of 25-500°C, which was not observed by any other catalyst including the Pt/MgO-CeO_2 solids which are presented in the next

subchapter. Moreover, the IF catalyst presents the largest amount of desorbed NH_3 in the area of 200-400°C, with the latter catalyst showing lower selectivity values towards N_2 ($S_{N2} < 70\%$) at the reaction temperatures close to the conversion maximum (Fig. 5.10b).

It is also noteworthy that the profile of desorbed gases during H_2-TPSR shifts to lower temperatures compared to the profiles of the He-TPSR experiments and NO-TPD (under He or 2%H_2/He flow). These differences, also concern the composition and amount of gases evolved and thus reflect the different kinetics of reactions that occur under He or H_2 gas [311]. Figure 5.40 presents the temperature shift of the desorbed NO peaks obtained during H_2-TPSR (compared to He-TPSR). It must be mentioned that under H_2-SCR reaction conditions, adsorbed NO_x, O, and H species are populated on the Pt and support surfaces. The surface coverage of adsorbed NO_x and their binding energy depends on the oxidation state of Pt, as mentioned before and on the presence of other coadsorbed reaction intermediates [285]. A hydrogen-assisted effect on the lowering of the bond strength of Pt-NO is also suggested to explain this significant shift in temperature [156]. Also, Hecker and Bell [314] suggested that the activation energy of the N-O bond dissociation is higher than that of hydrogen assisted N-O dissociation via the mechanism presented in Eq. 5.8.
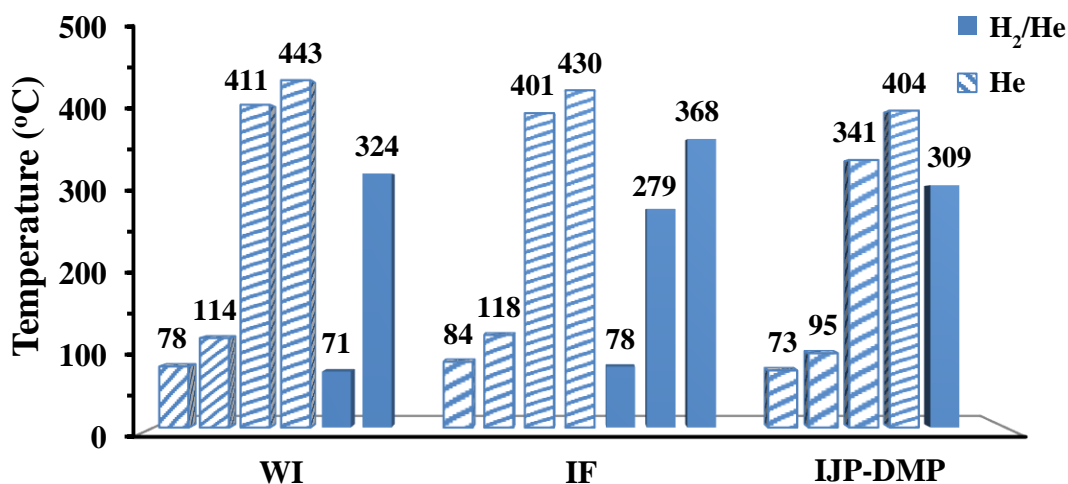
Figure 5.40: Desorption temperature of NO peaks obtained during TPSR under He and H_2/He flow on Pt/Al_2O_3 catalysts.

Additionally, during TPSR in 2%H_2/He flow, the coverage of adsorbed H is expected to be higher than that found under H_2-SCR of NO reaction conditions. Therefore, the shift of the NO transient response curve to lower temperatures regarding the ordinary NO-TPD curve under He flow could be justified [306]. Finally, the results obtained from the TPSR experiments confirm once more the great influence that the chemical composition of the

support has on the H_2-SCR of NO (activity and N_2 selectivity). Furthermore, the different chemical nature of the chemisorption sites of the support influences the structure of adsorbed NO_x species and their binding energy (thermal stability), thus determining the surface catalytic chemistry of the $NO/H_2/O_2$ reaction on supported Pt catalysts [73].

5.3.2.2. 0.1 wt% Pt/MgO-CeO₂ Catalysts

- WI Pt/MgO-CeO₂ catalyst

Figure 5.41 presents the transient response curves of NO, N_2O and N_2 obtained over WI Pt/MgO-CeO₂ catalyst according to Experiment C, described in Table 4.2 (subchapter 4.3). As shown in Fig. 5.41b, one complex and broad NO desorption band was obtained, ranging in the whole temperature range of 25-490°C. It should be mentioned that the straight line (Fig. 5.41) corresponds to the initial peak, while the dotted lines indicate the individual peaks which resulted after deconvolution of the initial peak (Origin). The desorbed NO peaks are centred at 157°C, 262°C, 366°C and 440°C. In addition, N_2 appeared in two desorption bands; the first one is a small peak centred at the low temperature of 34°C and the other one appears in the temperature range of 100-220°C. As seen in Fig. 5.41c, the latter band resulted in two peaks which are centred at $T_{M1} = 125$°C and $T_{M2} = 163$°C. As for the desorption of N_2O, one broad and complex band is also observed (Fig. 5.41d). The N_2O band was analyzed in three peaks ($T_{M1} = 163$°C, $T_{M2} = 320$°C and $T_{M3} = 395$°C) in the area of 100-480°C.

The quantities (μmol/g$_{cat}$) of all desorbed gases (NO, N_2, and N_2O) are reported in Table 5.7. The last column of the table reports the total amount (μmol/g) of N-containing species formed in the TPSR experiments for all the Pt/MgO-CeO₂ catalysts. It should be mentioned that N_2 and N_2O curves (Fig. 5.41c, d) were desorbed in lower intensity compared to NO (Fig. 5.41b), as also reported in Table 5.7. Specifically, the total amount of N-containing species is 64.7 μmol/g$_{cat}$ of which 78% is attributed to NO (50.49 μmol/g$_{cat}$).
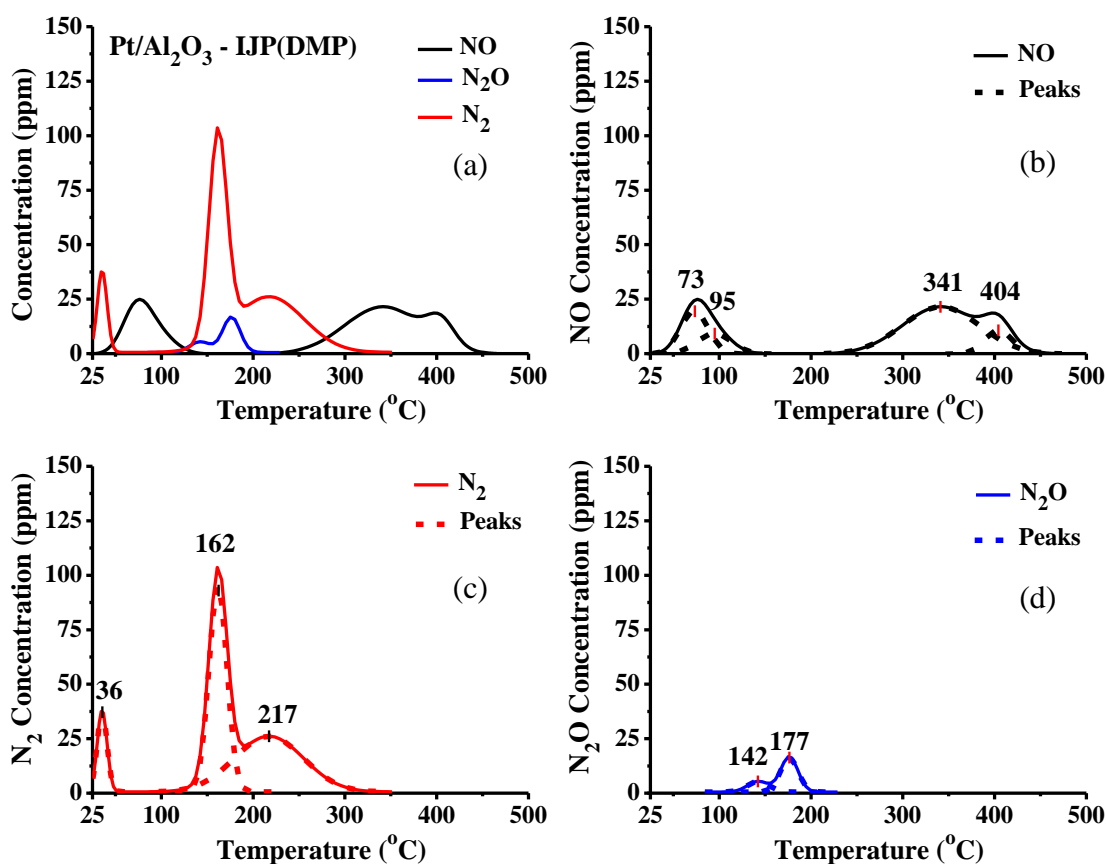
Vasiliki K. Chatziiona

Figure 5.41: Transient response curves of (a) NO, N_2O and N_2, (b) NO, (c) N_2 and (d) N_2O, obtained during TPSR in He flow following $NO/H_2/O_2$ reaction at 200°C, on the 0.1 wt% Pt/MgO-CeO_2 (WI) catalyst; m_{cat}= 0.15g, Q_{He}= 50cm³/min, β= 30°C/min.

As mentioned previously, the formation of NO during the TPSR run explains that not all of the adsorbed NO_x species can react with O_2/H_2 towards N_2 or N_2O, and thus these specific species might be considered as inactive [315]. On the other hand, the desorbed N_2 peaks can be taken as a good measure of the active intermediate species of the catalyst. As seen in Fig. 5.41c, the WI Pt/MgO-CeO_2 solid showed three N_2 peaks, thus it can be claimed that the catalyst could probably involve three active intermediate species of adsorbed NO_x which participate in the reaction pathway of N_2 formation. These active adsorbed NO_x intermediate species can also be formed near the interface between Pt nanoparticles and the support (MgO and CeO_2) [306]. This was also observed in the H_2-SCR of NO on a Pt/SiO_2 catalyst and Pt/$La_{0.5}Ce_{0.5}MnO_3$ [74], as well as in an ethanol-SCR reaction, where the active intermediate NO_x species were formed on the support close to the Ag metallic nano-particles [293].

Table 5.7: Amount (μmol/g_{cat}) of N-containing gases desorbed during Temperature-Programmed Surface Reaction (TPSR) experiments over 0.1 wt% Pt/MgO-CeO$_2$ catalysts.

Pt/MgO-CeO$_2$	Exp.	NO (μmol/g)	N$_2$O (μmol/g)	N$_2$ (μmol/g)	NH$_3$ (μmol/g)	Total N-containing species (μmol/g)
WI	C	50.5	3.9	3.2	-	64.7(θ= 13.6)
	D	7.1	3.5	15.5	19.7	64.7
IF	C	119.7	6.0	4.6	-	140.8 (θ= 43.4)
	D	14.0	2.7	33.0	55.4	140.7
IJP-DMP (NO/H$_2$/O$_2$)	C	83.6	2.2	-	-	87.9 (θ= 18.4)
	D	46.6	1.9	8.0	21.4	87.9
IJP-DMP (NO/H$_2$)	C	23.4	5.2	3.6	-	40.9 (θ= 8.6)
	D	11.4	4.2	10.6	-	40.9

Figure 5.42 presents the TPSR profiles of NO, N$_2$, N$_2$O and NH$_3$ obtained under 2% H$_2$/He flow on WI Pt/MgO-CeO$_2$. The evolution of NO is presented in Fig. 5.42b in one desorption band in the area of 25-250°C. After deconvolution, three peaks were obtained which are centred at 77°C, 105°C and 179°C. In the case of N$_2$, three peaks can be observed in Fig. 5.42c; the first peak is found at the low temperature of 33°C, the second peak is centred at 130°C and the last one is a shoulder at the descending part of the initial band (T$_M$= 171°C). N$_2$O evolution is also presented in Fig. 5.42c and shows a broad peak in the temperature range of 25-170°C (T$_M$= 98°C). Finally, as seen in Fig. 5.42d the TPSR profile included a quite sharp (125-225°C) and intense NH$_3$ peak which is centred at 180°C. The formation of NH$_3$ could be explained through the hydrogenation of the N-containing species from the excess hydrogen of the carrier gas (2% H$_2$/He flow).

Table 5.7 presents the desorbed amount of all the N-containing species obtained during the TPSR studies on the Pt/MgO-CeO$_2$ catalysts and as can be seen, NH$_3$ production (19.7 μmol/g_{cat}), attributes to 30.4% of the total amount of N-containing species (64.7 μmol/g_{cat}). The desorbed amount of nitrogen consists of 47.8% of the total amount of N-containing species. Moreover, by comparing the desorbed amounts of the catalyst, it is noted that during H$_2$-TPSR, the WI solid desorbed about seven times less NO than in the case of the He-TPSR experiment. This significant decrease can be explained through the reaction of adsorbed NO$_x$ species with H$_2$ (carrier gas) which as a result, produced N$_2$, N$_2$O and NH$_3$. Specifically, there was an increase of almost five times in the desorption of N$_2$, whereas there was a slight decrease of 11% in the amount of N$_2$O that was desorbed.

Regarding the temperature maximum (T_M) of the peaks, there was a clear shift at lower temperatures in all the peaks of NO and N_2O during the H_2-TPSR experiment, as hydrogen can lower the bond strength of Pt-NO (hydrogen-assisted effect) [157], [311]. On the other hand, the peaks of N_2 appeared practically at the same T_M or slightly higher temperatures (~$\Delta T= 5°C$), as in the case of the He-TPSR.
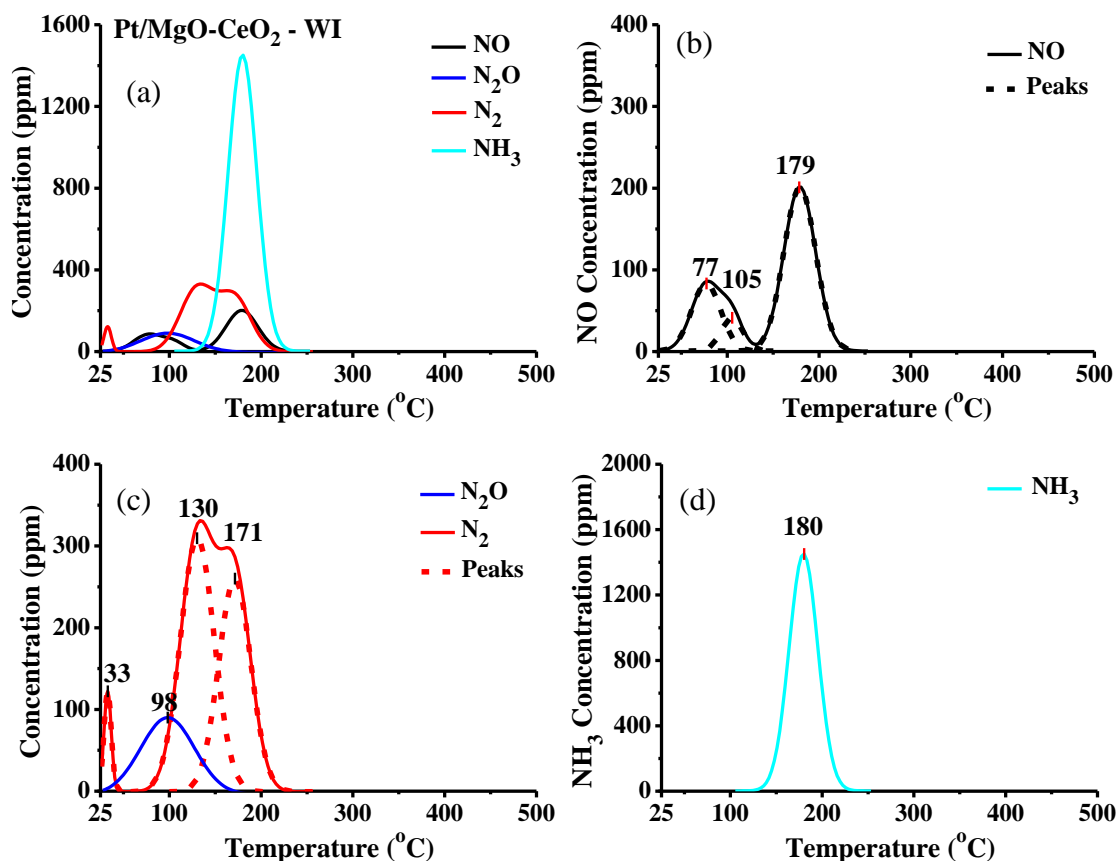
Figure 5.42: Transient response curves of (a) NO, N_2O, N_2 and NH_3, (b) NO, (c) N_2 and N_2O and (d) NH_3, obtained during TPSR in 2% H_2/He flow following NO/H_2/O_2 reaction at 200°C, on the 0.1 wt% Pt/MgO-CeO$_2$ (WI) catalyst; $m_{cat}= 0.15$g, $Q_{H2}= 50$cm^3/min, $\beta= 30°C$/min.

According to literature, Costa et al. [306], also performed TPSR studies on the same catalyst (WI Pt/MgO-CeO$_2$). The TSPR experiments were conducted following reaction with the mixture of 0.25% NO/1.0% H_2/5% O_2 and afterwards desorbed in He or 10% H_2/He flow. During the He-TPSR experiment, the authors reported three distinct NO peaks; the first was centred at 135°C, the second was a larger and broader peak in the area of 175-375°C and the last and largest peak was observed at 480°C. These peaks resulted in 17.2 μmol/g_{cat} of NO, which is almost three times less than what was observed on the WI catalyst of the present work. Moreover, the shape and temperature maximum of these peaks resemble the ones obtained in Fig. 5.41b. As for the H_2-TPSR experiment, the

authors reported the production of only NO (T_{M1}= 110°C and T_{M2}= 210°C) and N_2 gases (T_{M1}= 90°C and T_{M2}= 110°C). Therefore, the authors did not report any N_2 during the first experiment and any N_2O during the second experiment. On the contrary, during this work, N_2 and N_2O were observed during both TPSR studies (under He or H_2/He). It is also noted that the NO peaks observed during this work (H_2-TPSR) were desorbed at lower temperatures compared to the work of Costa et al. [306].

- IF Pt/MgO-CeO$_2$ catalyst

TPSR studies were also performed on the IF Pt/MgO-CeO$_2$ catalyst which was prepared and examined for the first time in the present work. Figure 5.43 presents the transient response curves of the desorbed NO, N_2 and N_2O, obtained during TPSR under He flow following NO/H_2/O_2 reaction at 250°C. Fig. 5.43b shows the evolution of NO, which is desorbed in one broad and complex desorption band in the area of 110-500°C (straight line). After careful deconvolution, five peaks were observed, which are centred at 145°C, 249°C, 323°C, 432°C and 458°C. The NO peaks were desorbed at high concentrations, as also seen in Table 5.7, as the desorbed amount of NO was 119.7 μmol/g$_{cat}$ and the total amount of N-containing species was 140.8 μmol/g$_{cat}$, thus NO attributed to 85% of the total desorbed N-containing species. It should be noted that some of these adsorbed NO$_x$ species could be considered as inactive or spectator species since not all of them are able to participate in the reaction path towards N_2 or N_2O [285], [315].

Fig. 5.43c presents the evolution profile of N_2, which shows two desorption bands, ranging in 25-65°C and 100-375°C. The first peak is observed at the low temperature of 35°C, and the other two peaks which are centred at 188°C and 250°C, resulted after deconvolution of the second band. In the case of N_2O, one distinct desorption band is observed, which resulted in two individual peaks (T_{M1}= 392°C, T_{M2}= 425°C), with the latter being a shoulder at the descending part of the initial peak (Fig. 5.43d). The amount of desorbed N_2 and N_2O was 4.6 μmol/g$_{cat}$ and 6 μmol/g$_{cat}$, respectively and collectively they attributed to 15% of the total desorbed amount of N-containing species.
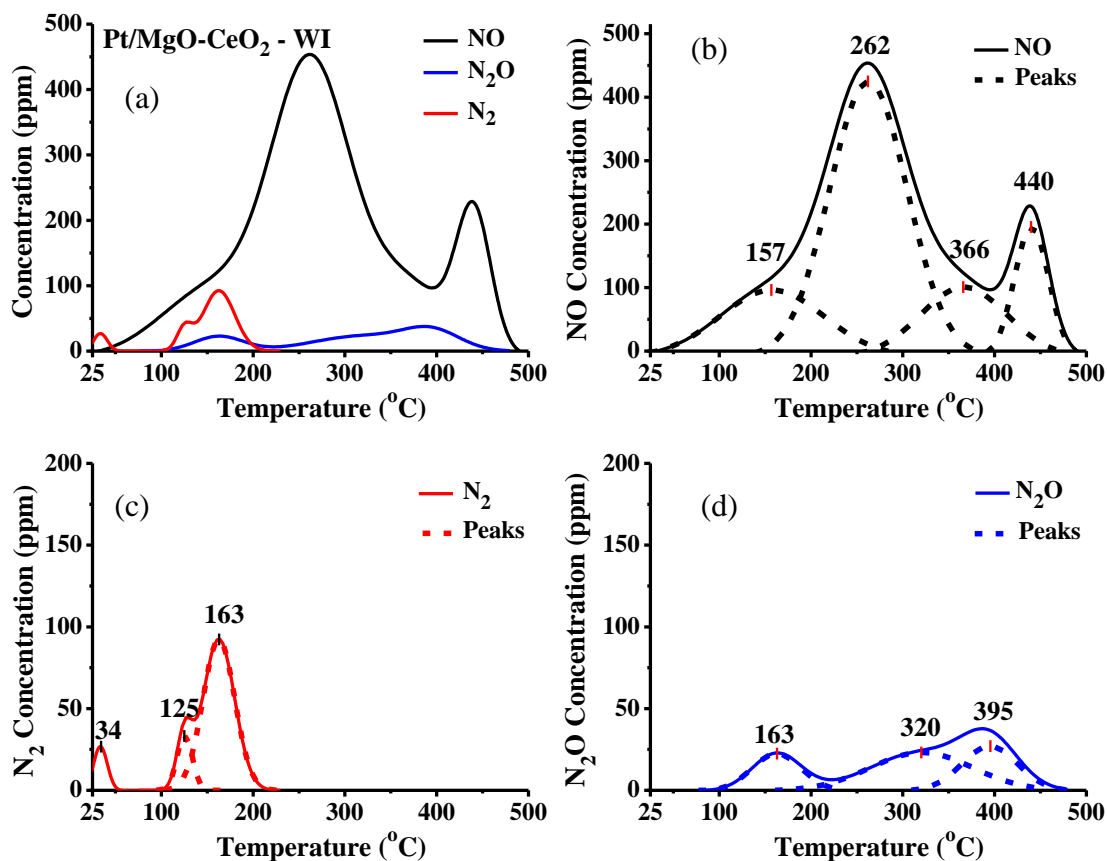
Figure 5.43: Transient response curves of (a) NO, N₂O and N₂, (b) NO, (c) N₂ and (d) N₂O, obtained during TPSR in He flow following NO/H₂/O₂ reaction at 250ºC, on the 0.1 wt% Pt/MgO-CeO₂ (IF) catalyst; m_{cat}= 0.15g, Q_{He}= 50cm³/min, β= 30ºC/min.

Figure 5.44 shows the TPSR profiles of NO, N₂, N₂O and NH₃ obtained under 2%H₂/He flow on the IF Pt/MgO-CeO₂ catalyst following H₂-SCR of NO at 250ºC for 45 min (steady-state reaction conditions). Fig. 5.44b presents the desorption profile of NO which includes one complex desorption band, which contains four peaks centred at 113ºC, 154ºC, 217ºC and 246ºC in the broad temperature range of 25-310ºC. Furthermore, N₂ appears to desorb in one well-resolved band in the range of 140-280ºC (Fig. 5.44c). After deconvolution, two peaks are obtained at T_M= 216ºC and at T_M= 249ºC, with the latter being a shoulder on the descending part of the initial N₂ band. The total amount of desorbed N₂ is 33 μmol/g_{cat}, as seen in Table 5.7 and corresponds to 47% of the total amount of desorbed N-containing species. Fig. 5.44c also presents the TPSR profile of NH₃ which includes one large NH₃ peak centred at 244ºC. Finally, N₂O desorption is depicted in Fig. 5.44d, showing a smaller desorption peak (100-215ºC), compared to the rest of the desorbed gases, which is also noted in Table 5.7, as its amount is significantly

less (2.7 $\mu mol/g_{cat}$) than the other desorbed species. In particular, two small N_2O peaks were obtained, centred at 155°C and at 179°C.

Figure 5.44: Transient response curves of (a) NO, N_2O, N_2 and NH_3, (b) NO, (c) N_2 and NH_3 and (d) N_2O, obtained during TPSR in 2%H_2/He flow following NO/H_2/O_2 reaction at 250°C, on the 0.1 wt% Pt/MgO-CeO_2 (IF) catalyst; m_{cat}= 0.15g, Q_{H2}= 50cm³/min, β= 30°C/min.

As reported in Table 5.7, the IF catalyst showed the same total amount of desorbed N-containing species (140 $\mu mol/g_{cat}$), in both experiments (under He and 2%H_2/He flow). However, during the H_2-TPSR run, the desorbed amount of NO was reduced by 88%, and the desorbed amount of N_2O by 55% compared to the respective amounts observed during the He-TPSR. As for the desorbed amount of N_2, it was increased by more than seven times during the H_2-TPSR. In addition, NH_3 was produced during the H_2-TPSR experiment but not during the He-TPSR run. As for the position of the peak maximum during the H_2-TPSR experiment, all the desorbed peaks of NO and N_2O shifted to lower temperatures, due to the hydrogen-assisted effect on the lowering of Pt-NO_x bond strength. Moreover, all the NO species were desorbed by 310°C in the case of H_2-TPSR, compared to 500°C in the case of He-TPSR. Also, N_2O was completely desorbed by 215°C under H_2/He flow, compared to 480°C during the He-TPSR run. Finally, N_2 was

Vasiliki K. Chatziiona

completely desorbed by 285°C during H_2-TPSR, compared to 375°C during the He-TPSR experiment, even though there was a shift to higher temperatures by one of the N_2 peaks during the H_2-TPSR (T_M= 216°C, Fig. 5.44c), compared to the He-TPSR experiment (T_M= 188°C, Fig. 5.43c).

- IJP-DMP Pt/MgO-CeO$_2$ catalyst

Figure 5.45 presents the TPSR profiles of NO and N_2O which were obtained over the novel IJP-DMP Pt/MgO-CeO$_2$ catalyst during TPSR in He flow following NO/H_2/O_2 reaction at 200°C. As seen in Figure 5.45, the IJP-DMP solid presented only NO and N_2O desorption peaks and did not desorb any nitrogen during Exp. C. This was the only time that this behaviour was observed during the He-TPSR experiments. Fig. 5.45a presents the desorption profile of NO, showing a complex and very broad NO desorption band in the temperature range of 25-500°C. After deconvolution of the initial complex band, four peaks were resolved and were centred at 139°C, 216°C, 416°C and 446°C. As seen in Table 5.7, the total amount of NO desorbed reached 83.6 µmol/g$_{cat}$, while the total amount of N-containing species is 87.9 µmol/g$_{cat}$, thus NO attributed to 98% of the total amount. The results presented in Fig. 5.45a and Table 5.7 are in complete agreement with the catalytic behaviour of the particular catalyst during NO/H_2/O_2 reaction, since this catalyst was found to be practically inactive (X_{NO}< 6%) for the NO/H_2/O_2 reaction in the temperature range of 60-400°C (Fig. 5.15, subchapter 5.2.2).
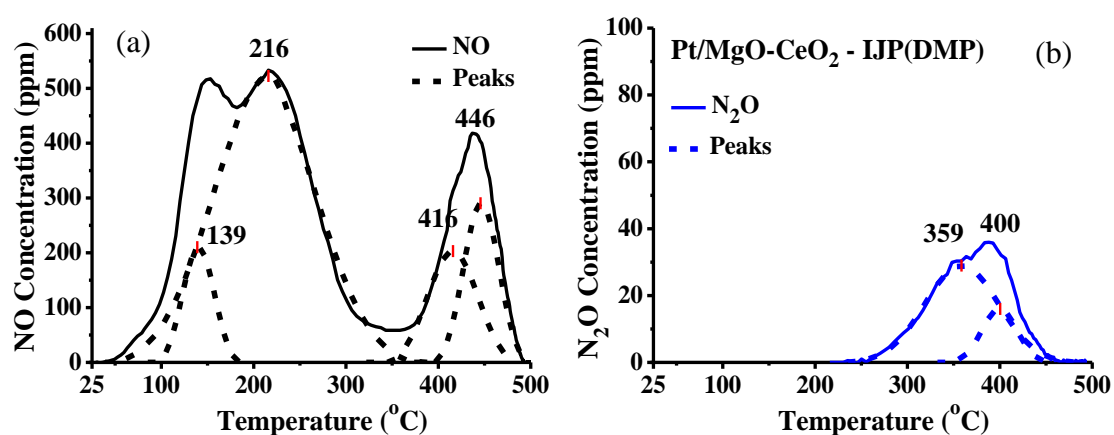
Figure 5.45: Transient response curves of (a) NO and (b) N_2O, obtained during TPSR in He flow following NO/H_2/O_2 reaction at 200°C, on the printed 0.1 wt% Pt/MgO-CeO$_2$ (IJP-DMP) catalyst; m_{cat}= 0.14g, Q_{He}= 50cm^3/min, β= 30°C/min.

As shown in Fig. 5.45b two N_2O peaks were observed during this experiment, in the area of 250-460°C. The first peak (after deconvolution) is centred at 359°C and the second one

is centred at 400°C. The desorbed amount of N_2O (2.2 μmol/g_{cat}) is also reported in Table 5.7, which is significantly less than the amount of desorbed NO.

H_2-TPSR was also performed on the IJP-DMP catalyst and the response curves of NO, N_2O, N_2 and NH_3 obtained are presented in Figure 5.46. As seen in Fig. 5.46b, NO is desorbed in the broad range of 30-300°C. After deconvolution of the original band (Origin), four peaks were resolved (T_{M1}= 88°C, T_{M2}= 145°C, T_{M3}= 188°C and T_{M4}= 213°C). NH_3 desorption is also presented on the same figure, which shows a single, quite sharp peak centred at 245°C. The desorbed amount of NO was found to be 46.6 μmol/g_{cat} (Table 5.7), which also attributes to the majority (53%) of the total amount of N-containing species, as noticed in the He-TPSR experiment.
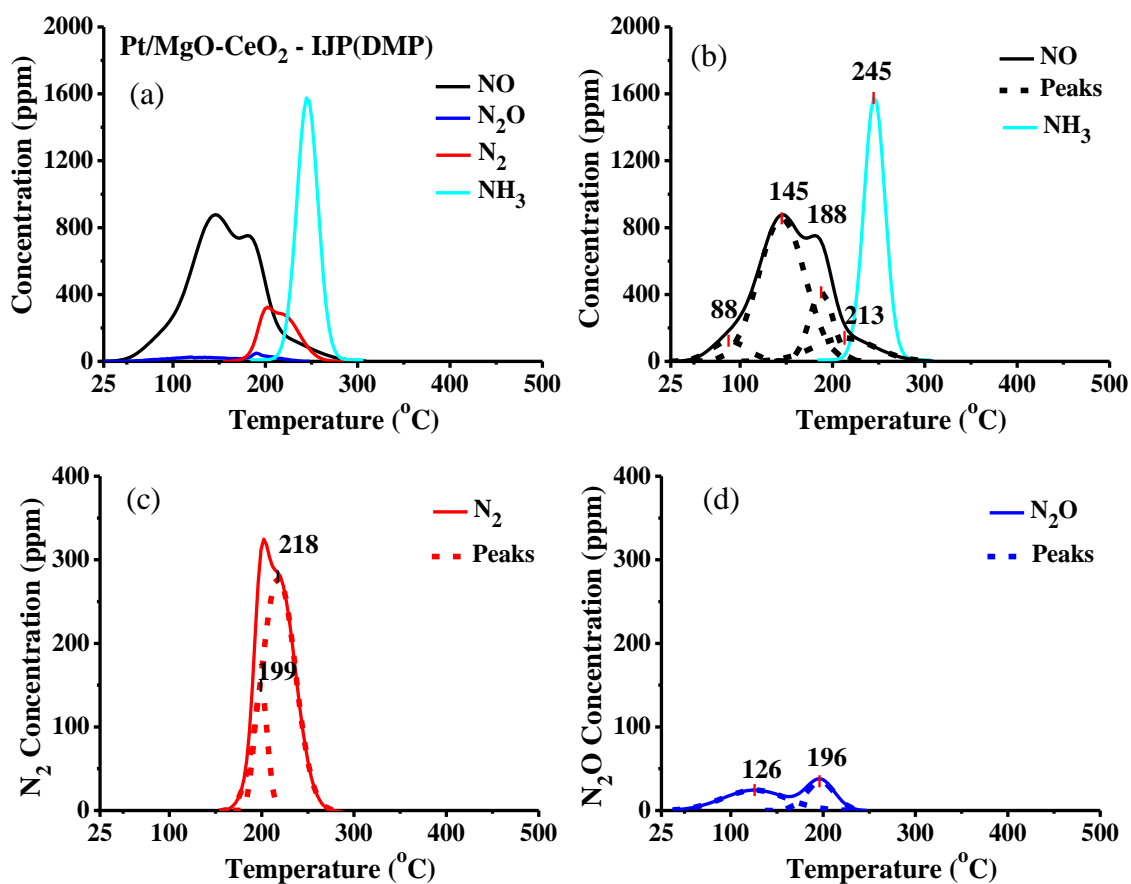
Figure 5.46: Transient response curves of (a) NO, N_2O, N_2 and NH_3, (b) NO and NH_3, (c) N_2 and (d) N_2O, obtained during TPSR in 2%H_2/He flow following NO/H_2/O_2 reaction at 200°C, on the printed 0.1 wt% Pt/MgO-CeO$_2$ (IJP-DMP) catalyst; m_{cat}= 0.14g, Q_{H2}= 50cm³/min, β= 30°C/min.

Fig. 5.46c presents the desorption profile of N_2, which includes a well-resolved N_2 band which is analysed in two peaks that are centred at T_{M1}= 199°C and T_{M2}= 218°C, with the latter appearing as a shoulder at the descending part of the initial band. Fig. 5.46d shows that two smaller N_2O peaks were also observed during this experiment and desorbed in

the area of 35-240°C (T$_{M1}$= 126°C and T$_{M2}$= 196°C). The desorbed amount of N$_2$ was found to be 8µmol/g$_{cat}$, while the amount of N$_2$O was 1.93µmol/g$_{cat}$, which is slightly less than the amount desorbed during He-TPSR. Finally, as seen in Table 5.7, the total amount of the N-containing species is the same between the two experiments (87.9 µmol/g$_{cat}$).

Due to the particular catalytic behaviour of the IJP-DMP catalyst and the unique results obtained during the TPSR studies, additional TPSR studies were conducted on the first-ever inkjet printed 0.1 wt% Pt/MgO-CeO$_2$ catalyst in order to better understand its unique characteristics. As mentioned in subchapter 5.2.2, the catalytic performance of this novel catalyst was affected drastically when it was exposed even to the slightest oxygen concentration in the feed. Therefore, additional TPSR studies were performed following NO/H$_2$ instead of NO/H$_2$/O$_2$ reaction.

Figure 5.47 shows the TPSR profiles obtained over the IJP-DMP Pt/MgO-CeO$_2$ solid under He flow following NO/H$_2$ reaction at 200°C. Fig. 5.47b shows the desorption profile of NO which includes one complex and very broad desorption band in the area of 50-500°C. After deconvolution, four peaks were resolved at 122°C, 147°C, 270°C and 385°C. During this experiment, one N$_2$ band (not well resolved) was observed in the range of 25-280°C (Fig. 5.47c). This particular band is consisted of a small sharp peak at the low temperature of 29°C and a small broad peak at 120°C. The desorption profile of N$_2$O (Fig. 5.47d) shows two small desorption bands. The first peak is centred at 149°C and the second well-resolved band provided two peaks in the area of 225-500°C (T$_{M1}$= 312°C and T$_{M2}$= 411°C). As seen in Table 5.7, the total desorbed amount of NO is 23.4 µmol/g$_{cat}$, which is the majority of the total desorbed amount of N-containing species (57%). As mentioned before, these species could be considered as spectators as they were not able to react with H$_2$ towards N$_2$ or N$_2$O. Moreover, the desorbed amount of N$_2$ was 3.6 µmol/g$_{cat}$ and the amount of N$_2$O was found to be 5.2 µmol/g$_{cat}$.

Figure 5.48 presents the transient response curves of NO, N$_2$ and N$_2$O which were obtained during TPSR in 2% H$_2$/He flow following NO/H$_2$ reaction at 200°C. It is noted that NO (Fig. 5.48b) and N$_2$O (Fig. 5.48d) desorption profiles showed only one peak which was centred at 95°C and 108°C, respectively. On the contrary, the desorption profile of N$_2$ showed two desorption bands; one very small peak at the low temperature of 28°C and a band in the area of 65-235°C. The latter band deconvoluted in two peaks at T$_{M1}$= 121°C and T$_{M2}$= 169°C. It is worth mentioning that NH$_3$ was not observed during this experiment.
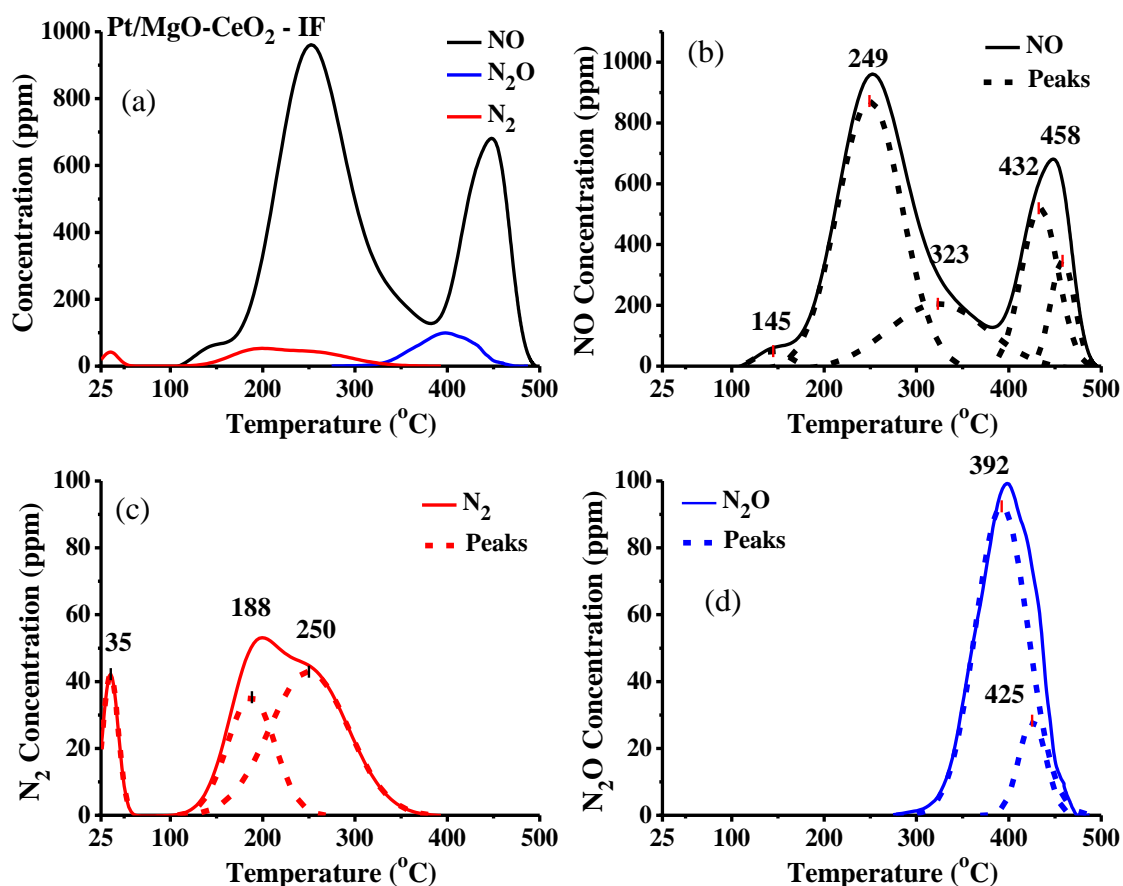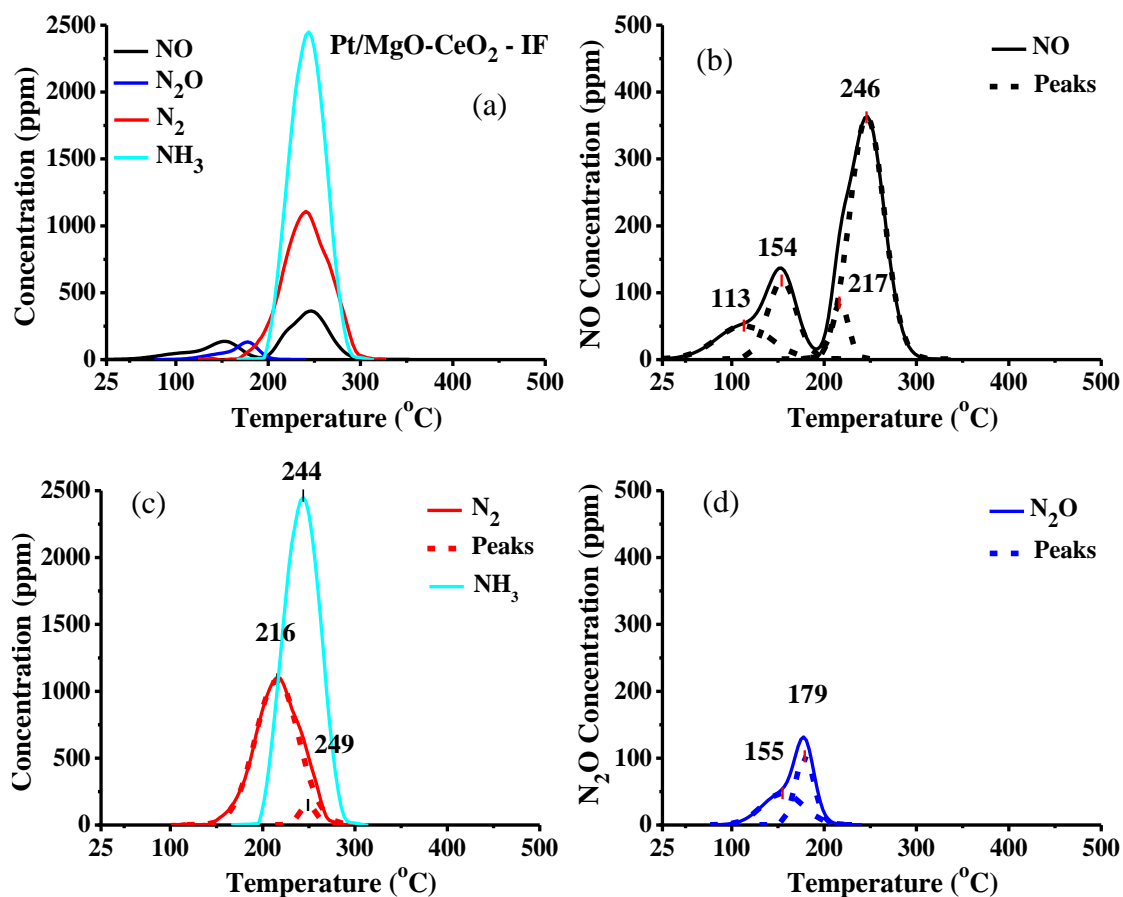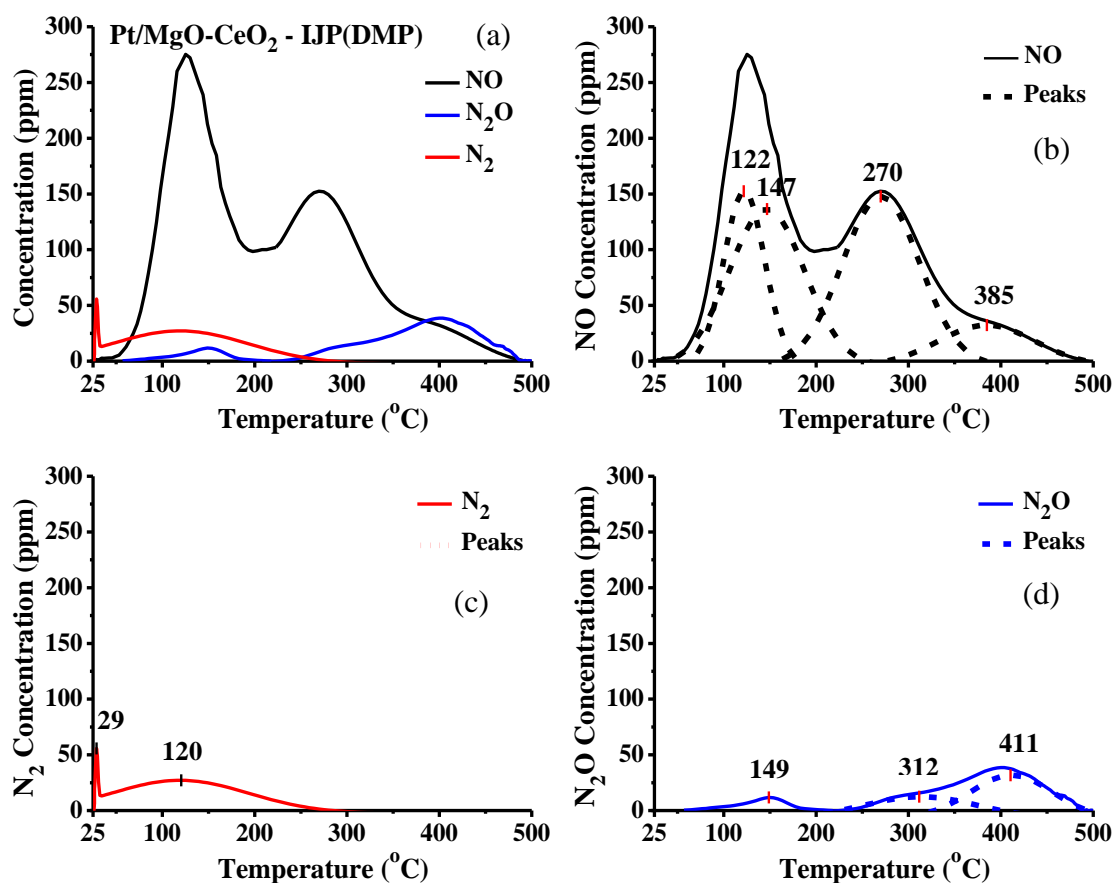
Figure 5.47: Transient response curves of (a) NO, N_2O and N_2, (b) NO, (c) N_2 and (d) N_2O, obtained during TPSR in He flow following NO/H_2 reaction at 200ºC, on the printed 0.1 wt% Pt/MgO-CeO$_2$ (IJP-DMP) catalyst; m_{cat}= 0.14g, Q_{He}= 50cm^3/min, β= 30ºC/min.

As reported in Table 5.7, the total amount of N-containing species remains the same (41 μmol/g$_{cat}$) for the innovative IJP-DMP catalyst in both experiments (Exps. C and D). As seen in Table 5.7, during H_2-TPSR, there is a decrease in the amount of desorbed NO and N_2O by 51% and 19%, respectively, whereas N_2 was increased by almost three times when compared to the He-TPSR results. As suggested in subchapter 5.3.1.2., a spillover process of NO_x species from Pt to the support may take please on the IJP-DMP Pt/MgO-CeO$_2$ catalyst. Therefore, a hydrogen spillover phenomenon is essential in order to explain the reduction of active adsorbed NO_x species which are located on the support. According to the H_2-TPD results presented earlier (subchapter 5.1.5), this specific catalyst, as well as the other Pt/MgO-CeO$_2$ catalysts examined, indicated that a hydrogen spillover is very possible on these solids. In particular, the IJP-DMP catalyst adsorbed high quantities of hydrogen, equivalent to ~45 monolayers based on Pt$_s$, thus a spillover mechanism was invoked to partially explain this very large amount of adsorbed hydrogen.
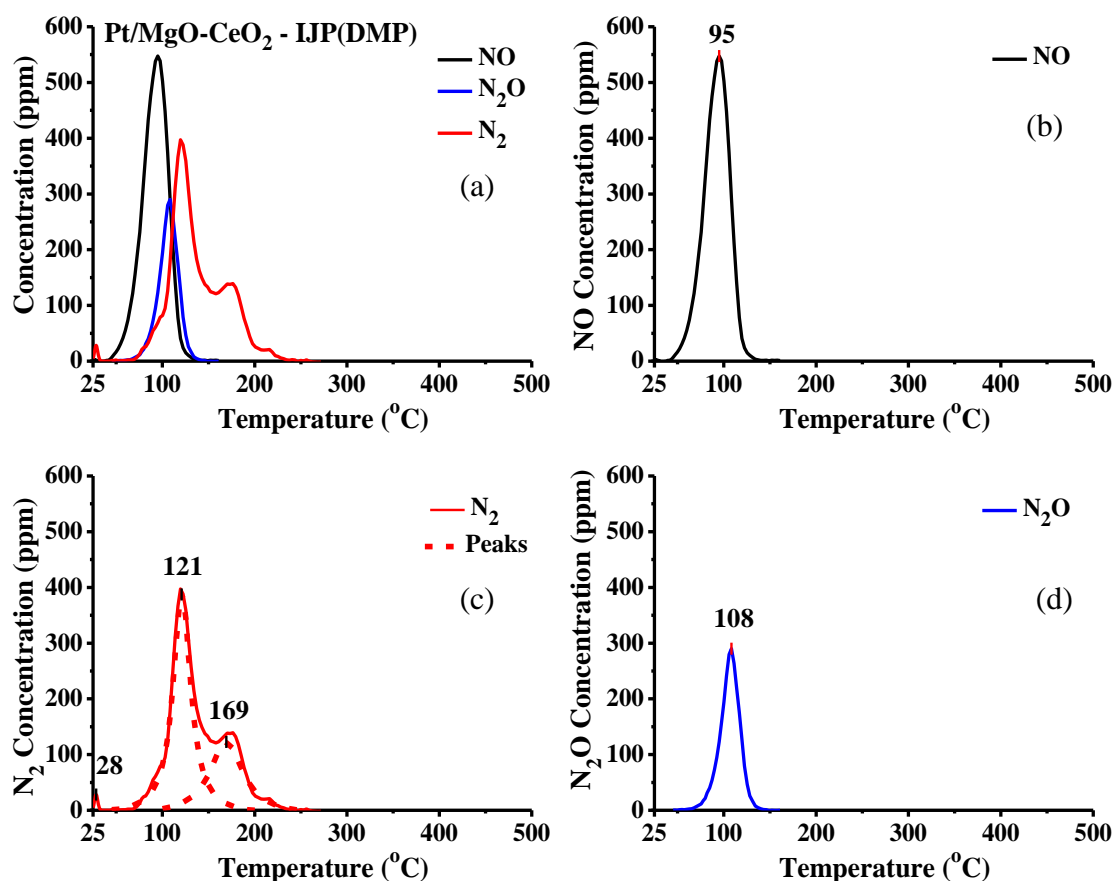
Figure 5.48: Transient response curves of (a) NO, N_2O and N_2, (b) NO, (c) N_2 and (d) N_2O, obtained during TPSR in 2%/H_2/He flow following NO/H_2 reaction at 200°C, on the printed 0.1 wt% Pt/MgO-CeO$_2$ (IJP-DMP) catalyst; m_{cat}= 0.14g, Q_{H2}= 50cm^3/min, β= 30°C/min.

It is important at this point to summarize the differences between the Pt/MgO-CeO$_2$ catalysts after comparing their TPSR profiles. In particular, the TPSR profiles under He flow that are presented in Figs. 5.41 (WI), and 5.43 (IF), 5.45 (IJP-DMP, NO/H_2/O_2) and 5.47 (IJP-DMP, NO/H_2), indicate that at desorption temperatures lower than 150°C, the WI and the IJP-DMP solid (NO/H_2) desorb N_2 and N_2O, while the IF catalyst desorbs only a small amount of N_2 and the IJP-DMP solid (NO/H_2/O_2) does not desorb any of them. The latter results can be used to explain to some degree the differences in the catalytic activity of the solids, as at 150°C, the WI showed X_{NO}= 64%, the IF and IJP-DMP showed X_{NO}= 12% and 2%, respectively, while the printed catalyst achieved 99.6% NO conversion during the NO/H_2 reaction. Also, the temperatures where maximum N_2 and N_2O desorption is observed comes in a good agreement with the maximum NO conversion obtained over the examined catalysts. It is noteworthy that N_2 and N_2O are both formed by active intermediate species during the TPSR process. The IF catalyst presented a broader desorption profile of N_2 (Fig. 5.43c) compared to the WI (Fig.

5.41c), which could be invoked to explain the better selectivity profile of IF towards N_2, as seen in Figure 5.14 (subchapter 5.2.2).

Based on the results of the He-TPSR experiments, the amount of desorbed NO varies significantly between the Pt/MgO-CeO_2 catalysts. The IF solid presented the highest amount (119.7 $\mu mol/g_{cat}$), while the WI catalyst the lowest (50.5 $\mu mol/g_{cat}$) as seen in Table 5.7. The same pattern is observed regarding the total amount of N-containing species. On the other hand, the amount of desorbed NO by the printed catalyst attributed to 98% of the total amount of N-containing species during the NO/H_2/O_2 reaction, and 57% during the NO/H_2 reaction. As mentioned before, the amount and percentage of the active species (N_2, N_2O) obtained from the TPSR profiles provide important intrinsic information. In particular, the IJP-DMP solid (during TPSR following NO/H_2 reaction) and the WI solid presented significant amounts of these species at low reaction temperatures, whereas the IF catalyst did not present significant desorption of the active species at T≤150ºC.

Regarding the H_2-TPSR experiments, all the catalysts exhibited a decrease in the amount of desorbed NO, as seen in Table 5.7, compared to the results obtained by He-TPSR. Specifically, the WI and IF solids presented less amount of NO by 86% and 88%, respectively and the IJP-DMP solid (following NO/H_2 reaction) by 51%. Furthermore, in the case of H_2-TPSR, more than half of the pre-adsorbed NO_x was reduced exclusively to N_2 gas in all the Pt/MgO-CeO_2 catalysts. Additionally, all the catalysts desorbed NH_3 during the H_2-TPSR experiment following NO/H_2/O_2 reaction. On the contrary, when the IJP-DMP catalyst was examined in the reaction without oxygen, it did not desorb any NH_3. It is noted that the differences in composition and the amount of desorbed gases observed on all the examined Pt/MgO-CeO_2 catalysts reflect the different kinetics of reactions that occur under He or H_2 gas [311].

As in the case of the Pt/Al_2O_3 catalysts, the profile of desorbed gases during H_2-TPSR (Figs. 5.42, 5.44 and 5.48) on Pt/MgO-CeO_2 catalysts presented a shift to lower temperatures compared to the profiles observed in He-TPSR and NO-TPD (under He or 2%H_2/He flow). The only exception are the H_2-TPSR profiles of the IJP-DMP solid that were obtained after NO/H_2/O_2 reaction (Fig. 5.46), as they presented a temperature shift compared to He-TPSR, but not compared to the NO-TPD profiles (under He or 2%H_2/He flow). Figure 5.49 presents the significant shift to lower temperatures of the desorbed NO peaks obtained through H_2-TPSR experiments. As suggested before, a hydrogen-

assisted effect is probably taking place on the lowering of the bond strength of Pt-NO [156]. Furthermore, it was reported that the activation energy of the N-O bond dissociation is higher than that of hydrogen assisted N-O dissociation [156], [306], [314], therefore the shifts in temperatures could be justified, as during TPSR in 2%H_2/He flow, the coverage of adsorbed H is higher than that found under the conditions of a TPSR-He run and a NO-TPD in 2%H_2/He flow experiment.
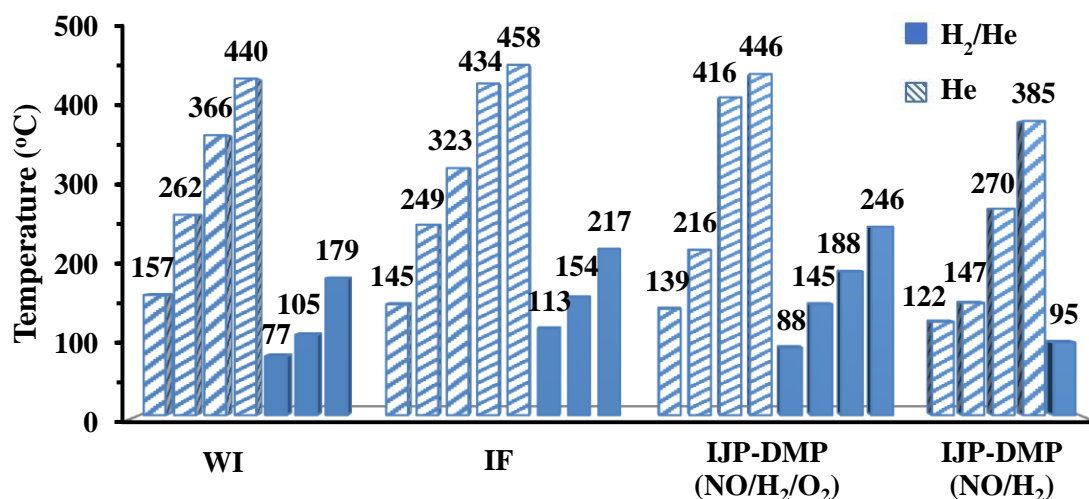
Figure 5.49: Desorption temperature of NO peaks obtained during TPSR under He and 2%H_2/He flow on Pt/MgO-CeO$_2$ catalysts.

The results obtained from the TPSR experiments of the present study confirm the great influence of the chemical composition of the MgO-CeO$_2$ support on the H_2-SCR of NO activity and N$_2$ selectivity. In particular, the chemical nature of the support's sites influences the structure of the adsorbed NO$_x$ species (active or spectators) and therefore affects the surface catalytic chemistry of the H_2-SCR of NO on supported Pt catalysts [73], [285]. Moreover, the mixed oxide support (MgO-CeO$_2$) might provide a positive synergetic effect [33], [279], [316]. In particular, Costa et al. [33] reported that the mechanism for N$_2$ production possibly involves two different intermediate adsorption species that are formed on different phases on the examined 0.1wt% Pt/MgO-CeO$_2$ catalyst. The adsorbed M-NO$^{\delta+}$ species was found on CeO$_2$, while M-O-(NO)-O-Pt was found on the interface of MgO and Pt. Further discussion on this issue will follow in the next chapter (DRIFTS studies).

5.4. DRIFTS Studies

In situ DRIFTS and combined SSITKA-DRIFTS studies have been performed on the inkjet-printed 0.1%Pt/MgO-CeO$_2$ (IJP-DMP) and 0.1%Pt/MgO-CeO$_2$ (IF) catalysts. The experiments were conducted in order to identify and evaluate the chemical structure of adsorbed NO$_x$ intermediate species that are formed on the catalytic surface during the NO/H$_2$/O$_2$ reaction at 200°C. The species were assigned based on the literature [60], [76]–[79] and other DRIFTS studies performed on similar catalysts [73], [75], [279], (see Table 1.2, subchapter 1.3.7.2.). It is noted that the IR spectrum of the solids that was recorded in He flow at 200°C was subtracted (background) from all the recorded spectra obtained after steady-state reaction conditions were achieved.

5.4.1. In-Situ DRIFTS

- IF Pt/MgO-CeO$_2$ catalyst

Figure 5.50 shows the IR spectrum in the 2300-1000cm^{-1} range recorded after 45 min of H$_2$-SCR of NO at 200°C over the Pt/MgO-CeO$_2$ (IF) catalyst. The band observed in the 2000-1900cm^{-1} range corresponds to nitrosyl species on Pt (NO$^{\delta+}$-Pt) [62], [73], [74]. The inset graph presented in Fig. 5.50 shows the deconvolution of the complex IR band in the range of 1710-1540cm^{-1} (Gaussian peak shape), which resulted in three IR peaks centred at 1659cm^{-1}, 1628cm^{-1} and 1582cm^{-1}. It is noted that the following IR band assignments were based on specific criteria such as the low Pt loading of the catalyst (0.1 wt%), the range of the IR bands in which the various kinds of NO$_x$ species appear (see Table 1.2), the integral band intensities and band widths shown in the inset of Fig. 5.50 and the support chemical composition [73].

In particular, the IR peak at 1659cm^{-1} corresponds to unidentate nitrates formed on Pt and bridged or bent NO on Pt (Pt$_n$-NO) [73], [74], [279]. The IR band at 1628cm^{-1} can be assigned to bridged NO on Pt, unidentate nitrates on Pt or bidentate (bridged) nitrates formed on the support (see Table 1.2). According to Savva and Efstathiou [75], the species corresponding to the specific IR band are the result of oxidation of Pt, due to the presence of gaseous oxygen (cofed with NO) or by the dissociation of adsorbed NO. Moreover, bending modes of adsorbed water molecules are also assigned to 1628cm^{-1} [73]–[75], [273], [317] since as reported by Ryczkowski [273], water is molecularly adsorbed on magnesium ions. The last peak that results after the deconvolution which is centred at 1582cm^{-1} is assigned to bidentate (chelated) nitrates on the support (M-O$_2$NO) [60], [73], [77]. It is noted

that the chelating species are a multidentate ligand (bidentate) that essentially uses more than one atom, in this case, two, to bind to a single metal ion on the catalyst's surface, forming a ring of atoms. The metal cation site of the support, is the electron-pair acceptor, while the chelating agent is the electron-pair donor [318], [319].
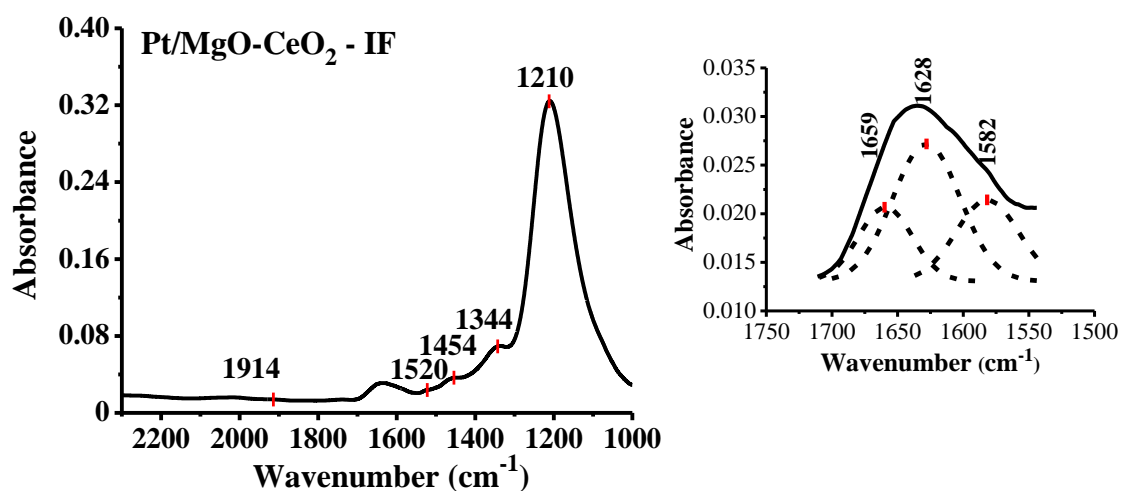
Figure 5.50: In situ DRIFTS spectra recorded over the 0.1 wt% Pt/MgO-CeO$_2$ (IF) catalyst after 45 min of ^{14}NO/H$_2$/O$_2$ reaction at 200°C. Inset graph: Deconvolution of the DRIFTS spectrum recorded in the 1710-1540cm^{-1} range. Feed gas composition: NO= 0.05 vol%, O$_2$= 5 vol%, H$_2$= 1 vol%.

Moreover, Fig. 5.50 shows four more bands in the range of 1550-1000cm^{-1}, which correspond to three adsorbed NO$_x$ species. The IR band that appears at 1520cm^{-1} is assigned to the asymmetric vibrational mode of unidentate nitrates on support (M-O-NO$_2$) [33], [60], [77], [274], [279]. A possible formation of the specific species is via NO adsorption on a pair of vacancy sites which are occupied by two chemisorbed oxygen atoms [60]. In addition, the IR band centred at 1454cm^{-1} is assigned to nitritos on support (^{v}(N=O)) [75]. Nitritos can be formed by the adsorption of NO on a coordinatively unsaturated surface oxygen atom [60]. Chelating nitrite (NO$_2^-$) species are found at 1344cm^{-1} (asymmetric, v_a) [60], [75], [76], [279] and it is noted that Huang et al. [60], who studied the adsorption of NO on La$_2$O$_3$, proposed that the formation of chelating nitrite ions, can be formed when NO molecules are adsorbed on surface sites, which consist of a single oxygen vacancy associated with a neighbouring lattice oxygen atom.

Finally, the strong IR band recorded at 1210cm^{-1} is assigned to the asymmetric vibrational mode of chelating (bidentate) nitrate species on the support [77], [79], [320], where the formation of these species may be due to the chemisorption of gaseous NO$_2$ on a surface metal cation site of the support; on Mg^{2+} and Ce^{4+} of the MgO and CeO$_2$ support phases,

respectively [279]. Consequently, the participation of gaseous oxygen in the formation of NO_2, via oxidation of adsorbed NO on the Pt surface, is needed for the formation of adsorbed nitrate species on the support [15], [74], [321]. Generally, surface nitrates are formed on the support through the reaction of NO_2 with the surface of metal oxides [322]. Figure 5.51 presents schematically the possible steps for the formation of chelating bidentate nitrates on the support.
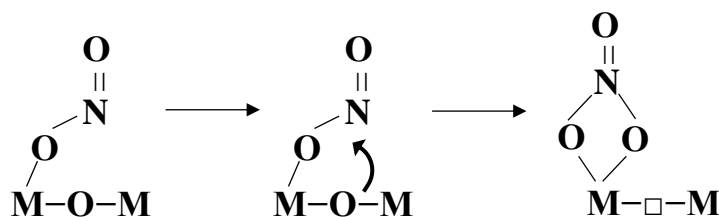
Figure 5.51: Schematic diagram of the formation of chelating bidentate nitrates on the support.

In situ DRIFTS spectra were also recorded after 60 min of NO/H_2 reaction at 200°C on the IF solid. Figure 5.52 shows the respective IR spectra obtained in the 2300-1000cm^{-1} range. It is noted that the species identified during the NO/H_2 reaction were the same (in nature) as with the $NO/H_2/O_2$ reaction mentioned before. Specifically, the IR band found at 2000cm^{-1} is assigned to nitrosyls on Pt ($NO^{\delta+}$-Pt) species [73]. The inset graph presented in Fig. 5.52 shows the deconvolution of the complex IR band in the range of 1700-1560cm^{-1} which results in three IR peaks centred at 1659cm^{-1}, 1621cm^{-1} and 1591cm^{-1}. These particular peaks correspond to unidentate nitrates on Pt (1659cm^{-1}) [74], [279], to bridged bidentate nitrates on the support [60], [76], [79], [323] and molecularly adsorbed water (bending mode) (1621cm^{-1}) [73]–[75], [273] and to bidentate (chelated) nitrates on the support ($M-O_2NO$, 1591cm^{-1}) [60], [73], [77].

Also, the IR band observed at 1520cm^{-1} corresponds to unidentate nitrates on the support ($M-O-NO_2$, asymmetric mode) [33], [60], [77], [274], [279], the peak recorded at 1454cm^{-1} to nitritos on the support [75] and the IR peak at 1337cm^{-1} to asymmetric chelating nitrite species on the support [60], [75], [76], [279]. It is noted that the strong IR band at 1210cm^{-1} is assigned to the asymmetric stretch of chelating (bidentate) nitrates on the support [77], [79], [320].
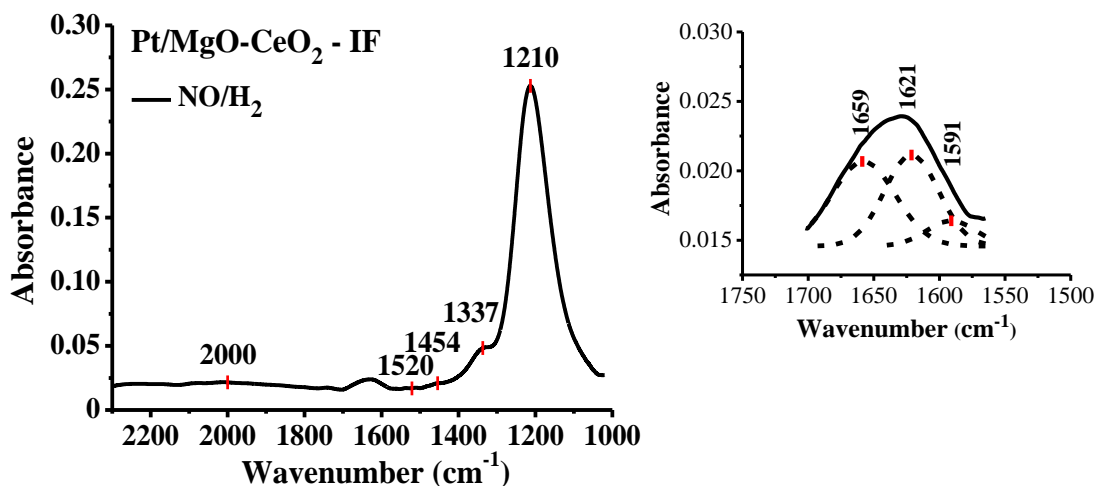
Figure 5.52: In situ DRIFTS spectra recorded over the 0.1 wt% Pt/MgO-CeO$_2$ (IF) catalyst after 60 min of ^{14}NO/H$_2$ reaction at 200°C. Inset graph: Deconvolution of the DRIFTS spectrum recorded in the 1700-1560cm^{-1} range. Feed gas composition: NO= 0.05 vol%, H$_2$= 1 vol%.

The DRIFTS spectra recorded in both reactions (NO/H$_2$/O$_2$ and NO/H$_2$) over the Pt/MgO-CeO$_2$ (IF) catalyst are comparatively presented in Figure 5.53. It is noted that the intensity of the bands (relevant to their surface coverage) observed in the range of 2300-1700cm^{-1} regarding the NO/H$_2$ reaction is slightly higher compared to the NO/H$_2$/O$_2$ reaction. On the contrary, in the range of 1700-1000cm^{-1}, the intensity of the bands decreased when the reaction was performed in the absence of oxygen (NO/H$_2$). Specifically, the last IR band at 1210cm^{-1} (1300-1050cm^{-1}) presented the largest decrease (0.07) in terms of absorbance values. This was also observed by Olympiou and Efstathiou [279] who examined a Pt/MgO-CeO$_2$ catalyst for the reaction at hand. The authors reported that the intensity of the IR bands recorded in 950-1250cm^{-1} increased with increasing oxygen feed concentration and suggested that those IR bands are due to chelating nitrite (NO$_2^-$) species formed upon chemisorption of gaseous NO$_2$ on surface metal cation sites (Mg^{2+} and Ce^{4+}) of MgO and CeO$_2$ support phases. As seen in Figs. 5.50, 5.51 and 5.53, the species formed during NO/H$_2$/O$_2$ and NO/H$_2$ reactions are the same (chemical composition). Consequently, it could be assumed that the nature of adsorbed intermediate species does not seem to be influenced by the absence of oxygen in the feed. However, the actual surface concentration of these species appears to be significantly affected by the presence of O$_2$ in the reaction feed stream.
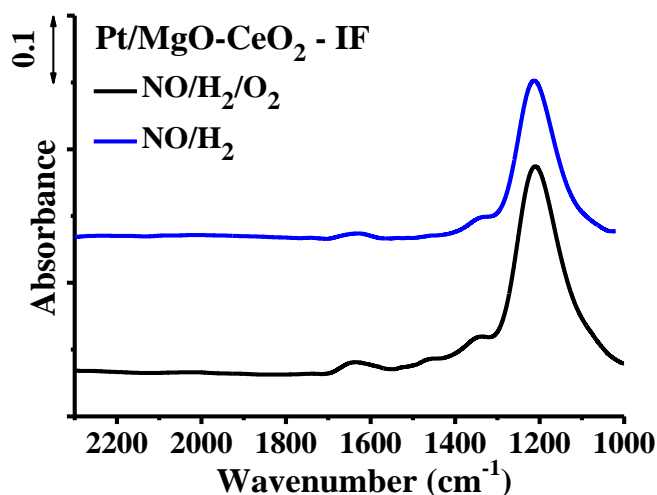
Figure 5.53: In situ DRIFTS spectra recorded over the 0.1 wt% Pt/MgO-CeO$_2$ (IF) catalyst after 45 min of ^{14}NO/H$_2$/O$_2$ (black line) and 60 min of ^{14}NO/H$_2$ (blue line) reactions at 200°C. Reaction conditions: NO= 0.05 vol%, H$_2$= 1 vol%, O$_2$=5 vol%, for the NO/H$_2$/O$_2$ reaction, and NO= 0.05 vol%, H$_2$= 1 vol%, for the NO/H$_2$ reaction.

- IJP-DMP Pt/MgO-CeO$_2$ catalyst

In situ DRIFTS studies were also performed on the inkjet-printed Pt/MgO-CeO$_2$ (IJP-DMP) catalyst. The same experimental protocol was followed as mentioned before, where the spectra were recorded after steady-state reaction conditions were achieved. Figure 5.54 presents the IR bands in the 2300-1000cm^{-1} range recorded after 45 min of H$_2$-SCR of NO at 200°C over the IJP-DMP catalyst. As seen in Fig. 5.54a (inset graph), the first IR band at 2220cm^{-1} is attributed to adsorbed nitrosyl (NO$^+$) coadsorbed with a nitrate (NO$_3^-$) species on adjacent metal cation-oxygen anion site-pair of support, specifically ceria [73], [75], [279]. It is noted that this specific band (2220cm^{-1}) is also characteristic of gaseous N$_2$O or of a weakly adsorbed nitrous oxide species [73], [79]. Based on the work of Costa and Efstathiou [73], this possibility was excluded. The authors examined a Pt/MgO-CeO$_2$ catalyst, and after passing 250ppm N$_2$O/Ar through the catalyst, they did not observe any IR band at 2220cm^{-1}. Moreover, these specific species (adsorbed nitrosyl coadsorbed with a nitrate species on adjacent metal cation-oxygen anion site-pair on ceria), were found to be an active NO$_x$ intermediate species during their work as it exhibited an isotopic IR band shift during the ^{14}NO/H$_2$/O$_2$ $\rightarrow$ ^{15}NO/H$_2$/O$_2$ switch on the Pt/CeO$_2$ catalyst [73]. However, during the experiments of the present work, these specific species were not characterized as active, as they did not indicate a significant isotopic shift during the ^{15}NO/H$_2$/O$_2$ reaction (Fig. 5.59, subchapter 5.4.2). Finally, as shown in Fig. 5.54a the band recorded in the 2000-1900cm^{-1} range corresponds to nitrosyls on Pt (NO$^{\delta+}$-Pt) species [62], [73], [74].

The other inset graph (Fig. 5.54b) shows the deconvolution of the complex IR band recorded in the range of 1720-1595cm^{-1}. The first peak (1683cm^{-1}) corresponds to bridged or bent NO on Pt [73], [75], while the second (1652cm^{-1}) and third (1634cm^{-1}) peaks are assigned to unidentate nitrates on Pt and to molecularly adsorbed water (bending mode) [74], [273], [279]. It is noted that the latter IR peaks can also be attributed to bridged NO on Pt [75]. The IR peak that appears at 1520cm^{-1} (Fig. 5.54) is assigned to unidentate nitrates on support (M-O-NO$_2$, asymmetric mode) [33], [60], [77], [274], [279], while the IR band at 1344cm^{-1} is attributed to chelating nitrite species (asymmetric mode) on the support [60], [75], [76], [279]. Finally, the IR peak at 1205cm^{-1} corresponds to the asymmetric vibrational mode of chelating (bidentate) nitrate species on the support [77], [79], [320].
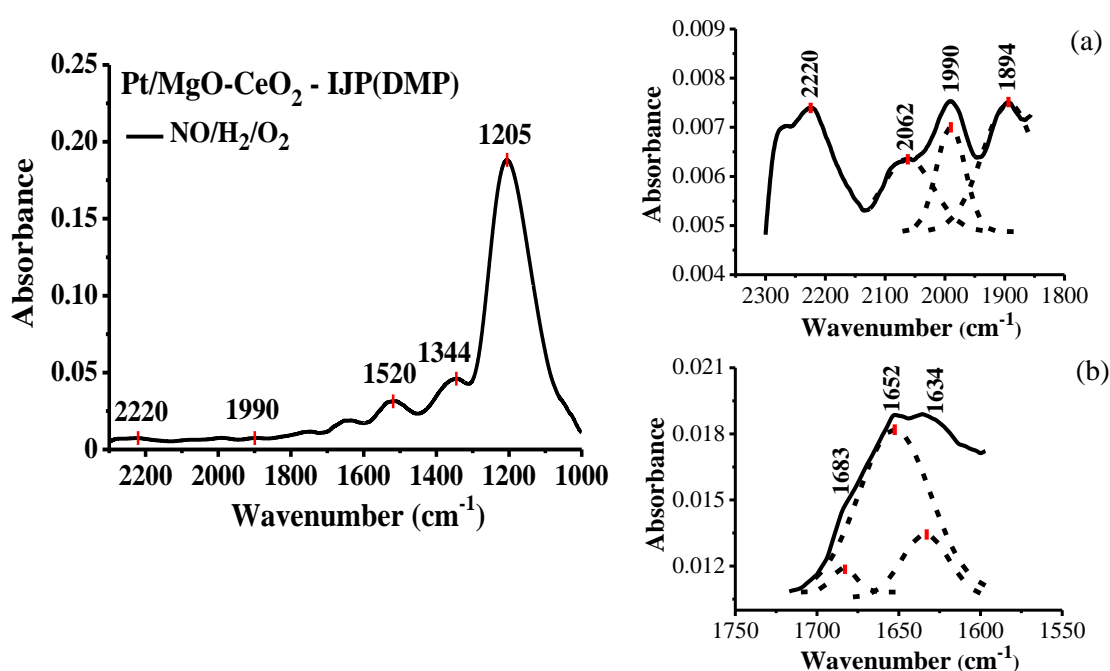
Figure 5.54: In situ DRIFTS spectra recorded over the inkjet-printed 0.1 wt% Pt/MgO-CeO$_2$ (DMP) catalyst after 45 min of ^{14}NO/H$_2$/O$_2$ reaction at 200°C. Inset graphs: Deconvolution of the DRIFTS spectrum recorded in the (a) 2300-1850cm^{-1} and (b) 1720-1595cm^{-1} range. Feed gas composition: NO= 0.05 vol%, O$_2$= 5 vol%, H$_2$= 1 vol%.

Figure 5.55 presents the recorded DRIFTS spectra in the range of 2300-1000cm^{-1} after 60 min of NO/H$_2$ reaction at 200°C on the IJP-DMP catalyst. The first inset graph (Fig. 5.55a) shows the IR bands obtained in the 2300-1875cm^{-1} range. It is noted that the first IR band at 2220cm^{-1} is attributed to adsorbed nitrosyl (NO$^+$) coadsorbed with a nitrate (NO$_3^-$) species on adjacent metal cation-oxygen anion site-pair on ceria [73], [75], [279]. As for the bands recorded in the range of 2000-1900cm^{-1}, these are attributed to nitrosyls on Pt (NO$^{\delta+}$-Pt) [62], [73], [74]. Fig. 5.55b (inset graph), presents the deconvoluted spectra

recorded in the range of 1730-1600cm^{-1}. It is noted that the IR peaks recorded at 1695 cm^{-1} and 1672cm^{-1} are attributed to bridged or bent NO on Pt [33], [73], [74]. As for the IR peaks at 1652cm^{-1} and 1634cm^{-1}, are assigned to unidentate nitrates on Pt [52], [74], but can also be assigned to bridged NO on Pt [75]. Figure 5.55 presents four more IR bands recorded in the range of 1600-1000cm^{-1}. In particular, the IR adsorption band recorded at 1520cm^{-1} is attributed to unidentate nitrates on the support (M-O-NO$_2$), as mentioned before, and the IR bands at 1352cm^{-1} and 1205cm^{-1} are assigned to the asymmetric vibrational mode of the chelating nitrite and chelating (bidentate) nitrate species formed on the support, respectively [60], [75], [76], [279]. Finally, the IR band recorded at 1035cm^{-1} is also attributed to chelating (bidentate) nitrate species (symmetric vibration mode) [77], [79], [320].
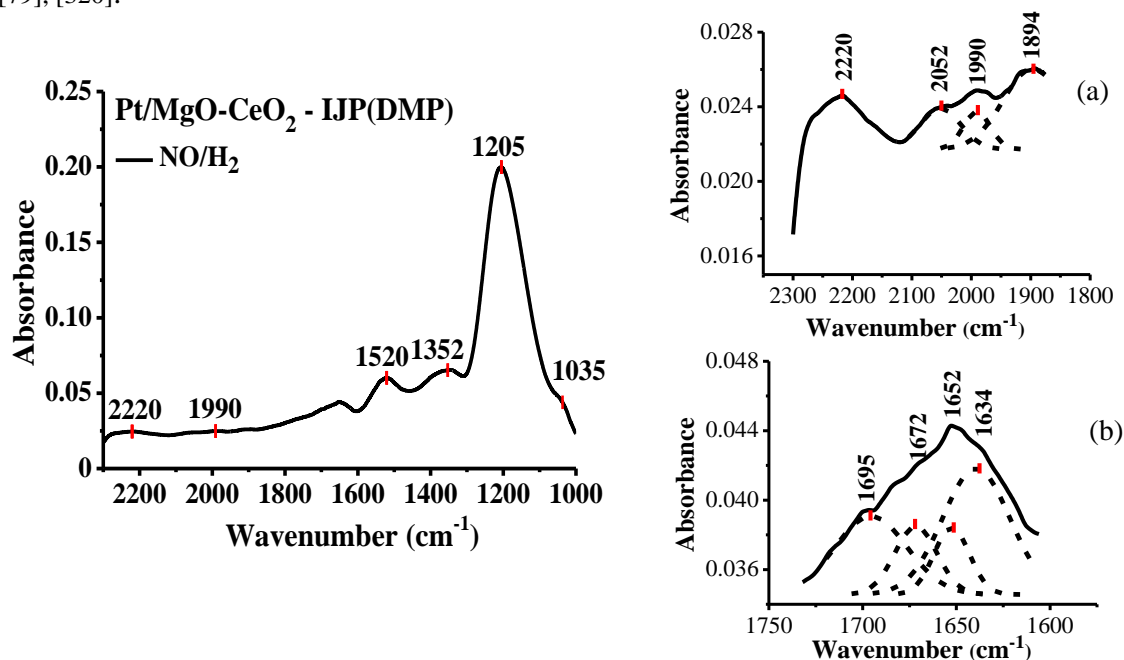
Figure 5.55: In situ DRIFTS spectra recorded over the inkjet-printed 0.1 wt% Pt/MgO-CeO$_2$ (DMP) catalyst after 60 min of ^{14}NO/H$_2$ reaction at 200ºC. Inset graphs: Deconvolution of the DRIFTS spectrum recorded in the (a) 2300-1875cm^{-1} and (b) 1730-1600cm^{-1} range. Feed gas composition: NO= 0.05 vol%, H$_2$= 1 vol%.

The DRIFTS spectra recorded in both reactions (NO/H$_2$/O$_2$ and NO/H$_2$) over the inkjet-printed Pt/MgO-CeO$_2$ (DMP) catalyst are comparatively presented in Figure 5.56. The specific solid presented an increase in the intensity of the observed IR bands in the range of 2300-1300cm^{-1} during the NO/H$_2$ reaction compared to the NO/H$_2$/O$_2$ reaction. In the range of 1300-1000cm^{-1}, the absorbance values were relatively the same for both reactions, with the exemption of the IR peaks at 1205cm^{-1} and 1035cm^{-1} which presented an increase of 0.01 and 0.02 in terms of absorbance values, respectively. On the contrary,

the IF catalyst (Fig. 5.53) presented a decrease in the intensity of the last IR peak at $1210 cm^{-1}$ ($1300-1050 cm^{-1}$), in the absence of O_2 in the reaction's feed. The formation of these species (chelating nitrates) includes the chemisorption of gaseous NO_2 on surface metal cation sites of the support as suggested by Olympiou and Efstathiou [279]. Therefore, in the absence of oxygen, the formation rate of gaseous NO_2 is expected to be decreased and consequently, the surface concentration of the chelating nitrates will be reduced, as was observed by the IF solid.

Figure 5.56: In situ DRIFTS spectra recorded over the inkjet-printed 0.1 wt% $Pt/MgO-CeO_2$ (DMP) catalyst after 45 min of $^{14}NO/H_2/O_2$ (black line) and 60 min of $^{14}NO/H_2$ (blue line) reactions at 200ºC. Reaction conditions: NO= 0.05 vol%, H_2= 1 vol%, O_2=5 vol%, for the $NO/H_2/O_2$ reaction, and NO= 0.05 vol%, H_2= 1 vol%, for the NO/H_2 reaction.

At this point, it should be noted that the differences in the intensity of the IR bands (e.g. higher absorbance values), affects the resulting area under the given IR band, which reflects (semi-quantitatively) the surface concentration of the adsorbed reaction intermediate species, either active or inactive [279]. As seen in Figs. 5.54-5.56, the species formed on the IJP-DMP catalyst during $NO/H_2/O_2$ and NO/H_2 reactions are the same in chemical composition but differ significantly in terms of surface concentration. In particular, the chelating nitrite species (NO_2^-) at $1344 cm^{-1}$ appear to be favoured in the absence of O_2 in the feed, as they presented an increase of 0.02 in terms of absorbance values. This result comes in good agreement with the observations of Huang et al. [60], who suggested that the NO_2^- species are formed on an oxygen vacancy-oxygen pair on the support. It is expected that the concentration of the oxygen vacancies of the support will be significantly lower in the presence of O_2 in the feed. As a consequence the formation of the NO_2^- species is expected to be partially hindered.

5.4.2. Combined SSITKA-DRIFTS Studies

Combined SSITKA-DRIFTS experiments were conducted on the inkjet-printed (DMP) and ink formula (IF) Pt/MgO-CeO$_2$ catalysts in order to differentiate the chemical structure of the active reaction intermediates from that of inactive (spectator) species. Figure 5.57 presents the DRIFTS spectra recorded after 45 min of H$_2$-SCR of NO at 200°C over the Pt/MgO-CeO$_2$ (IF) catalyst, using isotopic NO in the reaction, i.e. ^{15}NO. It is noted that the species identified during the isotopic reaction were the same (in nature) as with the ^{14}NO/H$_2$/O$_2$ reaction mentioned before. The IR band recorded at ~2015cm^{-1} is assigned to nitrosyl species on Pt [62], [73], [74]. The IR bands recorded in the 1660-1550cm^{-1} range (inset graph) correspond to unidentate nitrates on Pt (1636cm^{-1}) [52], [74], bidentate (bridged) nitrates (1603cm^{-1}) and bidentate (chelated) nitrates on the support (1583cm^{-1}) [60], [73], [77].The IR peaks recorded at 1490cm^{-1} and 1454cm^{-1} are assigned to unidentate nitrates and nitritos on the support, respectively [75], [76], while the last two IR peaks (1334cm^{-1} and 1193cm^{-1}), are assigned to chelating nitrite (NO$_2^-$) and chelating (bidentate) nitrate species on the support, respectively [60], [75]–[77], [79], [279], [320].
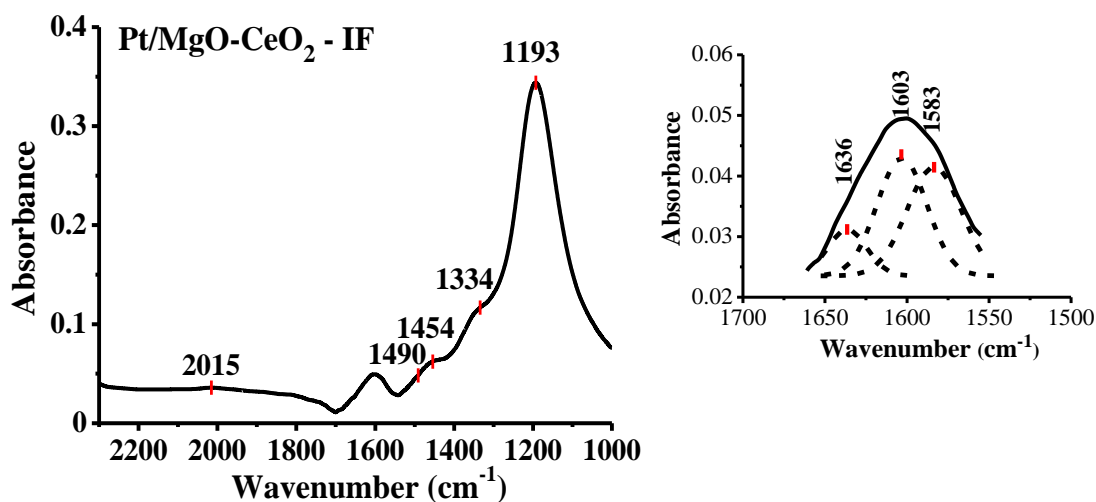
Figure 5.57: In situ DRIFTS spectra recorded over the 0.1 wt% Pt/MgO-CeO$_2$ (IF) catalyst after 45 min of ^{15}NO/H$_2$/O$_2$ reaction at 200°C. Inset graph: Deconvolution of the DRIFTS spectrum recorded in the 1660-1550cm^{-1} range. Feed gas composition: NO= 0.05 vol%, O$_2$= 5 vol%, H$_2$= 1 vol%.

The DRIFTS spectra recorded after ^{14}NO/H$_2$/O$_2$ and ^{15}NO/H$_2$/O$_2$ reactions over the Pt/MgO-CeO$_2$ (IF) catalyst are comparatively presented in Figure 5.58. In Figure 5.58 the IR bands that shifted to lower wavenumbers after the isotopic switch (^{14}NO → ^{15}NO) over the IF solid are marked with vertical lines. These specific bands correspond to active adsorbed intermediate NO$_x$ species that are formed during the NO/H$_2$/O$_2$ reaction and

eventually lead to N_2 and/or N_2O gas production. It is noted that the likelihood for the presence of inactive but exchangeable $^{14}NO_x$ species with gaseous ^{15}NO cannot be excluded [73]. The inset graph of Fig. 5.58 presents the deconvolution of the band in the 1710-1540cm^{-1} range, where it is noted that two IR peaks had shifted to lower wavenumbers. In particular, the IR peak recorded at 1659cm^{-1} and shifted to 1636cm^{-1} corresponds to unidentate nitrates on Pt, as previously noted. Also, the IR band that was recorded at 1628cm^{-1} shifted to 1603cm^{-1} and is attributed to bidentate (bridged) nitrates on the support. According to Huang et al. [60], the bridged nitrates on the support can be formed by the interaction of NO with two adjacent lattice oxygen atoms. In addition, the IR peak at 1520 shifted to 1490cm^{-1} after the isotopic switch and corresponds to unidentate nitrates on the support (M-O-NO$_2$, asymmetric mode) [33], [60], [77], [274], [279]. As for the strong IR peak at 1210cm^{-1}, it shifted to 1193cm^{-1} after the $^{15}NO/H_2/O_2$ reaction. The latter band was assigned to the asymmetric stretch mode of the chelating (bidentate) nitrate species on the support [77], [79], [320].
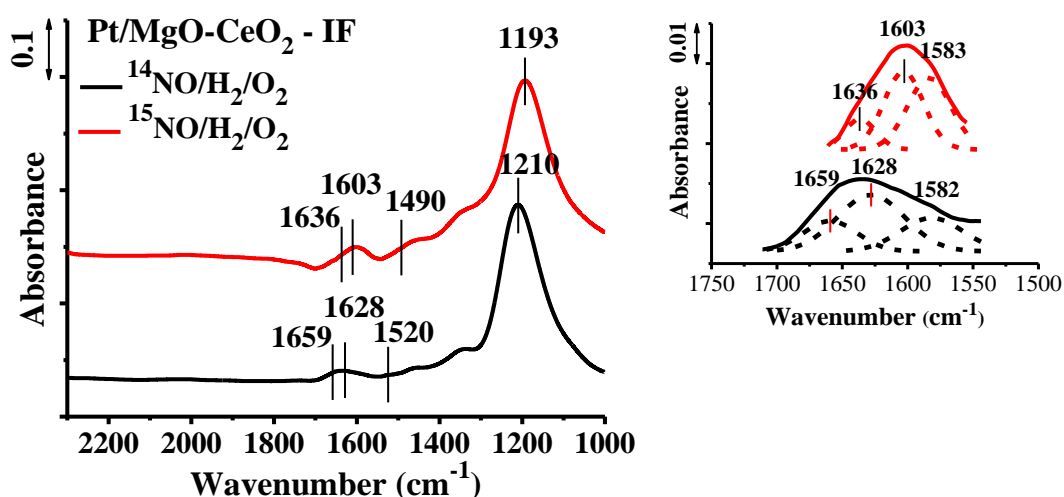
Figure 5.58: In situ DRIFTS spectra recorded before (black line) and after (red line) the isotopic switch $^{14}NO/H_2/O_2$ → $^{15}NO/H_2/O_2$ at 200ºC over the 0.1 wt% Pt/MgO-CeO$_2$ (IF) catalyst. Inset graph: Deconvolution of the DRIFTS spectrum recorded in the 1710-1540cm^{-1} range.

Consequently, four different active intermediate NO$_x$ species can be assigned in the case of the IF solid. Specifically, one of the active species identified is formed on the active metal (unidentate nitrates on Pt), while the other three species are formed on the support (bridged bidentate nitrates, unidentate nitrates and chelating bidentate nitrates). The rest of the species that were identified based on the results of Fig. 5.50, can be characterized as inactive (spectator) since no significant shift was observed to lower wavenumbers after

the isotopic switch. Table 5.8 presents the chemical structures and absorption IR bands of the adsorbed NO_x species found on the IF catalyst and identified as active or inactive.

Table 5.8: Chemical structures and absorption IR bands of adsorbed NO_x species formed on the Pt/MgO-CeO$_2$ (IF) catalyst, during NO/H$_2$/O$_2$ reaction at 200ºC.
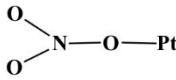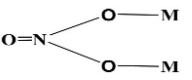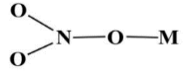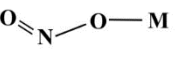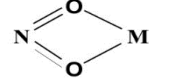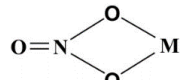
Species	Structure	Vibration	Wavenumber (cm^{-1})	Inactive	Active
Nitrosyls on Pt	$NO^{\delta+}$-Pt	$^\nu$(NO)	2000-1900	✓	
Unidentate nitrates on Pt			1659 → 1636		✓
Bidentate (bridged) nitrates on support		$^\nu$(NO)	1628 → 1603		✓
Unidentate nitrates on support		$^\nu$(NO$_2$,a)	1520 → 1490		✓
Nitritos on support		$^\nu$(N=O)	1454	✓	
Chelating nitrite on support		$^\nu$(NO$_2$,a)	1344	✓	
Chelating (bidentate) nitrates on support		$^{\nu\nu}$(N=O) $^\nu$(NO$_2$,a)	1582 1210 → 1193		✓

Figure 5.59 shows the DRIFTS spectra recorded in the range of 2300-1000cm^{-1} of the inkjet-printed (DMP) Pt/MgO-CeO$_2$ catalyst after 45 min of the isotopic reaction (^{15}NO/H$_2$/O$_2$) at 200ºC. The species identified during the isotopic reaction were the same (in nature) as with the ^{14}NO/H$_2$/O$_2$ reaction mentioned before (Fig. 5.54). As seen in Fig. 5.59, the first small IR band at 2215cm^{-1} is assigned to adsorbed nitrosyl (NO$^+$) coadsorbed with a nitrate (NO$_3^-$) species on adjacent metal cation-oxygen anion site-pair on ceria [73], [75], [279]. The IR band centred at 1980cm^{-1}, corresponds to nitrosyls on Pt (NO$^{\delta+}$-Pt) [62], [73], [74]. Two species were observed in the range of 1735-1600cm^{-1}, i.e. bridged or bent NO on Pt for the IR bands at 1700cm^{-1} and 1673cm^{-1} [73], [75], while unidentate nitrates on Pt were also identified based on the IR bands recorded at 1652cm^{-1} and 1637cm^{-1} [52], [74], [291]. Finally, unidentate nitrates on the support (M-O-NO$_2$, asymmetric mode) were assigned to the IR band at 1520cm^{-1} [33], [60], [77], [274], [279], chelating nitrite species to the IR band of 1344cm^{-1} (asymmetric mode) and chelating (bidentate) nitrate species on the support to the strong IR band at 1183cm^{-1} [60], [75]–[77], [279], [320].
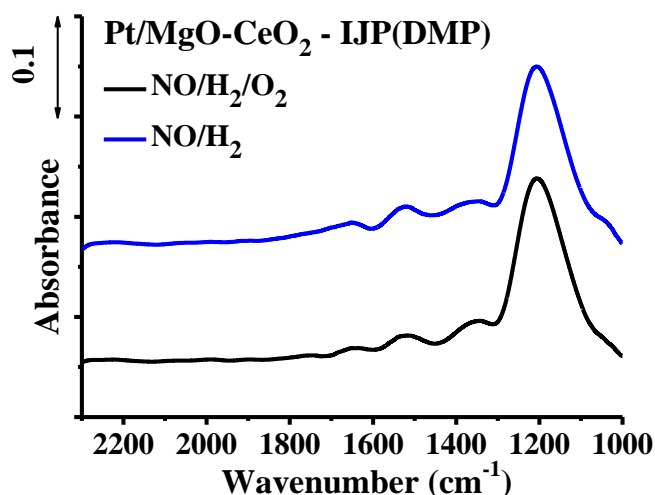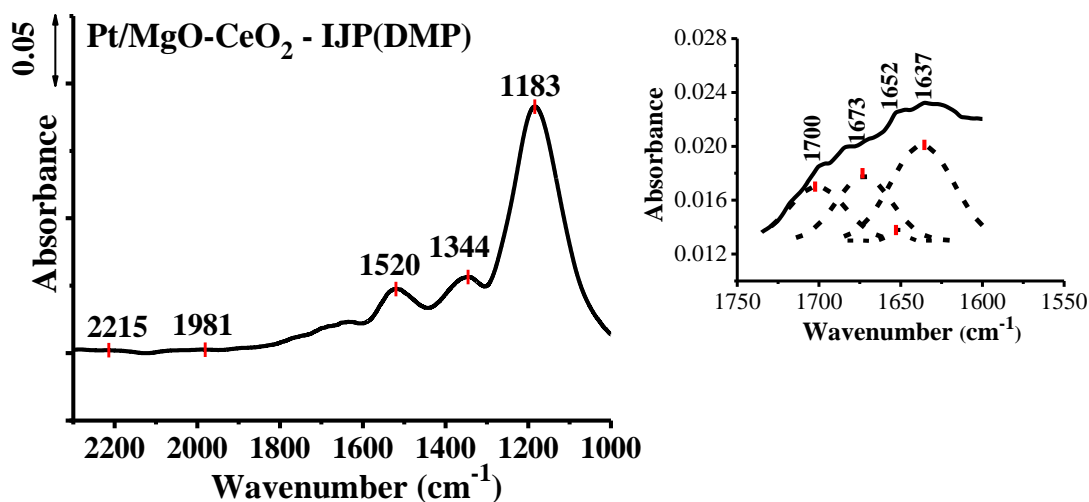
Figure 5.59: In situ DRIFTS spectra recorded over the inkjet-printed 0.1 wt% Pt/MgO-CeO$_2$ (DMP) catalyst after 45 min of $^{15}NO/H_2/O_2$ reaction at 200°C. Inset graph: Deconvolution of the DRIFTS spectrum recorded in the 1735-1600cm^{-1} range. Feed gas composition: NO= 0.05 vol%, O$_2$= 5 vol%, H$_2$= 1 vol%.

The DRIFTS spectra recorded before and after the isotopic switch $^{14}NO/H_2/O_2$ → $^{15}NO/H_2/O_2$ over the inkjet-printed Pt/MgO-CeO$_2$ (IJP-DMP) catalyst are comparatively presented in Figure 5.60. As seen in Fig. 5.60, the specific catalyst presented only one IR band that shifted to lower wavenumbers after the isotopic switch. The intense IR band at 1205cm^{-1} shifted to 1183cm^{-1} is attributed to chelating (bidentate) nitrate species [77], [79], [320], as previously mentioned. Since no other bands shifted to lower wavenumbers, one can safely claim that the rest of the NO$_x$ species are considered to be inactive during the H$_2$-SCR of NO on this particular catalyst. This observation is in agreement with the negligible NO conversion values (X$_{NO}$< 6%) observed on the IJP-DMP catalyst for the NO/H$_2$/O$_2$ reaction throughout the temperature range of 60-400°C (see Fig. 5.15). As noted before, this specific printed catalyst can be very easily oxidized and looses its catalytic activity with the slightest input of oxygen in the feed stream. Table 5.9 presents the chemical structures and IR bands of the adsorbed NO$_x$ species formed on the inkjet-printed catalyst (IJP-DMP), both active and inactive.
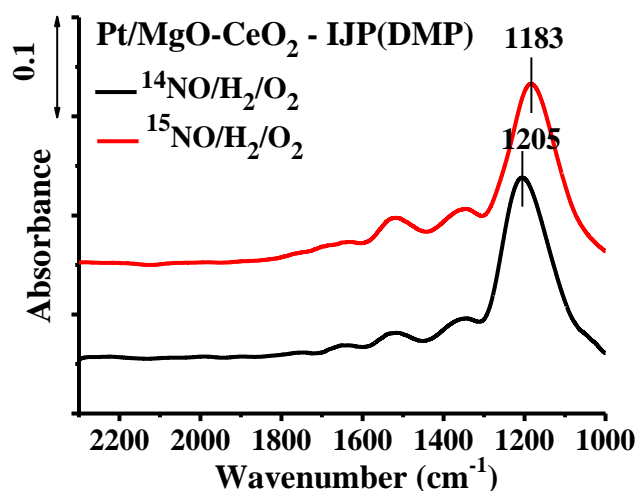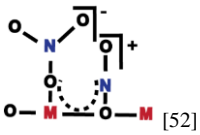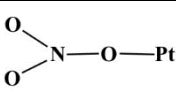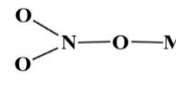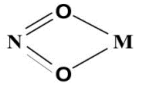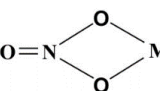
Figure 5.60: In situ DRIFTS spectra recorded before (black line) and after (red line) the isotopic switch $^{14}NO/H_2/O_2 \rightarrow {}^{15}NO/H_2/O_2$ at 200°C over the inkjet-printed 0.1 wt% Pt/MgO-CeO$_2$ (DMP) catalyst.

Table 5.9: Chemical structures and absorption IR bands of adsorbed NO$_x$ species formed on the inkjet-printed Pt/MgO-CeO$_2$ (DMP) catalyst, during NO/H$_2$/O$_2$ reaction at 200°C.

Species	Structure	Vibration	Wavenumber (cm^{-1})	Inactive	Active
Nitrosyl coadsorbed with a nitrate	[structure] [52]		2220	✓	
Nitrosyls on Pt	$NO^{\delta+}$-Pt	^{v}(NO)	2000-1900	✓	
Bridged or bent NO on Pt	Pt$_n$-NO	^{v}(NO)	1683	✓	
Unidentate nitrates on Pt	[structure]		1652, 1634	✓	
Unidentate nitrates on support	[structure]	^{v}(NO$_2$,a)	1520	✓	
Chelating nitrite on support	[structure]	^{v}(NO$_2$,a)	1344	✓	
Chelating (bidentate) nitrates on support	[structure]	^{v}(NO$_2$,a) ^{v}(NO$_2$,s)	1205 $\rightarrow$ 1183 1035		✓

By comparing the results of the two examined catalysts, it can be seen that the IF solid presented more active intermediate NO$_x$ species than the inkjet-printed catalyst (IJP-DMP). In particular, the Pt/MgO-CeO$_2$ catalyst prepared with the modified wet impregnation method using ink formula (IF), presented four active species on its catalytic

surface (see Table 5.8), specifically, unidentate nitrates on Pt and bridged bidentate nitrates, unidentate nitrates and chelating bidentate nitrate species on the support. The latter species was also found to be active in the case of the inkjet-printed (IJP-DMP) catalyst during H_2-SCR of NO (Table 5.9). As mentioned before, the rest of the species that were found on both catalysts can be characterized as inactive (spectator) and therefore are not reduced to N_2 or N_2O. The inactive species are located on both the metal and support surfaces. Figure 5.61 presents schematically the active and inactive adsorbed NO_x species of both examined Pt/MgO-CeO$_2$ catalysts, as were noted in Tables 5.8 and 5.9.
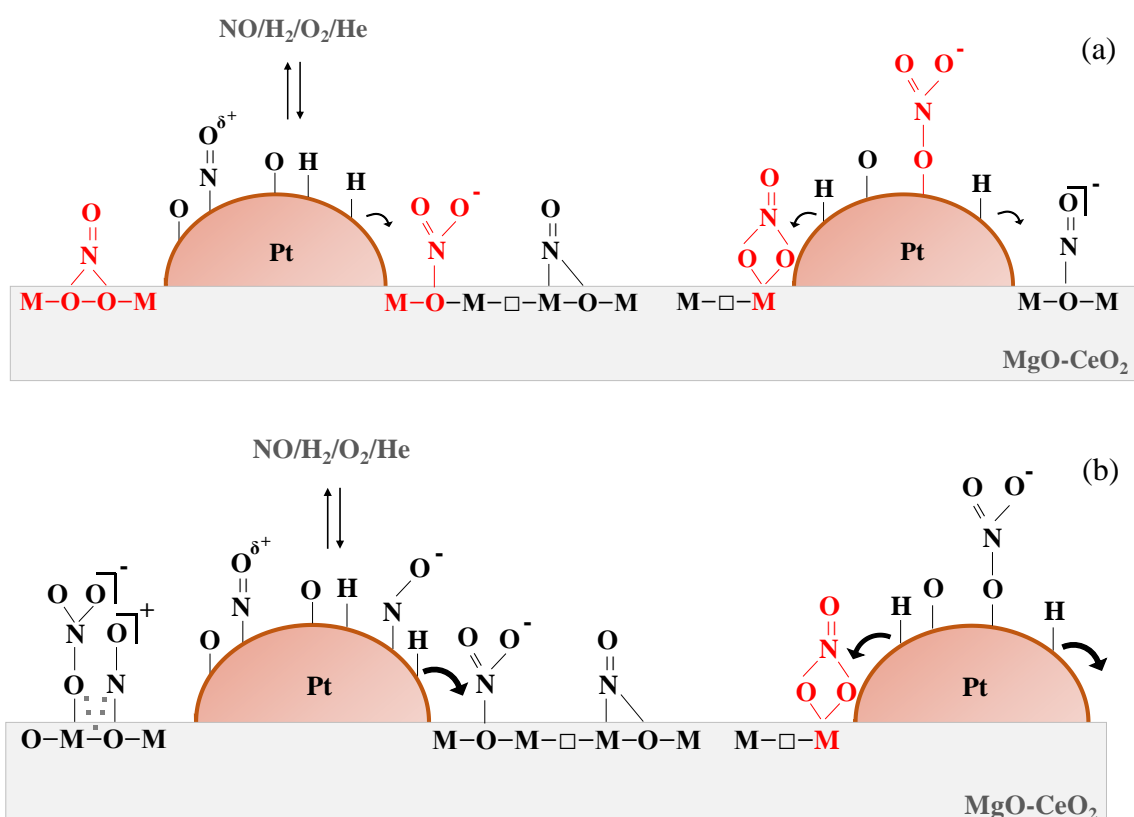
Figure 5.61: Schematic diagrams of the active (red colour) and inactive (black colour) adsorbed NO_x species found on the (a) IF and (b) IJP-DMP Pt/MgO-CeO$_2$ catalysts.

At this point, it should be mentioned that according to the literature, similar but not the same active species were found on the Pt/MgO-CeO$_2$ catalysts. In particular, Costa and Efstathiou [73], reported two active intermediate NO_x species, i.e., (a) nitrosyl species coadsorbed with a nitrate species on adjacent metal cation-oxygen anion site-pair of CeO$_2$ support at 2220cm^{-1}, which are able to exchange with gaseous NO (reversibly chemisorbed NO_x species) and (b) bidentate nitrate on the MgO support at 1580cm^{-1}. These two active species are formed within the metal-support interphase region (as also found in the present work), while the inactive species are populated on both the metal and

support surfaces during H_2-SCR of NO at $140^{\circ}C$. Savva and Efstathiou [75], also examined the Pt/MgO-CeO$_2$ catalyst and reported that the chemical structure of the second active NO$_x$ species depends on the reaction temperature. In particular, for $T_R <$ $200^{\circ}C$, it has the structure of bidentate or unidentate nitrate (NO$_3^-$) located in the vicinity of the Pt-MgO support interface, while at $300^{\circ}C > T_R > 200^{\circ}C$, it has the structure of chelating nitrite (NO$_2^-$), as the bidentate or unidentate nitrate species became inactive. As for the first NO$_x$ species (nitrosyl species coadsorbed with a nitrate species on adjacent metal cation-oxygen anion site-pair of CeO$_2$ support), they appeared to be active reaction intermediates throughout the examined temperatures.

The results described above (Tables 5.8 and 5.9), are in good agreement with the Tempreature-Programmed Surface Reactivity studies that were performed on both catalysts (subchapter 5.3.2.2.). Based on the transient response curves of desorbed N$_2$ and N$_2$O, obtained during TPSR in He following NO/H$_2$/O$_2$ reaction at $250^{\circ}C$ (Fig. 5.43) on the IF catalyst, two desorption peaks of N$_2$ (3 peaks, after deconvolution) and one desorption peak of N$_2$O (2 peaks, after deconvolution) were observed. Therefore, the four active species that were found during the combined SSITKA-DRIFTS studies are responsible for the production of N$_2$ and N$_2$O that were observed in the He-TPSR experiments. As for the inkjet-printed catalyst (IJP-DMP) during the He-TPSR following NO/H$_2$/O$_2$ reaction at $200^{\circ}C$, only one desorption band of N$_2$O was obtained (Fig. 5.45), which is in agreement with the active species found on the support (chelating bidentate nitrates), as seen by the isotopic shift in Fig. 5.59.

Considering the fact that the active NO$_x$ species are also formed on the support (bifunctional catalysis), therefore, a hydrogen spillover from the Pt sites to the metal-support interface via lattice oxygen (M^{n+}-O^{2-}-M^{n+} bridges) [306], is essential for the H$_2$-SCR of NO [73], [160]. More specifically, this bifunctional reaction mechanism involves the dissociative adsorption of H$_2$ and O$_2$ on the surface of Pt [324]–[326], as well as the dissociative adsorption of O$_2$ on the oxygen vacant sites of CeO$_2$ surface [33], [327]. Also, the chemisorption of NO occurs on the Pt surface [55], [236], as well as, at the periphery of the metal-support interface [73] and on the support (metal oxides) [68], [70], [71]. During the reaction, the H species are diffused to the support via a spillover effect, where the active intermediate NO$_x$ species, which are formed on the support or on the vicinity of the metal-support interface, are reduced to N$_2$ and N$_2$O.

As noted in subchapter 5.1.5, during the H_2-TPD results of the examined catalysts, a hydrogen spillover effect was indeed observed on both catalysts (IF and IJP-DMP) and thus the active species formed on the support are able to be involved in the pathway of N_2 and N_2O formation during the $NO/H_2/O_2$ reaction. Such a mechanism was reported in the literature for the $Pt/MgO-CeO_2$ catalyst [73], [75] and a Pd/MnO_x-CeO_2 catalyst [328], which is similar to the present support composition of $MgO-CeO_2$. It is worth mentioning that, the diffusion of H species from the active phase (Pt) to the MgO and CeO_2 support surfaces (spillover) is limited within a region around the Pt nanoparticles (4-5Å) [75], otherwise, all of the NO_x species that are formed on the support would be part of the H_2-SCR of NO as active intermediate species.

Furthermore, the inkjet-printed $Pt/MgO-CeO_2$ catalyst (IJP-DMP), exhibited much higher quantities of adsorbed NO (θ_{NO}=3) during the NO-TPD under He flow (Table 5.5), which was partially explained by a reverse-spillover process of NO_x species from the support to the Pt surface (Fig. 5.31) during the temperature desorption stage. Consequently, an alternative reaction mechanism of the H_2-SCR of NO of the IJP-DMP catalyst may involve a reverse spillover step of the NO_x species to the Pt surface and then their reduction by H atoms on Pt.

The unique behaviour of the inkjet-printed $Pt/MgO-CeO_2$ catalyst, regarding its negligible NO conversion during the H_2-SCR of NO under oxidizing conditions may be explained as follows. The fact that the chelating nitrates species that are formed on the support were found to be active during the isotopic reaction, does not imply that their decomposition rate is high. Even though the particular species are found at significant (high) surface concentration, these species are probably decomposed very slowly (kinetic rate of decomposition). This observation may also apply to the examined IF solid. However, the latter catalyst presented more active species, that may decompose faster, thus having better catalytic performance than the IJP-DMP solid during the $NO/H_2/O_2$ reaction.

Moreover, the relative strength of the nitrogen-oxygen bond in the active NO_x species must be considered as an important factor that controls the catalytic performance of the catalysts, i.e., the relative rates of N_2 formation [74]. It is noted that the species that absorb (in the IR spectrum) at higher frequencies, thus higher recorded wavenumber values, exhibit stronger nitrogen-oxygen bonds. For instance, the N=O bond in the bidentate (bridged) nitrates at 1590-1660cm^{-1} (see Table 1.2), is stronger than the N-O bond at 970-

$1035cm^{-1}$ (unidentate nitrates on the support). Regarding the active species of the IJP-DMP Pt/MgO-CeO$_2$ catalyst (bidentate chelated nitrates on the support, $1205cm^{-1}$), they exhibit a weak N-O(M-O$_2$N) bond compared to the other NO$_x$ species recorded at higher wavenumber values. Thus, since the N-O bond (M-O$_2$N, chelated bond) is weak, the N=O bond is expected to be stronger and thus more difficult to break. Consequently, the decomposition (reduction) rate of these species is expected to be quite low, as compared to the rest of the active species observed in the present work. This concluding observation is invoked to explain the negligible catalytic performance of the novel IJP-DMP Pt/MgO-CeO$_2$ catalyst during the H$_2$-SCR of NO under oxidizing conditions.

Finally, since, previous studies on the H$_2$-SCR reaction have proven that best catalytic behavior can be obtained by achieving optimum Pt oxidation state on supported-Pt catalysts, it can be concluded that the inkjet printing technique has led to the formation of a close-to-ideal state of Pt, probably due to the smaller Pt nanoparticles formed and the better contact between these particles and the support (via electronic interactions). However, the catalysts prepared with the wet impregnation method, exhibit larger Pt clusters, resulting in weaker electronic interactions between the Pt nanoparticles and the support, and present lower spillover and reverse-spillover of the diffused species (i.e., H, O and NO species), as shown in Figure 5.62i.

Regarding the IJP catalysts, on one hand, these fine Pt nanoparticles and the excellent contact between them and the support can facilitate the diffusion of intermediate species from the metal to the support and vice-versa, leading to increased catalytic activity as shown in Figure 5.62a (i.e., case of the inkjet-printed Pt/Al$_2$O$_3$ catalyst, proposed species based on literature [73], [121], [160]). On the other hand, the fine Pt nanoparticles are expected to be much more unstable and thus susceptible to oxidation by the reaction medium (Fig. 5.62b), a fact that can lead to the complete deactivation of the catalyst (i.e., case of the inkjet-printed Pt/MgO-CeO$_2$ catalyst).

In conclusion, the results of the present PhD dissertation have proven that inkjet printing of catalysts can be considered as a promising, innovative technique for catalysts' preparation. Significant work is still needed though, towards the regulation of the process details in order to achieve optimal catalytic results. The present work may be well considered as the basis of the future work that needs to be done within this field.
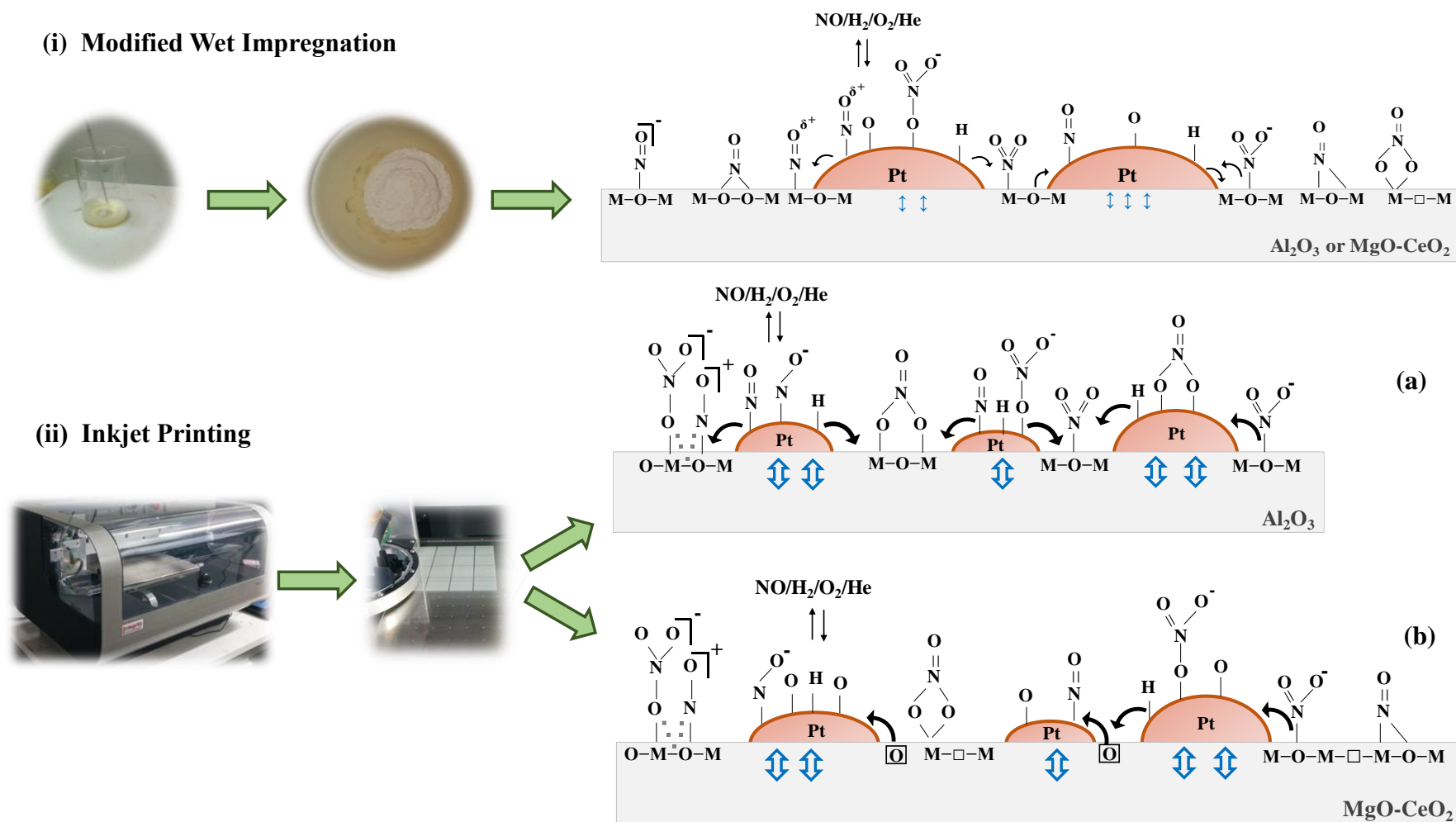
Figure 5.62: Schematic representation of the main mechanistic characteristics (at the nanoscale level) of the catalysts prepared by the modified WI and ink-jet printing methods: where ↕ and ⇕ indicate the electronic interactions between Pt nanoparticles and the support and the bent black arrows represent the diffusion of species from and to the metallic surface (larger arrows denote stronger interaction).

CHAPTER 6: CONCLUSIONS

The most important conclusions of this doctoral dissertation can be summarized as follows:

6.1. Preparation of Pt-supported catalysts with innovative synthesis methods.

The most significant contribution of this dissertation in respect to the development of efficient and innovative catalysts for the reduction of NO, is the successful preparation of the *three printed Pt-supported catalysts* that were developed for the *first-time-ever by novel inkjet printing*, using two different printing protocols. The inkjet printing process enabled the direct and precise fabrication of the Pt-supported catalysts. In particular:

1. Two Pt/Al_2O_3 catalysts were prepared by novel IJP using two different printers; the modified Epson L800 printer and the Dimatix Material Printer-2850, while one $Pt/MgO-CeO_2$ catalyst was prepared with the latter material printer (DMP). It is noted that the Epson L800 printer, was custom-modified for the needs of the current work and was able to print multiple layers of the support (Al_2O_3 formula ink) and the metallic phase (Pt formula ink) of the catalyst, on alternating and consecutive layers, creating a unique structure of the final printed catalyst.

2. The printed Pt/Al_2O_3 catalyst (IJP-Epson) was produced using the ink formula. The same ink formula was also used in order to prepare a Pt/Al_2O_3 and a $Pt/MgO-CeO_2$ catalyst, using a *modified wet impregnation method (IF)*. It must be mentioned that these catalysts were synthesized solely for the purposes of this dissertation and thus never been examined for the reaction at hand ($NO/H_2/O_2$). The morphology of these three catalysts was very distinct as they presented a honeycomb structure, which was not observed in any other catalysts. Moreover, the IJP-Epson Pt/Al_2O_3 catalyst indicated a relatively narrow size distribution of the catalyst's particles (d~150nm) with a practically spherical shape. It is noted that the nano-spherical shape of the particles is produced only during the printing process, and cannot be duplicated by the wet impregnation method, even when using the same ink formulation used for the preparation of the printed catalyst.

3. The inkjet-printed Pt/Al_2O_3 catalyst, using a Dimatix Material Printer, presented a distinct lego-like structure, where the primary grains were joint together composing a unique and uniform morphology throughout the sample. In particular, the latter

catalyst presented larger agglomerates that are consisted of much smaller particles (60-90nm) that have a spherical shape. The inkjet-printed $Pt/MgO-CeO_2$ catalyst, using the same material printer, maintained a uniform distribution of the spherically shaped catalyst's crystallites (<100nm), even after performing various experiments.

6.2. Catalytic performance of the Pt/Al_2O_3 and $Pt/MgO-CeO_2$ catalysts towards the H_2-SCR of NO.

1. The catalytic behaviour and especially the activity (X_{NO}) of the supported-Pt catalysts towards the $NO/H_2/O_2$ reaction was found to strongly depend on the catalyst's preparation technique.

2. All examined catalysts kept more than half of their maximum catalytic activity at temperatures up to 250^oC, while the IF $Pt/MgO-CeO_2$ catalyst up to 300^oC, even though most conventional Pt-based catalysts (reported in the literature) lose most of their catalytic activity at $T> 200^oC$.

3. The inkjet-printed Pt/Al_2O_3 catalysts (Epson and DMP) displayed a unique behaviour compared to the rest of the Pt/Al_2O_3 catalysts examined, namely, high NO conversion at very low reaction temperatures and wider temperature window of operation ($\Delta T= 150^oC$, $T_R= 100-250^oC$). The first-ever printed Pt/Al_2O_3 catalyst (IJP-Epson), presented 91% conversion of NO at 150^oC and was able to retain substantial catalytic activity even at reaction temperatures as high as $400°C$. The IJP-Epson catalyst is superior to the catalysts prepared by the wet impregnation method (WI and IF) particularly concerning the temperature of maximum NO conversion, which is $50°C$ lower in the case of the printed catalyst (Epson).

4. The IJP-DMP Pt/Al_2O_3 catalyst presented remarkable NO conversion for the low-temperature range of $140-200^oC$ (average $X_{NO}= 97\%$), where at 175^oC it achieves practically complete conversion of NO ($X_{NO}= 99.5\%$). It can be safely claimed that the printing protocol followed in the present work for the Pt/Al_2O_3 catalysts, has led to a unique surface structure that favours the conversion of NO at low reaction temperatures ($T= 100-200^oC$).

5. The WI and IF Pt/Al_2O_3 catalysts exhibited the same operating temperature window of $\Delta T= 110^oC$ and maximum NO conversion at the same reaction temperature ($T_M= 200^oC$), i.e. $X_{NO}= 81\%$ and $X_{NO}= 90\%$, respectively. The IF solid appears to be more active (by ~10%) compared to the conventional WI catalyst, in the $100-200°C$ low-

temperature range, as well as in the whole operating temperature window. It is noted that they both exhibited similar selectivity towards N_2, specifically an average value of 72% (IF) and 75% (WI), within ΔT (T_R= 140-250°C). The fact that the IF solid shows a slightly improved behaviour compared to the WI catalyst is probably due to the use of the "ink" solution, which leads to a larger B.E.T. surface area, and in general, a different surface structure.

6. The Epson printed Pt/Al$_2$O$_3$ catalyst, shows a slightly lower nitrogen selectivity value at the temperature of maximum conversion of NO, as compared to the catalysts prepared with the wet impregnation method (WI and IF). On the contrary, the Epson printed catalyst appears to be superior to the conventional catalysts at 300°C, especially in terms of N_2 selectivity. Specifically, at T_R> 250°C highest N_2 selectivity values were obtained by the catalysts prepared by inkjet printing (Epson and DMP), while the opposite is true for the lower temperature range (175-200°C) and at temperatures lower than 150°C, the DMP catalyst appears to be slightly superior. The latter results indicate that the inkjet printing method is able to lead to solid catalysts with unique catalytic characteristics.

7. The IF Pt/MgO-CeO$_2$ solid presented the highest NO conversion at 250°C (X_{NO}^{max}= 63%, S_{N2}= 78%), which was the highest T_M observed in all examined catalysts, as well as the lowest X_{NO}^{max}. This behaviour can be partially explained by the dispersion of Pt on the IF catalyst, since the specific solid presented the lowest Pt dispersion (D= 63.3%), compared to all examined catalysts.

8. The novel inkjet-printed Pt/MgO-CeO$_2$ solid (IJP-DMP), showed negligible NO conversion values (X_{NO}< 6%) throughout the temperature range of 60-400°C during NO/H$_2$/O$_2$ reaction. However, a completely different catalytic behavior was observed when O$_2$ was removed from the feed stream. In fact, the catalytic activity of the IJP-DMP solid, for the NO/H$_2$ reaction, was remarkable as it achieved absolute conversion (X_{NO}= 100%) at 150°C and 200°C and excellent selectivity towards N_2, S_{N2}= 90% at 150°C and S_{N2}= 100% at 200°C. Consequently, the IJP-DMP Pt/MgO-CeO$_2$ catalyst has the outstanding ability to completely convert NO selectively to N_2, without producing any NH$_3$ during the NO/H$_2$ reaction. These remarkable results, observed in the absence of O$_2$ in the feed, *have never been reported before* according to the author's knowledge.

Furthermore, the effect of O_2 concentration (0-5 vol%) and the concept of adding and then removing O_2 in the feed stream were further examined using a series of NO/H_2 – $NO/H_2/O_2$ cycles. It is noted that every time oxygen was absent from the feed, the printed catalyst regained most of its catalytic activity (X_{NO} and S_{N2}). It can be safely claimed that the printing protocol followed in order to prepare the IJP-DMP Pt/MgO-CeO_2 catalyst, clearly changed the properties of the solid and created a unique surface structure (metal-support interface) that can be very easily affected (oxidized) by even the slightest input of O_2 in the feed stream.

6.3. Mechanistic Studies: Surface Reactivity, DRIFTS and Isotopic Experiments.

1. The NO desorption profiles observed on the Pt/Al_2O_3, as well as on the Pt/MgO-CeO_2 catalysts, during the surface reactivity studies, strongly support the view of the existence of various kinds of NO_x species formed during NO chemisorption at room temperature (NO-TPD studies) or after $NO/H_2/O_2$ reaction at ~200°C (TPSR experiments). Some of these species are expected to have a stronger interaction with the active sites of the catalysts' surface, due to the higher desorption temperatures.

2. The formation of large amounts of NO during the He-TPSR experiment (especially at high temperatures) illustrates that not all of the adsorbed NO_x species are able to react with O_2/H_2 towards N_2 or N_2O, therefore, these species could be considered as inactive. On the contrary, the N_2 desorption peaks found during He-TPSR experiments are taken as a good measure of the active intermediate species of the examined catalysts. In fact, the active species might be different between the catalysts since the N_2 peaks were found to desorb at considerably different temperatures.

3. The profile of desorbed gases during H_2-TPSR on all examined catalysts (Pt/Al_2O_3 and Pt/MgO-CeO_2) presented a shift to lower temperatures compared to the profiles observed in He-TPSR. A hydrogen-assisted effect on the lowering of the bond strength of Pt-NO is suggested to explain this significant shift in temperatures, and that the activation energy of the N-O bond dissociation is higher than that of hydrogen assisted N-O dissociation. It is noted that the Pt/MgO-CeO_2 catalysts presented a greater shift to lower temperatures of the desorbed NO peaks compared to the Pt/Al_2O_3 solids.

4. The results obtained from the TPSR experiments confirm the great influence that the chemical composition of the support (Al_2O_3 and MgO-CeO_2) has on the H_2-SCR of

NO (activity and N_2 selectivity), since it can influence the structure of adsorbed NO_x species and consequently can be used to explain to some degree the differences in the catalytic activity of the solids.

5. The combined SSITKA-DRIFTS experiments indicated the formation of one active intermediate NO_x species (chelating bidentate nitrates) on the support of the IJP-DMP Pt/MgO-CeO$_2$ catalyst and four active NO_x species on the IF Pt/MgO-CeO$_2$ solid, during NO/H$_2$/O$_2$ reaction at 200°C. One of these species is formed on the active metal (unidentate nitrates on Pt), while the other three (bridged bidentate nitrates, unidentate nitrates, chelating bidentate nitrates) are found on the support of the IF solid. Consequently, since the active species are also formed on the support, or the interface between Pt nanoparticles and the support surface of MgO and CeO$_2$ and not just on the surface of the metallic phase (Pt), hydrogen spillover from the Pt sites to the metal-support interface is essential for the H$_2$-SCR of NO, so that the active species formed on the support are able to be involved in the pathway of N$_2$ and N$_2$O products. This hydrogen spillover effect was indeed observed on both catalysts (IF and IJP-DMP), during the H$_2$-TPD studies of the examined catalysts.

6. All the other species that were formed on the catalytic surface of both Pt/MgO-CeO$_2$ solids (IF and IJP-DMP), during the NO/H$_2$/O$_2$ reaction at 200°C, can be characterized as inactive, since no significant shift was observed to lower wavenumbers after the isotopic switch (combined SSITKA-DRIFTS). These species are located on both the metal and support surfaces. Specifically, nitrosyls on Pt, nitritos and chelating nitrites on the support were found on the IF solid, while for the IJP-DMP catalyst the following species were inactive; nitrosyls, bridged or bent NO and unidentate nitrates on Pt, and nitrosyl coadsorbed with a nitrate, unidentate nitrates and chelating nitrites on the support.

7. The presence (5 vol% O$_2$, NO/H$_2$/O$_2$) or absence of O$_2$ (NO/H$_2$), in the reaction feed does not influence the chemical composition of the active or inactive species that were formed on the IF and IJP-DMP Pt/MgO-CeO$_2$ catalysts. However, the actual surface concentration of these species appears to be significantly affected by the presence of O$_2$ in the reaction feed stream. Specifically, the chelating (bidentate) nitrate species, which were found to be active on both examined catalysts, appear to be favoured on the IJP-DMP catalyst, in the absence of O$_2$ in the feed (NO/H$_2$ reaction), while on the IF solid the opposite is true (NO/H$_2$/O$_2$ reaction).

8. The IJP-DMP Pt/MgO-CeO$_2$ catalyst presented some unique results. This novel catalyst did not desorb any NH$_3$ during the TPSR experiments following NO/H$_2$ reaction (absence of oxygen), which is in complete agreement with the catalytic performance of the solid during that reaction. In addition, it was the only catalyst that was found to desorb much higher quantities of NO (θ_{NO}= 3) during the TPD under He flow (NO-TPD studies). Additional sites for NO chemisorption, besides those on Pt and MgO-CeO$_2$ surfaces alone, may have been formed at the periphery of metal-support and/or a spillover process of NO$_x$ species from Pt to the support during the adsorption of NO at room temperature could be invoked to explain this observation. After the DRIFTS studies, it was found that four (nitrosyl coadsorbed with a nitrate, unidentate nitrates, chelating nitrite, chelating bidentate nitrates) out of seven (nitrosyl coadsorbed with a nitrate, unidentate nitrates, chelating nitrite, chelating bidentate nitrates, nitrosyls on Pt, bridged or bent NO on Pt, unidentate nitrates on Pt) species were formed on the support of the catalyst.

9. Finally, the fact that the novel IJP-DMP Pt/MgO-CeO$_2$ catalyst presented one active NO$_x$ species (chelating bidentate nitrate on the support, M-O$_2$NO) during the NO/H$_2$/O$_2$ reaction, explains the catalytic behaviour at the latter solid towards the H$_2$-SCR of NO. In particular, the N=O bond of the species is expected to be stronger compared to the weak N-O bond (M-O$_2$N, chelated bond), and thus more difficult to break. Consequently, the negligible NO conversion (X_{NO}< 6%) for the NO/H$_2$/O$_2$ reaction (T_R= 60-400°C) can be explained.

6.4. Effectiveness of the inkjet printing method

By combining the results summarized above (6.1-6.3) and taking into account the fact that the different catalyst preparation methods examined (WI or inkjet) were mainly found to have an effect on the reactivity and **not** on the chemical composition of the various intermediate NO$_x$ species formed during NO/H$_2$/O$_2$ reaction, it can be said that the inkjet printing technique possesses a unique capability for controlling the catalysts morphology and in particular the interaction/interphase between the various crystal phases of the catalyst. In particular, it can be safely claimed that the inkjet printing process has led to the formation of an excellent, or at least unique, contact between the metal (Pt) and the support (MgO and CeO$_2$), which facilitates the diffusion of species (i.e., H, O and NO species) from the metal to the support and vice-versa. The latter claim is based on the following results of the present work:

- The inkjet-printed catalyst was found to present higher Pt dispersion compared to the catalysts prepared by wet impregnation.
- The extent of the hydrogen spillover phenomenon, at low temperatures (T< 250°C), was found to be much larger on the inkjet-printed catalyst, as compared to the ones prepared by WI (H_2-TPD experiments).
- The inkjet-printed Pt/MgO-CeO$_2$ catalyst presented a much larger amount of spilled-over NO$_x$ during the NO-TPD experiments, as compared to the traditional catalysts examined.

Since, previous studies on the H_2-SCR reaction have proven that best catalytic behavior can be obtained by achieving optimum Pt oxidation state on supported-Pt catalysts, it can be concluded that the inkjet printing technique has led to the formation of a close-to-ideal state of Pt, probably due to the smaller Pt nanoparticles formed and the better contact between these particles and the support (via electronic interactions).

On one hand, these fine Pt nanoparticles and the excellent contact between them and the support can facilitate the diffusion of intermediate species from the metal to the support and vice-versa, leading to increased catalytic activity (i.e., case of the inkjet-printed Pt/Al$_2$O$_3$ catalysts). On the other hand, the fine Pt nanoparticles are expected to be much more unstable and thus susceptible to oxidation by the reaction medium (gaseous O$_2$), a fact that can lead to the complete deactivation of the catalyst (i.e., case of the inkjet-printed Pt/MgO-CeO$_2$ catalyst).

In conclusion, the results of the present PhD dissertation have proven that inkjet printing of catalysts can be considered as a promising, innovative technique for catalysts' preparation. Significant work is still needed though, towards the regulation of the process details in order to achieve optimal catalytic results. The present work may be well considered as the basis of the future work that needs to be done within this field.

FUTURE WORK

Additional studies could be conducted in order to extend the novel work that has been performed during this dissertation. There are several areas for further development and deeper analysis of particular mechanisms arising from this work which could be pursued.

- Additional in situ mechanistic studies on the IJP-DMP Pt/MgO-CeO$_2$ catalyst in order to better understand the remarkable catalytic behaviour of the solid in the absence of oxygen, including the reaction mechanism, compared to the rest of the catalysts, i.e., combined SSITKA-DRIFTS studies where the isotopic switch is performed on the NO/H$_2$ reaction, ^{14}NO/H$_2$ $\rightarrow$ ^{15}NO/H$_2$.

- In situ DRIFTS and combined SSITKA-DRIFTS studies on the IJP-Epson and IJP-DMP Pt/Al$_2$O$_3$ printed catalysts, so as to study essential mechanistic aspects of the selective catalytic reduction of NO by H$_2$ under strongly oxidizing conditions (H$_2$-SCR). In particular, investigate the chemical structure of the NO$_x$ species at different reaction temperatures (room temperature, temperature of maximum NO conversion, etc), for various time periods. As for the SSITKA-DRIFTS experiments, the use of both ^{15}NO and ^{18}O$_2$ stable isotopes will provide more information on the chemical structure of the active reaction intermediates and the inactive species, as well as, provide important mechanistic information about the oxygen pathway of the N$_2$ and N$_2$O formation during the H$_2$-SCR of NO. These studies will also provide the opportunity to compare the influence of the support (Al$_2$O$_3$ and MgO-CeO$_2$) on the reaction mechanism.

- Stability testing of all the catalysts, and especially for the inkjet-printed (IJP-DMP) Pt/MgO-CeO$_2$ catalyst for the NO/H$_2$ reaction, in order to test its ability to sustain perfect catalytic performance (X_{NO}= 100%, S_{N2}= 100%) in the absence of oxygen.

- Evaluation of the performance of the printed Pt/Al$_2$O$_3$ catalysts (IJP-Epson and IJP-DMP) during NO/H$_2$ reaction, in order to investigate if the absence of NH$_3$ formation during the catalytic reaction is related to the printing process.

- Detailed investigation of the actual effects of the catalyst multilayer printing technique, by examining different printing parameters, such as ink composition (metal precursors, stabilizing agents-polymer, type of solvent, etc), printing patterns, temperature of the substrate, etc.

REFERENCES

[1] A. M. Efstathiou, C. N. Costa, and J. L. G. Ferro, "Novel Catalyst for the Reduction of NO to N_2 with Hydrogen under NO_x Oxidation Conditions, Spanish Patent No. ES200300368 (2003); US Patent No. 7105137 (2006); European Patent Application No. 03704721; Japanese Patent Application No. 2003-567568."

[2] G. Centi, P. Ciambelli, S. Perathoner, and P. Russo, "Environmental catalysis: Trends and outlook," *Catal. Today*, vol. 75, no. 1–4, pp. 3–15, 2002.

[3] S. Roy, M. S. Hegde, and G. Madras, "Catalysis for NO_x abatement," *Appl. Energy*, vol. 86, no. 11, pp. 2283–2297, 2009.

[4] M. Wojciechowska and S. Lomnicki, "Nitrogen oxides removal by catalytic methods," *Clean Technol. Environ. Policy*, vol. 1, no. 4, pp. 237–247, 1999.

[5] A. M. Efstathiou, *Bachelor's Course Notes: Catalysis, CHEM-445*. Nicosia: University of Cyprus, 2005.

[6] H. Bosch and F. Janssen, "Formation and control of Nitrogen Oxides," *Catal. Today*, vol. 2, no. 4, pp. 369–379, 1988.

[7] R. Willi, "Low-Temperature Selective Catalytic Reduction of NO_x Catalytic behavior and kinetic modeling," 1996.

[8] F. Garin, "Mechanism of NO_x decomposition," *Appl. Catal. A Gen.*, vol. 222, pp. 183–219, 2001.

[9] S. C. Hill and L. D. Smoot, "Modeling of nitrogen oxides formation and destruction in combustion systems," *Prog. Energy Combust. Sci.*, vol. 26, no. 4, pp. 417–458, 2000.

[10] K. Skalska, J. S. Miller, and S. Ledakowicz, "Trends in NO_x abatement: A review," *Sci. Total Environ.*, vol. 408, no. 19, pp. 3976–3989, 2010.

[11] V. Vestreng, L. Ntziachristos, A. Semb, S. Reis, I. S. A. Isaksen, and L. Tarrasón, "Evolution of NO_x emissions in Europe with focus on road transport control measures," *Atmos. Chem. Phys.*, vol. 9, no. 4, pp. 1503–1520, 2009.

[12] M. Cîmpean, "Catalytic reduction of nitrogen oxides from the residual gases of the ^{15}N separation column," Babes-Bolyai, 2015.

[13] European Environment Agency, "National Emission Ceilings Directive emissions data viewer 1990-2016," 2018.

[14] D. Vallero, "Air Pollutant Hazards," in *Fundamentals of Air Pollution (Fifth Edition)*, 2014, pp. 197–214.

[15] A. Fritz and V. Pitchon, "The current state of research on automotive lean NO_x catalysis," *Appl. Catal. B Environ.*, vol. 13, pp. 1–25, 1997.

[16] V. I. Pârvulescu, P. Grange, and B. Delmon, "Catalytic removal of NO," *Catal. Today*, vol. 46, no. 4, pp. 233–316, 1998.

[17] D. A. Burns, J. Aherne, D. A. Gay, and C. M. B. Lehmann, "Acid rain and its environmental effects: Recent scientific advances," *Atmos. Environ.*, vol. 146, pp. 1–4, 2016.

[18] D. W. Schindler, "Effects of Acid Rain on Freshwater Ecosystems," *J. Sci.*, vol. 239, no. 4836, pp. 149–157, 1988.

[19] "Nitric Oxide-NIOSH Pocket Guide to Chemical Hazards," *National Institute for Occupational Safety and Health (NIOSH) Education and Information Division*. 2016.

[20] B. Guan, R. Zhan, H. Lin, and Z. Huang, "Review of state of the art technologies of selective catalytic reduction of NO_x from diesel engine exhaust," *Appl. Therm. Eng.*, vol. 66, no. 1–2, pp. 395–414, 2014.

[21] N. Akter and T. Kim, "Introduction of Heterogeneous Catalytic Materials for NO_x Treatment," *Ann. Mater. Sci. Eng.*, no. 3, 2014.

[22] European Parliament and Council of the European Union, "REGULATION (EC) No 715/2007 OF THE EUROPEAN PARLIAMENT AND OF THE COUNCIL of 20 June 2007 on type approval of motor vehicles with respect to emissions from light passenger and commercial vehicles (Euro 5 and Euro 6) and on access to vehicle repair and mai," 2007.

[23] European Environment Agency, "Emission reduction commitment for EU28 and Member States under the NEC Directive for 2020 and 2030," 2018.

[24] European Parliament and the council of the European Union, "Directive (EU) 2016/2284 of the European Parliament and of the Council of 14 December 2016 - on the reduction of national emissions of certain atmospheric pollutants, amending Directive 2003/35/EC and repealing Directive 2001/81/EC," 2016.

[25] J. Dumesic, G. Huber, and B. Michel, "Ch. 1.1 Principles of Heterogeneous Catalysis," in *Handbook of Heterogeneous Catalysis*, Wiley-VCH Verlag GmbH

& Co. KGaA, 2008, pp. 1–15.

[26]   M. Fadoni and L. Lucarelli, "Temperature programmed desorption, reduction, oxidation and flow chemisorption for the characterisation of heterogeneous catalysts. Theoretical aspects, instrumentation and applications," *Stud. Surf. Sci. Catal.*, vol. 120, pp. 177–225, 1999.

[27]   J. R. H. Ross, *Heterogeneous Catalysis Fundamentals and Applications*, vol. 1. Elsevier B.V., 2012.

[28]   P. A. Webb, "Introduction to Chemical Adsorption Analytical Techniques and their Applications to Catalysis," Georgia, 2003.

[29]   O. Deutschmann, H. Knözinger, K. Kochloefl, and T. Turek, *Heterogeneous Catalysis and Solid Catalysts*. Wiley-VCH Verlag GmbH & Co. KGaA, 2009.

[30]   M. W. Balakos, S. S. C. Chuang, G. Srinivas, and M. A. Brundage, "Infrared study of the dynamics of adsorbed species during CO hydrogenation," *Journal of Catalysis*, vol. 157, no. 1. pp. 51–65, 1995.

[31]   A. Likourgiotis and C. Cordoulis, *Catalysis*, vol. A'. Patra: Hellenic Open University, 2003.

[32]   M. Baerns and M. Holeňa, "Chapter 2: Approaches in the Development of Heterogeneous Catalysts," in *Combinatorial Development of Solid Catalytic Materials*, 2009, pp. 7–20.

[33]   C. N. Costa, "The Selective Catalytic Reduction of NO by Hydrogen under Strongly Oxidizing Conditions over Supported Pt Catalysts," University of Cyprus, 2003.

[34]   A. Wheeler, "Reaction Rates and Selectivity in Catalyst Pores," *Adv. Catal.*, vol. 3, pp. 249–327, 1951.

[35]   J. Wisniak, "The History of Catalysis. From the Beginning to Nobel Prizes," *Educ. Química*, vol. 21, no. 1, pp. 60–69, 2018.

[36]   A. Balandin, "Modern State of the Multiplet Theory of Heterogeneous Catalysis," *Adv. Catal.*, vol. 19, pp. 1–210, 1969.

[37]   M. Králik, "Adsorption, chemisorption, and catalysis," *Chem. Pap.*, vol. 68, no. 12, 2014.

[38]   T. Bligaard *et al.*, "From the Sabatier principle to a predictive theory of transition-metal heterogeneous catalysis," *J. Catal.*, vol. 328, pp. 36–42, 2015.

[39] T. Bligaard and J. K. Nørskov, "Chapter 4: Heterogeneous Catalysis," in *Chemical Bonding at Surfaces and Interfaces*, 2008, pp. 255–321.

[40] R. L. Burwell, G. L. Haller, K. C. Taylor, and J. F. Read, "Chemisorptive and Catalytic Behavior of Chromia," *Adv. Catal.*, vol. 20, pp. 1–96, 1969.

[41] H. S. Taylor, "A theory of the catalytic surface," in *Proceedings of the Royal Society of London. Series A*, 1925, no. 108, pp. 105–111.

[42] G. A. Somorjai, K. R. McCrea, and J. Zhu, "Active sites in heterogeneous catalysis: Development of molecular concepts and future challenges," *Top. Catal.*, vol. 18, no. 3–4, pp. 157–166, 2002.

[43] V. Kumar, "Defects on surfaces," *Bull. Mater. Sci.*, vol. 10, no. 1–2, pp. 161–172, 1988.

[44] J. A. Venables, *Introduction to Surface and Thin Film Processes*. Cambridge University Press, 2008.

[45] D. M. Ruthven, *Principles of adsorption and adsorption processes*. John Wiley & Sons. Inc. Ail, 1984.

[46] F. Rouquerol, J. Rouquerol, and K. Sing, "Chapter 1: Introduction," in *Adsorption by powders and porous solids*, 1999, pp. 1–26.

[47] D. S. Ballantine Jr *et al.*, "Chapter 4: Materials Characterization," in *Acoustic Wave Sensors*, 1997, pp. 150–221.

[48] A. Likourgiotis and C. Christos, *Bachelor's Course Notes: Catalysis*. Patra: University of Patras, 2010.

[49] D. C. Harris, *Quantitative Chemical Analysis, Seventh Edition*. W. H. Freeman and Company, 2006.

[50] J. E. Lennard-Jones, "Processes of Adsorption and Diffusion on Solid Surfaces," *Trans. Faraday Soc.*, vol. 28, pp. 306–321, 1932.

[51] H.-J. Freund, "Chapter 5: Elementary Steps and Mechanisms," in *Handbook of Heterogeneous Catalysis, 2nd Edition*, G. Etrl, H. Knözinger, F. Schüth, and J. Weitkamp, Eds. Wiley-VCH Verlag GmbH & Co. KGaA, Weinheim, 2008, pp. 1375–1415.

[52] G. G. Olympiou, "Selective Catalytic Reduction of NO_x with H_2 (H_2-SCR) over supported Pt Catalysts: Effect of Substrate and Promoters (Pd and V)," University of Cyprus, 2011.

[53] K. Nobuhara, H. Kasai, W. A. Diño, and H. Nakanishi, "H_2 dissociative adsorption on Mg, Ti, Ni, Pd and La surfaces," *Surf. Sci.*, vol. 566–568, pp. 703–707, 2004.

[54] J. Greeley and M. Mavrikakis, "Alloy catalysts designed from first principles," *Nat. Mater.*, vol. 3, no. 11, pp. 810–815, 2004.

[55] W. A. Brown and D. A. King, "NO Chemisorption and Reactions on Metal Surfaces: A New Perspective," *J. Phys. Chem. B*, vol. 104, no. 10, pp. 2578–2595, 2000.

[56] Q. Ge and D. A. King, "Energetics, geometry and spin density of NO chemisorbed on Pt{111}," *Chem. Phys. Lett.*, vol. 285, pp. 15–20, 1998.

[57] W. M. H. Sachtler, "Chapter: 5.3.3: Ensemble and Ligand Effects in Metal Catalysis," in *Handbook of Heterogeneous Catalysis*, G. Ertl, H. Knözinger, F. Schüth, and J. Weitkamp, Eds. Weinheim, Germany: Wiley-VCH Verlag GmbH & Co. KGaA, 2008, pp. 1585–1593.

[58] L. Vattuone, Y. Y. Yeo, and D. A. King, "Adatom bond energies and lateral interaction energies from calorimetry: NO, O_2, and N_2 adsorption on Ni{100}," *J. Chem. Phys.*, vol. 104, no. 20, pp. 8096–8102, 1996.

[59] G. L. Price and B. G. Baker, "The chemisorption of nitric oxide on (100) nickel studied by LEED, AES, UPS and thermal desorption," *Surf. Sci.*, vol. 91, pp. 571–580, 1980.

[60] S. J. Huang, A. B. Walters, and M. A. Vannice, "Adsorption and decomposition of NO on lanthanum oxide," *J. Catal.*, vol. 192, no. 1, pp. 29–47, 2000.

[61] O. Dulaurent and D. Bianchi, "Adsorption isobars for CO on a Pt/Al_2O_3 catalyst at high temperatures using FTIR spectroscopy: Isosteric heat of adsorption and adsorption model," *Appl. Catal. A Gen.*, vol. 196, no. 2, pp. 271–280, 2000.

[62] J. L. Freysz, J. Saussey, J. C. Lavalley, and P. Bourges, "In Situ FTIR Study of the NO+CO Reaction on a Silica-Supported Platinum Catalyst at Atmospheric Pressure Using a New Pulse Technique," *J. Catal.*, vol. 197, no. 1, pp. 131–138, 2001.

[63] M. Haneda, Y. Kintaichi, M. Inaba, and H. Hamada, "Infrared study of catalytic reduction of nitrogen monoxide by propene over Ag/TiO_2-ZrO_2," *Catal. Today*, vol. 42, no. 1–2, pp. 127–135, 1998.

[64] N. Bion, J. Saussey, M. Haneda, and M. Daturi, "Study by in situ FTIR

spectroscopy of the SCR of NO_x by ethanol on Ag/Al_2O_3 - Evidence of the role of isocyanate species," *J. Catal.*, vol. 217, no. 1, pp. 47–58, 2003.

[65]   N. N. Greenwood and A. Earnshaw, *Chemistry of the Elements, Second Edition*. London: Butterworths/Heinemann, 2001.

[66]   G. Broden, T. N. Rhodin, and C. Brucker, "Synchrotron radiation study of chemisorptive bonding of CO on transition metals - Polarization effect on Ir(100)," *Surf. Sci.*, vol. 59, pp. 593–611, 1976.

[67]   F. J. J. G. Janssen, F. M. G. van der Kerkhof, H. Bosch, and J. R. H. Ross, "Mechanism of the Reaction of Nitric Oxide, Ammonia, and Oxygen over Vanadia Catalysts. 1. The Role of Oxygen Studied by Way of Isotopic Transients under Dilute Conditions," *J. Phys. Chem*, no. 11, pp. 5921–5927, 1987.

[68]   H. Cordatos and R. J. Gorte, "CO, NO, and H_2 Adsorption on Ceria-Supported Pd," *J. Catal.*, vol. 159, pp. 112–118, 1996.

[69]   M. T. M. Koper and R. A. Van Santen, "Electric field effects on CO and NO adsorption at the Pt(111) surface," *J. Electroanal. Chem.*, vol. 476, no. 1, pp. 64–70, 1999.

[70]   R. Burch, J. A. Sullivan, and T. C. Watling, "Mechanistic considerations for the reduction of NO_x over Pt/Al_2O_3 and Al_2O_3 catalysts under lean-burn conditions," *Catal. Today*, vol. 42, no. 1–2, pp. 13–23, Jun. 1998.

[71]   D. R. Mullins, "The surface chemistry of cerium oxide," *Surf. Sci. Rep.*, vol. 70, no. 1, pp. 42–85, 2015.

[72]   Z. M. Liu, J. H. Li, and S. I. Woo, "Recent advances in the selective catalytic reduction of NO_x by hydrogen in the presence of oxygen," *Energy Environ. Sci.*, vol. 5, no. 10, pp. 8799–8814, 2012.

[73]   C. N. Costa and A. M. Efstathiou, "Mechanistic Aspects of the H_2-SCR of NO on a Novel $Pt/MgO-CeO_2$ Catalyst," *J. Phys. Chem. C*, vol. 111, pp. 3010–3020, 2007.

[74]   C. N. Costa and A. M. Efstathiou, "Transient Isotopic Kinetic Study of the $NO/H_2/O_2$ (Lean de-NO_x) Reaction on Pt/SiO_2 and $Pt/La−Ce−Mn−O$ Catalysts," *J. Phys. Chem. B*, vol. 108, no. 8, pp. 2620–2630, 2004.

[75]   P. G. Savva and A. M. Efstathiou, "The influence of reaction temperature on the chemical structure and surface concentration of active NO_x in H_2-SCR over $Pt/MgO-CeO_2$: SSITKA-DRIFTS and transient mass spectrometry studies," *J.*

Catal., vol. 257, no. 2, pp. 324–333, 2008.

[76] J. Müslehiddinoğlu and M. A. Vannice, "Adsorption of NO on promoted Ag/α-Al$_2$O$_3$ catalysts," *J. Catal.*, vol. 217, no. 2, pp. 442–456, 2003.

[77] J. W. London and A. T. Bell, "A Simultaneous Infrared and Kinetic Study of the Reduction of Nitric Oxide by Carbon Monoxide over Copper Oxide," *J. Catal.*, vol. 31, pp. 96–109, 1973.

[78] K. Hadjiivanov, V. Bushev, M. Kantcheva, and D. Klissurski, "Infrared Spectroscopy Study of the Species Arising during NO$_2$ Adsorption on TiO$_2$ (Anatase)," *Langmuir*, vol. 10, pp. 464–471, 1994.

[79] K. I. Hadjiivanov, "Identification of Neutral and Charged N$_x$O$_y$ Surface Species by IR Spectroscopy," *Catal. Rev. Sci. Eng.*, vol. 42, no. 1–2, pp. 71–144, 2000.

[80] J. W. Geus, "Production and thermal pretreatment of supported catalysts," *Stud. Surf. Sci. Catal.*, vol. 16, pp. 1–33, 1983.

[81] K. Foger, "Chapter 4: Dispersed Metal Catalysts," in *Catalysis (Science and Technology), vol 6*, A. J.R. and B. M., Eds. Springer, Berlin, Heidelberg, 1984, pp. 227–305.

[82] M. Campanati, G. Fornasari, and A. Vaccari, "Fundamentals in the preparation of heterogeneous catalysts," *Catal. Today*, vol. 77, no. 4, pp. 299–314, 2003.

[83] S. H. Overbury, P. A. Bertrand, and G. A. Somorjai, "The Surface Composition of Binary Systems. Prediction of Surface Phase Diagrams of Solid Solutions," *Chem. Rev.*, vol. 75, no. 5, pp. 547–560, 1975.

[84] M. Che, O. Clause, and C. Marcilly, "Chapter 2: Preparation of Solid Catalysts," in *Handbook of Heterogeneous Catalysis, Vol 1.*, G. Ertl, H. Knözinger, and J. Weitkamp, Eds. Wiley-VCH, Weinheim, 1997, pp. 138–264.

[85] J. A. Moulijn, A. E. Van Diepen, and F. Kapteijn, "Catalyst deactivation: is it predictable? What to do?," *Appl. Catal. A Gen.*, vol. 212, pp. 3–16, 2001.

[86] A. S. Russell and C. N. Cochran, "Alumina Surface Area Measurements," *Ind. Eng. Chem.*, vol. 42, no. 7, pp. 1332–1335, 1950.

[87] S. Coluccia and A. J. Tench, "Spectroscopic studies of hydrogen adsorption on highly dispersed MgO," *Stud. Surf. Sci. Catal.*, vol. 7, pp. 1154–1169, 1981.

[88] A. Trovarelli, C. De Leitenburg, M. Boaro, and G. Dolcetti, "The utilization of ceria in industrial catalysis," *Catal. Today*, vol. 50, no. 2, pp. 353–367, 1999.

[89] M. Fronzi, M. H. N. Assadi, and D. A. H. Hanaor, "Theoretical insights into the hydrophobicity of low index CeO_2 surfaces," *Appl. Surf. Sci.*, vol. 478, no. September 2018, pp. 68–74, 2019.

[90] X. Zheng, L. Liu, and X. Zhou, "Formation and Properties of Hydrophobic CeO_2 Nanoparticles," *Colloid J.*, vol. 76, no. 5, pp. 607–613, 2014.

[91] A. S. Prakash, C. Shivakumara, and M. S. Hegde, "Single step preparation of $CeO_2/CeAlO_3/\gamma-Al_2O_3$ by solution combustion method: Phase evolution, thermal stability and surface modification," *Mater. Sci. Eng. B*, vol. 139, no. 1, pp. 55–61, 2007.

[92] R. Ramírez-López, L. Balderas-Tapia, I. Elizalde-Martinez, and T. Viveros, "Complete oxidation of methane over $Pt/CeO_2-Al_2O_3$ catalysts," *Chem. Eng. Commun.*, vol. 196, no. 10, pp. 1189–1197, 2009.

[93] M. Haneda, T. Mizushima, and N. Kakuta, "Behaviour of oxygen species adsorbed on Al_2O_3-supported cerium oxide catalysts for methane oxidation," *J. Chem. Soc. Faraday Trans.*, vol. 91, no. 24, pp. 4459–4465, 1995.

[94] N. Kakuta *et al.*, "Oxygen storage capacity (OSC) of aged $Pt/CeO_2/Al_2O_3$ catalysts: roles of Pt and CeO_2 supported on Al_2O_3," *Appl. Surf. Sci.*, vol. 121/122, pp. 408–412, 1997.

[95] C. H. Bartholomew, "Mechanisms of catalyst deactivation," *Appl. Catal. A Gen.*, vol. 212, pp. 17–60, 2001.

[96] M. Argyle and C. Bartholomew, "Heterogeneous Catalyst Deactivation and Regeneration: A Review," *Catalysts*, vol. 5, no. 1, pp. 145–269, 2015.

[97] J. R. Rostrup-Nielsen, "Promotion by Poisoning," in *Catalyst Deactivation 2001 Proceedings of the 9th International Symposium*, 1991, pp. 255–262.

[98] C. H. Bartholomew, P. K. Agrawal, and J. R. Katzer, "Sulfur Poisoning of Metals," *Adv. Catal.*, vol. 31, pp. 135–242, 1982.

[99] D. L. Trimm, "Chapter 7: Deactivation and Regeneration," in *Handbook of Heterogeneous Catalysis*, vol. 3, J. W. G. Ertl, H. Knozinger, Ed. Wiley-VCH, Weinheim, 1997, pp. 1263–1282.

[100] D. C. McCulloch, "Chapter 4: Catalytic Hydrotreating in Petroleum Refining," in *Applied Industrial Catalysis, Volume 1*, B. E. Leach, Ed. New York: Academic Press, Inc., 1983, pp. 69–121.

[101] S. J. Tauster, S. C. Fung, and R. L. Garten, "Strong Metal-Support Interactions. Group 8 Noble Metals Supported on TiO_2," *J. Am. Chem. Soc.*, vol. 100, no. 1, pp. 170–175, 1978.

[102] G. Busca, "Chapter 6: Metal Oxides as Acid-Base Catalytic Materials," in *Heterogeneous Catalytic Materials*, 2014, pp. 103–195.

[103] S. J. Tauster, "Strong Metal-Support Interactions," no. 3, pp. 389–394, 1987.

[104] J. A. Horsley, "A Molecular Orbital Study of Strong Metal-Support Interaction between Platinum and Titanium Dioxide," *Am. Chem. Soc.*, vol. 101, no. 11, pp. 2870–2874, 1979.

[105] R. T. K. Baker, E. B. Prestridge, and R. L. Garten, "Electron Microscopy of Supported Metal Particles. II Further Studies of Pt/TiO_2," *J. Catal.*, vol. 59, no. 2, pp. 293–302, 1979.

[106] S. J. Teichner, "Recent Studies in Hydrogen and Oxygen Spillover and Their Impact on Catalysis," *Appl. Catal.*, vol. 62, pp. 1–10, 1990.

[107] S. Khoobiar, "Particle to Particle Migration of Hydrogen Atoms on Platinum-Alumina Catalysts from Particle to Neighboring Particles," *J. Phys. Chem.*, vol. 68, no. 2, pp. 411–412, 1964.

[108] P. A. Sermon and G. C. Bond, "Hydrogen Spillover," *J. Catal. Rev.*, vol. 8, no. 1, pp. 211–239, 1974.

[109] J. T. Miller, B. L. Meyers, M. K. Barr, F. S. Modica, and D. C. Koningsberger, "Hydrogen Temperature-Programmed Desorptions in Platinum Catalysts: Decomposition and Isotopic Exchange by Spillover Hydrogen of Chemisorbed Ammonia," *J. Catal.*, vol. 159, no. 1, pp. 41–49, 1996.

[110] W. Curtis Conner, G. M. Pajonk, and S. J. Teichner, "Spillover of Sorbed Species," *Adv. Catal.*, vol. 34, pp. 1–79, 1986.

[111] J. C. Musso and J. M. Parera, "Adsorption and Spillover of Hydrogen on Al_2O_3 and Pt/Al_2O_3," *Appl. Catal.*, vol. 30, pp. 81–90, 1987.

[112] K. Christmann, G. Ertl, and T. Pignet, "Adsorption of hydrogen on a Pt(111) surface," *Surf. Sci.*, vol. 54, no. 2, pp. 365–392, 1976.

[113] J. T. Miller, B. L. Meyers, F. S. Modica, G. S. Lane, M. Vaarkamp, and D. C. Koningsberger, "Hydrogen Temperature-Programmed Desorption (H_2 TPD) of Supported Platinum Catalysts," *J. Catal.*, vol. 143, no. 2, pp. 395–408, 1993.

[114] D. Bianchi, M. Lacroix, G. Pajonk, and S. J. Teichner, "Catalytic and infrared demonstrations of the effect of hydrogen spillover on a gel of silica," *J. Catal.*, vol. 59, no. 3, pp. 467–471, 1979.

[115] D. Maret, G. M. Pajonk, and S. J. Teichner, "Catalytic hydrognation of ethylene by amorphous alumina activated by hydrogen and/or oxygen spillover," *Stud. Surf. Sci. Catal.*, vol. 17, pp. 215–231, 1983.

[116] J. M. Fukuto, "Chemistry of Nitric Oxide: Biologically Relevant Aspects," *Adv. Pharmacol.*, vol. 34, pp. 1–15, 1995.

[117] Z. Liu, J. Hao, L. Fu, J. Li, and X. Cui, "Advances in catalytic removal of NO_x under leanburn conditions," *Chinese Sci. Bull.*, vol. 49, no. 21, pp. 2231–2241, 2004.

[118] K. Jellinek, "Über Zersetzungsgeschwindigkeit von Stickoxyd und Abhängigkeit derselben von der Temperatur," *Zeitschrift für Anorg. Chemie*, vol. 49, no. 1, pp. 229–276, 1906.

[119] F. Kaufman and J. R. Kelso, "Thermal decomposition of nitric oxide," *J. Chem. Phys.*, vol. 23, no. 9, pp. 1702–1707, 1955.

[120] F. Kaufman and J. R. Kelso, "Kinetics of decomposition of nitric oxide," *J. Chem. Phys.*, vol. 21, no. 4, p. 751, 1953.

[121] P. G. Savva and C. N. Costa, "Hydrogen Lean-$DeNO_x$ as an Alternative to the Ammonia and Hydrocarbon Selective Catalytic Reduction (SCR)," *Catal. Rev. Sci. Eng.*, vol. 53, no. 2, pp. 91–151, 2011.

[122] F. Nakajima, "Air Pollution Control with Catalysis: Past, Present and Future," *Catal. Today*, vol. 10, pp. 1–20, 1991.

[123] K. C. Taylor and R. L. Klimisch, "The catalytic reduction of nitric oxide over supported ruthenium catalysts," *J. Catal.*, vol. 30, no. 3, pp. 478–484, 1973.

[124] F. N. Teixeira and E. S. Lora, "Experimental and analytical evaluation of NO_x emissions in bagasse boilers," *Biomass and Bioenergy*, vol. 26, no. 6, pp. 571–577, 2004.

[125] J. Friebel and R. F. W. Köpsel, "The fate of nitrogen during pyrolysis of German low rank coals - a parameter study," *Fuel*, vol. 78, no. 8, pp. 923–932, 1999.

[126] R. D. Bell and F. P. Buckingham, "An overview of technologies for reduction of oxides of nitrogen from combustion furnaces," *Alexandria*, vol. 8, p. 2016, 2010.

[127] T. Sterner and B. Turnheim, "Innovation and diffusion of environmental technology: Industrial NO$_x$ abatement in Sweden under refunded emission payments," *Ecol. Econ.*, vol. 68, no. 12, pp. 2996–3006, 2009.

[128] L. J. Gill, P. G. Blakeman, M. V. Twigg, and A. P. Walker, "The Use of NO$_x$ Adsorber Catalysts on Diesel Engines," *Top. Catal.*, vol. 28, no. 1–4, pp. 157–164, 2004.

[129] T. W. S. Sitshebo, "HC-SCR of NO$_x$ emissions over Ag-Al$_2$O$_3$ catalysts using diesel fuel as a reductant," The University of Birmingham, 2010.

[130] W. S. Epling, J. E. Parks, G. C. Campbell, A. Yezerets, N. W. Currier, and L. E. Campbell, "Further evidence of multiple NO$_x$ sorption sites on NO$_x$ storage/reduction catalysts," *Catal. Today*, vol. 96, no. 1–2, pp. 21–30, 2004.

[131] L. Yang, V. Franco, A. Campestrini, J. German, and P. Mock, "NO$_x$ control technologies for Euro 6 diesel passenger cars: Market penetration and experimental performance assessment," *International Council on Clean Transportation*. p. 29, 2015.

[132] M. V. Twigg, "Haren Gandhi 1941–2010: Contributions to the Development and Implementation of Catalytic Emissions Control Systems," *Platin. Met. Rev.*, vol. 55, no. 1, pp. 43–53, 2011.

[133] F. Rohr *et al.*, "On the mechanism of sulphur poisoning and regeneration of a commercial gasoline NO$_x$-storage catalyst," *Appl. Catal. B Environ.*, vol. 56, no. 3, pp. 201–212, 2005.

[134] T. Nakatsuji, M. Matsubara, J. Rouistenmäki, N. Sato, and H. Ohno, "A NO$_x$ reduction system using ammonia-storage selective catalytic reduction in rich/lean excursions," *Appl. Catal. B Environ.*, vol. 77, no. 1–2, pp. 190–201, 2007.

[135] L. Masdrag, X. Courtois, F. Can, and D. Duprez, "Effect of reducing agent (C$_3$H$_6$, CO, H$_2$) on the NO$_x$ conversion and selectivity during representative lean/rich cycles over monometallic platinum-based NSR catalysts. Influence of the support formulation," *Appl. Catal. B Environ.*, vol. 146, no. x, pp. 12–23, 2014.

[136] S. Matsumoto and S. Matsumoto, "DeNO$_x$ catalyst for automotive lean-burn engine," *Catal. Today*, vol. 29, no. 1–4, p. 43, 1996.

[137] S. Matsumoto, Y. Ikeda, H. Suzuki, M. Ogai, and N. Miyoshi, "NO$_x$ storage-reduction catalyst for automotive exhaust with improved tolerance against sulfur

poisoning," *Appl. Catal. B Environ.*, vol. 25, no. 2–3, pp. 115–124, 2000.

[138] P. Forzatti, "Present status and perspectives in de-NO$_x$ SCR catalysis," *Appl. Catal. A Gen.*, vol. 222, no. 1–2, pp. 221–236, 2001.

[139] Z. Liu and S. I. Woo, "Recent advances in catalytic DeNO$_x$ Science and Technology," *Catal. Rev. Sci. Eng.*, vol. 48, no. 1, pp. 43–89, 2006.

[140] Z. Liu, Z. Zhou, G. Qi, and T. Zhu, "Selective catalytic reduction of NO$_x$ with NH$_3$ over MoO$_3$/Mn-Zr composite oxide catalyst," *Appl. Surf. Sci.*, vol. 466, no. x, pp. 459–465, 2019.

[141] I. Nova, L. Lietti, L. Casagrande, L. Dall'Acqua, E. Giamello, and P. Forzatti, "Characterization and reactivity of TiO$_2$-supported MoO$_3$ De-NO$_x$ SCR catalysts," *Appl. Catal. B Environ.*, vol. 17, no. 3, pp. 245–258, 1998.

[142] T. Komatsu, K. Tomokuni, and I. Yamada, "Outstanding low temperature HC-SCR of NO$_x$ over platinum-group catalysts supported on mesoporous materials expecting diesel-auto emission regulation," *Catal. Today*, vol. 116, pp. 244–249, 2006.

[143] R. Mrad, A. Aissat, R. Cousin, D. Courcot, and S. Siffert, "Catalysts for NO$_x$ selective catalytic reduction by hydrocarbons (HC-SCR)," *Appl. Catal. A Gen.*, vol. 504, pp. 542–548, 2014.

[144] M. Iwamoto and H. Yahiro, "Novel catalytic decomposition and reduction of NO," *Catal. Today*, vol. 22, pp. 5–18, 1994.

[145] M. Iwamoto, M. Nakamura, H. Nagano, S. Kagawa, and T. Seiyama, "Evidence for the Presence of Extraframework Oxygen Species In Partlally Metal-Ion-Exchanged Y Zeolltes," *Phys. Chem.*, vol. 86, no. 2, pp. 153–156, 1982.

[146] M. Iwamoto and H. Hamada, "Removal of nitrogen monoxide from exhaust gases through novel catalytic processes," *Catal. Today*, vol. 10, pp. 57–71, 1991.

[147] A. ObuchI, A. Ohl, M. Nakamura, A. Ogata, K. Mizuno, and H. Ohuchi, "Performance of platinum-group metal catalysts for the selective reduction of nitrogen oxides by hydrocarbons," *Appl. Catal. B Environ.*, vol. 2, pp. 71–80, 1993.

[148] R. Burch and D. Ottery, "The selective reduction of nitrogen oxides byhigher hydrocarbons on Pt catalysts underlean-burn conditions," *Appl. Catal. B Environ.*, vol. 13, pp. 105–111, 1997.

[149] R. Burch, J. P. Breen, and F. C. Meunier, "A review of the selective reduction of NO_x, with hydrocarbons under lean-burn conditions with non-zeolitic oxide and platinum group metal analysis," *Appl. Catal. B Environ.*, vol. 39, no. 4, pp. 283–303, 2002.

[150] O. Zegaoui, C. Hoang-van, and M. Karroua, "Selective catalytic reduction of nitric oxide by propane over vanadia-titania aerogels," *Appl. Catal. B Environ.*, no. 96, pp. 211–227, 1996.

[151] K. Shimizu, A. Satsuma, and T. Hattori, "Selective catalytic reduction of NO by hydrocarbons on Ga_2O_3/Al_2O_3 catalysts," *Appl. Catal. B Environ.*, vol. 16, pp. 319–326, 1998.

[152] K. I. Shimizu and A. Satsuma, "Selective catalytic reduction of NO over supported silver catalysts - Practical and mechanistic aspects," *Phys. Chem. Chem. Phys.*, vol. 8, no. 23, pp. 2677–2695, 2006.

[153] I. Aslan and A. Keskin, "Hydrogen applications in selective catalytic reduction of NO_x emissions from diesel engines," *Int. J. Hydrogen Energy*, vol. 9, pp. 1–6, 2017.

[154] J. M. Ogden, "Hydrogen: The Fuel of the Future?," *Phys. Today*, vol. 55, no. 4, pp. 69–75, 2002.

[155] Z. Liu, J. Wu, and C. Hardacre, "Research Progress in the Selective Catalytic Reduction of -NO_x by H_2 in the Presence of O_2," *Catal. Surv. from Asia*, vol. 22, no. 3, pp. 146–155, 2018.

[156] F. Solymosi and H. Knözinger, "Infrared study on the interaction of CO with alumina-supported rhodium," *J. Chem. Soc. Faraday Trans.*, vol. 86, no. 2, pp. 389–395, 1990.

[157] C. N. Costa, V. N. Stathopoulos, V. C. Belessi, and A. M. Efstathiou, "An investigation of the $NO/H_2/O_2$ (lean-deNO$_x$) reaction on a highly active and selective $Pt/La_{0.5}Ce_{0.5}MnO_3$ catalyst," *J. Catal.*, vol. 197, no. 2, pp. 350–364, 2001.

[158] M. Mihet, M. D. Lazar, V. Almasan, and V. Mirel, "H_2-SCR at Low Temperatures On Noble Metal Supported Catalysts," *Process. Isot. Mol.*, vol. 76, pp. 73–76, 2012.

[159] Z. Liu *et al.*, "Selective catalytic reduction of NO_x with H_2 over WO_3 promoted Pt/TiO_2 catalyst," *Appl. Catal. B Environ.*, vol. 188, pp. 189–197, 2016.

[160] X. Li, X. Zhang, Y. Xu, Y. Liu, and X. Wang, "Influence of support properties on H_2 selective catalytic reduction activities and N_2 selectivities of Pt catalysts," *Cuihua Xuebao/Chinese J. Catal.*, vol. 36, no. 2, pp. 197–203, 2015.

[161] H. P. Le, "Progress and Trends in Ink-jet Printing Technology," *J. Imaging Sci. Technol.*, vol. 42, no. 1, pp. 49–62, 1998.

[162] I. M. Hutchings, G. D. Martin, and S. D. Hoath, "Chapter 1: Introductory Remarks," in *Fundamentals of Inkjet Printing: The Science of Inkjet and Droplets, First Edition*, S. D. Hoath, Ed. Wiley-VCH Verlag GmbH & Co. KGaA, 2016, pp. 1–12.

[163] Rayleigh, "On the instability of jets," *Proc. London Math. Soc.*, vol. 10, no. 1, pp. 4–13, 1878.

[164] R. Elmqvist, "Measuring Instrument of the Recording Type," 1951.

[165] W. L. Buehner, J. D. Hill, T. H. Williams, and J. W. Woods, "Application of Ink Jet Technology to a Word Processing Output Printer," *IBM J. Res. Dev.*, vol. 21, no. 1, pp. 2–9, 1977.

[166] S. Kholghi Eshkalak, A. Chinnappan, W. A. D. M. Jayathilaka, M. Khatibzadeh, E. Kowsari, and S. Ramakrishna, "A review on inkjet printing of CNT composites for smart applications," *Appl. Mater. Today*, vol. 9, pp. 372–386, 2017.

[167] B. S. Cook *et al.*, "Inkjet catalyst printing and electroless copper deposition for low-cost patterned microwave passive devices on paper," *Electron. Mater. Lett.*, vol. 9, no. 5, pp. 669–676, 2013.

[168] C. Parra-Cabrera, C. Achille, S. Kuhn, and R. Ameloot, "3D printing in chemical engineering and catalytic technology: Structured catalysts, mixers and reactors," *Chem. Soc. Rev.*, vol. 47, no. 1, pp. 209–230, 2018.

[169] L. L. Da Luz *et al.*, "Inkjet Printing of Lanthanide-Organic Frameworks for Anti-Counterfeiting Applications," *ACS Appl. Mater. Interfaces*, vol. 7, no. 49, pp. 27115–27123, 2015.

[170] S. Sumaiya, K. Kardel, and A. El Shahat, "Organic solar cell by inkjet printing-An overview," *Technologies*, vol. 5, no. 3, p. 53, 2017.

[171] C. R. Tubío *et al.*, "3D printing of a heterogeneous copper-based catalyst," *J. Catal.*, vol. 334, no. January, pp. 110–115, 2016.

[172] P. Calvert, "Inkjet Printing for Materials and Devices," *Chem. Mater.*, vol. 13, pp.

3299–3305, 2001.

[173] R. P. Tortorich and J. Choi, "Inkjet Printing of Carbon Nanotubes," *Nanomaterials*, vol. 3, pp. 453–468, 2013.

[174] A. Soleimani-Gorgani, "Chapter 14: Inkjet Printing," in *Printing on Polymers: Fundamentals and Applications*, Elsevier Inc., 2016, pp. 231–246.

[175] B. Derby, "Inkjet Printing of Functional and Structural Materials: Fluid Property Requirements, Feature Stability, and Resolution," *Annu. Rev. Mater. Res.*, vol. 40, no. 1, pp. 395–414, 2010.

[176] T. Kitahara, "Ink Jet Head with Multi-Layer Piezoelectric Actuator," *Recent Prog. Ink-Jet Technol.*, pp. 125–128, 1995.

[177] "Epson L800 Datasheet," *Seiko Epson Corporation*. [Online]. Available: https://www.epson.eu/products/printers/inkjet-printers/for-home/ecotank-l800.

[178] "EPSON L800 User's Guide." Epson America, Inc, p. 95, 2012.

[179] A. Andreou, C. Andreou, and C. Louca, "Catalyst printer user's manual." Cyprus University of Technology, Limassol, pp. 1–9, 2015.

[180] A. Andreou, C. Andreou, and C. Louca, "CATAprint v2.O User's Manual." Cyprus University of Technology, Limassol, pp. 1–15, 2015.

[181] B. Smith, "FUJIFILM Dimatix Company Backgrounder," 2015.

[182] "FUJIFILM Dimatix launches new material printer DMP-2850," USA, 2016.

[183] "FUJIFILM Dimatix Materials Printer, DMP-2850, User Manual." FUJIFILM Dimatix, Inc, p. 168, 2016.

[184] P. G. Savva and C. N. Costa, "Inkjet Printing of Catalytic Materials," in *21st Century Nanoscience - A Handbook Design Strategies for Synthesis and Fabrication*, K. D. Sattler, Ed. Taylor and Francis, 2019.

[185] S. Magdassi, Ed., *The chemistry of Inkjet inks*. World Scientific Publishing Co. Pte. Ltd, 2010.

[186] X. Liu, T.-J. J. Tarn, F. Huang, and J. Fan, "Recent advances in inkjet printing synthesis of functional metal oxides," *Particuology*, vol. 19, pp. 1–13, Apr. 2014.

[187] X. Liu *et al.*, "Inkjet printing assisted synthesis of multicomponent mesoporous metal oxides for ultrafast catalyst exploration," *Nano Lett.*, vol. 12, no. 11, pp. 5733–5739, 2012.

[188] P. J. Smith and J. Stringer, "Chapter 15: Applications in Inkjet Printing," in *Fundamentals of Inkjet Printing: The Science of Inkjet and Droplets*, First., S. D. Hoath, Ed. Wiley-VCH Verlag GmbH & Co. KGaA, 2016, pp. 397–417.

[189] L. J. Deiner and T. L. Reitz, "Inkjet and Aerosol Jet Printing of Electrochemical Devices for Energy Conversion and Storage," *Adv. Eng. Mater.*, vol. 19, no. 7, pp. 1–18, 2017.

[190] S. Lee, T. Boeltken, A. K. Mogalicherla, U. Gerhards, P. Pfeifer, and R. Dittmeyer, "Inkjet printing of porous nanoparticle-based catalyst layers in microchannel reactors," *Appl. Catal. A Gen.*, vol. 467, pp. 69–75, 2013.

[191] H. Lee, K. Chou, and K. Huang, "Inkjet printing of nanosized silver colloids," *Nanotechnology*, vol. 16, pp. 2436–2441, 2005.

[192] P. C. Hiemenz and R. Rajagopalan, *Principles of Colloid and Surface Chemistry, Third Edition, Revised and Expanded*. 1997.

[193] J. E. Fromm, "Numerical calculation of the fluid dynamics of Drop-on-Demand jets," *IBM J. Res. Dev.*, vol. 28, no. 3, pp. 322–333, 1984.

[194] N. Reis and B. Derby, "Ink Jet Deposition of Ceramic Suspensions: Modeling and Experiments of Droplet Formation," *Mater. Res.*, vol. 625, pp. 117–122, 2000.

[195] D. Jang, D. Kim, and J. Moon, "Influence of Fluid Physical Properties on Ink-Jet Printability," *Langmuir*, vol. 25, no. 5, pp. 2629–2635, 2009.

[196] T. Driessen and R. Jeurissen, "Chapter 4: Drop Formation in Inkjet Printing," in *Fundamentals of Inkjet Printing: The Science of Inkjet and Droplets*, First., S. D. Hoath, Ed. Wiley-VCH Verlag GmbH & Co. KGaA, 2016, pp. 93–115.

[197] S. Schiaffino and A. A. Sonin, "Molten droplet deposition and solidification at low Weber numbers," *Phys. Fluids*, vol. 9, no. 11, pp. 3172–3187, 1997.

[198] S. Jung, H. J. Hwang, and S. H. Hong, "Chapter 8: Drops on Substrates," in *Fundamentals of Inkjet Printing: The Science of Inkjet and Droplets*, First., S. D. Hoath, Ed. Wiley-VCH Verlag GmbH & Co. KGaA, 2016, pp. 199–218.

[199] L. H. Tanner, "The Spreading of silicone oil drops on horizontal surfaces," *J. Phys. D. Appl. Phys.*, vol. 12, pp. 1473–1484, 1979.

[200] R. Rioboo, M. Marengo, and C. Tropea, "Time evolution of liquid drop impact onto solid, dry surfaces," *Exp. Fluids*, vol. 33, no. 1, pp. 112–124, 2002.

[201] D. Pesach and A. Marmur, "Marangoni Effects in the Spreading of Liquid

Mixtures on a Solid," *Langmuir*, vol. 3, no. 4, pp. 519–524, 1987.

[202] B. Derby, "Inkjet printing ceramics: From drops to solid," *J. Eur. Ceram. Soc.*, vol. 31, no. 14, pp. 2543–2550, 2011.

[203] R. D. Deegan, O. Bakajin, T. F. Dupont, G. Huber, S. R. Nagel, and T. A. Witten, "Capillary flow as the cause of ringstains from dried liquid drops," *Nature*, vol. 389, pp. 827–829, 1997.

[204] R. D. Deegan, O. Bakajin, T. F. Dupont, G. Huber, S. R. Nagel, and T. A. Witten, "Contact line deposits in an evaporating drop," *Phys. Rev. E*, vol. 62, no. 1, pp. 756–765, 2010.

[205] T. Liu, Z. G. Zeng, X. H. Wang, X. X. Yan, and Z. Y. Hu, "Application of Inkjet Printing to Fabricate Controllable Pt Catalyst Patterns for Low Temperature Catalytic Combustion," *Adv. Mater. Res.*, vol. 550–553, pp. 257–260, 2012.

[206] M. Siebert, R. R. Zimmermann, M. Armbrüster, and R. Dittmeyer, "Inkjet Printing of GaPd$_2$ into Micro-Channels for the Selective Hydrogenation of Acetylene," *ChemCatChem*, vol. 9, no. 19, pp. 3733–3742, 2017.

[207] J. Liu *et al.*, "A general synthesis of mesoporous metal oxides with well-dispersed metal nanoparticles via a versatile sol-gel process," *J. Mater. Chem. A*, vol. 1, no. 12, pp. 4038–4047, 2013.

[208] X. Liu *et al.*, "Supporting Information-Inkjet printing assisted synthesis of multicomponent mesoporous metal oxides for ultrafast catalyst exploration," *Nano Lett.*, vol. 12, no. 11, pp. 5733–5739, 2012.

[209] J. Fan, S. W. Boettcher, and G. D. Stucky, "Nanoparticle assembly of ordered multicomponent mesostructured metal oxides via a versatile sol-gel process," *Chem. Mater.*, vol. 18, no. 26, pp. 6391–6396, 2006.

[210] W. Michael, G. S. Herman, and B. A. Parkinson, "Combinatorial Approach to Identification of Catalysts for the Photoelectrolysis of Water," *Chem. Mater.*, vol. 17, no. 17, pp. 4318–4324, 2005.

[211] W. Michael and B. A. Parkinson, "Combinatorial Discovery and Optimization of a Complex Oxide with Water Photoelectrolysis Activity," *Chem. Mater.*, vol. 20, no. 7, pp. 2495–2502, 2008.

[212] J. N. Kondo, T. Yamashita, K. Nakajima, D. Lu, M. Hara, and K. Domen, "Preparation and crystallization characteristics of mesoporous TiO$_2$ and mixed

oxides," *J. Mater. Chem.*, vol. 15, no. 20, pp. 2035–2040, 2005.

[213] M. Arin *et al.*, "Inkjet printing of photocatalytically active TiO_2 thin films from water based precursor solutions," *J. Eur. Ceram. Soc.*, vol. 31, no. 6, pp. 1067–1074, 2011.

[214] J. He and B. A. Parkinson, "Combinatorial investigation of the effects of the incorporation of Ti, Si, and Al on the performance of α-Fe_2O_3 photoanodes," *ACS Comb. Sci.*, vol. 13, no. 4, pp. 399–404, 2011.

[215] A. D. Taylor, E. Y. Kim, V. P. Humes, J. Kizuka, and L. T. Thompson, "Inkjet printing of carbon supported platinum 3-D catalyst layers for use in fuel cells," *J. Power Sources*, vol. 171, no. 1, pp. 101–106, 2007.

[216] C. Wang, R. I. Tomov, T. B. Mitchell-Williams, R. V. Kumar, and B. A. Glowacki, "Inkjet printing infiltration of Ni-Gd:CeO_2 anodes for low temperature solid oxide fuel cells," *J. Appl. Electrochem.*, vol. 47, no. 11, pp. 1227–1238, 2017.

[217] M. A. Sukeshini, R. Cummins, T. L. Reitz, and R. M. Miller, "Ink-jet printing: A versatile method for multilayer solid oxide fuel cells fabrication," *J. Am. Ceram. Soc.*, vol. 92, no. 12, pp. 2913–2919, 2009.

[218] Z. Zhang *et al.*, "Patterning catalyst via inkjet printing to grow single-walled carbon nanotubes," *Chinese Chem. Lett.*, vol. 30, no. 2, pp. 505–508, 2019.

[219] K. Kordás *et al.*, "Inkjet Printing of Electrically Conductive Patterns of Carbon Nanotubes," *Small*, vol. 2, no. 8–9, pp. 1021–1025, 2006.

[220] J. R. Castrejon-Pita, W. R. S. Baxter, J. Morgan, S. Temple, G. D. Martin, and I. M. Hutchings, "Future, Opportunities and Challenges of Inkjet Technologies," *At. Sprays*, vol. 23, no. 6, pp. 541–565, 2013.

[221] G. H. Lim, J. M. Zhuo, L. Y. Wong, S. J. Chua, L. L. Chua, and P. K. H. Ho, "A transition solvent strategy to print polymer:fullerene films using halogen-free solvents for solar cell applications," *Org. Electron.*, vol. 15, no. 2, pp. 449–460, 2014.

[222] J. Haber, J. H. Block, and B. Delmon, "Manual of methods and procedures for catalyst characterization (Technical Report)," *Pure Appl. Chem.*, vol. 67, pp. 1257–1306, 1995.

[223] G. Busca, "Chapter 2 - Preparation of Solid Catalysts: A short Summary," in *Heterogeneous Catalytic Materials*, 2014, pp. 9–22.

[224] J. W. Van Honschoten, N. Brunets, and N. R. Tas, "Capillarity at the nanoscale," *Chem. Soc. Rev.*, vol. 39, no. 3, pp. 1096–1114, 2010.

[225] P. Munnik, P. E. de Jongh, K. P. de Jong, P. E. De Jongh, and K. P. De Jong, "Recent Developments in the Synthesis of Supported Catalysts," *Chem. Rev.*, vol. 115, no. 14, pp. 6687–6718, 2015.

[226] X. Liu, J. G. Khinast, and B. J. Glasser, "A parametric investigation of impregnation and drying of supported catalysts," *Chem. Eng. Sci.*, vol. 63, no. 18, pp. 4517–4530, 2008.

[227] B. A. T. Mehrabadi, S. Eskandari, U. Khan, R. D. White, and J. R. Regalbuto, "Chapter 1: A Review of Preparation Methods for Supported Metal Catalysts," in *Advances in Catalysis*, 1st ed., vol. 61, Elsevier Inc., 2017, pp. 1–35.

[228] C. Perego and P. Villa, "Catalyst preparation methods," *Catal. Today*, vol. 34, pp. 281–305, 1997.

[229] M. Behrens, "Catalyst Synthesis," *Fritz Haber Institute,* 2010.

[230] L. A. M. Hermans and J. W. Geus, "Interaction of nickel ions with silica supports during deposition-precipitation," *Stud. Surf. Sci. Catal.*, vol. 3, pp. 113–130, 1979.

[231] C. Cellier, S. Lambert, C. Lahousse, J. P. Pirard, P. Grange, and E. M. Gaigneaux, "Optimized conditions for the preparation of Pt supported catalysts by deposition-precipitation," *Stud. Surf. Sci. Catal.*, vol. 162, pp. 465–472, 2006.

[232] A. C. Pierre and G. M. Pajonk, "Chemistry of aerogels and their applications," *Chem. Rev.*, vol. 102, no. 11, pp. 4243–4265, 2002.

[233] R. D. Gonzalez, T. Lopez, and R. Gomez, "Sol-gel preparation of supported metal catalysts," *Catal. Today*, vol. 35, no. 3, pp. 293–317, 1997.

[234] M. V Landau, "Chapter 5: Sol-Gel Processing," in *Synthesis of Solid Catalysts*, K.P. de Jong, Ed. Wiley-VCH Verlag GmbH & Co. KGaA, Weinheim, 2009, pp. 83–109.

[235] K. Balakrishnan and R. D. Gonzalez, "Preparation of Pt/Alumina catalysts by the sol-gel method," *J. Catal.*, vol. 144, no. 2, pp. 395–413, 1993.

[236] R. Burch, P. J. Millmgton, and A. P. Walkerb, "Mechanism of the selective reduction of nitrogen mono oxide on platinum based catalysts in the presence of excess oxygen," *Appl. Catal. B Environ.*, vol. 4, no. 94, pp. 65–94, 1994.

[237] S. E. Van Bramer, "An Introduction to Mass Spectrometry." p. 38, 1998.

[238] H. Uchikawa, "Chapter 20: Specialized Techniques," in *Handbook of Analytical Techniques in Concrete Science and Technology*, 2001, pp. 820–934.

[239] J. Rajawat and G. Jhingan, "Chapter 11: Mass spectroscopy," in *Data Processing Handbook for Complex Biological Data Sources*, Elsevier Inc., 2019, pp. 1–20.

[240] P. H. Dawson, "Chapter 1: Introduction," in *Quadrupole Mass Spectrometry and its Applications*, 1976, pp. 1–7.

[241] J. H. Batey, "The physics and technology of quadrupole mass spectrometers," *Vacuum*, vol. 101, pp. 410–415, 2014.

[242] D. W. Koppenaal *et al.*, "MS Detectors," *Anal. Chem.*, vol. 77, no. 21, pp. 418 A–427 A, 2005.

[243] E. De Hoffmann, "Mass spectrometry," in *Kirk-Othmer Encyclopedia of Chemical Technology*, John Wiley & Sons, Inc., 2005, pp. 1–20.

[244] I. Tyrer-Tomkinson, "MASsoft Professional Version 7 Training Manual." HIDEN Analyticl, p. 84.

[245] O. D. Sparkman, Z. E. Penton, and F. G. Kitson, *Gas Chromatography and Mass Spectrometry*, Second. Academic Press. Inc., 2011.

[246] M. McMaster, *GC/MS: A Practical User's Guide*, Second. John Wiley & Sons, Inc., 2008.

[247] A.T. James and A. J. P. Martin, "Gas-liquid Partition Chromatography: the Separation and Micro-estimation of Volatile Fatty Acids from Formic Acid to Dodecanoic Acid," *Biochem. J.*, vol. 50, no. 5, pp. 679–690, 1952.

[248] O. D. Sparkman, Z. E. Penton, and F. G. Kitson, "Quantitation with GC/MS," *Gas Chromatogr. Mass Spectrom. A Pract. Guid.*, pp. 207–218, 2011.

[249] A. A. Ammann, "Inductively coupled plasma mass spectrometry (ICP MS): a versatile tool," *J. mass Spectrom.*, vol. 42, no. 7, pp. 419–427, 2007.

[250] *X Series ICP-MS System Overview*. Thermo Electron Corporation. All, 2005.

[251] R. Thomas, *Practicle guide to ICPMS*. New York: Marc el Dekker, Inc, 2004.

[252] K. S. W. Sing, "Reporting physisorption data for gas/solid systems with special reference to the determination of surface area and porosity," in *Pure and Applied Chemistry*, vol. 57, no. 4, 1984, pp. 603–619.

[253] S. Brunauer, P. H. Emmett, and E. Teller, "Adsorption of Gases in Multimolecular

Layers," *Am. Chem. Soc. (ACS Publ.*, vol. 60, no. 1, pp. 303–319, 1938.

[254] K. Sing, "The use of nitrogen adsorption for the characterisation of porous materials," *Colloids Surfaces A Physicochem. Eng. Asp.*, vol. 187–188, pp. 3–9, 2001.

[255] *Gemini V Operator's Manual V2*. Micromeritics Instrument Corporation, 2006.

[256] J. Zheng, "Silver-alumina Catalysts for Lean NO_x Reduction: Influence of Hydrothermal Ageing," Chalmers University of Technology, Sweden, 2011.

[257] W. Zhou, R. P. Apkarian, and Z. L. Wang, "Chapter 1: Fundamentals of Scanning Electron Microscopy," in *Scanning Microscopy for Nanotechnology: Techniques and Applications*, W. Zhou and Z. L. Wang, Eds. Springer, New York, NY, 2007, pp. 1–40.

[258] S. H. Aharinejad, A. Lametschwandtner, S. H. Aharinejad, and A. Lametschwandtner, "Chapter 3: Fundamentals of Scanning Electron Microscopy," in *Microvascular Corrosion Casting in Scanning Electron Microscopy*, Springer-Verlag/Wien, 1992, pp. 44–51.

[259] R. Anderhalt, "X-ray microanalysis in nanomaterials," in *Scanning Microscopy for Nanotechnology: Techniques and Applications*, W. Zhou and Z. L. Wang, Eds. Springer, New York, NY, 2007, pp. 76–100.

[260] A. Athappan, "Selective catalytic reduction of nitric oxide over cerium-doped activated carbons," University of Texas at Arlington, 2012.

[261] A. K. Chatterjee, "Chapter 8: X-Ray Diffraction," in *Handbook of Analytical Techniques in Concrete Science and Technology*, vol. 35, no. 2, V. S. Ramachandran and J. Beaudoin, Eds. 2001, pp. 275–332.

[262] A. Clearfield and N. Bhuvanesh, "X-Ray Powder Diffraction," *Encycl. Inorg. Chem.*, pp. 1–31, 2008.

[263] R. L. Snyder, "X-ray diffraction," in *X-ray Characterization of Materials*, E. Lifshin, Ed. Wiley-VCH Verlag GmbH, 1999, pp. 4–103.

[264] B. K. Tanner, "Chapter 1: Basic Dynamical X-Ray Diffraction Theory," in *X-ray Diffraction Topography*, 1976, pp. 1–23.

[265] J. Faber and T. Fawcett, "The Powder Diffraction File: present and future," *Acta Crystallogr. Sect. B Struct. Sci.*, vol. 58, no. 3, pp. 325–332, 2002.

[266] M. Devadas, "Selective Catalytic Reduction (SCR) of Nitrogen Oxides with

Ammonia over Fe-ZSM5," Swiss Federal Institute of Technology Zurich, 2006.

[267] T. Ishii and T. Kyotani, "Chapter 14: Temperature Programmed Desorption," in *Materials Science and Engineering of Carbon: Characterization*, Elsevier Inc., 2016, pp. 287–305.

[268] V. Rakić and L. Damjanović, "Chapter 4: Temperature-Programmed Desorption (TPD) Methods," in *Calorimetry and Thermal Methods in Catalysis*, Springer-Verlag Berlin Heidelberg, 2013, pp. 131–174.

[269] M. E. Davis and R. J. Davis, "Chapter 5: Heterogeneous Catalysis," in *Fundamentals of Chemical Reaction Engineering*, vol. 4, 2012, pp. 133–183.

[270] J. M. Thomas and W. J. Thomas, *Principles and Practice of Heterogeneous Catalysis*. VCH Verlagsgesellschaft mbH, 1997.

[271] M. P. Fuller and P. R. Griffiths, "Diffuse Reflectance Measurements by Infrared Fourier Transform Spectrometry," *Anal. Chem.*, vol. 50, no. 13, pp. 1906–1910, 1978.

[272] A. Drochner and G. H. Vogel, "Chapter 14: Diffuse Reflectance Infrared Fourier Transform Spectroscopy: an In situ Method for the Study of the Nature and Dynamics of Surface Intermediates," in *Methods in Physical Chemistry, First Edition*, R. Schäfe and P. C. Schmidt, Eds. Wiley-VCH Verlag GmbH & Co. KGaA, 2012, pp. 445–475.

[273] J. Ryczkowski, "Spectroscopy in Catalysis," *Catal. Today*, vol. 68, no. 4, pp. 263–381, 2001.

[274] B. Klingenberg and M. A. Vannice, "NO adsorption and decomposition on La2O3 studied by DRIFTS," *Appl. Catal. B Environ.*, vol. 21, no. 1, pp. 19–33, 1999.

[275] B. Stuart, "Infrared spectroscopy," *Kirk-Othmer Encycl. Chem. Technol.*, vol. 4, pp. 1–18, 2015.

[276] "Infrared Radiation," in *Van Nostrand's Encyclopedia of Chemistry.*, Fifth., John Wiley & Sons, Inc., 2005, pp. 1–19.

[277] P. Kubelka and F. Munk, "An Article on Optics of Paint Layers," *Z. Tech. Phys*, vol. 12, pp. 593–601, 1931.

[278] C. M. Kalamaras, *Master Course Notes, CHEM-800: FTIR and EELS Spectroscopy Techniques: Basic Principles and Applications in Heterogeneous Catalysis*. Nicosia: University of Cyprus, 2007.

[279] G. G. Olympiou and A. M. Efstathiou, "Industrial NO_x control via H_2-SCR on a novel supported-Pt nanocatalyst," *Chem. Eng. J.*, vol. 170, no. 2–3, pp. 424–432, 2011.

[280] A. M. Efstathiou, J. T. Gleaves, and G. S. Yablonsky, "Transient Techniques: Temporal Analysis of Products and Steady State Isotopic Transient Kinetic Analysis," *Charact. Solid Mater. Heterog. Catal. From Struct. to Surf. React.*, vol. 2, pp. 1013–1073, 2012.

[281] S. L. Shannon and J. G. Goodwin, "Characterization of Catalytic Surfaces by Isotopic-Transient Kinetics during Steady-State Reaction," *Chem. Rev.*, vol. 95, pp. 677–695, 1995.

[282] J. Happel, "Transient Tracing," *Chem. Eng. Sci.*, vol. 33, pp. 1567–1568, 1978.

[283] C. O. Bennett, "Understanding Heterogeneous Catalysis Through the Transient Method," *Am. Chem. Soc. (ACS Publ.*, no. 14, pp. 1–32, 1982.

[284] P. Biloen, "Transient Kinetic Methods," *J. Mol. Catal.*, vol. 21, no. 1–3, pp. 17–24, 1983.

[285] K. Tamura and S. Naito, "Chapter 5.2.5.: Isotopic Labeling and Kinetic Isotope Effects," in *Handbook of Heterogeneous Catalysis, 1st Edition*, G. Ertl, H. Knözinger, and J. Weitkamp, Eds. VCH Verlagsgesellschaft mbH., 1997, pp. 911–1051.

[286] R. P. Bell, "Recent Advances in the Study of Kinetic Hydrogen Isotope Effects," *Chem. Soc. Rev.*, vol. 3, no. November, pp. 513–544, 1973.

[287] C. Kemball, "The Catalytic Exchange of Hydrocarbons with Deuterium," *Adv. Catal.*, vol. 11, no. C, pp. 223–262, 1959.

[288] G. Liu, D. Willcox, M. Garland, and H. H. Kung, "The role of CO_2 in methanol synthesis on CuZn oxide: An isotope labeling study," *J. Catal.*, vol. 96, no. 1, pp. 251–260, 1985.

[289] R. Burch, A. A. Shestov, and J. A. Sullivan, "A steady-state isotopic transient kinetic analysis of the $NO/O_2/H_2$ reaction over Pt/SiO_2 catalysts," *J. Catal.*, vol. 186, pp. 353–361, 1999.

[290] C. M. Kalamaras, I. D. Gonzalez, R. M. Navarro, J. L. G. Fierro, and A. M. Efstathiou, "Effects of reaction temperature and support composition on the mechanism of water - Gas shift reaction over supported-Pt catalysts," *J. Phys.*

Chem. C, vol. 115, no. 23, pp. 11595–11610, 2011.

[291] P. G. Savva, C. N. Costa, and A. M. Efstathiou, "The mechanism of reduction of NO with H_2 in strongly oxidizing conditions (H_2-SCR) on a novel Pt/MgO-CeO$_2$ catalyst: Effects of reaction temperature," *Kinet. Catal.*, vol. 49, no. 5, pp. 743–747, 2008.

[292] *Microactivity Reference User's Manual - MA0890COSTA*. PID Eng&Tech, 2009.

[293] L. Valanidou, C. Theologides, A. A. Zorpas, P. G. Savva, and C. N. Costa, "A novel highly selective and stable Ag/MgO-CeO$_2$-Al$_2$O$_3$ catalyst for the low-temperature ethanol-SCR of NO," *Appl. Catal. B Environ.*, vol. 107, no. 1–2, pp. 164–176, 2011.

[294] A. Janbey, W. Clark, E. Noordally, S. Grimes, and S. Tahir, "Noble metal catalysts for methane removal," *Chemosphere*, vol. 52, no. 6, pp. 1041–1046, 2003.

[295] *SPECTRUM 100 Series, User's Guide*. PerkinElmer, Inc, 2009.

[296] B. C. Smith, *Fundamentals of Fourier Transform Infrared Spectroscopy*, Second. Taylor & Francis Group, 2011.

[297] E. Xue, K. Seshan, and J. R. H. Ross, "Roles of supports, Pt loading and Pt dispersion in the oxidation of NO to NO$_2$, and of SO$_2$, to SO$_3$," *Appl. Catal. B Environ.*, vol. 11, pp. 65–79, 1996.

[298] T. Ioannides and X. E. Verykios, "Charge Transfer in Metal Catalysts Supported on Doped TiO$_2$: A Theoretical Approach Based on Metal–Semiconductor Contact Theory," *J. Catal.*, vol. 161, pp. 560–569, 1996.

[299] S. L. Schroeder and M. Gottfried, "Temperature-Programmed Desorption (TPD), Thermal Desorption Spectroscopy (TDS)," *Adv. Phys. Chem. Lab, FU Berlin*. pp. 1–22, 2002.

[300] C. Zupanc, A. Hornung, O. Hinrichsen, and M. Muhler, "The interaction of hydrogen with Ru/MgO catalysts," *J. Catal.*, vol. 209, no. 2, pp. 501–514, 2002.

[301] S. Subramanian, "Temperature-Programmed Reduction of Platinum Group Metals Catalysts," *Platin. Met. Rev.*, vol. 36, no. 2, pp. 98–103, 1992.

[302] K. Kunimori and T. Uchijima, "The interaction of H_2 with Pt/Al$_2$O$_3$ and Pt/TiO$_2$ catalysts at high temperatures," *Stud. Surf. Sci. Catal.*, vol. 17, pp. 197–206, 1983.

[303] R. Kramer and M. Fischbacher, "Hydrogen pretreatment effects on the hydrogenolysis of methylcyclopentane on Pt/SiO$_2$ and Pt/Al$_2$O$_3$ catalysts," *J. Mol.*

Catal., vol. 51, pp. 247–259, 1989.

[304] Z. Paál and P. G. Menon, "Hydrogen Effects in Metal Catalysts," *Catal. Rev. Sci. Eng.*, vol. 25, no. 2, pp. 229–324, 2007.

[305] C. N. Costa, P. G. Savva, J. L. G. Fierro, and A. M. Efstathiou, "Industrial H_2-SCR of NO on a novel Pt/MgO-CeO_2 catalyst," *Appl. Catal. B Environ.*, vol. 75, no. 3–4, pp. 147–156, 2007.

[306] C. N. Costa and A. M. Efstathiou, "Low-temperature H_2-SCR of NO on a novel Pt/MgO-CeO_2 catalyst," *Appl. Catal. B Environ.*, vol. 72, pp. 240–252, 2007.

[307] C. N. Costa and A. M. Efstathiou, "Pt/Mg-Ce-O catalyst for NO/H_2/O_2 lean de-NO_x reaction," *Environ. Chem. Lett.*, vol. 2, no. 2, pp. 55–58, 2004.

[308] C. Zhang *et al.*, "The influence of Pt loading and dispersion on the NO_x storage and reduction performance of Pt/K_2CO_3/$Co_1Mg_2Al_1O_x$ catalysts," *Catal. Today*, pp. 1–11, 2018.

[309] M. Shelef and H. S. Gandhi, "Ammonia Formation in Catalytic Reduction of Nitric Oxide by Molecular Hydrogen. II. Noble Metal Catalysts," *Ind. Eng. Chem. Prod. Res. Dev.*, vol. 11, no. 4, pp. 393–396, 1972.

[310] M. A. P. Dekkers, M. J. Lippits, and B. E. Nieuwenhuys, "Supported gold/MO_x catalysts for NO/H_2 and CO/O_2 reactions," *Catal. Today*, vol. 54, no. 4, pp. 381–390, 1999.

[311] C. N. Costa *et al.*, "An Investigation of the NO/H_2/O_2 (Lean De-NO_x) Reaction on a Highly Active and Selective Pt/$La_{0.7}Sr_{0.2}Ce_{0.1}FeO_3$ Catalyst at Low Temperatures," *J. Catal.*, vol. 209, no. 2, pp. 456–471, 2002.

[312] H. J. Kreuzer and L. C. Wang, "Field induced surface chemistry of NO," *J. Chem. Phys.*, vol. 96, no. 8, pp. 6065–6069, 1990.

[313] E. Shustorovich and A. T. Bell, "Decomposition and reduction of NO on transition metal surfaces: bond order conservation Morse potential analysis," *Surf. Sci.*, vol. 289, no. 1–2, pp. 127–138, 1993.

[314] W. C. Hecker and A. T. Bell, "Reduction of NO by H_2 over Silica-Supported Rhodium: Infrared and Kinetic Studies," *J. Catal.*, vol. 92, pp. 247–259, 1985.

[315] A. Väliheikki *et al.*, "Selective catalytic reduction of NO_x by hydrogen (H_2-SCR) on WO_x-promoted $Ce_zZr_{1-z}O_2$ solids," *Appl. Catal. B Environ.*, vol. 156–157, no. x, pp. 72–83, 2014.

[316] A. M. Efstathiou, C. N. Costa, and L. G. Fierro, "Catalyst for the reduction of NO to N_2 with hydrogen under NO_x oxidation conditions. US 7,105,137 B2," 2006.

[317] M. Kantcheva, "Identification, Stability, and Reactivity of NO_x Species Adsorbed on Titania-Supported Manganese Catalysts," *J. Catal.*, vol. 204, pp. 479–494, 2001.

[318] K. A. Anderson, *Encyclopedia of Separation Science*. Elsevier Ltd., 2000.

[319] B. Breit, "Supramolecular Approaches to Generate Libraries of Chelating Bidentate Ligands for Homogeneous Catalysis," *Angew. Chemie Int. Ed.*, vol. 44, pp. 6816–6825, 2005.

[320] K. Nakata, Y. Kayama, K. Shimazu, A. Yamakata, S. Ye, and O. Masatoshi, "Surface-Enhanced Infrared Absorption Spectroscopic Studies of Adsorbed Nitrate, Nitric Oxide, and Related Compounds 2: Nitrate Ion Adsorption at a Platinum Electrode," *Langmuir*, vol. 24, no. 8, pp. 4358–4363, 2008.

[321] S. S. Mulla *et al.*, "Reaction of NO and O_2 to NO_2 on Pt: Kinetics and catalyst deactivation," *J. Catal.*, vol. 241, no. 2, pp. 389–399, 2006.

[322] A. L. Goodman, T. M. Miller, and V. H. Grassian, "Heterogeneous reactions of NO_2 on NaCl and Al_2O_3 particles," *J. Vac. Sci. Technol.*, vol. 16, no. 4, pp. 2585–2590, 1998.

[323] M. Schraml-Marth, A. Wokaun, and A. Baiker, "Surface Structure of Crystalline and Amorphous Chromia Catalysts for the Selective Catalytic Reduction of Nitric Oxide. IV. Diffuse Reflectance FTIR Study of NO Adsorption and Reaction," *J. Catal.*, vol. 138, pp. 306–321, 1992.

[324] A. Eichler and J. Hafner, "Molecular Precursors in the Dissociative Adsorption of O_2 on Pt (111)," *Phys. Revie Lett.*, vol. 79, pp. 4481–4484, 1997.

[325] N. B. Arboleda, H. Kasai, W. A. Diño, and H. Nakanishi, "Potential Energy of H_2 Dissociation and Adsorption on Pt (111) Surface: First-Principles Calculation," *Jpn. J. Appl. Phys.*, vol. 46, no. 7A, pp. 4233–4237, 2007.

[326] A. C. Luntz, J. K. Brown, and M. D. Williams, "Molecular beam studies of H_2 and D_2 dissociative chemisorption on Pt (111)," *Chem. Phys.*, vol. 97, pp. 5240–5246, 1990.

[327] M. A. Nygren and L. G. M. Pettersson, "Theoretical rnodelling of metal oxides. Influence of field strength on atomic oxygen adsorption and a simple model

reaction: $O_{adS}+CO \rightarrow CO_2$," *Chem. Phys. Lett.*, vol. 230, pp. 456–462, 1994.

[328] M. Machida, D. Kurogi, and T. Kijima, "Role of hydrogen-spillover in H_2-NO reaction over Pd-supported NO_x-adsorbing material, M_nO_x-CeO_2," *J. Phys. Chem. B*, vol. 107, no. 1, pp. 196–202, 2003.